

Inaugural dissertation
for
obtaining the doctoral degree
of the
Combined Faculty of Mathematics, Engineering and Natural Sciences of
the
Ruprecht - Karls - University
Heidelberg

Presented by
M.Sc. Martin Würtz
Born in Ludwigshafen am Rhein
Oral examination: 19.03.2024

Integrative structural biology of recombinant γ -tubulin-related complexes

Referees: Prof. Dr. Elmar Schiebel

Dr. Stefan Pfeffer

Acknowledgments

First of all, I would like to thank my supervisors, Prof. Dr. Elmar Schiebel and Dr. Stefan Pfeffer, as well as my defense committee, Prof. Dr. Michael Knop and Dr. Niccolò Banterle, for reading my thesis and attending my defense. I am incredibly fortunate to have conducted my PhD research in an environment characterized by the close collaboration between the Schiebel and Pfeffer groups. This synergy not only made my work more interesting, but also underlined the essence of interdisciplinary teamwork in scientific progress. I am especially grateful to Elmar for his inspiring passion for science, his always-open door, and the freedom he gave me to develop and conduct research independently. I am equally grateful to Stefan for his insightful guidance and unwavering support throughout my journey. Both have been incredibly accessible and supportive. Their commitment was clearly demonstrated in the countless hours spent in sub-group meetings over the last four years.

I would also like to express my sincere thanks to Dr. Sebastian Eustermann and the entire Eustermann group at EMBL. Sebastian has been instrumental in my journey, not only as a TAC member, but his valuable suggestions, especially in the early stages of my project, and advice beyond my specific topic have been crucial. I am grateful to have been welcomed so warmly into his laboratory and supported by the whole group, especially after the collapse of the ZMBH building. My time as part of the Eustermann lab has been important in shaping my path towards becoming an independent scientist.

Collaboration has been a fundamental aspect of my PhD. I would like to thank all my collaborators, such as Dr. Enrico Atorino, for their invaluable help with experiments and advice. Special thanks go to my tandem partner, Dr. Erik Zupa, whose collaboration was not only scientifically productive, but also created a pleasant working environment in which I learned a lot together with him. The first half of 2021, during which we had a run, will be remembered as a time of exciting new insights, and the “Aprilscherz” we organized with Bram Vermeulen remains a fond memory of our teamwork.

A big thank you also goes to Dr. Annett Neuner and the entire γ -tubulin sub-group for their collaborative spirit and teamwork in tackling various challenges. I am deeply grateful to the entire Schiebel Lab, both current and former members. It's rare to find a group that works so harmoniously, where members are not just colleagues but friends who are happy to help each other. I'm grateful for the polite laughter at my jokes and memes (Labless4ever), the patience with my embarrassing attempts to speak Italian (Jlenia ☺), and our daily coffee routines. Also, many thanks to Enzo and his team for providing much-needed afternoon fuel. I would also like to thank my students - Ariani, Teresa, Arnas, Nethaji, Annika and Giulia - for not only enduring me as a supervisor, but also for their enthusiastic contribution to our projects. Special thanks go to Giulia and Bram, whose collaboration was not only fun but also a great source of motivation. In addition, the engaging discussions with the entire Pfeffer office were much appreciated.

Ein ganz besonderer Dank gilt Ursula Jäkle. Uschi, das Urgestein im Labor Schiebel, hat mir unzählige Tricks und Kniffe beigebracht. Immer hilfsbereit und mit einer gehörigen Portion Humor ausgestattet, hat sie mir vor allem die nötige Gelassenheit im Laboralltag vermittelt. Vielen Dank, Uschi.

Danke an TKKG für die vielen Online-Rätsel, die wir gemeinsam gelöst haben und natürlich an den Stammtisch, der von Anfang an ein wichtiger Ausgleich war. Apropos Ausgleich, danke auch an Julian und Robert. Last but not least danke ich natürlich meiner Familie, meinen Eltern, die mich immer in allem unterstützt haben und mir letztendlich diese Möglichkeiten eröffnet haben und Mona, ohne die ich gar nicht weiß, was es heißt, Wissenschaftler zu sein.

Summary

Microtubules, dynamic cytoskeletal filaments with a cylindrical shape made up of $\alpha\beta$ -tubulin dimers, are essential for the process of mitosis and meiosis, where their precise control in the spatial and temporal dimension is critical. γ -tubulin complexes, universally present in eukaryotes, are the most important factors for microtubule nucleation, the *de novo* formation of microtubules from $\alpha\beta$ -tubulin dimers. Recent cryo-electron microscopy (cryo-EM) studies of γ -tubulin complexes marked a breakthrough in the microtubule nucleation field. In these studies, the structure of the vertebrate γ -tubulin ring complex (γ -TuRC) was determined, uncovering that 14 gamma-tubulin complex proteins (GCP) bound to 14 γ -tubulin proteins (14 spokes) together with the microproteins MZT1/2 and one actin molecule assemble into a defined asymmetrical left-handed spiral that forms a structural template for a 13-protofilament microtubule. However, the absence of a finely tunable system for a bottom-up dissection of the individual components' functions hinders a comprehensive understanding of γ -TuRC's action in microtubule organizing centers (MTOCs), like the centrosome.

Building upon the architectural consensus of the γ -TuRC subunits determined by cryo-EM studies, my PhD work focused on the development of a recombinant expression system in insect cells for the reconstitution of human γ -TuRC and related complexes. This recombinant system yielded protein complexes with structural and functional properties highly similar to the native γ -TuRC and enabled targeted analysis of individual γ -TuRC components, such as the function of the actin molecule that was surprisingly found in the lumen of the vertebrate γ -TuRC. In collaboration with Erik Zupa, I could demonstrate by cryo-EM analysis that the absence of actin in mutant γ -TuRC does not compromise the assembly and structural integrity of the complex, but its integration in the luminal bridge is important for controlling γ -TuRC conformation and its function inside cells. Additionally, I discovered novel MZT1 docking sites and a modular assembly pathway of the human γ -TuRC, evolving from a 4-spoke GCP4-GCP5-GCP4-GCP6 intermediate to the 14-spoke asymmetric ring by successive addition of γ -tubulin small complexes (GCP2-GCP3).

Furthermore, I studied the augmin complex, a hetero-octamer of HAUS (homologous to augmin subunits) proteins, which is a crucial γ -TuRC recruiting factor and enables microtubule nucleation from pre-existing microtubules. Augmin plays a conserved role across species, from plants to humans, orchestrating microtubule amplification via the microtubule branching pathway, which is especially relevant to build the mitotic spindle. Despite its central role, a lack of structural information limits our understanding of augmin's functional sites. Employing an integrative approach, I determined the molecular architecture of the augmin complex in collaboration with Erik Zupa, revealing the collective contribution of the N-termini of HAUS2, 6, 7, and 8 to the formation of a composite microtubule binding unit.

In summary, this work represents a significant advance in the characterization of two key components of the microtubule branching pathway. Moreover, it lays the foundation for further targeted investigations of γ -TuRC and augmin, in particular their cooperation on microtubules, a fundamental aspect of cell division.

Zusammenfassung

Mikrotubuli, dynamische Filamente des Zytoskeletts mit zylindrischer Form, die aus $\alpha\beta$ -Tubulin-Dimeren aufgebaut sind, bilden die grundlegendsten Einheiten für den Prozess der Mitose und Meiose, wo ihre präzise räumliche und zeitliche Regulation entscheidend ist. γ -Tubulin-Komplexe, die in Eukaryoten universell vorkommen, sind die wichtigsten Faktoren für die Mikrotubuli-Nukleation, die Neubildung von Mikrotubuli aus $\alpha\beta$ -Tubulin-Untereinheiten. Ein Durchbruch auf dem Gebiet der Mikrotubuli-Nukleation wurde durch aktuelle Kryo-Elektronenmikroskopie (cryo-EM)-Studien an γ -Tubulin-Komplexen erzielt. In diesen Studien wurde die Struktur des γ -Tubulin-Ringkomplexes (γ -TuRC) von Wirbeltieren bestimmt. Es zeigte sich, dass 14 Gamma-Tubulin-Komplex-Proteine (GCP), die an 14 γ -Tubulin-Proteine gebunden sind (14 Speichen), zusammen mit den Mikroproteinen MZT1/2 und einem Aktin-Molekül eine definierte asymmetrische linkshändige Spirale bilden, die ein Strukturmuster für einen 13-Protofilament-Mikrotubulus darstellt. Das Fehlen eines kontrollierbaren Systems verhindert jedoch eine Bottom-up-Analyse der verschiedenen Funktionen der einzelnen γ -TuRC-Komponenten. Dies erschwert weiterhin unser Verständnis der Rolle von γ -TuRC in Mikrotubuli-Organisationszentren (MTOCs) wie dem Zentrosom.

Basierend auf dem architektonischen Konsens der γ -TuRC Untereinheiten, der durch cryo-EM Studien identifiziert wurde, konzentrierte sich meine Doktorarbeit auf die Entwicklung eines rekombinanten Expressionssystems in Insektenzellen für die Rekonstitution des humanen γ -TuRC und verwandter Komplexe. Dieses rekombinante System lieferte Proteinkomplexe mit strukturellen und funktionellen Eigenschaften, die dem nativen γ -TuRC sehr ähnlich sind, und ermöglichte die gezielte Analyse einzelner Komponenten des γ -TuRC, wie z.B. die Funktion des Aktinmoleküls, welches überraschenderweise im Lumen des Vertebraten- γ -TuRC gefunden wurde. In Zusammenarbeit mit Erik Zupa konnte ich durch cryo-EM-Analysen zeigen, dass das Fehlen von Aktin in mutiertem γ -TuRC die Assemblierung und strukturelle Integrität des Komplexes nicht beeinträchtigt, obschon die Integration von Aktin in die Lumenale-Brücke wichtig für die Kontrolle der Konformation von γ -TuRC und dessen Funktion in der Zelle ist. Darüber hinaus entdeckte ich neue MZT1-Bindungsstellen sowie einen modularen Assemblierungsmechanismus des humanen γ -TuRC. Letzterer bildet sich aus einem 4-speichigen GCP4-GCP5-GCP4-GCP6-Zwischenprodukt durch sukzessive Addition von Einheiten des kleinen γ -Tubulin-Komplexes (GCP2-GCP3) zu einem 14-speichigen asymmetrischen Ring.

Weiterhin habe ich den Augmin-Komplex untersucht, ein Hetero-Oktamer von HAUS-Proteinen (homologe zu Augmin-Untereinheiten), welcher ein entscheidender γ -TuRC-Rekrutierungsfaktor ist und die Nukleation von Mikrotubuli von der Oberfläche bereits existierender Mikrotubuli ermöglicht. Augmin spielt eine konservierte Rolle, von Pflanzen bis zum Menschen, indem es die Mikrotubuli-Vermehrung über den Mikrotubuli-Verzweigungsweg orchestriert, was besonders wichtig für den Aufbau der mitotischen Spindel ist. Trotz seiner zentralen Rolle schränkt der Mangel an strukturellen Informationen unser Verständnis der Funktion von Augmin ein. Mit Hilfe eines integrativen Ansatzes habe ich in Zusammenarbeit mit Erik Zupa die molekulare Architektur des Augmin-Komplexes bestimmt und den kollektiven Beitrag der N-Termini von HAUS2, 6, 7 und 8 zur Bildung einer mehrkomponentigen Mikrotubuli-Bindungseinheit aufgezeigt.

Zusammenfassend stellt diese Arbeit einen bedeutenden Fortschritt in der Charakterisierung von zwei Schlüsselkomponenten des Mikrotubuli-Verzweigungsweges dar. Darüber hinaus legt sie den Grundstein für weitere gezielte Untersuchungen von γ -TuRC und Augmin, insbesondere ihrer Interaktion mit Mikrotubuli, einem der grundlegenden Aspekte der Zellteilung.

Table of content

1	Introduction.....	1
1.1	<i>Integrative structural biology</i>	1
1.1.1	Proteins	1
1.1.2	Molecular cloning, protein expression and biochemical sample preparation.....	2
1.1.3	Electron microscopy	5
1.1.4	Crosslinking mass spectrometry and neural network-based protein structure prediction..	6
1.2	<i>Cells.....</i>	7
1.2.1	Cellular organization and cytoskeleton	7
1.2.2	Microtubules (MTs).....	8
1.3	<i>γ-tubulin and γ-tubulin complexes</i>	10
1.3.1	The vertebrate γ -TuRC	12
1.3.2	γ -TuRC architecture	13
1.3.3	MT nucleation.....	17
1.4	<i>The centrosome as the main MT organizing center</i>	20
1.4.1	The centrosome architecture	20
1.4.2	γ -Tubulin associated factors of the PCM.....	21
1.4.3	Other MTOCs	23
1.4.4	Centrosomal factors and diseases.....	24
1.5	<i>The cell cycle.....</i>	25
1.5.1	Cell cycle regulation and centrosome cycle	25
1.6	<i>The mitotic spindle</i>	28
1.6.1	Structural units of the mitotic spindle	28
1.6.2	The RanGTP pathway	29
1.6.3	The augmin complex.....	30
1.6.4	MT branching by γ -TuRC and augmin	31
1.6.5	Molecular composition of the augmin- γ -TuRC network	33
1.7	<i>Aims of this thesis</i>	35
2	Results.....	36
2.1	<i>The recombinant γ-TuRC expression system.....</i>	36
2.1.1	General cloning strategy of the recombinant γ -TuRC expression system.....	36
2.1.2	Workflow of recombinant reconstitution experiments	38
2.1.3	Reconstitution and characterization of the recombinant human γ -TuRC with a minimal set of co-expressed proteins	40
2.1.4	Optimization of the recombinant system allows cryo-EM analysis of γ -TuRC	43
2.2	<i>Cryo-EM analysis of recombinant human γ-TuRC</i>	47

2.2.1	Reconstruction of assembly intermediates reveal a modular assembly pathway of the vertebrate γ -TuRC	47
2.2.2	MZT1 modules have multiple binding sites on the γ -TuRC	49
2.3	<i>Modularized production and characterization of γ-TuRC compartments</i>	53
2.3.1	Reconstitution of recombinant human γ -TuSC	53
2.3.2	Reconstitution of the 4-spoke intermediate γ -TuRC ^{ΔGCP2/3}	56
2.4	<i>The role of actin in the lumen of γ-TuRC</i>	58
2.4.1	Actin IP experiments identify the GCP6 _{N126} -MZT1 module as actin binding domain.....	58
2.4.2	Recombinant γ -TuRC ^{ΔN56-GCP6} shows that actin integration is not essential for γ -TuRC's structural integrity.....	59
2.4.3	Analysis of GCP6 mutants in cell culture models indicate that actin integration into γ -TuRC is relevant for its function	65
2.5	<i>Unraveling the molecular architecture of the augmin complex by an integrative structural biology approach</i>	70
2.5.1	Characterization of the augmin TIII tetramer.....	71
2.5.2	Characterization of the augmin octamer architecture.....	79
2.5.3	The HAUS architecture reveals the N-clamp as composite MT binding unit	83
3	Discussion	87
3.1	<i>The recombinant γ-TuRC expression system allows structural and functional analysis of γ-tubulin complexes</i>	87
3.2	<i>Cryo-EM analysis of recombinant human γ-TuRC reveals a modular assembly mechanism</i>	90
3.3	<i>Actin is not required for γ-TuRC assembly and structural integrity but modulates its function in vivo</i>	95
3.4	<i>Identification of all 7 MZT1 modules on γ-TuRC</i>	98
3.5	<i>The molecular architecture of the augmin complex reveals a composite MT binding unit</i>	99
3.6	<i>Conclusions and perspectives on the γ-TuRC-augmin axis</i>	103
4	Material and Methods	106
4.1	<i>Materials</i>	106
4.2	<i>Molecular cloning methods</i>	110
4.2.1	PCR	110
4.2.2	Gel electrophoresis	110
4.2.3	InFusion/NEBuilder Hifi assembly, mutagenesis, and Cre-recombination	111
4.2.4	Transformation into <i>E. coli</i>	111
4.2.5	Mini DNA preparation.....	112
4.2.6	DNA construct verification and Sequencing	113
4.2.7	Molecular cloning of the recombinant human γ -TuRC	115

4.2.8	Molecular cloning of the recombinant <i>X. laevis</i> augmin complex.....	115
4.2.9	Molecular cloning of <i>E. coli</i> expression constructs.....	116
4.2.10	Molecular cloning of GCP6 constructs for experiments in human cell culture system ...	119
4.3	<i>Protein expression</i>	120
4.3.1	General handling of <i>E. coli</i> strains for baculovirus production and protein expression...	120
4.3.2	Protein expression in <i>E. coli</i> for actin IP experiments.....	120
4.3.3	Insect cell culture	120
4.3.4	Recombinant baculovirus production	120
4.3.5	Recombinant protein expression in insect cells.....	122
4.4	<i>Protein purification</i>	122
4.4.1	Protein purification of constructs expressed in insect cells.....	122
4.4.2	Purification of minimal recombinant γ -TuRC	123
4.4.3	Purification of optimized γ -TuRC, γ -TuRC ^{ΔN56-GCP6} , γ -TuSC and γ -TuRC ^{ΔGCP2/3}	123
4.4.4	Purification of augmin complexes.....	124
4.4.5	Size exclusion chromatography and anion exchange chromatography.....	124
4.5	<i>Biochemistry methods</i>	125
4.5.1	SDS-polyacrylamide gel electrophoresis (SDS-PAGE).....	125
4.5.2	Immunoblot analysis	125
4.5.3	Actin IP experiment.....	126
4.5.4	<i>In vitro</i> MT nucleation assay for negative stain EM.....	127
4.5.5	<i>In vitro</i> MT nucleation assay for comparing recombinant γ -TuRC constructs	127
4.6	<i>Electron microscopy methods</i>	128
4.6.1	Negative staining and general EM data processing.....	128
4.6.2	Negative stain EM of minimal γ -TuRC	129
4.6.3	Negative stain EM of γ -TuRC, γ -TuRC ^{ΔN56-GCP6} , γ -TuSC and γ -TuRC ^{ΔGCP2/3}	130
4.6.4	Negative stain EM of augmin complexes.....	130
4.6.5	Cryo-EM experiments	131
4.7	<i>Integrative structural biology methods</i>	131
4.7.1	Liquid chromatography tandem-MS of recombinant γ -TuRC	131
4.7.2	Crosslinking MS	132
4.7.3	Crosslinking MS data analysis	132
4.7.4	AF-Multimer predictions.....	132
4.8	<i>Cell biology methods</i>	133
4.9	<i>Image processing and statistical analysis</i>	134
4.9.1	Image processing.....	134
4.9.2	Statistical analysis.....	134
5	Publications	135
6	References	136

1 Introduction

1.1 Integrative structural biology

Analysis of the three-dimensional structure of biologically relevant macromolecular complexes is pivotal in contemporary life sciences. A prime example is the discovery of the deoxyribonucleic acid (DNA) helix by Watson and Crick in 1953. This breakthrough unveiled not just the molecule's chemical composition and structure but immediately revealed its cellular function and two modes of replication depending on strand orientation [1]. To probe the intricacies of life's molecules, particularly proteins and multi-protein assemblies, a variety of long-established and more recent advanced techniques come into play. An integrative approach is essential, melding various sources of evidence to elucidate the architecture of the molecule and derive its function. The subsequent sections will briefly describe the relevant techniques and aspects this thesis touches upon.

1.1.1 Proteins

Beyond essential molecule classes like lipids and sugars, nucleic acids and proteins establish the central dogma of life [2]. Genetic information is encoded in the double-stranded DNA helix, which is then transcribed to single-stranded ribonucleic acid (RNA) as messengers. Subsequently, this RNA, along with proteins, translates the information into functional units. Interestingly, life on Earth employs D-nucleic acids and L-amino acids. This fact might be a single event “decision” at the beginning of the evolution of life on Earth and is likely to be different on other planets in the universe. Recent endeavors are directed at producing 'mirrored' versions of these primary molecules [3–5]. This theoretical idea has been a topic since the discovery of molecular chirality [6,7]. In this context it is important to note that D-amino acids are also relevant for processes inside cells although not as building blocks of proteins [8]. Proteins are macromolecules composed of amino acid chains. Each amino acid possesses an amino group, a carboxyl group, a single H-atom, and a distinct functional group anchored to a central C-atom (C_α). These amino acids are linked together via peptide bonds to form the polypeptide chain. Therefore, each unmodified polypeptide chain has an end with a free amino group, known as the N-terminus, and another end with a free carboxyl group, termed the C-terminus. Earth's living organisms utilize 22 distinct amino acids (20 canonical amino acids plus

Introduction

selenocysteine and pyrrolysine) to build their polypeptides. The variance in these amino acids lies in their functional group, the side chain, ranging from a simple H-atom (as in glycine) to hydrophobic groups (like leucine), polar ones (such as serine), charged amino acids (e.g., arginine), or unique functional groups like the one in cysteine. Driven by their amino acid sequence, biochemical surroundings, and interaction partners, these linear polypeptide chains fold into specific 3D structures. Common structural motifs include the α -helix and the β -sheet. This three-dimensional conformation is crucial, dictating a protein's role, whether as a structural component, an enzyme, or in another function [9].

1.1.2 Molecular cloning, protein expression and biochemical sample preparation

Molecular cloning of genes into circular DNA plasmids has a 50-year-long history [10–12], decisively empowering molecular biology to systematically investigate the components of life and utilize biotechnology approaches for a variety of applications. Over the years, the cloning toolbox has been continually refined, as exemplified by the integration of the Cre/loxP system, which uses a bacteriophage protein for specific DNA site recognition and subsequent recombination [13–15]. A multitude of improved commercialized methods (Gibson Assembly, NEBuilder Hifi DNA assembly, InFusion) do not rely on specific DNA sequences and restriction enzymes, but rather on the polymerase chain reaction (PCR) [16,17] based amplification of DNA fragments with the introduction of complementary overhangs, which allows seamless fusion of two or more DNA fragments under the action of additional proteins like exonucleases [18].

Molecular cloning has allowed to use host organisms to produce recombinant proteins, which is one of the most important branches of biotechnology today. The simplest and most used system is the expression of recombinant proteins in *Escherichia coli* (*E. coli*) [19]. For certain target proteins, an alternative to the *E. coli* expression system is necessary, particularly when expressing genes from another organism that, due to incompatibility of for example protein folding or modifications, the host cannot produce as functional proteins. Consequently, the baculovirus-based expression in insect cells is a common system to produce recombinant vertebrate proteins [20,21]. Improvements over the years, from systems where a plaque assay was required to test for the presence of viruses that carry the gene of interest (GOI),

Introduction

to *E. coli*-based methods (known as Bac-to-Bac) where a site-specific insertion of target genes under baculovirus promoters into cloned baculoviral DNA (bacmids) [22] allowed for easier screening of positive recombinant baculoviruses. Further improved systems are using Tn7-based transposition of the GOI under baculovirus promoters [23,24]. Figure 1 depicts the process of baculovirus generation and protein expression in insect cells. It is important to achieve a balance of the baculovirus titer, and therefore between the amount of protein expressed and the decline in sample quality, which results from increasing cell death over time (manifesting as protein degradation, presence of free proteases, etc.). Particularly for multi-gene constructs, the quality of the recombinant baculovirus is paramount. Although the integrity of viruses generally diminishes over storage time, a more significant concern is that each virus generation increases the likelihood of unwanted gene excisions and replication errors. These errors can compromise effective expression [25,26].

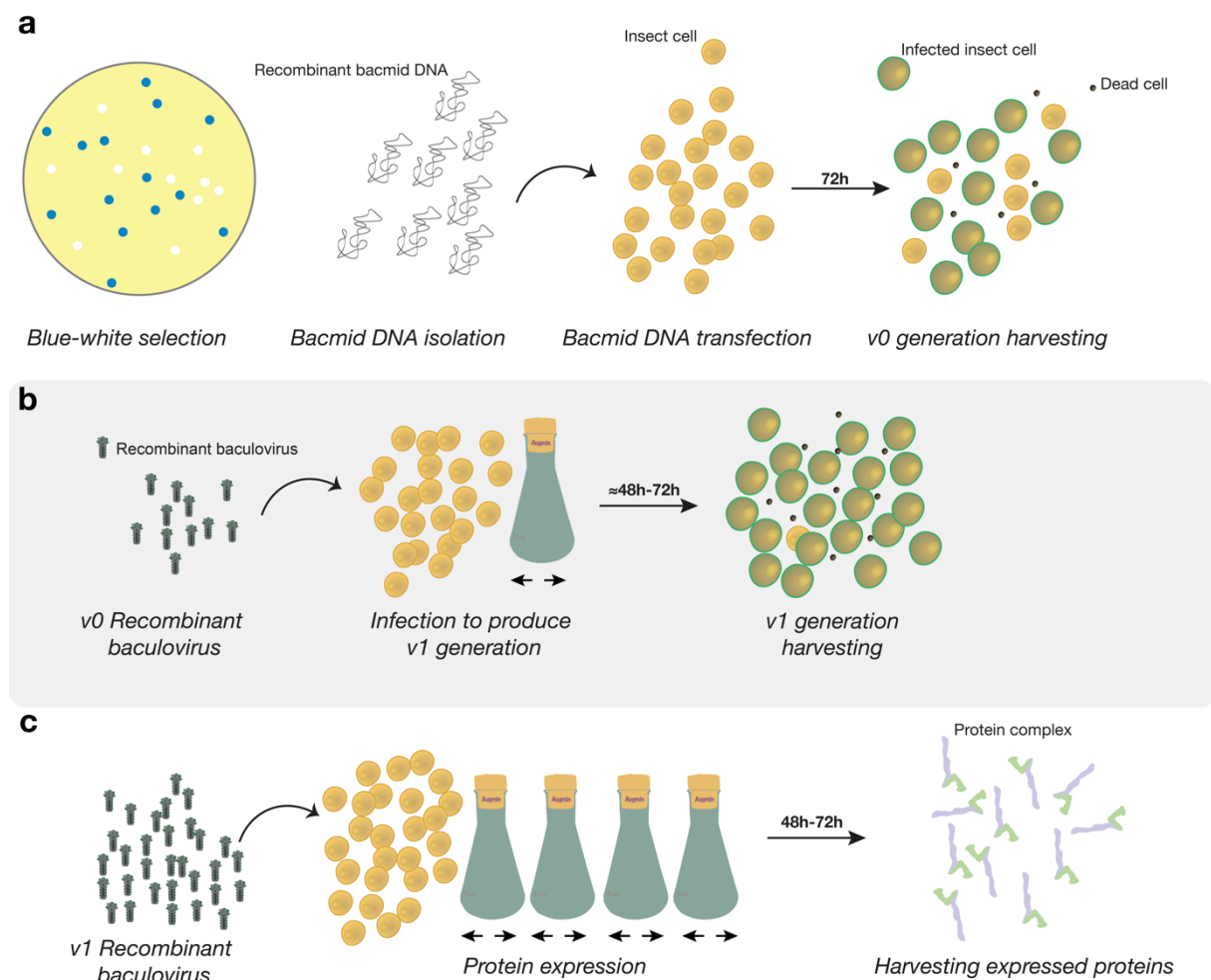


Figure 1 Protein expression in insect cells: a, *E. coli* strains with recombinant bacmids, large plasmids ≈100 kbp (kilo base pairs) with the integrated GOI under baculoviral promoters, are selected via Blue-white screening. After screening, bacmids are isolated from transformation-positive colonies and used for transfection into insect cells. Insect cells take up the bacmids and

Introduction

*produce recombinant baculoviruses and proteins. Infected cells show a significant increase in cell diameter. At a late phase of the infection, cells are lysed (cells die) and release the first generation of viruses (v0). **b**, v0 recombinant baculoviruses are amplified by infecting new insect cells in shaking cultures at the logarithmic expansion phase. In comparison to **a**, more cells get infected and produce a larger amount of the second recombinant baculovirus generation (v1). **c**, usually v1 recombinant baculoviruses are used to infect insect cells in shaking cultures at the logarithmic expansion phase to produce the recombinant proteins.*

Recently improved plasmids and protocols allow for the expression of multi-protein complexes [27–30]. One of the established methods is the MultiBac system (Geneva Biotech), based on acceptor and donor vectors with multiple cloning sites of baculoviral expression cassettes with Cre-loxP recombination of donor and acceptor plasmids to create the multi-gene constructs for the translocation into bacmids [31]. For the biochemical purification of proteins, a variety of affinity TAGs [32] and subsequent chromatography methods, like size exclusion chromatography (SEC) or ion exchange chromatography (IEC) can be used. The design of the purification protocol depends on the target proteins and their intended applications. This is particularly relevant for protein complexes that comprise multiple proteins and exhibit varied component stoichiometries. For instance, to illustrate purification strategies for related protein complexes, two literature examples are given. The recombinantly expressed chromatin remodeler INO80 was successfully purified for structural analysis either through tandem purifications using two distinct affinity tags on a single component followed by IEC [33], or using a single affinity TAG on one component and subsequent IEC [34]. In contrast, strategies for purifying native γ -tubulin complexes are more variable. Some methods relied on the affinity for a component with high stoichiometry without further purification [35], while others utilized the affinity for a tagged component complemented by additional chromatography steps [36]. Another method leveraged a binding partner (fused to an affinity TAG) of the γ -tubulin complexes, which was followed by proteolytic digestion of the affinity tag and sucrose gradient centrifugation [37]. These examples underscore that while specific target optimizations can yield analogous protocols, there is also room for diverse strategies or some fluidity in the purification scheme. Such approaches aim to isolate multiprotein complexes and secure adequate sample purity and concentration for structural examinations, like cryogenic electron microscopy (cryo-EM), which typically demands concentrations around 0.5 mg/ml. These nuances warrant consideration during the experimental design.

1.1.3 Electron microscopy

Electron microscopy (EM) is a detection (analytical) method that uses electrons instead of photons, unlike light microscopy. Since the wavelength of electrons depends on their energy and they scatter upon impacting a specimen, electrons can, in theory, be used to achieve high-resolution imaging of the material being studied. However, due to the relatively high energy required, image acquisition presents technical challenges for radiation-sensitive biological material, which provides low inherent contrast. A notable past example of EM experiments are the micrographs showing "beads-on-a-string". These represented isolated chromatin fibers, displaying DNA wrapped around nucleosomes for the first time [38,39].

This was achieved by using negative/positive staining in combination with transmission electron microscopy (TEM) [40]. In negative stain EM, samples are placed on a grid covered by a continuous thin layer of carbon with a thickness in the nanometer range. These particles, once attached to the surface, are treated with heavy metal salts, such as uranyl acetate. The stain encapsulates the particles, providing strong amplitude contrast of the particles outer shells when imaged in TEM. This method offers insights into the organization and general structure of protein complexes, though the attainable resolution is significantly restricted (Figure 2d). In cryo-EM, a stain-free technique for TEM sample preparation, the sample is vitrified. This process prevents the water molecules from forming crystals, ensuring preservation of the sample in its native state [41,42]. Thus, the sample is applied onto a carbon grid, and rapidly plunge frozen in liquid ethane. Afterwards the vitrified grids are stored in liquid N₂ and the sample is imaged using a transmission electron microscope.

Cryo-EM has recently experienced a transformative leap in application possibilities. The term "resolution-revolution" emerged from a comment [43] on an article describing the 3D cryo-EM structure of the yeast mitochondrial large ribosomal subunit [44]. An essential advance that positioned cryo-EM as a leading method for determining molecular structures was the introduction of a new generation of electron detectors: the direct detector devices (DDD) [45]. DDD cameras have a significant edge over charge-coupled devices (CCD). These modern cameras can capture images in a dose fraction mode, where the final dose is spread across multiple frames. This is crucial for correcting stage drift and beam-induced particle movements during

Introduction

acquisition, known as motion correction, effectively mitigating the blurring of micrographs.

In this context, another crucial aspect of the resolution revolution were refined image processing algorithms based on maximum likelihood, for example the regularized likelihood optimization (RELION) [46] to process the cryo-EM data. In a general single particle analysis (SPA) data processing pipeline, the movie frames are aligned through correct for motion (motion correction) and summed to generate an integrated image with improved contrast. Afterwards the contrast transfer function (CTF) is estimated, which is the Fourier transform of the point spread function of the microscope and describes the preservation of signal at different spatial frequencies of the image. Cryo-EM data is typically captured with a certain range of defocus values. Importantly, high spatial frequencies (best preserved when close to focus) provide high-resolution details, while low spatial frequencies (best preserved when defocused) offer lower resolution information, influencing the visibility and contrast of particles in 2D images, which is important for initial particle identification and alignment. To generate 2D or 3D representations of the sample, thousands of 'particles' are identified from the images either manually or using various picking algorithms that might need a template or training [46–49]. Subsequently, the picked particles are used for 2D and/or 3D classification procedures to generate structurally homogenous particle sets, and subsequent subjected to high-resolution 3D refinement. Today's cryo-EM instruments, cameras, and SPA workflows allow for the reconstruction of 3D structures with a resolution in the Ångström (Å) regime and, in special cases, up to 1 Å resolution (0.1 nm) [50,51].

1.1.4 Crosslinking mass spectrometry and neural network-based protein structure prediction

In addition to methods of protein structure determination like X-ray crystallography, nuclear magnetic resonance (NMR) spectroscopy and cryo-EM, the integrative structural biology field has additional techniques at its disposal. These provide orthogonal information to structural methods, helping to provide a more complete picture of the sample being analyzed. Advances in mass spectrometry (MS) analysis allow to get important information about protein-protein interactions, especially in large protein complexes via crosslinking MS. Here, protein complexes are incubated with crosslinkers like bis[sulfosuccinimidyl] (BS3), which have reactive groups

Introduction

separated by a spacer, and covalently link nearby amino acids. Afterwards, the protein complex gets digested and analyzed via tandem liquid chromatography-MS (LC-MS/MS) [52,53]. Important improvements in estimating the false discovery rate (FDR) [54] allow for a broader field of application [55–57].

The most recent development facilitating structural biology on much broader scale is neural network-based protein structure prediction. In 2021, DeepMind presented their open-source tool AlphaFold2 (AF), which enables protein structure prediction based on the amino acid sequence [58]. AF uses neural network approaches on physical and geometrical constraints of proteins, the large data base of known protein structures, as well as evolutionary aspects by incorporation of multiple sequence alignments (MSA) into the workflow [58]. AF and similar applications like RoseTTAFold [59], or extensions like AlphaFold-Multimer (AF-Multimer) [60] for the prediction of protein complexes, allow an easy visual overview of potential domains of proteins, the identification of proteins in experimental structure data [61,62] and assistance in the identification of interaction interfaces between proteins [63,64].

1.2 Cells

“What is life?” – Erwin Schrödinger, a physicist who got the Nobel Prize for his contribution to quantum theory, addressed this question at a time when the actual molecules and structure of the genetic information and its proteinaceous products were much less clear than today (see [65,66]). Life is the result of the fundamental laws of nature, and life on Earth, which began about 3.8 billion years ago [67], is organized into cells [68,69]. Evolution on this planet led to three branches of cellular organisms - the domains of life - including Bacteria, Archaea and Eukaryotes [70,71]. Since the protein complexes studied in this thesis are eukaryotic, the following chapters focus primarily on eukaryotic biology.

1.2.1 Cellular organization and cytoskeleton

A crucial part of eukaryotic cellular organization is the cytoskeleton, which consists of three main types of polymers: actin filaments, intermediate filaments, and microtubules (MTs).

The most abundant protein in eucaryotic cells is actin [72], which forms helical polar filaments (F-actin) by oligomerization. The dynamic actin network is essential for cell shape as well as cellular motility [73,74]. Actin has an adenosine triphosphate (ATP)

Introduction

binding site and exhibits ATPase activity, and in humans and other organisms, it has three very closely related isoform classes: α -, β -, and γ -actin, along with several actin-related proteins (ARPs) [75].

Another component of the cytoskeleton are intermediate filaments [76]. They are made up of various proteins and can form diverse oligomers, always consisting of a single type of protein. These filaments are the most flexible elements of the cytoskeleton [77]. Intermediate filaments are also found in the nucleus, where they are assembled by lamin proteins [78] and define in a crosstalk with chromatin and other components the nuclear architecture [79].

The third type of the cytoskeleton components are the MTs [80,81] (Figure 2). These hollow cylinders, with a diameter of 25 nm [82], act as tracks for intracellular transport and allow cells to exert forces. They are crucial for forming the mitotic and meiotic spindle to segregate genetic material and are also involved in the formation of cellular extensions like cilia and flagella [83].

1.2.2 Microtubules (MTs)

MTs consist of oligomers of $\alpha\beta$ -tubulin dimers (Figure 2a) that form longitudinal head-to-tail interactions, the so-called protofilaments [84]. Tubulin proteins are folded in an ATP-dependent manner by the chaperonin TRiC/CCT in concert with prefoldin [85,86]. The assembly of the $\alpha\beta$ -tubulin heterodimer is assisted by the tubulin cofactors TBCA-TBCE [87,88]. In addition to the longitudinal interaction of tubulin dimers, tubulins undergo also lateral interactions to form the polar MT tubes (Figure 2b), which present a varying protofilament number when assembled *in vitro* [89]. However, *in vivo*, MTs generally consist of 13 protofilaments [90] (Figure 2c). Importantly, in a 13-protofilament MT with a 3-start helical arrangement, a so-called seam exists. At the seam, β -tubulin directly interacts laterally with an α -tubulin, creating a notable structural discontinuity within the MT lattice, which is otherwise characterized by homotypic interactions between neighboring protofilaments [91](Figure 2b).

Introduction

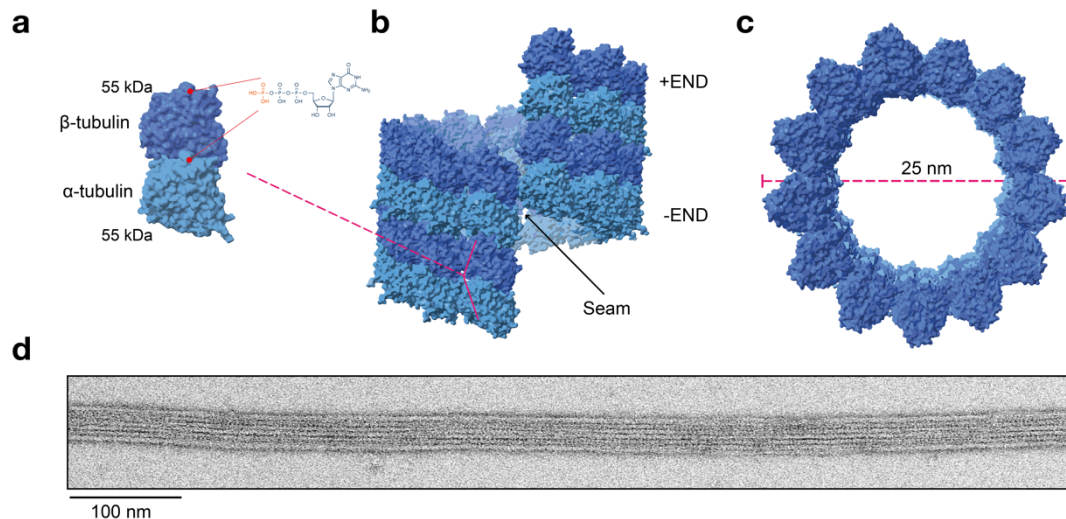


Figure 2 MT are $\alpha\beta$ -tubulin oligomers: **a**, α - and β -tubulin form tubulin heterodimers. The tubulins have Guanosine-5'-triphosphate/Guanosine diphosphate (GTP/GDP)-binding pockets, where α -tubulin is always bound to GTP. Highlighted is the chemical formula of GTP, the phosphate group that gets hydrolyzed in β -tubulin is indicated in orange. **b,c** $\alpha\beta$ -tubulin dimers oligomerize into hollow cylinders, with 25 nm diameter when consisting of 13 protofilaments. The seam is indicated. **d**, negative stain EM micrograph of Taxol-stabilized MT polymerized by porcine tubulin. Scale bar is given. Schemes of $\alpha\beta$ -tubulin and MT are generated based on PDB-6EW0 [92].

MTs are polar oligomers and they have a faster growing +END (β -tubulin as last subunit) [93], where binding of additional tubulin dimers preferentially occurs. The α -tubulin side is called the -END. $\alpha\beta$ -tubulins possess GTP/GDP binding pockets; α -tubulin's pocket is always GTP-bound, while β -tubulin can hydrolyze GTP and exchange GDP for GTP [94]. MT elongation at the +END is also linked to GTP hydrolysis [95]. Importantly, the GTP/GDP state of the β -tubulin pocket at the +END of the MT is important for the dynamics of the MT [96]. In the GTP state the MT is stable, whereas in the GDP state it is less stable [97]. Therefore, MT follow a dynamic instability behavior where MT growth can end in the so-called catastrophe - a rapid shrinkage once GTP hydrolysis occurs faster than the addition of new $\alpha\beta$ -tubulin subunits, which on the other hand can be rescued and growth can reoccur [98].

In human and other higher eukaryotes several isoforms of α - and β -tubulin exist, which mainly differ in their C-terminal tail region [99]. Of note, plant species often have multiple genes encoding for α - and β -tubulin, like *Arabidopsis thaliana* (*A. thaliana*) with more than 5 genes of each [100,101]. For further reading on MTs in plants, see [102]. The role and functions of different tubulin isoforms and modifications are under active investigation [103]. Importantly, MTs can be formed independent of other proteins *in vitro* in the presence of Mg-GTP, through polymerization of $\alpha\beta$ -tubulin dimers [104]. Cryo-electron tomography (Cryo-ET) analysis of *in vitro* nucleated MTs indicates that

Introduction

there is a heterogeneity in the overall configuration including variation in seam number and thereby induced holes in the MT lattice where individual dimers are missing [91]. In this context, an interesting example are neuronal cells, where long-lived MTs are essential for axonal transport [105]. On the other hand, in mitosis thousands of MTs need to be nucleated in a relatively short timescale, resulting in the complex network of the mitotic spindle [106]. Therefore, the nature of MTs *in vivo* is highly dynamic and tightly regulated depending on the cell fate by various tubulin or MT binding factors [107,108]. One important example of a group of MT +END tracking proteins are end-binding (EB) proteins [109].

Given their complexity and the requirement for spatial and temporal-specific nucleation, MTs are organized by MT-organizing centers (MTOCs) (see Chapter 1.4). The primary regulator of MT assembly is γ -tubulin, a definitive marker for MTOCs and part of the tubulin superfamily. γ -tubulin, more precisely the *mipA* (MT interacting protein) gene, was first discovered in *Aspergillus nidulans* (*A. nidulans*) [110], but γ -tubulin turned out to be highly conserved in eukaryotic organisms and crucial for organizing MT networks [111–114].

1.3 γ -tubulin and γ -tubulin complexes

In the following years, the role of γ -tubulin dependent MT nucleation was established in many organisms, like in *Saccharomyces cerevisiae* (*S. cerevisiae*) where the γ -tubulin homologue is encoded by the *TUB4* gene [115]. The conservation of γ -tubulin is underlined by experiments, which showed that expression of γ -tubulin from different organisms in *Saccharomyces pombe* (*S. pombe*) results in functional MT organization [116,117], indicating the universal functionality of γ -tubulin in concert with $\alpha\beta$ -tubulin. Human cells encode two γ -tubulin genes (*TUBG1*, *TUBG2*) [112], where *TUBG1* is the isoform constitutively expressed in most cell types. *TUBG2* is mainly expressed in the neuronal system [118,119]. γ -tubulin has a similar structural architecture as α - and β -tubulin, and is therefore also a GTPase [120–122]. There is evidence that suggests that GTP binding of γ -tubulin affects its function [123,124], but the role of GTP hydrolysis remains unclear. Of note, the behavior of recombinant γ -tubulin *in vitro* indicates that it can form filamentous oligomers via lateral interactions, which is also observed and studied *in vivo* (summarized in [113]). Nonetheless, findings from experiments conducted in *Xenopus laevis* (*X. laevis*) egg extracts suggest a significant disparity in the abundance of γ -tubulin compared to $\alpha\beta$ -

Introduction

tubulin, with γ -tubulin exhibiting a mere 1% expression level [125]. This observation underscores the underlying requirement for finely tuned and specific regulatory mechanisms, contingent upon the involvement of additional proteins.

Consequently, a few years subsequent to the initial discovery of γ -tubulin, several research groups embarked on elucidating γ -tubulin complexes from diverse organisms. In the case of *X. laevis*, Zhang et al. isolated and characterized the γ -tubulin complex, employing negative stain EM to reveal its distinctive structure which was described as "rings that appear as left-handed helices". Moreover, they identified its role in capping the MT -END, facilitating MT nucleation [126]. Zhang et al. detected at least 7 different proteins with very different molecular masses and various stoichiometries in their purification of the γ -tubulin ring complex (γ -TuRC). In *S. cerevisiae*, it was found that two copies of γ -tubulin form a heterotetramer with the two proteins Spc97 and Spc98 (Figure 3) [127,128]. The mammalian counterparts of these two proteins are referred to as γ -tubulin complex proteins (GCP) [120]. In *Drosophila melanogaster* (*D. melanogaster*), two compositionally different γ -tubulin complexes could be purified [129]. The smaller complex consisted of γ -tubulin and Dgrip84-Dgrip91 (homologues to GCP2 and GCP3), similar to the composition observed in the yeast complex. In contrast, the larger complex includes additional Dgrip proteins (163, 128, 75s) in comparatively lower stoichiometry. Consequently, this biochemical data, combined with structural analysis [130], has elucidated that the γ -TuRC of *D. melanogaster* comprises a complex resembling a "lockwasher" characterized partially by repeating units of the γ -tubulin small complex (γ -TuSC), consisting of GCP2 (Dgrip84/Spc97), GCP3 (Dgrip91/Spc98) and two γ -tubulin proteins.

After conducting negative stain EM analysis of the *S. cerevisiae* γ -TuSC, a distinct Y-shaped structure emerged, providing strong evidence that γ -tubulin complexes serve as templates for MT formation (Figure 3) [131]. In agreement, further structural analysis on yeast γ -TuRC underlined this template model [132], where γ -tubulin proteins arrange in a ring-like spiral that matches the 13-fold MT geometry. This template serves as a seed for MT nucleation (Figure 3b) and subsequently caps on the other hand the MT -END (Figure 3c) [133]. Recent studies have provided high-resolution information on γ -tubulin complexes in yeast [134,135]. Importantly, as described

Introduction

above, there is a major difference in the γ -tubulin complexes from fungi species like *S. cerevisiae* and *Candida albicans* (*C. albicans*) to other, especially vertebrate cells. The γ -TuRC from these fungi species is built by repeating units of γ -TuSCs, whereas in most other species the γ -TuRC contains additional GCP proteins. The following chapter focuses on the vertebrate γ -TuRC and its molecular architecture.

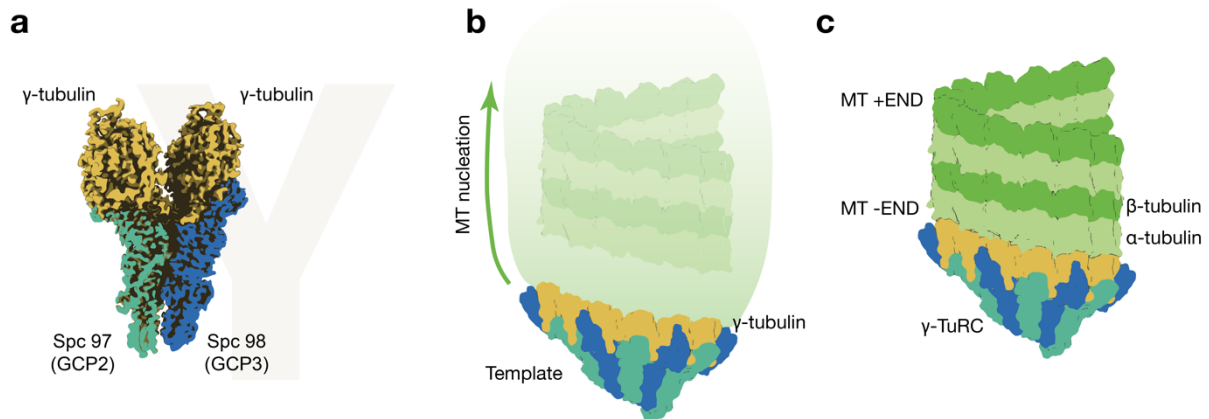


Figure 3 γ -tubulin complexes and MT nucleation: **a**, the basic unit of γ -tubulin complexes is the γ -TuSC, a heterotetramer built by two γ -tubulin proteins bound to one copy of Spc97 (GCP2) and Spc98 (GCP3) arranged in a Y-shape structure. Scheme is prepared based on the structure (EMD-11835 PDB-7ANZ) and adapted from [135]. **b**, in the template model, γ -TuSCs arrange laterally to form a ring of γ -tubulin that templates the formation of MT. **c**, the γ -TuRC template binds the MT -END while allowing growth of the MT +END. The schemes **b**, **c** were prepared based on (PDB-6DPV and PDB-6TF9).

1.3.1 The vertebrate γ -TuRC

In 2001, all GCP proteins (GCP2-GCP6) of the human γ -TuRC were identified [136]. The authors raised the question: why are there so many different GCP proteins with similar domain architecture and, therefore, probably similar functions? This was underlined by the crystal structure of GCP4 [137], which shed light on the architecture of conserved γ -tubulin ring protein domains 1 and 2 (GRIP1 and GRIP2) [129,136,138], where GRIP1 is the N-terminal domain and GRIP2 the C-terminal domain of GCPs. In addition, this study introduced the theory that the GRIP2 domain of all GCP proteins binds to γ -tubulin [137], while the GRIP1 domain is important for the GCP-GCP interaction.

Based on initial experiments with *D. melanogaster* and *X. laevis* it was established that the γ -TuRC comprises over a dozen γ -tubulin molecules and a similar number of GCP proteins with a molecular mass between 70-250 kilodalton (kDa). The γ -TuRC is a substantial molecular assembly exceeding clearly two megadalton (MDa) in size. In addition to the GCPs, the γ -TuRC includes non-GRIP domain-containing proteins.

Introduction

Notably, a component featuring WD40 repeats was first identified in the purification of the *D. melanogaster* γ -TuRC. This protein was named the gamma ring protein with WD repeats (Dgp71WD) [139]. The human orthologue, named “neural precursor cell expressed, developmentally down-regulated 1” (NEDD1) was shown to be an important γ -TuRC targeting factor [140,141]. Of note, the gene of NEDD1 was identified more than 10 years earlier in the context of central nervous system development [142,143]. Early experiments on NEDD1 depletion highlighted its pivotal role in γ -TuRC recruitment to the centrosome, while also revealing that it is not essential for γ -TuRC integrity. NEDD1 was found to be essential in plants, especially crucial for MT organization in mitosis [144]. In this context, the mitotic phosphorylation of NEDD1 serves as a key regulatory mechanism for multiple pathways (see Chapter 1.4 - 1.6), such as MT nucleation during spindle formation in proximity to chromosomes [141].

In addition to *NEDD1*, *C13orf37* and *FAM128A/B* were identified in a systematic screen in human cell lines as interactors to γ -TuRC and they were therefore called mitotic-spindle organizing proteins associated with a ring of γ -tubulin (MOZART1, MOZART2A/B, here MZT1, MZT2A/B) [145–147]. Besides γ -TuRC recruitment factors, the small nucleoside diphosphate kinase 7 (NME7) was consistently identified in γ -TuRC purifications [145,147,148] and in this respect, it is considered a γ -TuRC component.

Of note, there has been a debate about the nomenclature, proposing to name NEDD1 as GCP-WD, MZT1 as GCP7, and MZT2 as [141,147], because they are part of the γ -TuRC. However, because they lack GRIP domains and have no significant sequence or structural similarity to the GCP proteins that form the primary scaffold of the γ -TuRC, only the proteins containing GRIP domains are referred to as GCPs today.

1.3.2 γ -TuRC architecture

As briefly described in Chapter 1.1.2, three different approaches in independent studies resulted in the characterization of the basic architecture of native γ -TuRC from *X. laevis* egg extract [35] and human cells [36,37]. Almost 30 years have passed since the first descriptions of γ -tubulin complexes from *X. laevis* before its structural elucidation by cryo-EM (see [135,149]).

The cryo-EM analysis unraveled a (GCP2-3)₄-GCP4-GCP5-GCP4-GCP6-(GCP2-3)₁ asymmetric arrangement of GCP proteins, conserved from frog to man, which results

Introduction

in a 5:5:2:1:1 stoichiometry of the different GCP proteins. They are organized in a left-handed spiral (Figure 4). Via the GRIP1 domains the GCP proteins form strong interactions with each other, while γ -tubulin is bound to the GRIP2 domains (Figure 4b). Thus, the γ -TuRC comprises 14 GCP- γ -tubulin units, subsequently referred to as spokes. Position 1 is characterized by the first GCP2- γ -tubulin, while position 14 is marked by the last GCP3- γ -tubulin unit. Notably, due to the left-handed spiral arrangement, spoke 14 partially overlaps with spoke 1 along the spiral axis (Figure 4a). In addition to the spoke arrangement of γ -tubulin and the GRIP domains, a rigid structural scaffold spans across the inner surface of the spiral core. The so-called luminal bridge spans from spokes 9-12 (GCP4, GCP5, GCP4, GCP6) to spoke 2 (GCP3). It was speculated that this luminal bridge is formed by the large GCP6 insertion domain [35], but extensive analysis of the cryo-EM data of the human γ -TuRC showed that it consists of a complex of multiple γ -TuRC components [150]. Within the luminal bridge two molecules of MZT1 are intercalated with the N-terminus of one molecule of GCP3 and GCP6. This nicely confirmed previous studies, that suggested that MZT1 can interact with N-termini GCPs like GCP3 or GCP6 [151,152] (Figure 4c). Moreover, recent cryo-EM and X-ray crystallography data, showed that GCP3 and GCP5 N-Termini can form complexes with MZT1 [153], further supporting that MZT1 can form such modules with all three GCP proteins (GCP3,5,6) [150,153]. However, only the GCP6-N-terminus and two potential GCP3 binding sites could be visualized at the ring complex: one in the luminal bridge and one additional density located at spoke 14. However, the resolution attained in all cryo-EM reconstruction did not allow unambiguous identification. This leads to the open question of the function of these MZT1 modules. Their location in this central part of the γ -TuRC, the luminal bridge, suggests a crucial role for γ -TuRC integrity in agreement with efficient MZT1 depletion experiments causing the disassembly of the γ -TuRC [152]. In contrast, another study has suggested that MZT1 is dispensable for the integrity of the γ -TuRC, but instead plays a crucial role in the recruitment of γ -TuRC, potentially through its interaction with NEDD1 [151]. This finding could indicate a multi-faceted role for MZT1, especially since the location of a significant portion of the bound MZT1 molecules could not be elucidated by cryo-EM, likely due to the inherent flexibility of the MZT1-GCP-N-terminus modules when they are not firmly docked to the γ -TuRC scaffold. Similarly, Wieczorek et al. were able to identify a single MZT2 molecule in a

Introduction

complex with the GCP2 N-terminus, due to their centrosomin (Cnn) motif 1 (CM1)-based purification method. MZT2 was found to interact with coiled-coil helices of the CM1 (see Chapter 1.4.2), situated at the specific interface between spoke 12 and 13 [37,150]. Importantly, this sheds light on a potential recruitment mechanism for γ -TuRC through CM1-containing proteins, in which the MZT2 module engages in a stable interaction at a defined interface. However, the remaining four potential MZT2 modules could not be resolved using cryo-EM, much like the "missing" MZT1 modules, due to their flexibility and lack of specific binding partners (Figure 4c).

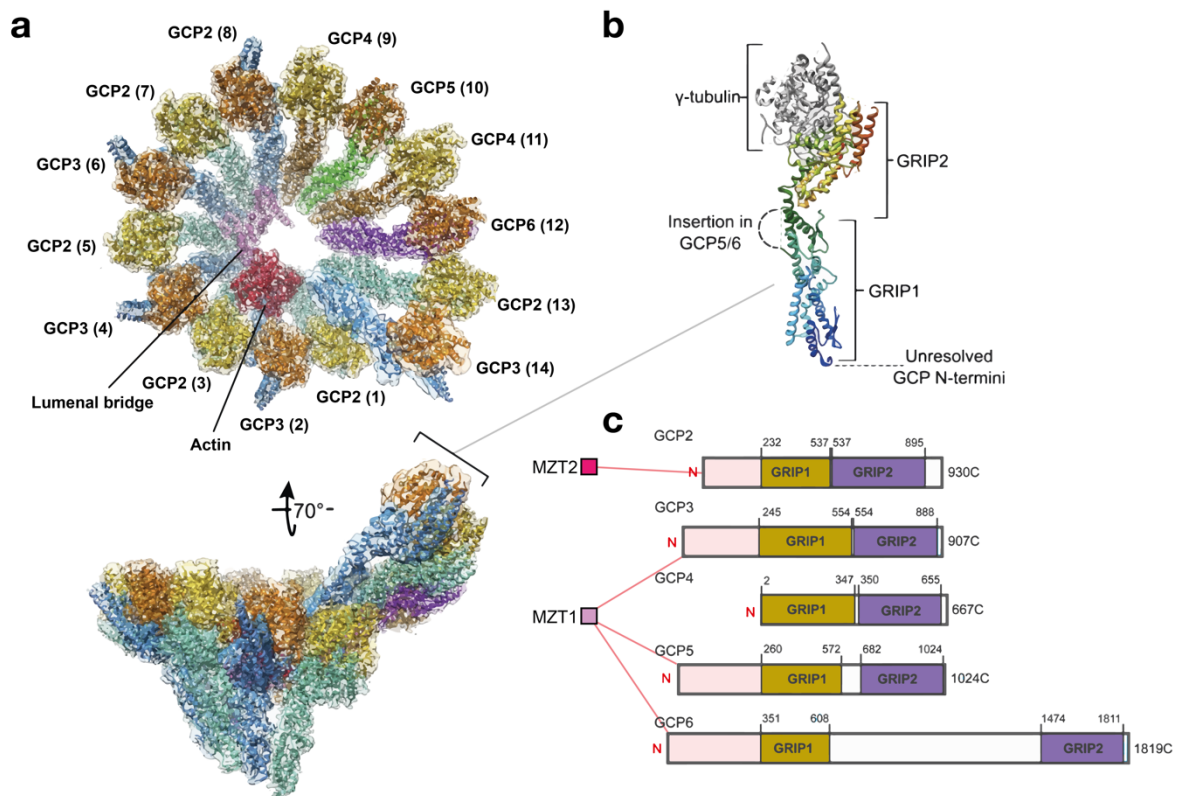


Figure 4 Architecture of the vertebrate γ -TuRC: **a**, shown is the density and structure of the human γ -TuRC (PDB-6V6S and EMD-21074) from two different views. The 14 γ -tubulin proteins (orange, yellow) are arranged on 14 GCP proteins (2-6). This complex called spoke is highlighted in **(b)**. Numbering is indicating the position on the ring complex spiral. Color scheme: GCP2 (light blue), GCP3 (dark blue), γ -tubulin (orange/yellow), GCP4 (brown), GCP5 (green), GCP6 (purple), luminal bridge (pink) and actin (red). **b**, a spoke consists of one γ -tubulin molecule and one GCP protein. Features common to GCP proteins are indicated. GCP helices are colored from N-terminus (red) to C-terminus (blue). **c**, bar representation of the human GCP proteins with indicated N-terminal extension (transparent red), the GRIP1 (yellow) and GRIP2 (purple) domains. Data indicate that the protein MZT2 can interact with the N-terminal extension of GCP2, whereas the protein MZT1 can interact with the N-terminal extensions of GCP3, 5, 6. Panel **a,b** are adapted from [154], and panel **c** from [111].

Introduction

Like the MZT1/2 modules, the GCP6 and GCP5 insertion domains, NEDD1, NME7 and other potential interactors could not be resolved in the cryo-EM studies. However, one of the most interesting and least expected finding in these studies was the identification of one molecule of actin buried in the lumen of γ -TuRC. Previously, single actin molecules were already observed as part of macromolecular complexes such as the dynein motor complex [155], histone acetyl-transferase NuA4 [156], and chromatin remodeling complexes like INO80 [34], SWR1 [157]. Within these complexes, actin plays a crucial role in either recruiting or enhancing the ATPase activity of the catalytic subunit. This brings forth the question regarding the function of actin within the γ -TuRC. Actin is specifically bound to the end of the luminal bridge (see Figure 18), where the helical segments of the MZT1 modules extend toward the barbed end of actin, while the D-loop extends towards spoke 2 [154]. The available resolution did not allow to identify the actin isoform incorporated in γ -TuRC, nor its nucleotide state. The luminal bridge location of actin suggested that it is necessary for the γ -TuRC assembly and structural integrity of the 14-spoke complex. Moreover, it could affect γ -TuRC geometry and flexibility of the spokes which could be important for MT nucleation activity of the ring complex (see next chapter). In addition, the function of actin could be related to actin-interacting proteins [158], as recent publications also highlight the interplay between the centromere and actin network [159,160]. Notably, on specific occasions, actin filaments have been observed within the lumen of MTs [161]. Experiments involving actin polymerization have indicated that γ -TuRC does not enhance actin polymerization [35], aligning with the spatial orientation of actin within the lumen of γ -TuRC. MT nucleation assays conducted after prior incubation with DNase1, a strong interactor of actin competing with the γ -TuRC-binding interface, have suggested a reduction in nucleation activity in the presence of DNase1 [35].

In addition to the surprising discovery of actin within the lumen of γ -TuRC, another noteworthy aspect is the asymmetry within the complex. On one hand, there is compositional asymmetry, where the first half of the ring comprises repeating units of γ -TuSC (spokes 1-8) along with the inner scaffold of the luminal bridge, while the second half consists of GCP4-GCP5-GCP4-GCP6, along with an additional γ -TuSC unit. Although the assembly of this complex remained poorly understood, it is

Introduction

significant to note that repeating units integrated at different positions consistently result in the same organizational pattern. Biochemical data suggest that GCP4-GCP5-GCP4-GCP6 may form the core of γ -TuRC, as this arrangement of four spokes has shown the greatest resistance in salt destabilization experiments [35,162]. However, there are still major gaps in our understanding of the reasons for this specific architecture and assembly pathway of γ -TuRC.

Significantly, the molecular architecture of the vertebrate γ -TuRC leads to conformational asymmetry concerning the MT lattice structure. The first half of the ring closely aligns with the MT geometry, particularly with respect to the positions of γ -tubulins 1-8. However, emanating from the asymmetric core, there is a substantial difference from MT symmetry [154]. This divergence appears to limit its capacity to serve as an efficient template for MT nucleation, possibly providing an explanation for the observed low nucleation activity of isolated γ -TuRC in various previous studies. This adds an intriguing dimension to the regulation of MT nucleation, suggesting that it may require a coordinated concert or dance of γ -TuRC with other factors to enable the specific MT formation inside the cell [149]. Further exploration of this interesting aspect will be discussed in more detail in the following section.

1.3.3 MT nucleation

MT nucleation, the assembly of MTs from $\alpha\beta$ -tubulin subunits, is an intrinsically dynamic process. Cells, however, require precise regulation of MT formation in both temporal and spatial dimensions. Since the discovery of γ -tubulin, it has been firmly established that the majority of nucleation events depend on γ -tubulin complexes. Nevertheless, although in general the absence of γ -tubulin is lethal, there are pathways that allow cells to form MT networks in the absence of γ -tubulin [163]. While γ -TuRC components and recruiting factors have been identified and characterized for several years, our understanding of the nucleation process from γ -TuRC remains limited. During the nucleation reaction from γ -TuRC, it is suggested that $\alpha\beta$ -tubulin binds to γ -tubulin. This α - γ -tubulin interactions, facilitate lateral interactions among $\alpha\beta$ -tubulins, ultimately overcoming the rate-limiting step of $\alpha\beta$ -tubulin oligomerization [132]. The structural insights into the architecture of γ -TuRC offer the potential, in combination with single-molecule techniques, to systematically investigate and comprehend the nucleation process in the future. However, the identified asymmetric

Introduction

conformation of γ -TuRC, which deviates from the MT geometry, introduces another puzzle into our understanding of the process. This deviation suggests the existence of pathways that transform the initially inactive γ -TuRC through conformational changes into an active form, ultimately resulting in a "perfect template" with high nucleation ability. Yet, it remains elusive whether and how this conformational change could be triggered.

The best described γ -tubulin complex interacting motif is the CM1, conserved in several organisms like *D. melanogaster* [164], Mto1 in fission yeast [165], Spc110 in *S. cerevisiae* and *C. albicans* [152,166], and for example CDK5 Regulatory Subunit Associated Protein 2 (CDK5RAP2) also known as centrosomal protein of 215 kDa (CEP215), as well as its homologue myomegalin in humans [167]. Different studies showed that nucleation activity of the γ -TuRC is increased by interaction with proteins containing the CM1 motif [148,149,152,168]. Of note, this motif has also been referred to as the γ -tubulin nucleation activator (γ -TuNA). Additionally, a split γ -TuNA has been described, although it remains unclear whether it can form in a manner similar to classical CM1 domains [169]. The mechanism by which the CM1 motif activates γ -TuRC remains unclear. Structural assessments of γ -TuRC, conducted through negative staining EM experiments [35], and the cryo-EM structure determined in the presence of the CM1 motif [37], have revealed that the addition of the CM1 motif did not alter the overall structure. Both structures displayed a nearly identical asymmetric open conformation compared to purified samples without the bound CM1 motif. However, it cannot be ruled out that CM1 binding may influence the "flexibility" of the surrounding spokes or their ability to interact with other factors. For instance, in *X. laevis* egg extract, the CM1 motif only had an impact on MT nucleation when the Ran-GTP pathway was activated (see Chapter 1.4.2) [35]. Interestingly, an elongated CM1 motif including 100 amino acids showed an increased effect of activation [170]. Moreover, the data from Tovey et al. indicate that in *D. melanogaster*, a steric autoinhibition pathway tightly regulated via phosphorylation exists [170]. Whether this also applies to the vertebrate system needs to be investigated.

More recently, the cooperative action of the tubulin polymerase *Xenopus* MT assembly protein with 215 kDa (XMAP215) [171], in human colonic hepatic tumor-

Introduction

overexpressed gene (ch-TOG), together with γ -tubulin complexes was highlighted for several species. In yeast, it was shown that the homologues Stu2 (*S. cerevisiae*) and Alp14 (*S. pombe*) can directly interact and act together with γ -TuSC [172,173]. Interestingly, also in the realm of vertebrates, recent findings have proposed a direct interaction between XMAP215/ch-TOG and γ -TuRC. This conclusion was drawn from SEC experiments involving purified human γ -tubulin and recombinant *X. laevis* XMAP215/ch-TOG constructs [174]. However, the stability and mechanisms underpinning this interaction remain elusive. Multiple investigations, including single-molecule total internal reflection fluorescence (TIRF) studies, have demonstrated that XMAP215/ch-TOG can significantly enhance the nucleation efficiencies of isolated γ -TuRC [36,174,175]. These experiments led to the model that the polymerase could directly deliver $\alpha\beta$ -tubulin to the growing MT at the γ -TuRC via their tumor overexpressed gene (TOG) domains [149,176]. In that context, single-molecule TIRF experiments could not detect an effect of other potential nucleation promoting factors besides the clear cooperative effect of XMAP215/ch-TOG. One potential candidate in this context is the nucleoside diphosphate kinase NME7. In batch reactions, NME7 was found to impact MT nucleation activity [177]. Interestingly, this effect did not manifest in single molecule measurements [175]. These findings underscore the complexity underlying the interplay between γ -TuRC and its associated factors. Importantly, the different *in vitro* experiments show that the MT nucleation activity of γ -TuRC in absence of XMAP215/ch-TOG is lower than expected, which suggests that multiple factors, including post-translational modifications (PTMs) and the interplay of various elements, likely play pivotal roles in γ -TuRC-templated nucleation.

Another model that merits consideration is the concept of "closing by nucleating". In this scenario, the binding of $\alpha\beta$ -tubulin entities and their interactions dynamically and allosterically alter the geometry of γ -TuRC, potentially aligning it more closely with the MT geometry [175]. Consequently, there might not be a need for a conformational change prior to nucleation. Instead, modifications or interactions with γ -TuRC could influence its ability to adapt its conformation through multiple contacts with $\alpha\beta$ -tubulin. Therefore, comprehending the interactions between γ -TuRC and its associated factors during nucleation requires two key elements. Firstly, gaining structural insights into the γ -TuRC-capped -END is crucial. Secondly, developing a

tunable recombinant system becomes equally essential. Such a system would enable researchers to explore the impact of various factors and modifications systematically. Importantly, this approach allows for more comparable and well-defined experimental conditions compared to using complexes purified from native sources.

1.4 The centrosome as the main MT organizing center

γ -TuRC is the central player for the regulation of MTs in space and time. In cells MTs are organized by MTOCs [178], and the centrosome is the main MTOC. The centrosome is a complex organelle that plays a central role in various cellular processes such as cell division, cellular transport, and the assembly of cilia and flagella. The term "centrosome" was already coined by Theodor Boveri [179], during the late 19th century. Boveri's work, carried out around the same time as Edouard van Beneden, involved the description of spindle pole-associated structures as cell organelles with their own replication cycle [180,181]. The function of the centrosome is tightly coupled to its special architecture. It is a membrane-free organelle that is composed of two centrioles, cylindrical structures made of MTs, surrounded by an amorphous structure called the pericentriolar material (PCM).

1.4.1 The centrosome architecture

The two centrioles, which are the main component of the centrosome, are composed of MTs that are organized into a cylindrical 9-fold triplet symmetry [182,183]. The triplets emerge from the central A-tubule composed of 13 MT protofilaments, directly linked to the B-tubules of 10 MT protofilaments and the 10 MT protofilament C-tubule (Figure 5). This configuration forms a barrel-like structure that is free of MTs in the center. Centrioles exhibit distinct proximal and distal ends. The proximal end is surrounded by the PCM, while the distal end features both distal and subdistal proteinaceous appendages. The distal appendages play a crucial role in orchestrating the formation of the primary cilium [184,185]. On the other hand, from the subdistal appendages MT emerge that are important for centriole cohesion and centrosome-related transport. The two centrioles are coupled at the proximal end via the centrosome linker which consists of rootletin [186], oligomeric filaments crosslinked by CEP68 and anchored by the CEP250 rings which surround the centrioles, as revealed by super-resolution microscopy [187].

Introduction

The 9-fold symmetry of the centrioles is determined by a scaffold, the so-called cartwheel. The main component SAS-6 that consists of a globular N-terminal domain and a C-terminal coiled-coil and unstructured region [188] forms 9-spoked rings potentially determining the symmetry and serving as anchor points for the assembly of centrioles [189]. The action of PLK4 is important for the cartwheel assembly [190], which overall is crucial for the centrosomal cycle, which is closely coupled to the cell cycle (see Chapter 1.5). Recently, it was suggested that γ -TuRC interacts directly with SAS-6 and is thereby recruited and involved in centriole duplication [191], potentially templating the formation of the A-tubule [192]. Besides the scaffolding cartwheel, additional factors and structural modules have been described that are crucial for the formation and stability of this centrosomal substructure [193]. Interestingly, using expansion microscopy [194,195] a pool of γ -TuRC inside the lumen of the centrioles could be shown [196]. Furthermore, knockdown experiments have revealed a dependence between the localization of the augmin complex (see Chapter 1.6) and the presence of the inner centriole component, protein of centriole 5 (POC5) - a documented centrin-interacting protein [197]. However, the precise function of this γ -TuRC/augmin pool within the centriole remains enigmatic.

It is well established that γ -TuRC, guided by specific recruiting factors, becomes recruited to the PCM to initiate MT nucleation. The +END of these MTs is directed toward the cell periphery during both interphase and mitosis [198] (Figure 5). The PCM is an assembly of large proteins with extensive coiled-coil interactions surrounding the wall of centrioles towards the proximal end [199]. Some of the main proteins are pericentrin (or PCNT), centrosomal protein of 192 kDa (CEP192), and CDK5RAP2. This meshwork of proteins has a higher order organization [198] and serves as a platform for a variety of interaction partners that are crucial for example to regulate the cell cycle. The following chapter focuses on PCM proteins that are associated with γ -TuRC.

1.4.2 γ -Tubulin associated factors of the PCM

In the PCM γ -TuRC nucleates MTs and caps their -ENDs [200]. During the onset of mitosis, the recruitment of γ -TuRC to the centrosome increases [201,202]. This recruitment is dependent on specific recruiting proteins. The large protein PCNT is one of the main components of the PCM [203,204], localizing to the outer wall of the

Introduction

centriole MTs with its C-terminus and expanding into the cytoplasm with its N-terminus. PCNT was shown to form a scaffold interacting with CDK5RAP2 and γ -TuRC [205]. CDK5RAP2, already introduced before (Chapter 1.3), is known to anchor γ -TuRC to the PCM and might be important for the activation of MT nucleation [148,167]. Additionally, CDK5RAP2 plays a pivotal role in several interactions within the PCM.

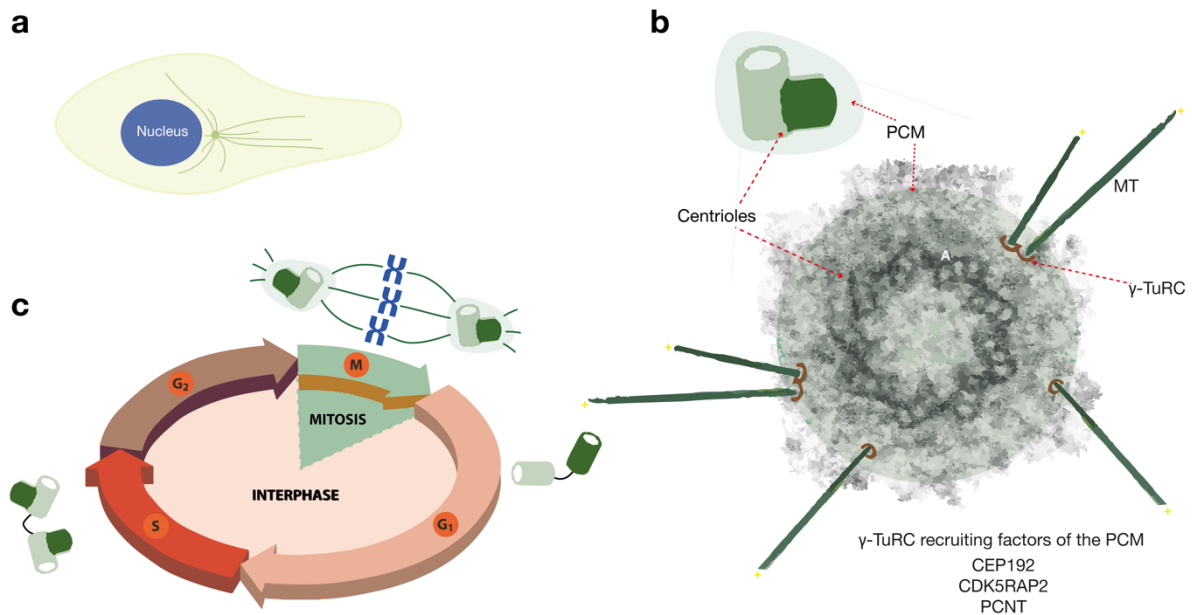


Figure 5 The centrosome during the cell cycle: **a**, inside cells, the centrosome (green) is the main MTOC and is usually located near the nucleus (blue). **b**, schematic illustration of the membrane-free organelle, the centrosome, with important structural units and players. The centrioles form the main structure. In the small icon the mother centriole (light green), and daughter centriole (dark green) are indicated. The centriole architecture with 9-fold symmetry of MT triplets is depicted and the position of one A-tubule is highlighted (white A). MTs are nucleated in the PCM, the dense network of proteins that surrounds the centrioles, towards the cell periphery. MT nucleation depends on γ -TuRC (red circle). **c**, illustration of the cell cycle and schematic representation of the state of the centrosome during the cycle. Mother centrioles are shown in light green, daughter centriole in dark green. During G1 phase the mother and daughter centrioles separate but are still connected via the centrosome linker. During S and G2 phase centrosomes mature to become fully functional units that separate at the onset of mitosis to form the spindle poles. The figure was adapted from Garland Science [9].

Independent of the CM1 motif, NEDD1, a γ -TuRC component is vital for most recruitment events [140,141,206], and can be considered as the main γ -TuRC adapter. A key network is the CEP192 pathway [202,207], which is NEDD1 dependent. Experiments in *X. laevis* egg extracts and human cells revealed that the CEP192 pathway leads to the recruitment of γ -TuRC to the centrosomal MTOC during mitosis [208] (see Chapter 1.5.1). Notably, the PCM forms a dense structure, with CEP192

Introduction

recruitment during mitosis relying on PCNT and CDK5RAP2 [209,210]. Thus, these three proteins may create a scaffold critical for PCM assembly, recruitment, and ultimately MT nucleation function (Figure 5b). On the other hand, advanced microscopy techniques have shown that CEP192 positions γ -TuRC/NEDD1 on the centriole's outer surface [196,198]. Moreover, CEP192 was shown to be important for γ -TuRC dependent MT nucleation during interphase [211]. It will be important to dissect the pathways that lead to the recruitment and anchoring of γ -TuRC to the PCM and the mechanisms that allow MT nucleation during interphase as well as in mitosis. In agreement, research indicates that γ -TuRC anchored differently at the centrosome serve distinct roles [212].

1.4.3 Other MTOCs

The centrosome is the most studied MTOC and serves as the main MT source for most higher eukaryotic cells. However, there are also non-centrosomal MTOCs, discussed briefly here. Importantly, all MTOCs involve γ -tubulin complexes for MT nucleation and anchoring, working alongside both centrosomal and unique factors. Notably, γ -TuRC is not solely found at the MTOCs but is also present in the cytoplasm [213].

1 MT branching

A significant non-centrosomal MTOC is the nucleation from preexisting MTs, essential for MT amplification during spindle assembly and cell division. MT generation from other MTs was discovered in *S. pombe* [214] and plant cells [215]. Notably, MT branching clusters were already observed in MT regrowth assays in green algae [216]. With the discovery of key factors [217], the investigation into this mechanism, often termed MT branching, began. A detailed introduction on MT branching is reported later (see Chapter 1.6).

2 Golgi Apparatus

MTs are also important for the organization of the Golgi apparatus [218], and thus the Golgi apparatus functions as a MTOC. There are several studies showing that γ -TuRC is recruited by AKAP450 [219] to the Golgi, enabling MT nucleation and anchoring of MTs to Golgi membranes [220]. In addition, CDK5RAP2 is another Golgi recruiting

Introduction

factor that is also important for γ -TuRC recruitment to the centrosome [221]. Overall, MTs play a crucial role for the integrity of the Golgi membranes and to organize trafficking between the membranes [222].

3 Plasma membrane and nuclear envelope

MT organization from the plasma membrane or the nuclear envelope is less well understood compared to the other MTOCs. Due to the lack of a centrosome, the prominence of nuclear envelope and plasma membrane pathways is more evident and well-described in plants [223,224]. However, similar pathways also exist in other organisms, including human cell types [225,226].

4 The spindle pole body (SPB)

The SPB is the functional equivalent of the centrosome in specific fungal species, notably within the *Saccharomyces* class. The most studied SPB is that of *S. cerevisiae*. Unlike organisms like humans with centrosomes in the cytosol, these species undergo closed mitosis, where the nuclear envelope remains intact throughout the entire cell cycle. The SPB, a multi-layered organelle embedded in the nuclear envelope, can nucleate MTs from within the nucleus and in the cytoplasm [227]. It duplicates as centrosomes exactly once in the cell cycle, where the older structure is the seeding point of the new SPB, enabling the cell to form a bipolar spindle with each SPB functioning as a spindle pole later in the cell cycle [228,229]. Importantly, SPBs and centrosomes have similarities in their relevant proteins. The MT nucleation is dependent on the γ -TuRC formed by oligomerization of γ -TuSCs (Figure 3) in concert with proteins like CM1-motif containing proteins Spc110, Spc72, or the MT polymerase Stu2 (XMAP215/ch-TOG) [172,230–232], but also MZT1 as in *C. albicans* [152]. Comparing the vertebrate γ -TuRC system with the evolutionarily simplified nucleation machinery of the *Saccharomyces* class, which lacks GCP4-6 [135], has historically led to the identification of factors in the general nucleation mechanism. As our structural understanding of MT nucleation grows, this comparison might enable the characterization of individual modules' functions in the future.

1.4.4 Centrosomal factors and diseases

The core components of γ -TuRC, along with numerous associated proteins such as the augmin complex, belong to the group of essential genes. These genes were

identified through independent genome-wide screenings [233,234], highlighting their essential function. Therefore, it is not surprising that the disruption of genes involved in cell cycle and regulation of MTs is a critical determinant of the onset or progression of serious diseases, including cancer. Notably, a hallmark of cancer progression is centrosome amplification [235], and also overexpression of γ -tubulin related proteins is relevant for cell transformation [236–238]. This underscores the significance of understanding and managing these cellular processes to combat such conditions. For a more detailed overview see [239,240]. Moreover, abnormal expression and mutation of γ -TuRC and augmin subunits have been recently reviewed [241]. Another common phenotype is observed in germline mutations in γ -TuRC related genes for example *TUBGCP2*, *TUBGCP4*, *TUBGCP5* or *CDK5RAP2*, which are often observed to lead to neuro-developmental diseases like microcephaly [242–245].

1.5 The cell cycle

Nucleated by γ -TuRC, MT originating from the centrosome play an essential role in orchestrating chromosome organization during cell division, a pivotal process for the accurate segregation of genetic material. This intricate orchestration is governed by a complex network of signaling pathways, enzymes, and transcription factors. Specifically, centrosomal factors are key players in regulating the cell cycle, facilitating its transition through various stages. Furthermore, the centrosome's activity and its own cycle are controlled by multiple checkpoint pathways, which serve the dual purpose of ensuring proper cell cycle progression and preventing errors during mitosis.

1.5.1 Cell cycle regulation and centrosome cycle

The cell cycle and the cycle of the centrosomes are tightly linked (Figure 5c). Gap phase 1 (G1), S, and G2 collectively form the interphase. During G1 and G2, the cell responds to environmental cues and G2 prepares cells for mitosis, for example checkpoints, gene expression, and growth. After mitosis the cell is in G1, the mother and daughter centrioles disengage (late M phase). In the G1 phase, based on external signals, the cell may enter the G0 phase, a resting stage where it can remain indefinitely without advancing in the cell cycle. The G1 checkpoint serves as a pivotal regulatory junction in the cell cycle, often viewed as the commitment point. Once past this checkpoint, the cell is set on its path with no turning back into the cell cycle [246].

Introduction

The cycle proceeds or halts dependent on the interplay of growth-promoting and growth-inhibiting signaling pathways, regulated by cell division cycle (Cdc) genes [247]. One of the main transmitters of cell cycle progression is the phosphorylation of target genes during the beginning of mitosis, a significant portion of the proteome gets phosphorylated [248], and therefore the cyclin-dependent kinases (CDKs), like CDK1 [249], are key players. As the name indicates, CDKs are dependent on cyclins which undergo their own cycle of production and degradation, again indicated by their name [250]. The oscillation of cyclins is regulated by the action of cyclin-activating or -inhibiting proteins [251,252]. Another essential regulatory mechanism is proteolysis regulated by E3 ubiquitin ligases. For the regulation, by the targeting of cell cycle regulators and their subsequent degradation, of the G1/S transition as well as the G2/M transition, the Skp1-Cul1-F-box protein (SCF) complex is crucial [253–255]. Another key player is the multi-subunit machinery, the anaphase promoting complex, cyclosome (APC/C) [256,257], which is a central regulator for entering anaphase.

An important step of the cell cycle is the S phase, where DNA replication occurs [9]. Moreover, in S phase the so-called centriole-to-centrosome conversion starts [258,259]. PLK4 drives the duplication of centrioles [190], with additional factors like SCL/TAL-interrupting locus protein (STIL) [260,261] and SAS6. After duplication, each centrosome pair consists of a parental mother centriole with PCM and a daughter centriole. Both centrosome pairs are connected by the centrosome linker. In G2/early mitosis, the linker is resolved in a mechanism that is dependent on the action of kinases like NEK2 [262] and the centrosomes can migrate away from each other in order to form the mitotic spindle.

In the G2 phase, following the S phase, the cell undergoes further growth and prepares for mitosis by producing factors essential for cell division. Apart from the commitment point preceding DNA replication (S phase), another crucial cell cycle checkpoint is located at the conclusion of the G2 phase. Here, the cell decides whether to initiate mitosis. It assesses DNA damage and may pause the cycle briefly to facilitate DNA repair. At this junction, as with many stress responses, the *TP53* gene family plays a pivotal role as highly conserved regulators [263,264]. This crucial role is underlined by the fact that *TP53* is the most common altered gene in human cancers [265]. One of the best understood pathways for the action of the p53

Introduction

transcription factor in regulating the cell cycle is the regulation of transcription of the *CDKN1A* gene encoding the p21 protein [266], which act as a CDK inhibitor via the binding to CDK-cyclin complexes [267–269].

The first identified CDK, CDK1 (at the time Cdc2) [270,271] is one of the main drivers of the cell cycle. The CDK1-CyclinB1 complex determines entry into mitosis [272,273]. At the G2/M transition, the expansion of the PCM, and the centrosome maturation occurs through the action of CDK1-CyclinB. [199]. As discussed in the previous chapter, a significant amount of the γ -TuRC is recruited to the centrosome during the expansion of the PCM at the onset of mitosis. This recruitment is dependent on phosphorylation sites, best characterized for the targeting factor NEDD1 [274]. One main signal for the γ -TuRC recruitment via NEDD1 is the phosphorylation via CDK1 and especially polo-like kinase 1 (PLK1) [275–277]. For instance, a key pathway for recruitment and facilitating MT nucleation from γ -TuRC involves a two-step cascade of the mitotic serine/threonine kinases, Aurora kinase A (Aurora A) and PLK1. Through this pathway, Aurora A undergoes autophosphorylation at threonine 288 (T288) in humans and T295 in *X. laevis*, which then leads to the phosphorylation of PLK1 (T210 in humans and T201 in *X. laevis*) [208]. This activation is crucial for the formation of a bipolar spindle [278]. CEP192 provides the scaffold for this process at centrosomes, by initially binding to Aurora A [279]. Once activated, PLK1 can bind to CEP192, specifically at the phosphorylated sites T44 and T46 in *X. laevis*. This binding triggers the phosphorylation of multiple residues on CEP192, creating interaction sites for γ -TuRC. This interaction relies on NEDD1, subsequently transforming these sites into MT nucleation spots [208]. Similarly, PLK1-dependent phosphorylation is also important for the initiation of MT-based MT nucleation [280], as described in the following chapters.

Another critical aspect of the mitotic entry is the breakdown of the nuclear envelope (NEBD) [281]. After NEBD, the cell cycle continues with the mitosis through the traditional five phases prophase, prometaphase, metaphase, anaphase, and telophase [9]. The entire cell cycle is marked by phases and regulated at checkpoints. The subsequent two chapters will delve into the mitotic spindle and the importance of γ -TuRC dependent MT nucleation in ensuring accurate cell division, a cornerstone of cellular life.

1.6 The mitotic spindle

The mitotic spindle, with its three-dimensional shape reminiscent of a spindle used to spin cotton, is responsible for separating the duplicated chromosomes and ensuring their proper segregation between daughter cells. It is a sophisticated assembly of various factors that govern large macromolecular structures, executing the mechanical role of chromosome separation.

1.6.1 Structural units of the mitotic spindle

MTs are the basic structural scaffold of the spindle and together with its associated factors like MT motor proteins, such as kinesins (+END directed movement) [282,283] or dynein (-END directed movement) [284,285], important for spindle alignment and chromosome movement to spindle poles [286]. Among various motors, the most essential for spindle bipolarity is Eg5 (Kinesin-5) [287].

Another important structural unit is the kinetochore, a multi-subunit structure that serves as a platform for MT attachment to the chromosomes [288]. Chromosomes basically consist of the DNA which is wrapped with about 150 base pairs (bp) around the histone protein octamer, built by two molecules of each histone H2A, H2B, H3 and H4, where H3 and H4 can form a tetramer that is joined by H2A-H2B dimers [289,290]. Histone modifications [291] and histone variants [292] are determinant for the chromatin state and regulation. Similarly, the linker Histone H1 which is important for further compaction of chromatin [293,294]. Kinetochores form at the centromere, a region of chromosomes hallmarked by the presence of a special histone H3 variant, centromere protein A (CENP-A) [295–297]. The kinetochore is organized into an inner side with a building block around CENP-A [56] and the outer kinetochore where for example the Ndc80 complex is crucial for MT binding via its calponin homology (CH) domains [298,299] and a positively charged unstructured N-terminal extension [300–302]

The third crucial structural unit in the mitotic spindle is the centrosome, whose activity is largely increased during mitosis along with PCM expansion [199,203,303], in order to build and orchestrate the mitotic spindle. Of note, in special cases, cells can form bipolar spindles in absence of centrosomes dependent on non-centrosomal pathways for MT generation [304].

The mitotic spindle consists of MTs originating from various sources. These include astral MTs from the centrosome, which do not extend towards chromosomes but

Introduction

instead to the cell cortex [305]; kinetochore MTs that eventually capture chromosomes [306]; and interpolar MTs, which are highly dynamic and emanate from the spindle poles [307]. Initially, spindle assembly was proposed to occur through the "search and capture" model, wherein MTs nucleated from the centrosome experienced growth and shrinkage and would randomly attach to kinetochores [308]. However, subsequent research suggested this process might be too inefficient by itself [309] and is likely augmented by other mechanisms [310]. This perspective aligns with key experiments demonstrating that DNA-coated beads can form bipolar spindles in *X. laevis* extract even in the absence of centrosomes [311]. Therefore, spindle function arises from the combined interactions of structures like kinetochores, spindle poles, MTs from diverse sources, and regulatory pathways. A particularly well-understood regulatory mechanism is the RanGTP pathway.

1.6.2 The RanGTP pathway

The Ran protein is a small guanosine triphosphatase (GTPase) of the Ras family [312] that is involved in many cellular processes, including nucleocytoplasmic transport, and the regulation of the mitotic spindle. During mitosis, Ran is activated by a guanine nucleotide exchange factor (RanGEF), regulator of chromosome condensation 1 (RCC1), which is enriched at the chromosomes [313,314]. Upon activation to its active form (formation of RanGTP), RanGTP binds to importin beta [315]. This activation is counterbalanced by RanGTPase-activating proteins (RanGAPs), which, in contrast to RanGEFs, are more evenly distributed throughout the cytoplasm. The interaction with RanGAPs mediates GTP hydrolysis, converting RanGTP to its "inactive" form, RanGDP. Inactive RanGDP is unable to associate with importins [316]. This coordinated interplay leads to a steep biochemical gradient of RanGTP around the condensed chromosomes [317]. By interacting with importins, RanGTP facilitates the release of MT-associated proteins, which were previously bound to the importins. A prime example of such a protein is the targeting protein for Xklp2 (TPX2) [318,319]. This release, in turn, stimulates MT polymerization via the branching pathway [316,320,321]. The branching factor TPX2 is highly studied in *X. laevis* [322–324]. TPX2 possesses a MT-binding domain that associates with the interface between α - and β -tubulin subunits [325]. In *X. laevis*, TPX2 is proposed to enhance local $\alpha\beta$ -tubulin concentrations through the formation of condensates on the MT lattice [323,326]. Additionally, TPX2 features an Spc110/Pcp1 domain, bearing resemblance

Introduction

to SPC110 in yeast [166] and has also a split CM1 domain, suggesting that TPX2 can potentially bind and activate γ -TuRC [169]. However, this potential interaction warrants further investigation.

PTMs play a crucial role in regulating MT nucleation within the spindle, including modifications influenced by the RanGTP pathway. As previously highlighted, one of the primary targets is the γ -TuRC adapter, NEDD1. There are various pathways through which MT nucleation by the γ -TuRC is activated; one of them involves the combined action of TPX2 and Aurora A [327,328].

Both PLK1 and CDK1 have been demonstrated to be essential for the interaction and activity of the γ -TuRC/NEDD1 complex in mitosis, especially with the augmin complex [329]. Augmin, the central component of the MT branching pathway (introduced in Chapter 1.4.3), is also activated by RanGTP [141,324,330,331]. MT branching is not only essential for MT amplification and spindle integrity but also represents a conserved non-centrosomal MTOC. Consequently, the concluding chapters will focus on the augmin complex and the indispensable γ -TuRC-augmin interplay in MT-based nucleation.

1.6.3 The augmin complex

About 20 years ago, MT branching was associated with a multi-protein complex first discovered in a functional study in *D. melanogaster* [217]. The identified proteins were named Dgt (2-6) for dim γ -tubulin [217], as it was found that these are important for the recruitment of the γ -tubulin complex. The following year, the complex formed by the Dgt proteins was named "augmin", derived from the Latin "augmentare" meaning "increase", reflecting its role in amplifying the MT number within the spindle [330]. One year afterwards, the human homologues were discovered. It was demonstrated that both the human and *D. melanogaster* augmin complexes comprise 8 'Homologous to Augmin Subunits' (HAUS) proteins, named HAUS1-8 [332].

Apart from the initial findings in *D. melanogaster* and human cells, augmin subunits have been identified in *A. nidulans* [333]. Intriguingly, the crucial role of the augmin complex in plants for MT generation was established early on [334,335]. This is not only significant during mitosis, but also for MT branching in interphase [336,337], recently summarized [338,339]. The absence of a centrosome in plants accentuates the importance of MT-based nucleation, as discussed in Chapter 1.4.3. Notably, in *A.*

thaliana, multiple versions of the HAUS8 subunit have been described. These are incorporated in augmin complexes that are used in different cellular phases [340]. These examples highlight the functional conservation of the interplay between augmin and the γ -TuRC in mediating the nucleation of branched MTs (see [241]). Besides conservation, experiments have revealed the significance of augmin in various organisms. In *D. melanogaster*, depletion of augmin has been linked to spindle defects [330,341]. Similarly, in *X. laevis* egg extracts, augmin plays a pivotal role in spindle formation and integrity [324,342]. For human cell lines, studies have established augmin as a crucial factor for mitotic spindle MT mass, particularly for kinetochore fiber connection and integrity [330,332,343]. These findings have been further corroborated through live cell imaging [344] and advanced techniques such as super-resolution microscopy [345–347] or EM tomography attempts [348]. These experiments suggest that a significant portion of spindle MTs depend on augmin. Furthermore, the synergy between augmin and γ -TuRC plays a central role in organizing non-centrosomal neuronal MT networks in neurons. This interaction is especially vital for axonal MTs [349] and their polarity [350]. Moreover, it holds significance in the development of the mammalian central nervous system [351,352]. Of note, the augmin component HAUS6 was shown to be part of a liquid-like meiotic spindle domain, among other MT regulatory factors, in mouse metaphase 1 oocyte spindles, which lack centrosomes [353]. In addition, it is not surprising that the knock-out of HAUS6 in mouse embryos is lethal [354].

1.6.4 MT branching by γ -TuRC and augmin

Research in the last years has established that the γ -TuRC-augmin interplay, including the direct interaction and coordination of both complexes and other factors on MTs, is vital for the MT branching pathway (Figure 6). As described before, studies have shown that TPX2 plays a key role in the MT branching reaction in *X. laevis* egg extract [324,355]. This process begins with the formation of TPX2 droplets on MTs, which then leads to the recruitment of γ -TuRC-augmin and subsequent MT nucleation [241,323,326,356]. However, research in other organisms like *D. melanogaster*, where TPX2 is not essential [357–359] or studies involving complexes from human cells [329] suggest that TPX2 is not inherently vital for the MT branching reaction. Still, many aspects of TPX2-facilitated MT branching require further exploration.

Introduction

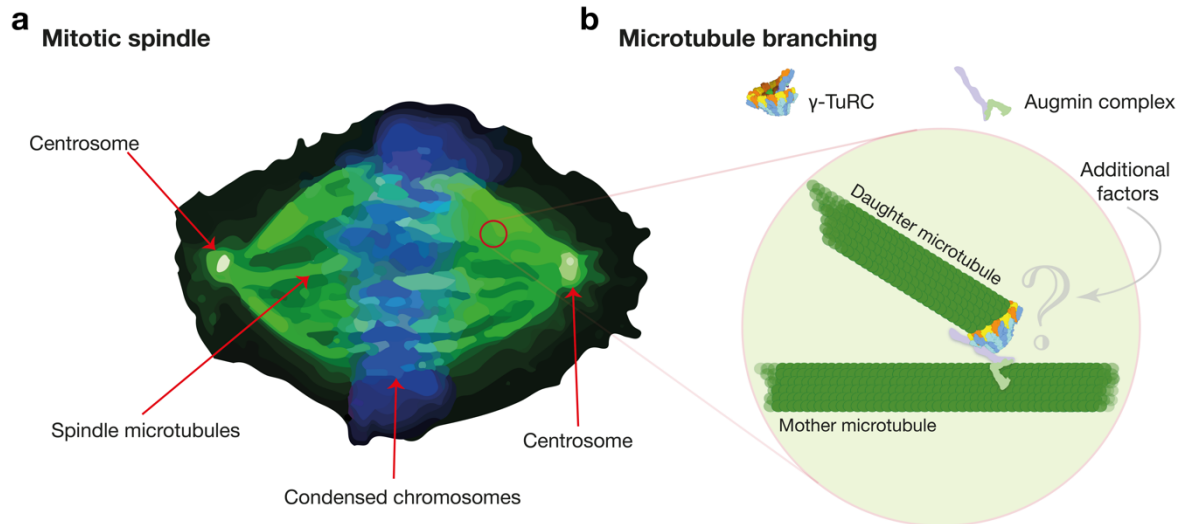


Figure 6 MT branching by augmin and γ -TuRC: **a**, schematic of the mitotic spindle showing two centrosomes as spindle poles (white). A dense MT network (green) links the spindle poles to the chromosomes (blue). A primary pathway for spindle MT amplification, “MT branching,” is highlighted in a close-up view. **b**, schematic of MT branching in the mitotic spindle. Key components are γ -TuRC and the augmin complex. Augmin recruits γ -TuRC to a mother MT, from which a daughter MT nucleates in a specific orientation. The exact binding mode of γ -TuRC and augmin to the MT and interactions with other factors or PTMs are not fully understood. The schematic of the γ -TuRC symbol was created using PDB-6TF9. The figure was adapted from [149].

Both with and without TPX2, MT branching can be observed *in vitro* using a minimal set of components. Single-molecule TIRF studies, conducted with both natively purified complexes and recombinant reconstitutions [329,355,356,359] demonstrated the interaction of branching factors on the mother MT lattice. When these factors are timely recruited to specific locations on the mother MT and tubulin is present, daughter MTs are assembled (Figure 6). The branching angle of the resulting daughter MT varies depending on the experimental setup and the species considered. However, for multiple organisms and experimental setups, the branching angle has been identified as rather shallow, typically less than 60° [329,337,355,356,359,360]. In addition to the previously mentioned branching factors, XMAP215/ch-TOG may also play a role in branching reactions working in synergy with γ -TuRC to polymerize the daughter MT [174,355]. Furthermore, evidence from one study indicates that the echinoderm MT-associated protein-like 3 (EML3) acts as a MT-binding protein and may help recruit augmin to MTs [361]. Notably, components of augmin and the kinetochore-associated Ndc80 complex have been found to interact [362,363]. While this interaction may not directly influence the MT branching reaction, the collaboration between these complexes could be crucial for k-fiber formation and stability.

Moreover, the discovery of γ -TuRC-augmin within the centriole lumen is noteworthy as well [196]. Understanding how this axis is positioned and anchored within the centriole and deciphering the role of this unique γ -TuRC-augmin configuration, represents a captivating area of study.

1.6.5 Molecular composition of the augmin- γ -TuRC network

The studies introduced in this chapter have demonstrated the essential role of augmin, acting in synergy with γ -TuRC, for MT branching. But what is the molecular basis of their function? It has been found that the HAUS8 subunit, specifically its positively charged unstructured N-terminus, is crucial for the MT binding function of the augmin complex [364–366]. Biochemical experiments, along with the reconstitution of the augmin complex in insect cells have uncovered interesting details. For human genes, studies revealed that HAUS8 forms a subcomplex with HAUS2, HAUS6, and HAUS7 [364]. This tetrameric structure has been termed TII for human genes, and, curiously, TII for *X. laevis* [365]. For the purpose of continuity, the name TII will be used hereafter. Additionally, experiments focused on human genes have indicated the presence of another subcomplex centered around HAUS6. This sub-complex also includes HAUS4 and HAUS1 [364]. However, this sub-complex has not been observed in *X. laevis*, raising questions about the integration of HAUS3 and HAUS5 into the complex. Contrary to the study in humans, Song et al. successfully reconstituted a complementary tetramer to TII, termed TIII, composed of HAUS1, HAUS3, HAUS4, and HAUS5. This indicates that the octamer can be divided into two distinct units (Figure 7). When analyzing recombinant augmin complexes using negative stain EM, it was observed that the complex assumes an elongated h-shape, with TIII forming the extended rod, as shown in Figure 7 [364,365]. These observations, combined with additional data, suggest that both tetramers can also serve as distinct functional units. Specifically, TII, which includes HAUS8, may play a pivotal role in MT binding [364–366]. Conversely, the N-termini of HAUS3 and HAUS5 have been suggested to interact with NEDD1 [57,365]. As a result, TIII could represent the γ -TuRC binding module, potentially involving the long, unstructured C-terminus of HAUS6 [343,367,368]

Introduction

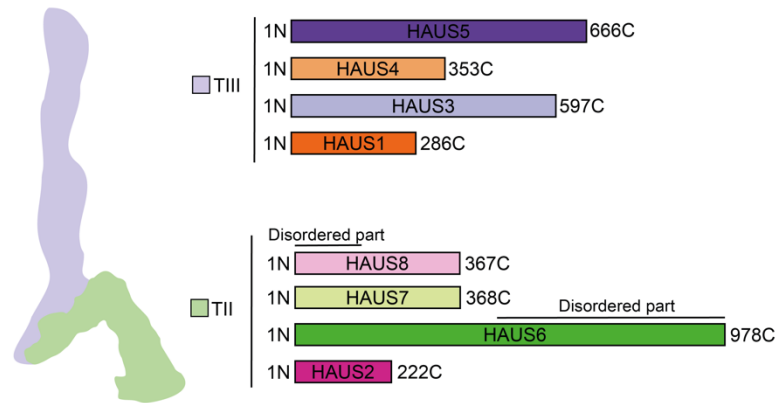


Figure 7 The augmin complex: The augmin complex consists of an octamer of HAUS proteins (HAUS1-8). Experiments indicated that the complex from *X. laevis* can be separated into two tetramers, TII (green) and TIII (purple), where TII was assigned to MT binding while TIII to γ -TuRC interaction. The *X. laevis* HAUS gene lengths are highlighted in bars sorted into two groups corresponding to the respective tetramers. The figure was adapted from [369].

The γ -TuRC-recruiting component NEDD1 seems to be essential also for the augmin- γ -TuRC interaction. It is not surprising that PTMs play a fundamental role in the γ -TuRC-augmin interplay, as highlighted in recent overexpression experiments in human cell lines [329]. This study demonstrated the indispensability of phosphorylation by PLK1 and CDK1 on both γ -TuRC and augmin for stable copurification independent of the MT. The connection between γ -TuRC and NEDD1 seems to be mediated by MZT1-GCP3 N-terminus modules [329]. Previously, mitotic phosphorylation of NEDD1 was shown to be critical for the interaction between γ -TuRC and augmin [343,368]. Additionally, augmin is modified by both Aurora A [370] and PLK1 [280], pointing to a finely tuned regulation of its activity.

Notably, a deeper understanding of augmin's molecular architecture, of how the HAUS subunits interact with one another to form functional modules, as well as how the complex aligns with γ -TuRC and MT respectively, is essential. Thus, an in-depth structural characterization of the augmin complex is a crucial next step towards fully grasping the intricacies of MT branching.

1.7 Aims of this thesis

The aim of this thesis is to comprehensively investigate the principal MT nucleator γ -TuRC and its associated factors using a bottom-up approach. To achieve this, I plan to establish a recombinant expression system that will allow subsequent cryo-EM analysis. This system will specifically address the principles governing the unique sub-complex architecture of γ -TuRC and elucidate the functional roles of individual components, such as the embedded actin molecule or the MZT1/2 microproteins. To address these goals, I propose a modularized design that allows flexibility in the expression and adaptation of components. In parallel, I aim to develop a synchronized sample preparation pipeline to ensure accurate and coherent structural characterization of the multi-protein complexes under study. In addition, a significant part of my research is dedicated to the molecular characterization of the augmin complex, a key γ -TuRC interaction partner. Given the limited structural knowledge available at the start of my PhD, my aim is to elucidate its intricate architecture. Achieving this will provide a comprehensive structural and functional foundation, which is crucial to understand the γ -TuRC-augmin interplay. This understanding should shed light on its important role in evolutionarily conserved cellular mechanisms, particularly cell division.

2 Results

Contributions:

If not stated otherwise, I performed the experiments described in this thesis under the supervision of Prof. Dr. Elmar Schiebel. In each chapter and in the corresponding figure legends, contributions from other people are stated in the collaboration statements. In general, negative staining and EM data acquisition were done by Dr. Annett Neuner; cryo-EM plunge freezing, SPA data acquisition and processing were done by Dr. Erik Zupa. Experiments in the human cell culture system were done by Dr. Enrico Salvatore Atorino.

2.1 The recombinant γ -TuRC expression system

The main aim of my thesis was to create an insect cell-based expression system for recombinant γ -TuRC, which forms the basis for all subsequent experiments. The objective of such a system is to reproducibly isolate multi-subunit protein complexes in a sufficient yield for further research, such as cryo-EM studies. To make this system applicable to a variety of associated factors and protein complexes, I considered a cloning strategy that allows expression of γ -TuRC subunit modules, as discussed in the following chapter.

2.1.1 General cloning strategy of the recombinant γ -TuRC expression system

My general cloning strategy was based on the MultiBac system (Geneva Biotech) [31], with published modifications [34]. This includes the usage of exclusively the polyhedrin (polH) expression cassette, for an equal expression of all components, which required adaptation of the original MultiBac vectors. I used modified versions of pIDK and pIDS (Figure 8a) [34]. To accelerate and optimize cloning conditions for a large number of target genes, I used a standardized cloning method, namely Gibson Assembly using InFusion or NEBuilder technology (see Methods Chapter 4.2). Moreover, I used universal integration sites for targeted gene integration. For insect cell expression, GOIs were inserted directly downstream of the polH promoter sequence (Figure 8a,b) [34], allowing a standardized primer design.

In the context of investigating the function of γ -TuRC, a multi-subunit assembly, and a variety of associated factors, modularization was an important aspect of the cloning strategy. Modules were pACEBac1 as acceptor and three donor vectors (pIDC, pIDK,

Results

pIDS) in which I cloned the GOIs. I designed primer sets for combining two complete expression cassettes (see Table 19-22), regardless of the plasmid backbone, to allow combination of two GOI in one of the four plasmids (Figure 8a,c). Subsequently, I combined the modules with single or double GOI via Cre-recombination to assemble the construct for baculovirus production (Figure 8a,d). This modular approach enabled me to flexibly combine the GOI in various permutations, optimizing the construct composition for efficient protein expression. Simultaneously, leveraging the array of intermediate constructs facilitated the straightforward creation of final constructs. The list of relevant plasmids constructed during this thesis is given in Table 25 (see Methods, Chapter 4.2). As an example, two constructs are shown in Figure 8d. In the following, only final constructs used for protein expression are mentioned in the result section.

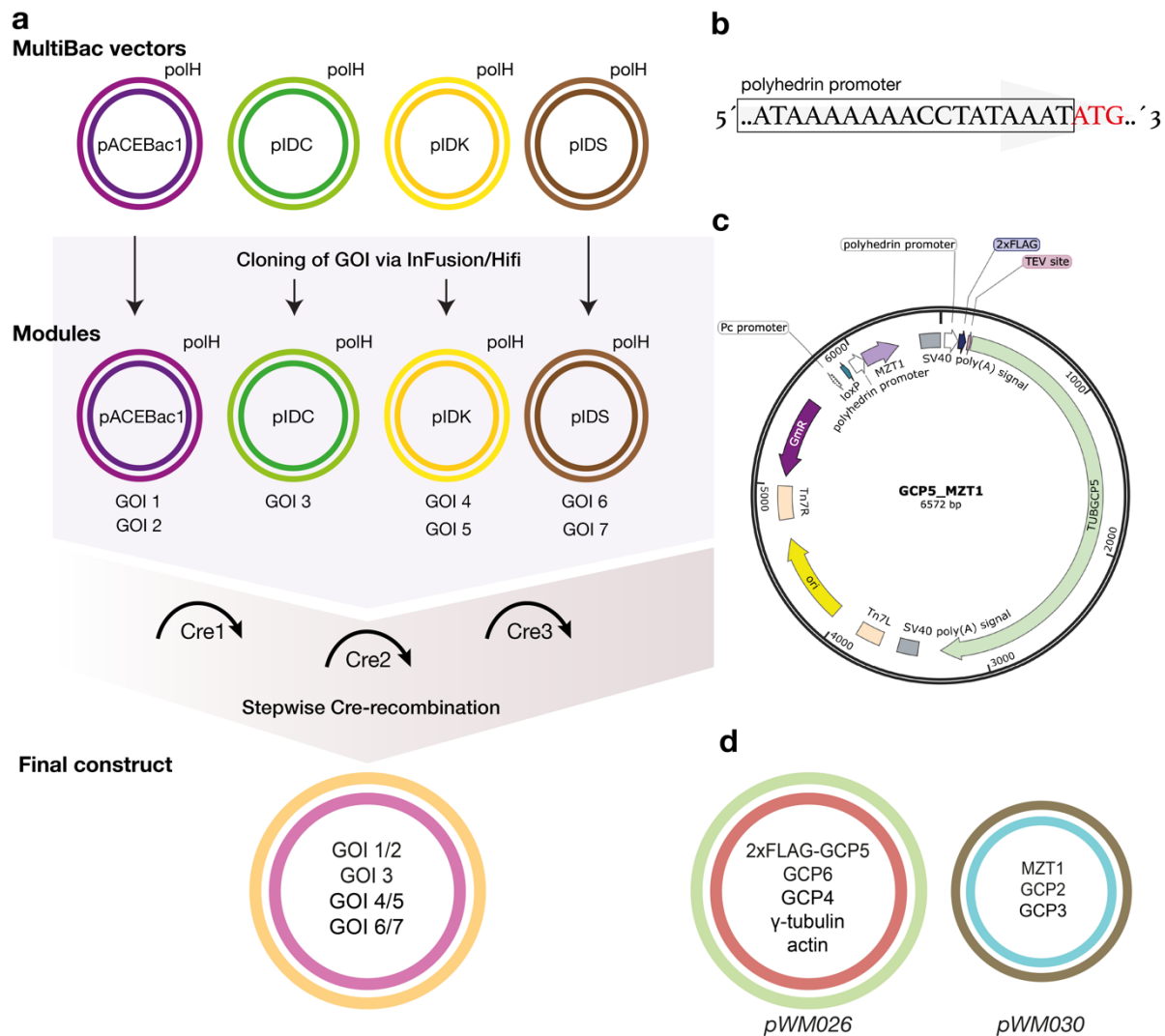


Figure 8 Molecular cloning strategy for insect cell expression: a, cloning strategy of multi-protein complexes based on the MultiBac system and protocols established in this thesis [369,371,372]. MultiBac plasmids were modified to carry the polH expression cassette (b).

Results

*Individual GOI were cloned via InFusion/NEBuilder Hifi assembly into individual expression cassettes of the acceptor or donor plasmids, and potentially combined via standardized primer design. Modules with one or maximally two gene cassettes are combined via subsequent Cre-recombination reactions, with antibiotic selection for all combined resistances. Final constructs carrying multiple expression cassettes with different GOIs were used for recombinant baculovirus production. **b**, promoter sequence with indicated start codon (red) of expression constructs. **c**, exemplary plasmid map of the pACEBac1 plasmid with the combined gene cassettes (2x polH promotor, 2x SV40 terminator) MZT1 and TUBGCP5. All relevant sites of the acceptor vector are indicated. **d**, two exemplary constructs (pWMM026, pWMM030) used for baculovirus production and protein complex expression.*

Another important consideration is the usage of affinity TAGs. In the here presented thesis, I used a double FLAG TAG (2xFLAG TAG) fused to a single, central component within the complex as basic affinity TAG (Figure 8c; Figure 10a). I selected the 2xFLAG TAG due to its high affinity binding to commercial anti-FLAG resin and ability to sufficiently elute the sample using 3xFLAG peptide [34].

2.1.2 Workflow of recombinant reconstitution experiments

The here exemplary for the γ -TuRC described methods apply to all insect cell experiments in this thesis. For the reconstitution of γ -TuRC, I used the human genes listed in Table 23 (see Methods, Chapter 4.2). I confirmed the DNA sequence accuracy of each individual GOI through Sanger sequencing conducted by the Microsynth Seqlab company. Additionally, the validation of Cre-recombination intermediates was carried out using antibiotics as selection markers. Furthermore, I assessed the integration of each GOI at every intermediate stage.

The verification of plasmid intermediates proved crucial due to the multiple occurrences of sequences such as promoters/terminators within a plasmid. After confirming the final constructs, I generated bacmid DNA employing bacterial cell lines sourced from the MultiBac system (see Methods, Chapter 4.3). For every construct, I screened several white colonies (Figure 9a) and confirmed the incorporation of all GOIs using PCRs, as shown for the pWMM030 construct (Figure 9b). I utilized multiple positive clones to generate baculoviruses, assessing the condition of each recombinant baculovirus through test expressions (see Methods, Chapter 4.3-4.4).

Results

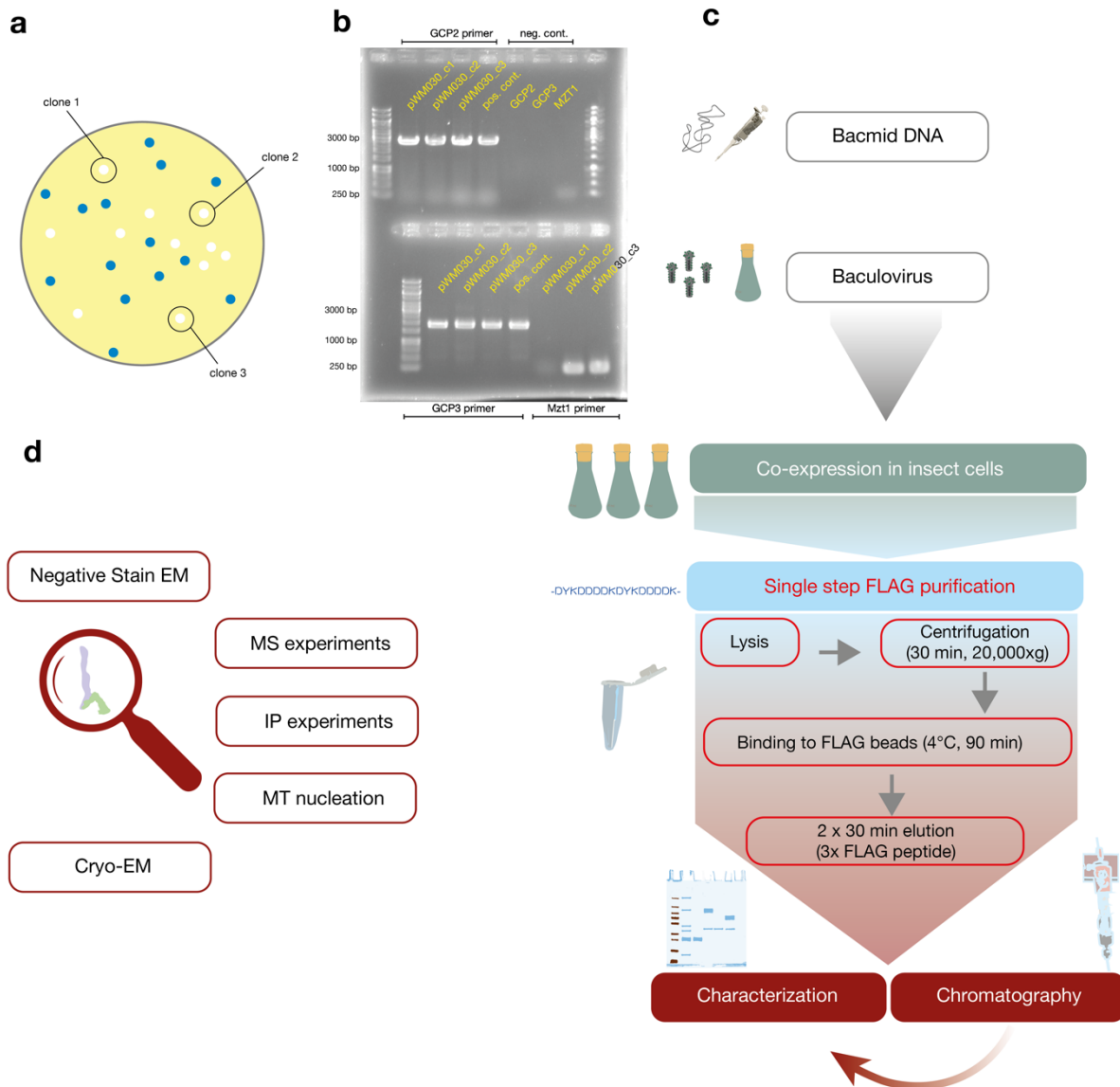


Figure 9 Experimental workflow: **a**, schematic representation of the blue-white selection of bacmid DNA obtained from DH10MultiBac cells. **b**, DNA from white colonies was verified via PCR screening with specific primers for all GOIs, which is illustrated here for the pWM030 construct. PCR products and controls were run on a 1% agarose gel. Negative control was represented by water. **c**, schematic illustration of the experimental workflow from the isolation of bacmid DNA to purified protein. The basic procedure of the batch FLAG purification is highlighted. **d**, schematic list of follow-up experiments performed to characterize purified protein complexes obtained in this thesis.

Following the production of recombinant baculoviruses and protein expression, I established an efficient single-step 2xFLAG TAG purification protocol involving batch washing steps and elutions. This protocol was in some cases expanded by a chromatography step, yielding sample quality and quantity suitable for direct utilization in subsequent experiments. Typically, experiments involving multi-subunit protein complexes were conducted using insect cell culture volumes ranging from 100 ml to 400 ml (Figure 9c). As part of this workflow, negative stain EM served as a method to assess sample quality.

2.1.3 Reconstitution and characterization of the recombinant human γ -TuRC with a minimal set of co-expressed proteins

Results described in this paragraph are published [371] and collaborations are indicated. The negative staining of protein samples and the acquisition of negative stain EM data in this thesis were performed by Dr. Annett Neuner (RG Schiebel). If not stated otherwise, I performed image analysis of negative stain EM data.

For the initial experiments, I designed two constructs (Figure 8d; Figure 10a) for co-expression of eight genes, which I expected to represent the minimal γ -TuRC. In cryo-EM studies, GCP2-6, γ -tubulin, and actin have been structurally identified in the vertebrate γ -TuRC reconstruction [35–37]. Due to the limited resolution of the cryo-EM structures and the overall similarity between the actin isoforms, it could not be determined which actin isoform is integrated in γ -TuRC. Based on MS analysis from different studies narrowing down the isoform to either β - or γ -actin [35,36,148], I used β -actin for the reconstruction in addition to the GCP proteins and γ -tubulin. As described in Chapter 1.3, the microprotein MZT1, encoded by an essential gene, was described to be important for γ -TuRC integrity, and later described to be part of the luminal bridge [150]. Therefore, I included MZT1 in the initial reconstitutions. As a position for the single 2xFLAG TAG, I chose the N-terminus of GCP5 due to its stoichiometry and a central position in the complex (Figure 10a).

Following a single-step FLAG purification, multiple proteins were co-purified with 2xFLAG GCP5 (Figure 10b). To ensure the correct assembly and integrity of the reconstituted γ -TuRC, I subjected the FLAG elutions to negative stain EM analysis. The particles marked by the yellow boxes show regularly ring-shaped γ -TuRCs (Figure 10c). For the validation of the purified particles, I used the native *X. laevis* γ -TuRC, purified as previously described [35], as a control. To compare the structures of the recombinant human and native *X. laevis* γ -TuRC, I performed 2D and 3D class averaging (Figure 10c).

The EM densities reaffirm the consistent overall molecular architecture of the γ -TuRC, in accordance with prior cryo-EM findings [154]. The recombinant γ -TuRC consists of a 14-spoke complex organization and a luminal bridge on the inner surface of the γ -TuRC (Figure 10c). This unequivocally verifies the successful integration of MZT1 and

Results

actin into the complex. Noteworthy, in the resolution range accessible by negative stain EM, I could not distinguish between the native and recombinant γ -TuRC, as indicated by the identical fit of the γ -TuRC atomic model (PDB-6V6S) into the two densities (Figure 10e). To further validate the reconstitution of functional recombinant γ -TuRC, negative staining EM analysis of *in vitro* nucleated MTs from the recombinant γ -TuRC template was performed by Anna Böhler (RG Schiebel) and Annett Neuner. Representative micrographs depict a cap-like structure on the suggested MT -END, while the opposite end, the +END, appears frayed or open, aligning with expectations for the MT +END (Figure 10e). This observation underscores the capacity of the reconstituted complexes to nucleate MTs and cap the MT -END.

In conclusion, these data show that I could establish a recombinant system to reconstitute the human γ -TuRC and purify structurally intact complexes via a single-step purification protocol. Moreover, expression of the eight γ -TuRC components proved to be sufficient to build a structurally intact γ -TuRC and thus they can be considered as the minimal core components of the γ -tubulin-GCP spiral. However, the yield achieved in these experiments did not allow cryo-EM analysis. Therefore, I further optimized and adapted the system to be able to characterize γ -tubulin complexes of various composition.

Results

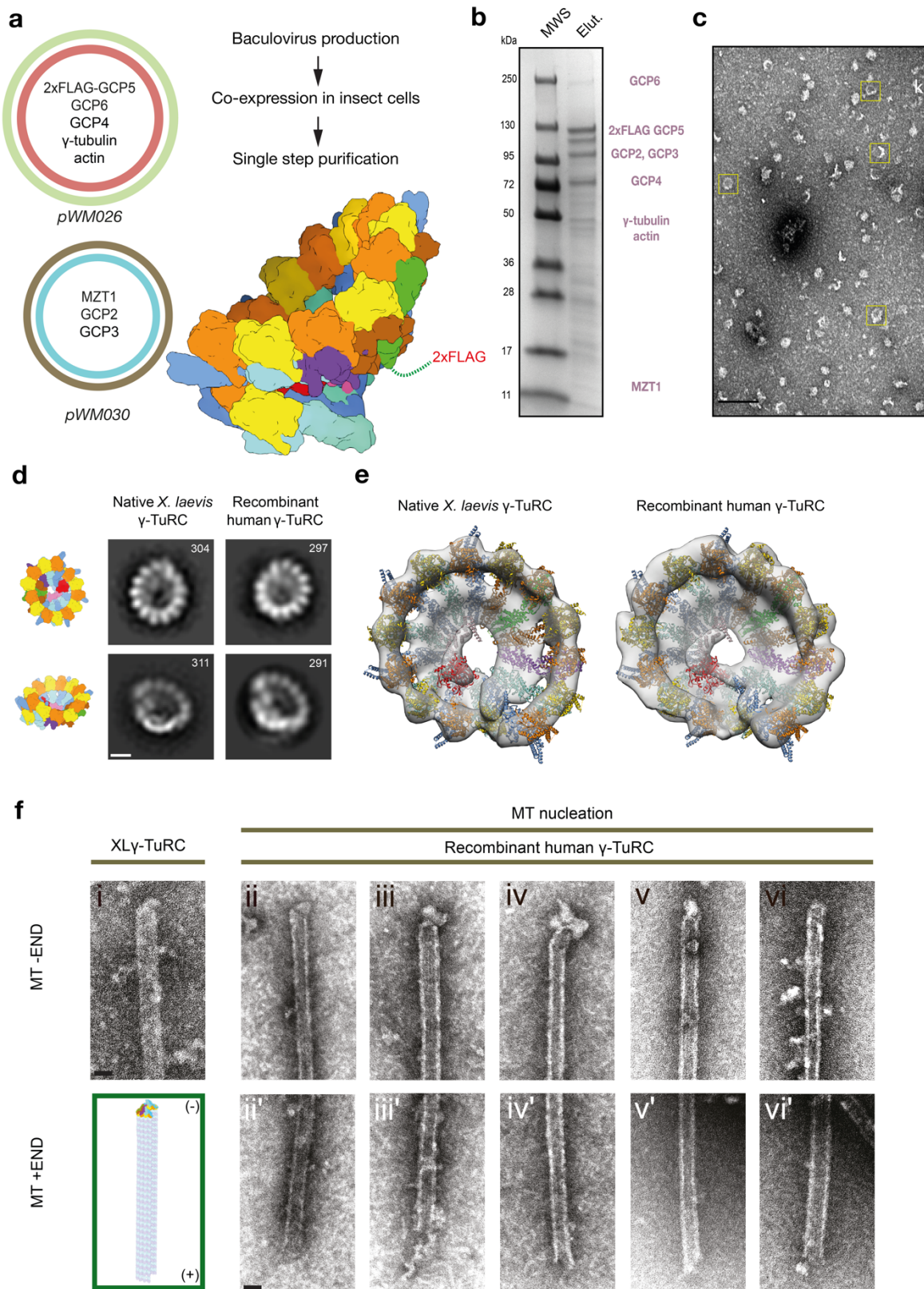


Figure 10 Reconstitution of the minimal recombinant human γ -TuRC: **a**, *pWM026* and *pWM030* were used to produce baculoviruses for co-expression in insect cells, followed by single-step purification. Schematic vertebrate γ -TuRC indicates the expected position of the used 2xFLAG on GCP5 (green). Other colours: GCP2 (light blue), GCP3 (dark blue), γ -tubulin (orange/yellow), GCP4 (brown), GCP6 (purple), actin (red). **b**, Coomassie blue-stained SDS-PAGE of FLAG elution of recombinant γ -TuRC purification showing: left molecular weight standard (MWS); right FLAG elution (Elut.). The expected protein size is indicated in purple. **c**, section of a representative

Results

negative stain EM micrograph of the FLAG elutions. Boxes highlight ring-shaped, γ -TuRC-like particles. Scale bar: 100 nm. **d**, representative 2D class averages of negative stain EM data of native *X. laevis* (left) and recombinant human γ -TuRC (right). Cartoons indicate different views of the complexes. Number of particles is given; Scale bar: 10 nm. **e**, representative 3D class averages of negative stain EM data of native *X. laevis* (left) and recombinant human γ -TuRC (right). Atomic model of the native human γ -TuRC (PDB-6V6S) was docked as a rigid body into the EM densities. **f**, negative stain EM analysis of *in vitro* nucleated MTs from recombinant γ -TuRC. Representative sections of *X. laevis* γ -TuRC; (i; XLY-TuRC) and recombinant human γ -TuRC (ii-vi, rHY-TuRC) are shown. For the recombinant human γ -TuRC, the capped -END was shown along with the flared MT +END of the same MT. Scale bars: 25 nm. Negative stain EM imaging was done by Dr. Annett Neuner and EM analysis was done in collaboration with Dr. Annett Neuner and Dr. Erik Zupa. MT nucleation was done in collaboration with Anna Böhler. The figure was adapted from [371].

2.1.4 Optimization of the recombinant system allows cryo-EM analysis of γ -TuRC

For the optimization of the system to increase the yield of recombinant protein complexes, I considered several aspects. During this optimization process, two additional publications reported different approaches for the reconstitution of the recombinant γ -TuRC [373,374]. Thus, I compared the three approaches and included the recent methods for purifying γ -TuRC from native sources (see Table 1).

Table 1 Comparison of recombinant γ -TuRC expression systems and γ -TuRC isolation methods: Summary of the approaches used for the isolation of vertebrate γ -TuRC for cryo-EM analysis (yellow) and the recombinant system (purple) considering the listed parameters. The table was adapted from [111].

Study	Source	Over-expressed proteins	Tagged γ -TuRC proteins	Basic purification scheme
Liu et al. 2019	<i>X. laevis</i> extract	-	-	-Affinity beads -Elution with small molecule/peptide
Wieczorek et al. 2020	HeLa S3 cells	GFP- γ -TuNA	-	-Binding to purified GFP- γ -TuNA -Binding column -Elution via proteolytic digestion -Sucrose gradient centrifugation.
Consolati et al. 2020	HeLa-Kyoto cells	GCP2	GCP2-TEV-mTagBFP-BAP	-Binding column -Elution with small molecule/peptide -Size exclusion chromatography
Zimmermann et al. 2020	Insect cells (Sf9)	γ -tubulin, GCP2-6, MZT1, MZT2, GCP2-6, RUVBL1, RUVBL2	GCP6-3C-Twin-Strep GCP3-His ₆	-Binding column -Elution via proteolytic digestion
Wieczorek et al. 2021	Insect cells (Sf9)	γ -tubulin, GCP2-6, MZT1, MZT2, β -actin, NEDD1	ZZ-TEV-MZT2-EGFP γ -tubulin-TEV-His ₆	-Binding column -Elution via proteolytic digestion -Size exclusion chromatography -Sucrose gradient centrifugation.
Würtz et al. 2021	Insect cells (Sf21)	γ -tubulin, GCP2-6, MZT1, β -actin	2xFLAG-TEV-GCP5	-Affinity beads -Elution with small molecule/peptide

Following this comparison, I decided to employ the pioneered protocol using single-step FLAG purification, described in the previous chapter. However, as the pellet fraction of the purifications before showed a large portion of insoluble proteins and MZT2 was reported to bind the N-terminus of GCP2 [150], I included MZT2B in the recombinant γ -TuRC constructs to potentially increase solubility of the complex

Results

MZT2-GCP2 N-terminus. Additionally, due to the high demand for γ -tubulin, 14 copies per γ -TuRC, I included an additional *TUBG1* gene into the constructs. Moreover, Zimmermann et al. described that the small ATPases RuvB-like protein 1 and 2 (RUVBL1/2) increase the efficiency of the γ -TuRC reconstitution in insect cells [373]. Therefore, I included the two genes into the γ -TuRC constructs, which resulted in two final plasmids, which in the following were considered as basic constructs (Figure 11a). The γ -TuRC constructs described in this thesis contain at least 11 over-expressed genes, with two copies of *TUBG1*. Coomassie blue-stained SDS-PAGE of FLAG purification from insect cells expressing the basic constructs showed clearly detectable bands of proteins that copurified with 2xFLAG GCP5, indicating the successful reconstitution of the γ -TuRC (Figure 11b). Sections of negative stain EM micrographs (Figure 11c) indicate the high abundance of γ -TuRC particles, with clearly increased yield compared to the minimal γ -TuRC system (Figure 10). Representative 2D class averages of recombinant human γ -TuRC negative stain EM experiments highlight the successful purification of complexes and visualize the most abundant views of γ -TuRC achieved in negative stain EM 2D classes. In addition, I subjected samples of the FLAG elutions of recombinant human γ -TuRC with the basic construct (Figure 11a) to LC-MS/MS analysis, which was done by the Core Facility for MS & Proteomics at the ZMBH. The results of this analysis (presented in Table 2) confirm that all co-expressed genes are present in the elution sample, demonstrating their co-purification alongside 2xFLAG GCP5. Besides the ATPases RUVBL1/2, all other components were detected in high abundance (Table 2).

Table 2 LC-MS/MS analysis of recombinant human γ -TuRC: Analysis showing the coverage (percentage of identified sequence) of the peptides and unique peptides identified in $n=3$ independent repetitions of the co-expression of the *pWM026* and *pWM086* constructs with subsequent FLAG purification. LC-MS/MS analysis was done by the Core Facility for MS & Proteomics at the ZMBH.

Protein	Coverage (%)	Unique/total peptides
γ -tubulin	100	20/73
GCP2	87	134/134
GCP3	91	144/144
GCP4	84	80/80
2xFLAG-TEV-GCP5	89	177/177
GCP6	70	139/139
MZT1	80	7/7
MZT2B	90	15/15
β -actin	86	2/43
RUVBL1	52	21/21
RUVBL2	48	22/22

Results

This observation underscores the accuracy of the constructs and the successful reconstitution of the recombinant human γ -TuRC. The low coverage of the ATPases in LC-MS/MS and the absence of a significant band in Coomassie blue-stained SDS-PAGE as well as negative stain 2D classes suggest that the ATPases do not represent a stoichiometric component of the γ -TuRC. Nevertheless, it is essential to note that, based on the data I acquired here, I cannot unequivocally determine the extent of ATPase influence on the reconstitution of γ -TuRC and its related sub-complexes. Furthermore, I cannot rule out the possibility that binding sites for ATPases may exist within the assembled sub-complexes.

Besides the quality of the baculoviruses and the overproduction of crucial components, I also found that the usage of the insect cell line exerts an impact on the reconstitution of the complexes. In my reconstitutions of the human γ -TuRC, expression in High5 insect cells led to a smaller soluble fraction of eluted complexes compared to Sf21 cells, as indicated by the strong band of the 2xFLAG tagged GCP5 protein in comparison to other components (Figure 11e). Importantly, several GCP bands were observed in the pellet fraction, indicating that the recombinant proteins could not be properly folded, or they aggregated. Consistent with these observations, reconstitutions in Sf21 cells without the co-expression of MZT1, a crucial component for the γ -TuRC reconstitution, also showed a predominant fraction of proteins in the pellet (Figure 11e). In contrast, reconstitution in Sf21 cells co-expressing *MZT1* clearly showed less abundance of proteins in the pellet fractions and clear bands of proteins with the expected size co-eluting with 2xFLAG-GCP5. Taken together, these data indicate the successful reconstitution of the γ -TuRC complex. Importantly, it is challenging to compare these reconstitutions, as several factors like the baculovirus quality and the final constructs might impact the outcome. These aspects need to be considered in the evaluation of results, as I did not perform a complete systematic analysis of the impact of High5 compared to Sf21 cells, and with and without *MZT1*. However, the strong abundance of pelleted band fractions of GCP2 and GCP3 in the absence of MZT1 aligns with the previously observed behavior in the absence of MZT2, which suggests that both MZT proteins are important for the efficient assembly of the γ -TuRC. This indicates that the binding of the MZT proteins to the N-terminal extensions of the GCPs is important for their solubility in the recombinant system,

Results

besides the suggested structural role of MZT1 as component of the luminal bridge [150]. Having optimized the recombinant reconstitution of γ -TuRC, I turned to cryo-EM analysis of the obtained samples to further investigate the individual roles of the γ -TuRC components.

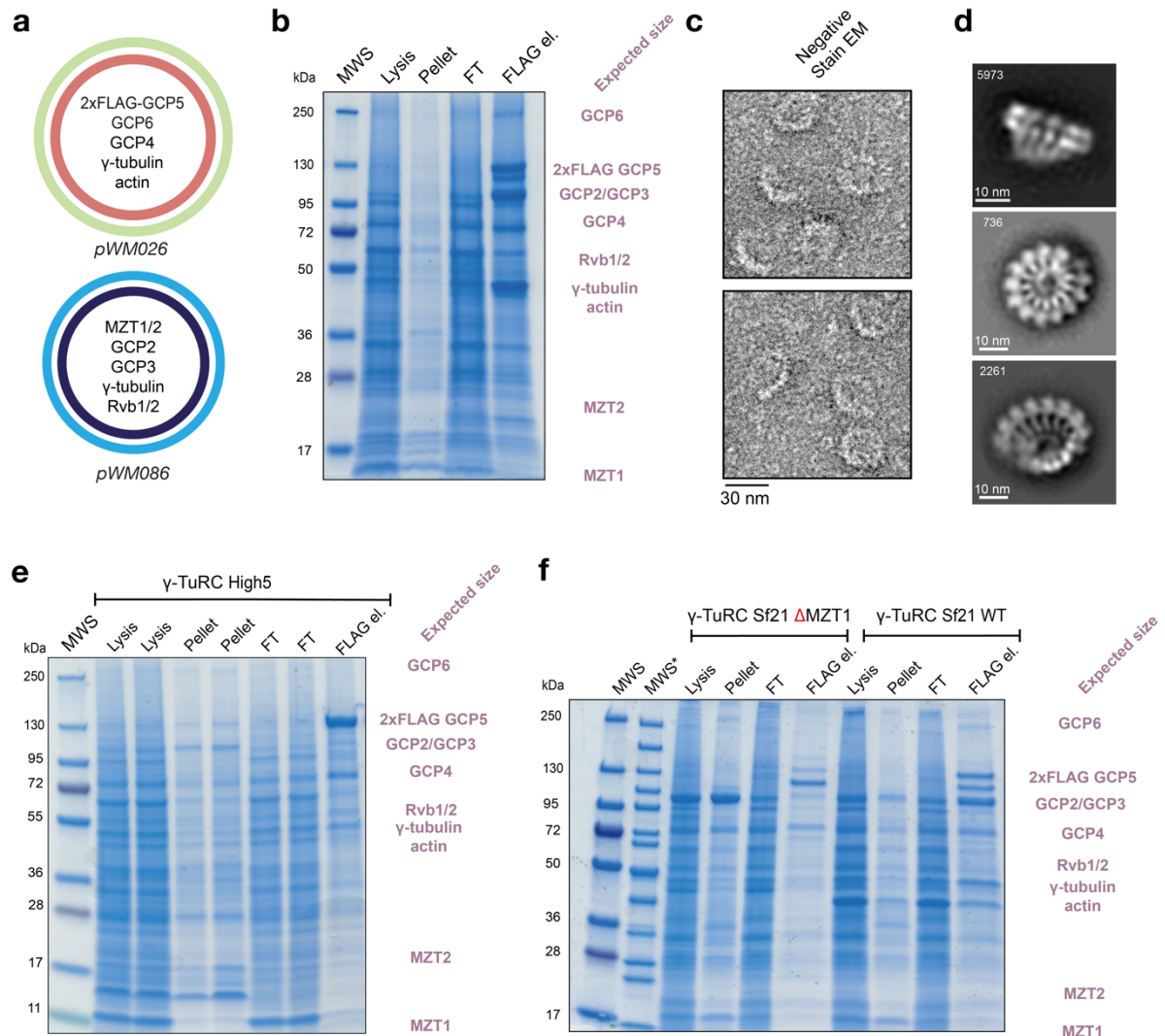


Figure 11 Optimized reconstitution of the recombinant human γ -TuRC: **a**, *pWMM026* and *pWMM086* were used to produce baculoviruses for co-expression in insect cells, followed by single-step purification. Besides γ -tubulin, the constructs contained MZT1, MZT2B, GCP2, GCP3, RUVBL1/2 (*Rvb1/2*), 2xFLAG-GCP5, GCP4, GCP6, β -actin. This construct combination is herein considered as the basic γ -TuRC expression construct. **b**, Coomassie blue-stained SDS-PAGE of recombinant γ -TuRC purification showing: Molecular weight standard (MWS); Lysis; Pellet; Flow through (FT); FLAG elution (FLAG el.). Expected protein size is indicated in purple. **c**, sections of a representative negative stain EM micrograph of the FLAG elutions. Scale bar is given. **d**, representative 2D class averages of negative stain EM data of optimized recombinant human γ -TuRC. Number of particles and scale bar are given. **e**, Coomassie blue-stained SDS-PAGE of recombinant γ -TuRC purification of *pWMM026* and *pWMM086* expressed in High5 insect cells showing: Molecular weight standard (MWS); Lysis sample 1; Lysis sample 2; Pellet sample 1; Pellet sample 2; Flow through (FT) sample 1; FT sample 2; FLAG elution (FLAG el.). Expected protein size is indicated in purple. **f**, Coomassie blue-stained SDS-PAGE gel of recombinant γ -TuRC purification of *pWMM026*, *pWMM111* (γ -TuRC Sf21 Δ MZT1 (no MZT1)) left and *pWMM026* and *pWMM086* (γ -TuRC Sf21 WT) right showing: Molecular weight standard (MWS); MWS (different standard sizes not indicated *); Lysis Δ MZT1; Pellet Δ MZT1; Flow through (FT) Δ MZT1; FLAG

Results

elution (FLAG el.) Δ MZT1; Lysis WT; Pellet WT; Pellet WT; Flow through (FT) WT; FLAG elution (FLAG el.) WT. Expected protein size is indicated in purple. Negative stain EM imaging was done by Dr. Annett Neuner. Parts of the figure were adapted from [372].

2.2 Cryo-EM analysis of recombinant human γ -TuRC

Results described in this chapter are published [372]. Cryo-EM experiments and data analysis were done in collaboration with Dr. Erik Zupa (RG Pfeffer).

2.2.1 Reconstruction of assembly intermediates reveal a modular assembly pathway of the vertebrate γ -TuRC

After I had successfully established the recombinant γ -TuRC expression system, the subsequent phase of this project involved the analysis of the γ -TuRC samples using cryo-EM. To achieve this, I conducted the purification of the γ -TuRC from a 100 ml culture of Sf21 cells, employing the well-established single-step batch FLAG purification method. Subsequently, Erik Zupa undertook plunge freezing, followed by cryo-EM SPA. In addition to these steps, I also subjected the sample to analysis through SDS-PAGE (Figure 12a) and negative stain EM 2D class averaging (Figure 12b). The results from the 2D classification reveal a notable presence of classes exhibiting partially assembled ring complexes, characterized by 6 or 8 spokes (γ -tubulin-GCP complex, Figure 12b). Concurrently, the examination of the cryo-EM dataset yielded particles of sufficient quality to facilitate an in-depth analysis. This analysis uncovered several distinct classes with varying spoke numbers within this purification (Figure 12c).

Analysis of the specific subclasses indicate that they correspond to assembly intermediates of the γ -TuRC. These arise from the modular expansion of a core with the sequence GCP2-3-4-5-4-6, which is the most prevalent class in the dataset (Figure 12c). Crucially, the γ -TuRC intermediate is expanded by the stepwise addition of one γ -TuSC subunit at a time. The expansion begins when a γ -TuSC unit is added to form spokes 5 and 6 on the GCP2₍₇₎-oriented side, causing displacement of the GRIP2 domains and related γ -tubulin copies (Figure 12c,d(2)). In the subsequent phase, another γ -TuSC unit joins the GCP2₍₅₎-oriented side, taking up positions 3 and 4. Here, the GRIP2 domains of the γ -TuSC_(5,6) unit shift, settling into their final placement along γ -TuRCs helical axis (Figure 12c,d(3)). Notably, once spokes 3 and 4 are in place, the luminal bridge components MZT1-GCP3, MZT1-GCP6, and actin become stably attached, highlighting the luminal bridge role in guiding and stabilizing

Results

γ -TuRC assembly. Importantly, the N-terminus of GCP6 is crucial for the initialization (Figure 14a,b) and the stabilization of the assembly via multiple contacts provided by extensive helical elements (Figure 13b).

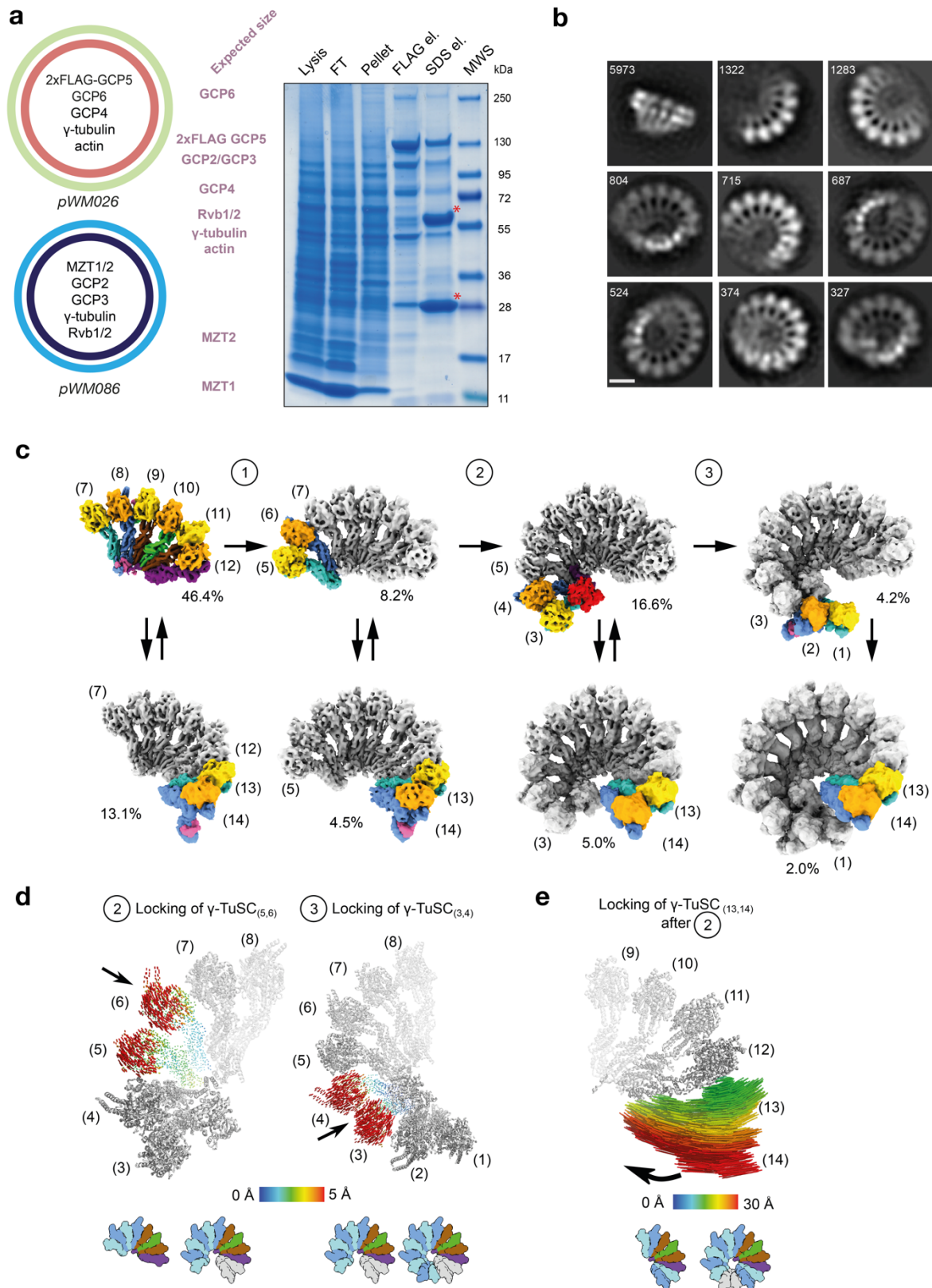


Figure 12 Cryo-EM analysis of recombinant human γ -TuRC reveals a modular assembly mechanism: a, left: pWVM026, and pWVM086 were used to produce baculoviruses for co-expression

Results

*in insect cells, followed by single-step purification. Besides γ -tubulin, the constructs contained MZT1, MZT2B, GCP2, GCP3, RUVBL1/2 (Rvb1/2), 2xFLAG-GCP5, GCP4, GCP6, β -actin. Right: Coomassie blue-stained SDS-PAGE of recombinant γ -TuRC purification used for cryo-EM experiments showing: Lysis; Flow through (FT); Pellet; FLAG elution (FLAG el.); SDS elution (after FLAG elution); Molecular weight standard (MWS). Red asterisks indicate heavy and light chains of FLAG antibodies. Expected protein size is indicated in purple. **b**, representative 2D class averages of negative stain EM data of recombinant human γ -TuRC achieved from the same preparation used for cryo-EM experiments. Number of particles is given, scale bar: 10 nm. **c**, cryo-EM reconstructions of γ -TuRC assembly intermediates ordered into a γ -TuRC assembly mechanism indicated by one-sided arrows. Color scheme: GCP2 (light blue), GCP3 (dark blue), γ -tubulin (orange/yellow), GCP4 (brown), GCP5 (green), GCP6 (purple), MZT1 (pink) and actin (red). Newly added γ -TuSC units are colored, while the other components are depicted in grey. Spokes are numbered according to the position found in the 14-spoke γ -TuRC. For each stage, there is an equilibrium with subcomplexes that have γ -TuSC_(13,14), which are placed below with an arrow pointing in both directions. Percentages are given for homogeneous sets of particles representing different assembly states. **d**, visualization of conformational locking of γ -TuSC units using vector representation linking the C α atoms in the two conformations. Spokes that do not undergo conformational displacement are shown in grey, and relevant positions are colored according to the scale bar. Direction of motion is indicated by the arrow. Schematic γ -TuRC icons indicate the set of classes used for the analysis. Spokes that are sub-stoichiometric in the reconstructions are shown in grey. **e**, left: representation of the slide-in motion of the γ -TuSC_(13,14) unit as consequence of the comparison of classes before and after the docking of the luminal bridge. Visualization as in panel (d). Negative stain EM imaging was done by Dr. Annett Neuner. Cryo-EM data acquisition, and analysis were done by Dr. Erik Zupa and results were jointly evaluated. The figure was adapted from [372].*

The last addition on this end is the terminal γ -TuSC unit (spokes 1 and 2). Here, the 3D classes concerning this step of the assembly process indicate that this unit seamlessly integrates upon initial binding, aligning with the configuration of the fully assembled complex. Importantly, the data feature two structural variants for each assembly intermediate: one with the γ -TuSC_(13,14) unit and one without. The consistent ratio between intermediates containing and lacking γ -TuSC_(13,14) across the different assembly stages implies a continuous equilibrium of γ -TuSC_(13,14) associating and dissociating. Intriguingly, upon the γ -TuSC_(3,4) recruitment completing the luminal bridge formation, the γ -TuSC_(13,14) unit shifts by up to 30 Å relative to the neighboring GCP6 subunit (Figure 12e). This shift potentially enables the γ -TuSC_(13,14) unit to directly connect with the γ -TuSC_(1,2) unit through the MZT1-GCP3₍₁₄₎ module (see Figure 13a), thus securing it within the complex and preventing its disengagement. These data suggest that the γ -TuRC structure results from selective stabilization of γ -TuSC units, their integration into ring arrangement, followed by a conformational lock.

2.2.2 MZT1 modules have multiple binding sites on the γ -TuRC

After examining the composition of the various intermediates in the data set, Erik Zupa focused the analysis to the fully assembled γ -TuRC. He analyzed it along with the intermediate assemblies of 10-12 spokes and achieved a global resolution of 7.5Å. At

Results

this resolution, the global architecture of the 14 GCPs and the luminal bridge, which included stable integration of actin and two MZT1-modules could be confirmed (Figure 13a,b). Surprisingly, the reconstruction revealed four MZT1-containing modules on the γ -TuRC outer surface, including three MZT1-GCP3 modules (Figure 13a,c) and one MZT1-GCP5 module (Figure 14).

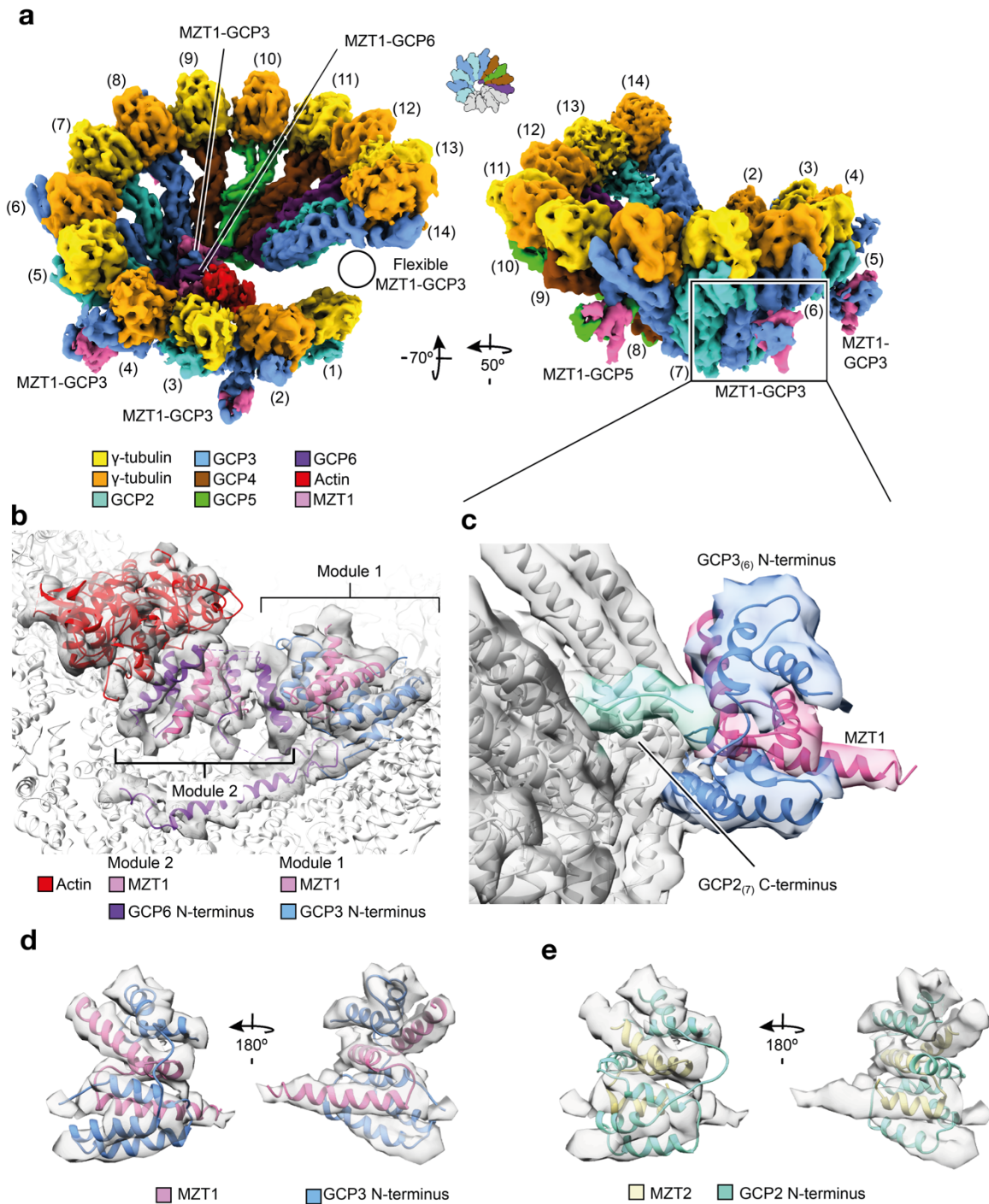


Figure 13 Identification of all MZT1 module binding sites on recombinant γ -TuRC: a, side views on the cryo-EM reconstruction of the fully assembled recombinant human γ -TuRC sample analyzed in Figure 12. Schematic γ -TuRC icons indicate the set of particle classes used, indicating

Results

*sub-stoichiometry of the γ -TuSC_(1,2) and γ -TuSC_(13,14), which are shown in grey. Due to the indicated sub-stoichiometry, the MZT1 module on GCP3₍₁₄₎ was not detectable in this reconstruction but can be identified in intermediates (black circle). **b**, close-up view of the luminal bridge, in which the atomic model (PDB-6X0U) was docked into the corresponding density. Coloring is indicated. **c**, close-up view of the density of the MZT1-GCP3 module associated with GCP3₍₆₎. The atomic model of the MZT1-GCP3 module (PDB-6X0U) was docked as rigid body. MZT1-GCP3 directly interacts with the adjacent γ -TuSC units, as highlighted via the GCP2 C-terminus. Coloring as in (a). **d**, views of the rigid body fit of the MZT1 (pink) - GCP3 (blue) module (PDB-6X0U) into the α -helical density segment associated with GCP3₍₆₎ of the γ -TuRC reconstruction. This GCP3₍₆₎ density segment covers the density segments on GCP3₍₂₎, GCP3₍₄₎ and GCP3₍₁₄₎. **e**, rigid body fit of the MZT2 (khaki) - GCP2 (cyan) module (PDB-6X0V) into the same density shown in (d). The length and number of resolved α -helices do not fit the density, in contrast to the segment of MZT1-GCP3 (d). Cryo-EM data acquisition, and analysis were done by Dr. Erik Zupa, and results were jointly evaluated. The figure was adapted from [372].*

The modules are located in direct proximity to the GRIP2 domains of the GCP3 subunits. A seamless rigid body fit clarified that the densities relate to MZT1 modules, not the previously described MZT2-GCP2 module found at the interface between GCP6_(spoke12) and GCP2_(spoke13) [150] (Figure 13c). Combined with earlier findings of the MZT1-GCP3 module on spoke 14 and in the luminal bridge [35,150], the current reconstruction of the purified human recombinant γ -TuRC confirms a total of 7 MZT1-modules within the complex.

The 6-spoke intermediate was the prime candidate to further confirm the identity of the MZT1 module attached to the γ -TuRC exterior at position GCP3₍₈₎ (Figure 13). Erik Zupa's focused processing resolved this 6-spoke assembly intermediate to 5.3Å resolution. This allowed to unequivocally identify the spokes based on the secondary structure elements of the individual GCP proteins (Figure 14). Notably, this intermediate comprises one γ -TuSC unit and all other γ -TuRC-specific GCP proteins in a sequential GCP2-3-4-5-4-6 arrangement, matching spokes 7-12 of the complete complex. Intriguingly, apart from the MZT1 module on the exterior of γ -TuRC (Figure 14c,d), the cryo-EM density revealed the initial module of the luminal bridge is already at this stage formed by the MZT1-GCP3 module attachment to the GCP3₍₈₎ GRIP1 domain (Figure 14b). With only a single GCP3 in this intermediate, it is clear, the MZT1-N-GCP3 module of GCP3₍₈₎ forms the luminal bridge, most likely also in the context of the full ring complex.

Moreover, docking of published structures [150] onto the outer surface of GCP3₍₈₎ identified it as MZT1-GCP5 module (Figure 14c,d,e). MZT1-GCP5 at this position distinctly differs from the MZT1-GCP6 (PDB-6M33) that forms the luminal bridge. The unique binding site for the MZT1-GCP5 module on GCP3₍₈₎ could result from the neighboring GCP4₍₉₎ subunit. This likely explains why MZT1-GCP5 binds exclusively

Results

to the GCP3₍₈₎ exterior, leaving MZT1-GCP3₍₈₎ to form the initial module of the luminal bridge (Figure 14f). Because of the role of MZT1 as N-GCP3 and N-GCP5 binder, its absence in the recombinant system leads to GCP3, 5, and 6 insolubility (Figure 11f). The MZT1/GCP3/5/6 modules serve distinct roles, from complex assembly and integrity (luminal bridge, spoke 14) to asymmetric recruitment of interaction partners (spoke 2-9).

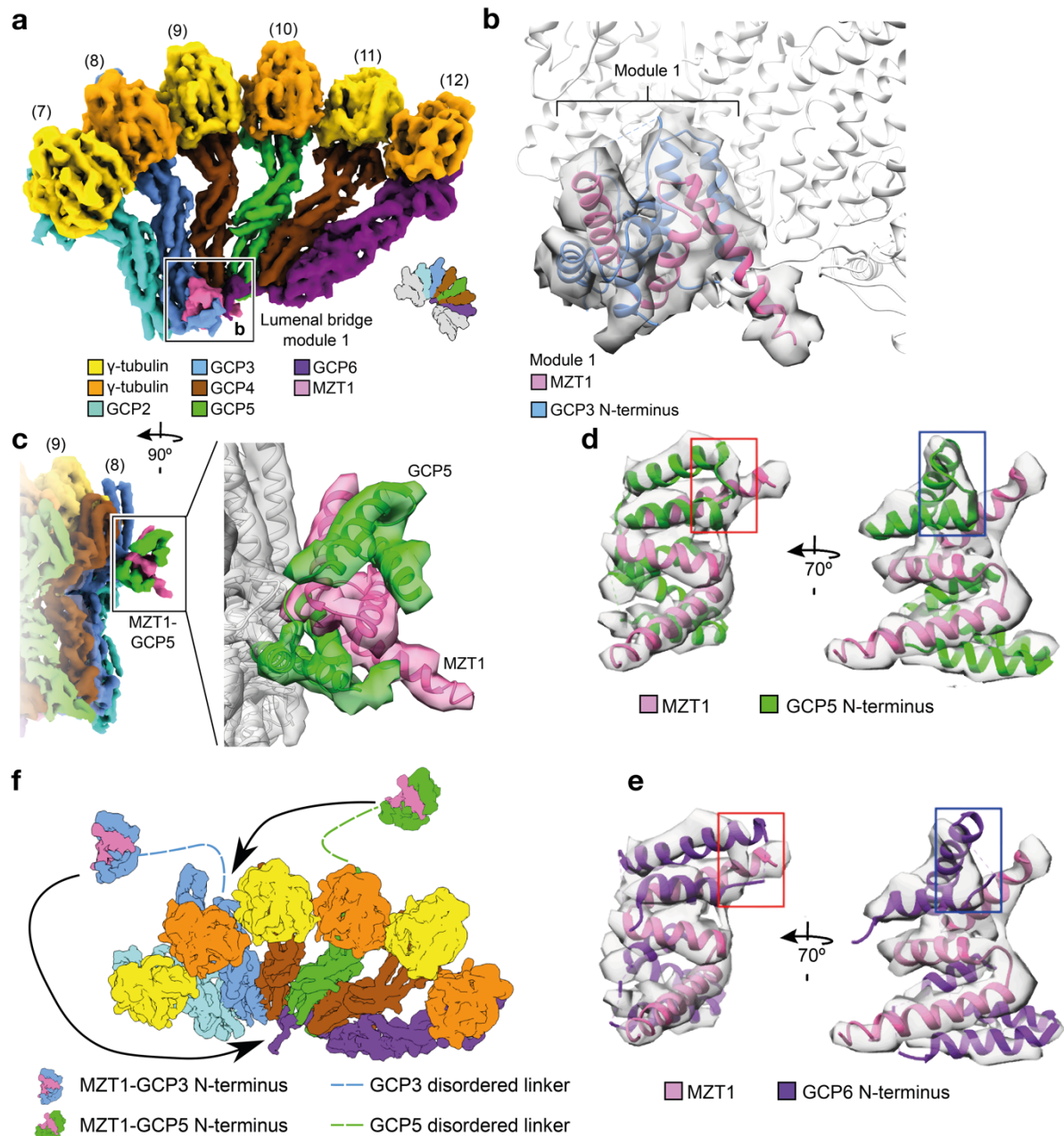


Figure 14 MZT1 modules of the 6-spoke intermediate: **a**, cryo-EM reconstruction of the 6-spoke intermediate. The coloring of the components is indicated, and numbering is according to the 14-spoke γ -TuRC. Schematic γ -TuRC icon indicates the set of particle classes used for the reconstructions. Grey color indicates sub-stoichiometry of γ -TuSC_(5,6) and γ -TuSC_(13,14) in the used particle set. Box highlights the MZT1-GCP3 module as starting seed of the luminal bridge. **b**, atomic model (PDB-6X0U) docked into the density of the luminal bridge module 1. Zoom as indicated in panel (a) and the luminal bridge components are colored as indicated. **c**, zooms on

Results

*the MZT1-GCP5 module. The atomic model (PDB-6L81) was docked into the α -helical bundle density on the outer surface of the 6-spoke assembly. **d**, rigid body fit of MZT1 (pink) and GCP5 N-terminus (green) (PDB-6L81) into the α -helical density segment associated with GCP3₍₈₎ of the 6-spoke intermediate. Red and blue boxes highlight density segments important for the identification of the GCP variant. **e**, like (**d**) with MZT1 (pink) in complex with the GCP6 N-terminus (purple) (PDB-6M33). Red and blue boxes highlight density segments important for identification of the GCP variant. **f**, the MZT1-GCP5 module docks onto the outer surface of the GCP3₍₈₎, and the MZT1-GCP3₍₈₎ is available to build the first module of the luminal bridge. Cryo-EM data acquisition, and analysis were done by Dr. Erik Zupa, and results were jointly evaluated. The figure was adapted from [372].*

2.3 Modularized production and characterization of γ -TuRC compartments

Results described in this chapter are published in [372]. Cryo-EM experiments and data analysis were done in collaboration with Dr. Erik Zupa and Giulia Tonon (RG Pfeffer).

2.3.1 Reconstitution of recombinant human γ -TuSC

To explore the function and composition of a smaller segments of the recombinant human γ -TuRC, I utilized the established system to recreate the foundational structural unit, the γ -TuSC. I rearranged the components within the MultiBac system and expressed a single construct with a 2xFLAG TAG at the GCP3 C-terminus (Figure 15a). I isolated γ -TuSC using GCP3-2xFLAG affinity purification followed by anion exchange chromatography (AEC) (Figure 15b). SDS-PAGE analysis revealed distinct bands for γ -tubulin, GCP2, and GCP3-2xFLAG (Figure 15c) with clearly increased purity after AEC. Notably, RUVBL1/2 protein bands, especially post-AEC, were absent, suggesting they were not firmly attached to the γ -TuSC. Negative stain EM 2D class averaging (Figure 15c) confirmed γ -TuSCs typical fold. Despite the faint staining of the corresponding bands, MZT2B and MZT1 seemed to be incorporated into the complex. Consistent with this, 2D classes showed small globular domains, possibly representing MZT2-GCP2 or MZT1-GCP3 modules. Nevertheless, partial MZT1 or MZT2B release from the γ -TuSC complex during purification cannot be excluded.

Moreover, I noticed a minor proportion of γ -TuSC oligomers in the data set. The oligomerization of γ -TuSC is noteworthy since γ -TuSC-to- γ -TuSC interactions are crucial for γ -TuRC assembly. Yet, in the concentration range used for negative stain EM analysis, I did not identify oligomers with more than four spokes, which is in contrast with the formation of the fully assembled γ -TuRC at much lower

Results

concentrations. The cryo-EM analysis of the γ -TuRC suggested a modular assembly involving specific rearrangements and stabilization of γ -TuSC units within the γ -TuRC spiral. Therefore, I hypothesized that γ -TuSC oligomerization may be a concentration-dependent effect and the observed oligomers might be unstable outside the γ -TuRC context.

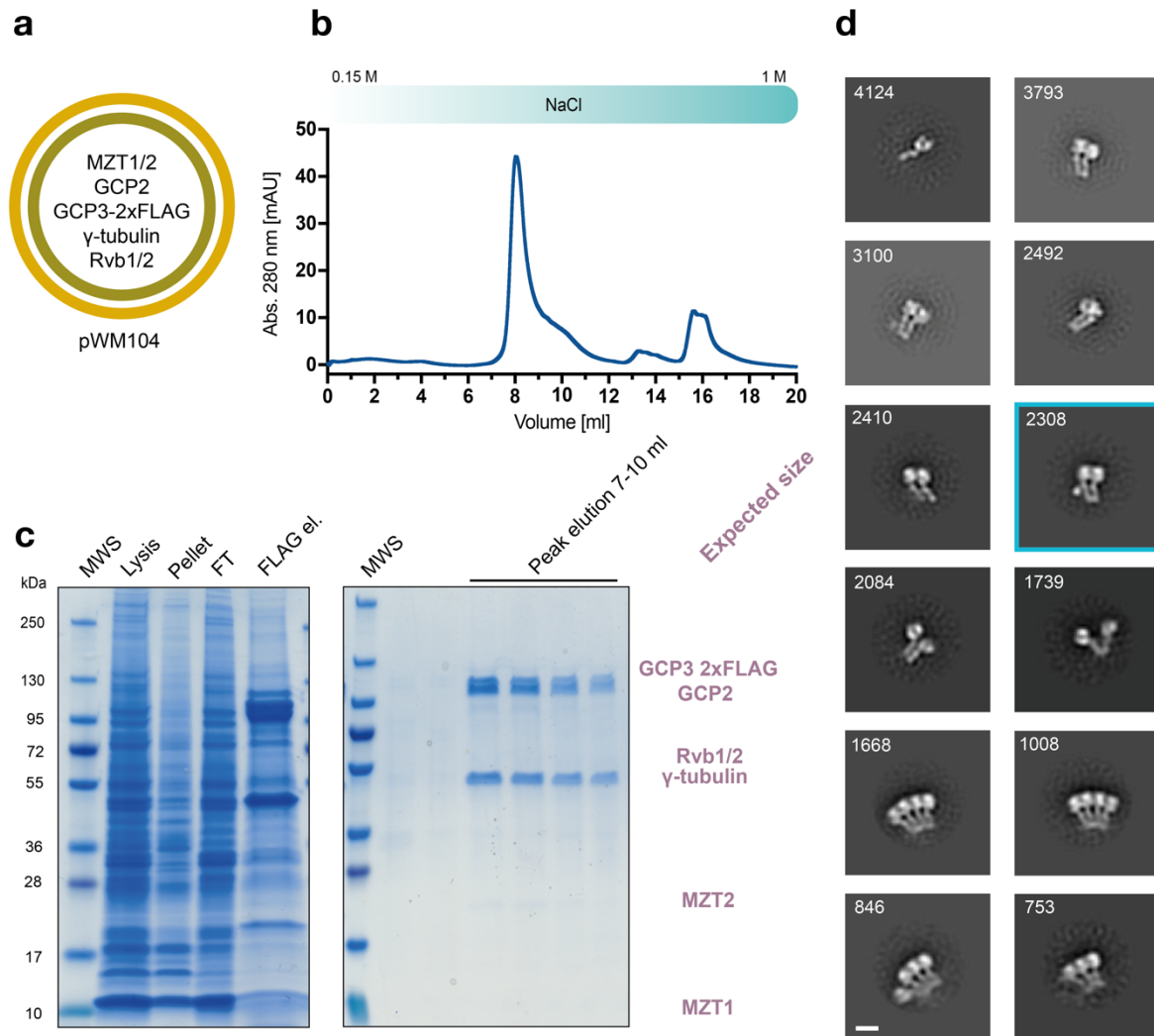


Figure 15 Recombinant reconstitution of human γ -TuSC: **a**, pWM104 was used to produce baculoviruses for co-expression in insect cells, followed by FLAG purification and AEC (**b**). Besides γ -tubulin, the construct contained MZT1, MZT2B, GCP2, GCP3-2xFLAG, RUVBL1/2 (Rvb1/2). **b**, chromatogram of AEC purification of recombinant γ -TuSC using a MonoQ (5/50 GL, Cytiva) column run with a gradient from 150 mM - 1 M NaCl. **c**, Coomassie blue-stained SDS-PAGE of γ -TuSC purifications showing left: Molecular weight standard (MWS), Lysis, Pellet, Flow through (FT), and FLAG elution (FLAG el.). Right: peak fractions of AEC run. The expected protein sizes are indicated (purple). **d**, representative negative stain EM 2D class averages of γ -TuSC particles after AEC. Particle numbers are given. Scale bar: 10 nm. Class with visible globular domain is highlighted with a turquoise box. Negative stain EM data acquisition was done by Dr. Annett Neuner. The figure was adapted from [372].

Therefore, I measured the oligomeric state of purified γ -TuSC at varying concentrations using negative stain EM and 2D class averaging (Figure 16a,b). After concentrating the purified protein complex to 3.6 μ M, I conducted a dilution series.

Results

The findings revealed a concentration-dependent increase in both the proportion of oligomerized γ -TuSC units and oligomer size (Figure 16c,d). This showcased the inherent ability of γ -TuSC units to self-assemble into oligomers. Spontaneous oligomerization required high γ -TuSC concentrations ($>0.5\mu\text{M}$).

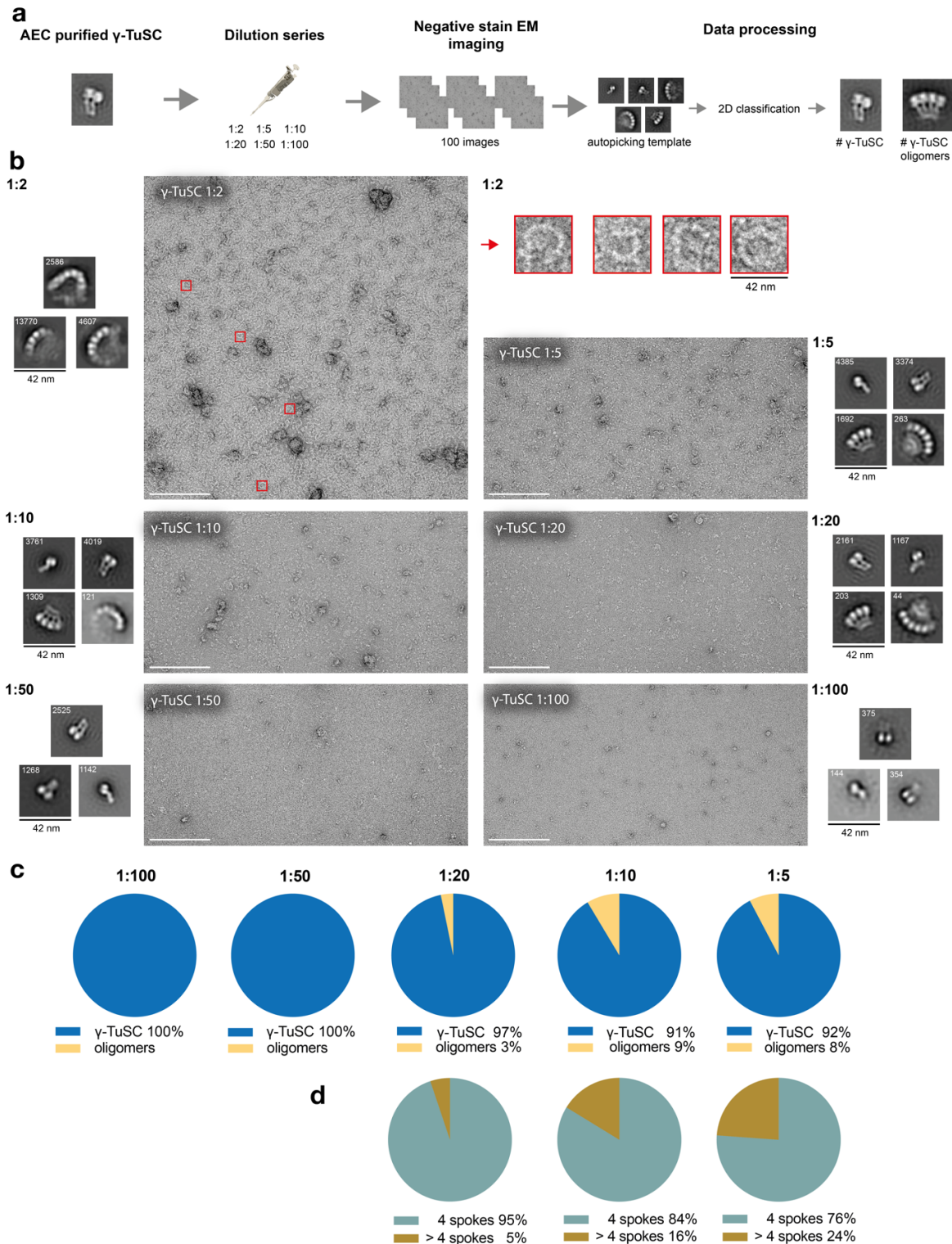


Figure 16 γ -TuSC oligomer formation is concentration-dependent: **a**, Experimental scheme of the γ -TuSC dilution experiment. AEC-purified recombinant γ -TuSC was concentrated to $3.6\mu\text{M}$ (Amicon 30 kDa), diluted to the indicated concentrations and directly used for negative staining and

Results

EM image acquisition. For each sample, 100 negative stain EM images were processed in the same way (see Methods, Chapter 4.6). For each sample, particles corresponding to single γ -TuSC units and γ -TuSC oligomers in the resulting 2D classes were quantified. **b**, for each dilution, a section of a representative micrograph is shown, together with representative 2D class averages of single γ -TuSC units or γ -TuSC oligomers. For the 1:2 dilution sample, zoomed individual particles are highlighted (red boxes). Particle numbers contributing to the respective classes are given. Scale bars: micrograph section 250 nm; other scale bars are given. **c,d** relative abundance of single γ -TuSC units (blue) vs. γ -TuSC oligomers (yellow) (**c**), and of 4-spoked (turquoise) vs. larger γ -TuSC oligomers (brown) (**d**). Numbers in the individual classes (**c**): 1:100, γ -TuSC ($n=873$); 1:50, γ -TuSC ($n=11,296$); 1:20, γ -TuSC ($n=25,685$), oligomers ($n=856$); 1:10, γ -TuSC ($n=30,008$), oligomers ($n=2,815$); 1:5, γ -TuSC ($n=42,055$), oligomers ($n=3,513$). Numbers in the individual classes (**d**): 1:20, 4 spokes ($n=812$), > 4 spokes ($n=44$); 1:10, 4 spokes ($n=2,358$), > 4 spokes ($n=457$); 1:5, 4 spokes ($n=2,675$), > 4 spokes ($n=838$). Negative stain EM data acquisition was done by Dr. Annett Neuner. The figure was adapted from [372].

Biochemical and EM data from different groups confirmed that the purified γ -TuRC from human and *Xenopus* remains stable post-isolation at significantly lower concentrations. This suggests that other elements besides γ -TuSC- γ -TuSC interactions stabilize γ -TuSC binding after being added to the growing γ -TuRC spiral. The accumulated data, from assembly intermediates and γ -TuSC experiments, suggests that γ -TuRCs asymmetric architecture is crucial for its formation and stability as a 14-spoke unit. While γ -TuSC is the γ -TuRCs foundational unit, it appears that the asymmetric segment, specifically GCP4-5-4-6, is the complex's seed. Hence, I centered my focus on GCP4, GCP5, and GCP6.

2.3.2 Reconstitution of the 4-spoke intermediate γ -TuRC ^{Δ GCP2/3}

In experiments co-expressing γ -TuRC-specific GCPs with 2xFLAG-GCP5 FLAG, I found no evidence of 4-spoke or smaller assemblies in the FLAG elutions. I then constructed a γ -TuRC ^{Δ GCP2/3} co-expression plasmid (pWMM127) by omitting *TUBGCP2* and *TUBGCP3* (Figure 17a). I proceeded with recombinant expression and the standard single-step FLAG purification. I validated the co-purification of GCP4, GCP6, and γ -tubulin with 2xFLAG-GCP5 using Coomassie blue-stained SDS-PAGE and immunoblot analysis (Figure 17b,c). Negative stain EM micrographs and 2D class averages displayed a 4-spoke structure. Notably, this complex can form independently of the ring, which suggests that it represents the starting γ -TuRC assembly unit.

Interestingly, there was also a high prevalence of a single-spoked class, possibly representing 2xFLAG GCP5 in complex with γ -tubulin (single-spoke). To further validate the γ -TuRC module GCP4-GCP5-GCP4-GCP6, I subjected the sample to cryo-EM SPA. Erik Zupa and Giulia Tonon achieved a 7.8 Å global resolution reconstruction of this 4-spoke assembly intermediate (Figure 17e). The GCP

Results

identification was based on the GCP N-termini length and specific extensions (Figure 17f). Importantly, it is likely that MZT1 forms part of the complex wherein it interacts with the N-termini of GCP5 and GCP6, although not resolved via negative stain EM and cryo-EM, most likely due to the flexibility of the N-terminal extensions of GCP5 and GCP6.

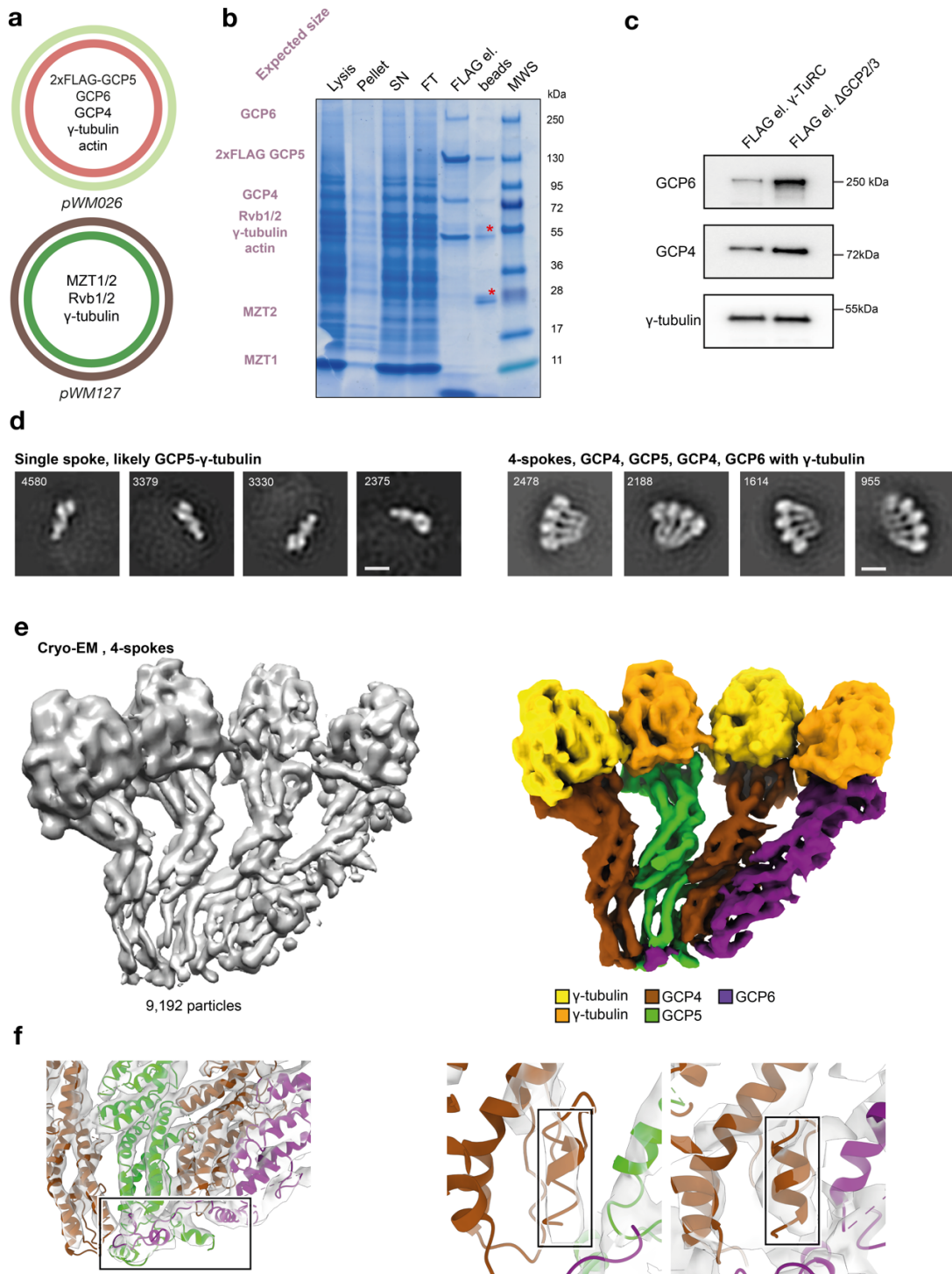


Figure 17 Recombinant reconstitution and structural characterization of the human GCP4-5-4-6 4-spoke intermediate: a, pWVM026 and pWVM127 were used to produce baculoviruses for co-expression in insect cells, followed by single-step FLAG purification. Besides γ-tubulin, the constructs contained MZT1, MZT2B, RUVBL1/2 (Rvb1/2), 2xFLAG-GCP5, GCP4, GCP6, β-actin.

Results

b, Coomassie blue-stained SDS-PAGE showing: Lysis, Pellet, Supernatant (SN), Flow through (FT), FLAG elution (Flag el.), SDS elution of FLAG beads (after FLAG elution, beads), molecular weight standard (MWS). Expected protein sizes are indicated (purple). Red asterisks indicate heavy and light chains of FLAG antibodies. **c**, sections of immunoblot analysis of FLAG elutions (FLAG el.) from wild-type (WT; γ -TuRC) (Figure 12) and γ -TuRC $^{\Delta GCP2/3}$ ($\Delta GCP2/3$), against GCP6, GCP4 and γ -tubulin antibodies. **d**, representative negative stain EM 2D class averages. Left: single spokes (likely 2xFLAG-GCP5- γ -tubulin), and 4-spoke sub-complexes corresponding to GCP4-5-4-6 in complex with γ -tubulin. Particle numbers are given. Scale bar: 10 nm. **e**, left: cryo-EM density of the 4-spoke intermediate after multi-body refinement at 7.8 Å global estimated resolution. Right: density colored in the γ -TuRC scheme, as indicated. **f**, zoom on density segments and atomic models of the GCP N-termini in the 4-spoke intermediate for GCP identification. Left: N-terminal extension of GCP5 (green model) and GCP6 (purple model). Right: last N-terminal helix in GCP4₍₉₎ and GCP4₍₁₁₎ (brown model). Negative stain EM data acquisition was done by Dr. Annett Neuner. Cryo-EM data acquisition, analysis and visualization were done by Dr. Erik Zupa and Giulia Tonon and results were jointly evaluated. The figure was adapted from [372].

In summary, the accumulated data suggest a sequential formation in which a GCP4-5-4-6 intermediate is followed by a rapid integration of a γ -TuSC unit, resulting in a 6-spoke intermediate. This becomes the foundational structure in γ -TuRC assembly. Noteworthy, the structural findings described here align with biochemical data from [162]. Hence, using my recombinant expression system, I could segment the γ -TuRC expression into γ -TuSC and 4-spoke units. Overall, the data unveiled a modular assembly process, underscoring the importance of γ -TuRCs unique composition for its specific 14-spoke ring assembly and stability.

2.4 The role of actin in the lumen of γ -TuRC

The recombinant system established here enables cryo-EM analysis of the γ -TuRC and its components. This system's primary advantage is the ability to modify components and study their specific roles within the complex. To demonstrate this, I explored the function of actin integration in the γ -TuRC lumen. The results from this chapter have been published in [372]. Dr. Erik Zupa (RG Pfeffer) collaborated on the cryo-EM experiments and data analysis, while Dr. Enrico Salvatore Atorino (RG Schiebel) performed experiments in the human culture system.

2.4.1 Actin IP experiments identify the GCP6_{N126}-MZT1 module as actin binding domain

The discovery of actin within the γ -TuRC lumen was a significant revelation when the cryo-EM structures of the native vertebrate γ -TuRCs were determined. The resolution of these structures, however, did not enable to unambiguously discern the precise identity or function of this actin molecule. Within the γ -TuRC, actin bridges from the end of the luminal bridge to GCP3/ γ -tubulin at spoke 2 (Figure 18a). The cryo-EM maps indicate the potential interaction interface between the luminal bridge and

Results

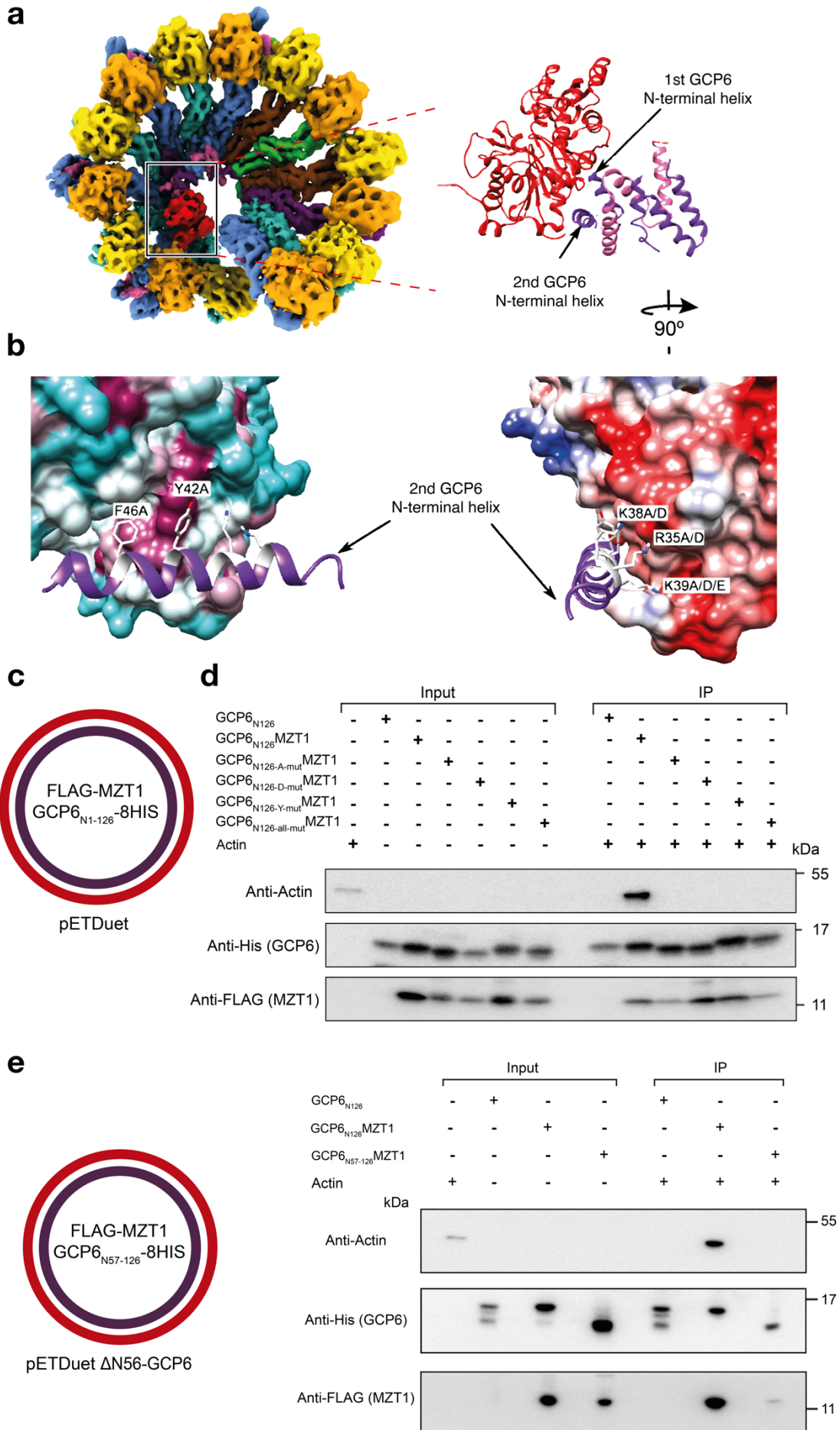
actin. Specifically, this interface might be formed by the two N-terminal helices of GCP6, with amino acids R35, K38, K39, Y42, and F46 (Figure 18b). Notably, the GCP6 N-terminal helices interact with the three α -helices (H1-H3) of MZT1, potentially ensuring the proper folding of the GCP6 N-terminus and its subsequent interaction with actin.

To further study this biochemically, I, along with Anna Böhler, supervised an *in vitro* actin-IP experiment conducted by a master student, Ariani S. Rahadian. I guided the creation of *E. coli* expression constructs consisting of the first 126 amino acid residues of *TUBGCP6* (GCP6_{N126}-His₈) and FLAG-*MZT1* (Figure 18c). Co-IP experiments revealed that the MZT1-GCP6 module could bind actin (Figure 18d). In contrast, in the absence of MZT1 or when specific point mutations were introduced, this interaction was suppressed. This suggests that the properly folded MZT1-GCP6 module strongly interacts with actin, possibly enabling its recruitment to the γ -TuRC, even without other interactions. I then guided the production of a truncated version of the actin-interacting GCP6 interface (GCP6_{N57-126}-His₈). As expected, this construct (Figure 18e) did not bind to actin, underscoring the importance of the first two GCP6 α -helices in actin binding and suggesting that removing this region could prevent actin's integration into the γ -TuRC lumen.

2.4.2 Recombinant γ -TuRC ^{Δ N56-GCP6} shows that actin integration is not essential for γ -TuRC's structural integrity

To probe whether the removal of the first two helices from GCP6 abrogates actin integration into the γ -TuRC and whether its integration is crucial for the 14-spoke ring complex integrity, I utilized the established recombinant expression system in insect cells. I substituted the full-length GCP6 with its N-terminal truncated version (Δ N56-GCP6) and reconstituted the γ -TuRC ^{Δ N56-GCP6}. Following a single-step FLAG batch purification, I conducted SDS-PAGE, immunoblot, and negative stain EM analysis (Figure 19a-d). The results of this integrated analysis revealed that several GCPs, notably GCP6, co-purified with 2xFLAG GCP5 (Figure 19b-c). Similarly to the wild-type, γ -TuRC particles were observed in the negative stain EM 2D class averaging (Figure 19d).

Results



Results

Figure 18 MZT1-GCP6 is an actin binding motif: **a**, left: top view of the γ -TuRC, with components colored: GCP5 (green), GCP2 (light blue), GCP3 (dark blue), γ -tubulin (orange/yellow), GCP4 (brown), GCP6 (purple), actin (red), MZT1 (pink). Box highlights the actin molecule in the lumen. Right: close-up view on the molecular representation of actin and the N-terminus of MZT1-GCP6 found in the luminal bridge (PDB-6M33, PDB-6XOU). The interacting helices of the GCP6 are indicated. **b**, view on the actin GCP6 interface. Actin surface is colored according to hydrophobicity on the left panel (cyan: hydrophilic, white: neutral, maroon: hydrophobic), and on the right according to coulombic potential (blue: positive charge, white: neutral, red: negative charge). Residues of the N-terminal GCP6 helices interacting with actin are shown in stick representation and colored white. Introduced mutations are indicated. **c**, scheme of the plasmid construct used for the generation of the IP samples. The two gene cassettes of the MZT1-FLAG and TUBGCP6_{N126}-His₈ constructs. Wild-type or point mutations were cloned into pETDuet vectors. **d**, immunoblot analysis of the actin IP experiment. Constructs were pulled via His-tagged GCP6. Samples were GCP6_{N126} without co-expression of FLAG-MZT1, GCP6_{N126}-MZT1 and constructs with point mutations indicated in (**b**): GCP6_{N126}-A-mut-MZT1 (R35A, K38A, K39A); GCP6_{N126}-D-mut-MZT1 (R35D, K38D, K39D); GCP6_{N126}-Y-mut-MZT1 (Y42A, F46A); GCP6_{N126}all-mut-MZT1 (R35D, K38D, K39D, Y42A, F46A). Anti-actin, anti-His (GCP6) and anti-FLAG (MZT1) antibodies were used for immunoblot analysis. IP experiments were performed in (n=3) independent experiments. **e**, GCP6 deletion construct (GCP6_{N57-126}-His₈) was used for actin IP experiments and immunoblot analysis similar to (**d**). Constructs were: GCP6_{N126}-His₈ and GCP6_{N57-126}-His₈ co-expressed with FLAG-MZT1 and GCP6_{N126}-His₈ without co-expression of MZT1-FLAG as control. IP experiments and immunoblot analysis were done in (n = 3) independent experiments. Analysis of the actin GCP6 interface was done in collaboration with Dr. Erik Zupa. Actin IP experiments were done in collaboration with Anna Böhler and Ariani S. Rahadian. The figure was adapted from [372].

In collaboration with Anna Böhler and Dr. Lukas Rohland (RG Mayer), I further investigated the role of actin in MT nucleation by the γ -TuRC through an *in vitro* MT nucleation assay. The fluorescence signal intensity of polymerized MTs in the presence of either wild-type or γ -TuRC ^{Δ N56-GCP6} at varying concentrations was measured (see Methods, Chapter 4.5.5, Figure 19e). The results of this batch assay showed that under the utilized conditions, γ -TuRC ^{Δ N56-GCP6} could nucleate MTs to a similar extent as wild-type in all used concentrations. Of note, this shows that both recombinant complexes can facilitate MT nucleation *in vitro*, further highlighting the reconstitution of functional complexes.

Results

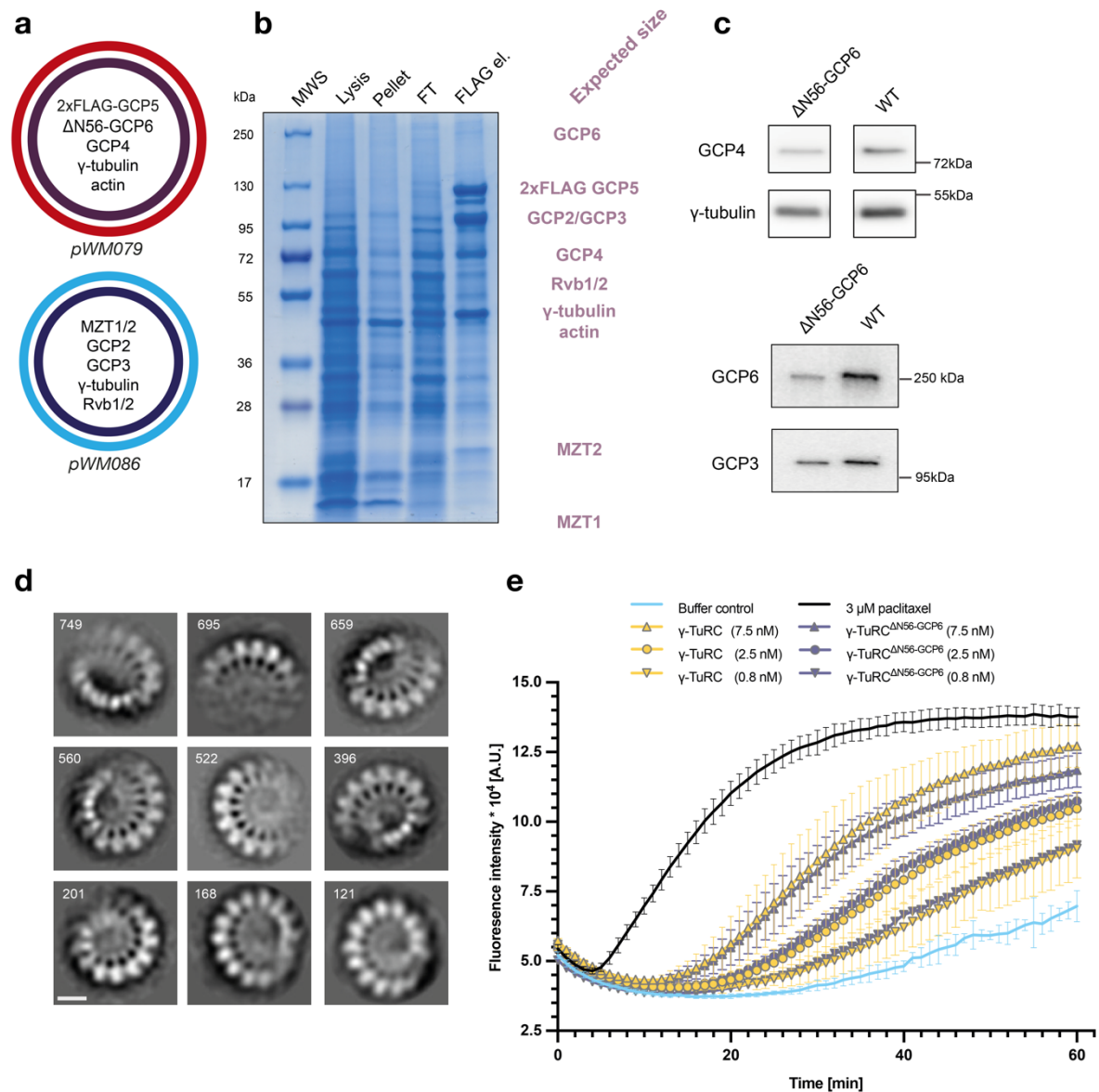


Figure 19 Reconstitution of γ -TuRC^{ΔN56-GCP6}: **a**, pWM079, and pWM086 were used to produce baculoviruses for co-expression in insect cells, followed by single-step purification. Besides γ -tubulin, the constructs contained MZT1, MZT2B, GCP2, GCP3, RUVBL1/2 (Rvb1/2), 2xFLAG-GCP5, GCP4, ΔN56-GCP6, β -actin. **b**, Coomassie blue-stained SDS-PAGE of recombinant γ -TuRC^{ΔN56-GCP6} purification used for cryo-EM experiments (Figure 20) showing: Molecular weight standard (MWS); Lysis; Pellet; Flow through (FT); FLAG elution (FLAG el.). Expected protein size is indicated (purple). **c**, immunoblot analysis of FLAG elution of wild-type γ -TuRC (WT) and γ -TuRC^{ΔN56-GCP6} (ΔN56-GCP6), against GCP4, γ -tubulin, GCP3 and GCP6 antibodies. **d**, representative 2D class averages of negative stain EM data of recombinant human γ -TuRC^{ΔN56-GCP6}. Number of particles is given, scale bar: 10 nm. **e**, batch in vitro MT nucleation assay (Cytoskeleton, Denver Com cat. no. BK011P) comparing recombinant wild-type γ -TuRC (γ -TuRC) and γ -TuRC^{ΔN56-GCP6}. Shown are error bars for the standard deviation of the mean of (n=4) replicates for buffer control (blue), 3 μ M Paclitaxel as positive control (black), and three different concentrations of γ -TuRC (yellow) and γ -TuRC^{ΔN56-GCP6} (purple) samples. Concentrations given in the figure correspond to the γ -tubulin concentration of the sample determined by immunoblot analysis in comparison to recombinant human γ -tubulin. Negative stain EM data acquisition was done by Dr. Annett Neuner. MT nucleation assay was done in collaboration with Anna Böhler and Dr. Lukas Rohland. The figure was adapted from [372].

Results

As a next step, to further characterize the γ -TuRC ^{Δ N56-GCP6}, I prepared the sample for cryo-EM SPA analysis. Erik Zupa's cryo-EM reconstruction attained 7.1 Å global resolution, confirming the reconstitution of fully assembled 14-spoke- γ -TuRC ^{Δ N56-GCP6} complexes (Figure 20a). Importantly, the GCP architecture matched that of the wild-type complexes (Figure 20a), including all MZT1 modules. As anticipated, actin was absent in the γ -TuRC ^{Δ N56-GCP6}, which is evident from the missing cryo-EM density for this component (Figure 20b). Consistently, the first two N-terminal GCP6 α -helices showed no cryo-EM density, as expected. Notably, the residual luminal bridge segments were properly folded, allowing the identification of the MZT1 modules within this structure (Figure 20c). The H1-H3 segments of the MZT1 linked with GCP6 were distinct, suggesting that the deleted helices are not essential for the MZT1-GCP6 module's stable fold.

Collectively, the co-IP experiments and cryo-EM analysis of the γ -TuRC ^{Δ N56-GCP6} identify the primary role of MZT1-GCP6 in the binding interface with actin and reveal that actin is not essential for the assembly of the γ -TuRC and for its structural integrity. A comparison between the conformations of wild-type γ -TuRC and γ -TuRC ^{Δ N56-GCP6} showed only minor differences (Figure 20d). However, the absence of actin in the proximity of the first γ -TuSC (at spokes 1 and 2) led to a distinct conformation. The primary spokes, where actin might bind via its D-loop [35], were displaced by approximately 10 Å from the center, suggesting that actin drives these spokes into a more closed conformation. This hints that actin may not be vital for γ -TuRC assembly, but it might be involved in defining the conformation of spokes 1 and 2, which may crucially impact the γ -TuRC function.

Results

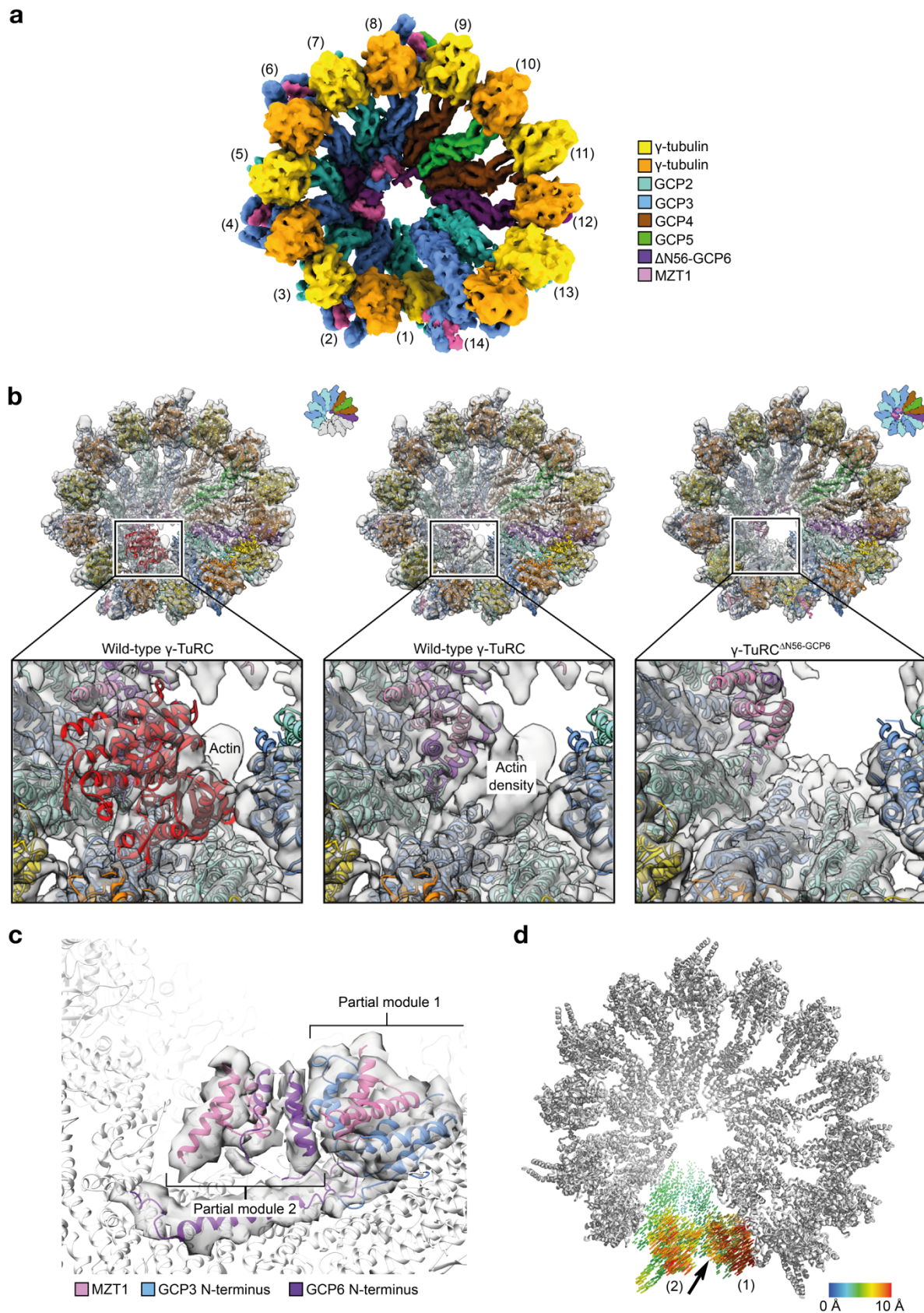


Figure 20 Cryo-EM analysis of γ -TuRC ^{Δ N56-GCP6} reveals that actin is not essential for γ -TuRC assembly and integrity: **a**, cryo-EM reconstruction of γ -TuRC ^{Δ N56-GCP6}. Coloring is indicated and spokes are numbered. Actin was co-expressed but could not be detected in the cryo-EM density. **b**, comparison of the cryo-EM densities obtained for recombinant wild-type γ -TuRC (left and middle) and recombinant γ -TuRC ^{Δ N56-GCP6} (right). The zoomed views highlight the density segments

Results

corresponding to the luminal bridge of the two reconstructions. For the wild-type, two representations are shown. Left: fitted model with actin; middle: luminal bridge without actin for a better comparison with the γ -TuRC ^{Δ N56-GCP6} on the right. **c**, close-up view of the luminal bridge in the γ -TuRC ^{Δ N56-GCP6}. The atomic model of the resolved components (PDB-6X0U) was docked and coloring is indicated. **d**, effect of actin binding/docking on the γ -TuRC geometry, as indicated by vectors linking the C α atoms in the two conformations (wild-type and γ -TuRC ^{Δ N56-GCP6}). Vector coloring for spokes 1,2 is indicated. Direction of movement is indicated by an arrow. Cryo-EM data acquisition, analysis and visualization were done by Dr. Erik Zupa, and results were jointly evaluated. The figure was adapted from [372].

2.4.3 Analysis of GCP6 mutants in cell culture models indicate that actin integration into γ -TuRC is relevant for its function

The structural characterization of the γ -TuRC ^{Δ N56-GCP6} showed that while actin is not crucial for γ -TuRC formation, it does influence the conformation at spokes 1 and 2 and possibly its function. In the *in vitro* MT nucleation batch assay, no differences were observed between the wild-type γ -TuRC and γ -TuRC ^{Δ N56-GCP6}. However, the ability of this *in vitro* methodology to differentiate the nucleation mechanisms of γ -TuRC with and without actin, independent of other variables, remains uncertain. Consequently, I shifted my focus to human cell culture system experiments to assess the implications of preventing actin integration into the γ -TuRC. This involved exploring GCP6 mutants within a cellular context inclusive of all regulatory mechanisms and interaction partners.

To study the impact of blocking actin's incorporation into γ -TuRC under more native conditions, after jointly designing the strategy, Dr. Enrico Salvatore Atorino (later denoted as Enrico) established endogenous Δ N60-TUBGCP6 cell lines (Δ N-GCP6), in retinal pigment epithelial-1 (RPE1) cells using the CRISPR-Cas9 system [375]. Here, the very N-terminus of GCP6 was removed, initializing the methionine at position 61 as the start codon (Figure 21a). Collaborating with Enrico, I verified two independently constructed clones through PCR and sequencing, later utilized for *in vivo* characterization (#1, #2, Figure 21b,c). Additionally, Enrico confirmed these findings via immunofluorescence microscopy and immunoblot analysis, demonstrating that in Δ N-GCP6 cells, GCP6 biosynthesis and localization were consistent with wild-type TUBGCP6 cells (Figure 21d-f).

Subsequent characterizations involved analysis of mitotic cells. Cells with proper chromosome alignment at the metaphase plate exhibited an increased accumulation of the spindle assembly checkpoint protein BubR1 [376] on individual kinetochores in Δ N-GCP6 cells compared to wild-type cells (Figure 21g,i). This suggests a delay in chromosome positioning due to flawed kinetochore-MT connections. Moreover,

Results

during late pro-metaphase to metaphase, the ΔN -GCP6 cells showed a higher frequency of centrosome detachment from spindle poles than the control cells (Figure 21h,j). These observed phenotypes were also evident in siRNA depletion experiments (Figure 21l,m), which Enrico conducted using stably integrated siRNA-resistant ΔN -TUBGCP6-FLAG and TUBGCP6-FLAG constructs in RPE1-hTERT cells.

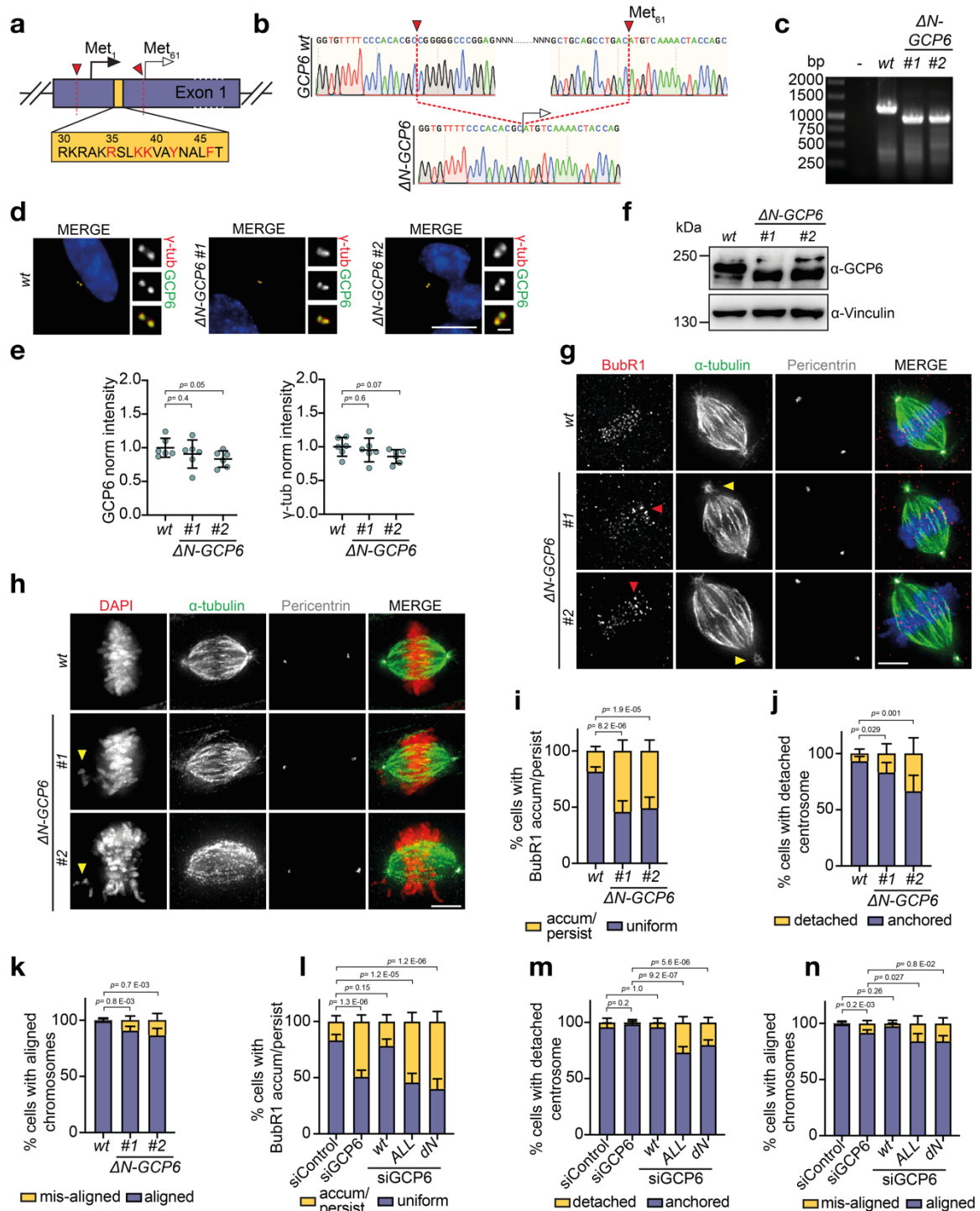


Figure 21 Characterization of ΔN -GCP6 RPE1 cell lines: **a**, scheme of the RPE1 ΔN -GCP6 cell line generation. The red arrowheads point to the single guide RNA (sgRNA) target sites in TUBGCP6 Exon 1 (purple) with the region interacting with actin (yellow). The black arrow represents the endogenous start codon Met₁, while the white arrow represents the resulting start codon (Met₆₁)

Results

in ΔN -GCP6. **b**, sequence chromatogram of the TUBGCP6 exon 1 locus of the GCP6 wild-type (WT) and ΔN -GCP6 cells around the modification sites. Colors of the different nucleotides as indicated. As in **(a)** red arrowheads indicate the sgRNA target sites and the white arrow indicates the newly generated start codon. **c**, genomic PCR of the locus indicated in **(a,b)**. The PCR product in the ΔN -GCP6 clones reflects the calculated loss of 205 nucleotides (nt) compared to the WT control. **d**, immunofluorescence (IF) analysis of γ -tubulin and GCP6 levels at centrosomes of WT and ΔN -GCP6 cells. Scale bars: 10 μm ; magnification 1 μm . **e**, quantification of the γ -tubulin and GCP6 signal intensity in the IF analysis **(d)**. **f**, immunoblot of the endogenous GCP6 levels in WT and ΔN -GCP6 (clone #1, #2). Downshift of the GCP6 bands in the samples of the two ΔN -GCP6 clones can be observed. **g**, representative IF images of metaphase WT and ΔN -GCP6 (#1, #2) mitotic cells. MT (α -tubulin) and BubR1 were labeled to detect their accumulation (red arrowheads) on chromosomes stained with DAPI. Centrosomes were stained with antibodies against pericentrin. Yellow arrowheads indicate detached centrosomes from the spindle pole. Scale bar: 5 μm . **h**, similar to **(g)**, representative IF images of metaphase WT and ΔN -GCP6 (#1, #2) mitotic cells in which the chromosomes were aligned/close to the alignment in the metaphase plate. Yellow arrowheads indicate mis-aligned chromosomes. Scale bar: 5 μm . **i**, quantification (mean \pm s.d) of metaphase cells (%) in which BubR1 accumulated or persisted (accum/persist) on centromeres non-uniformly, see **(g)**. *p* values are given. **j**, quantification (mean \pm s.d) of metaphase cells (%) in which centrosomes detached from the spindle pole, see **(g)**. *p* values are given. **k**, quantification (mean \pm s.d) of metaphase cells (%) in which chromosomes did not align accurately in the metaphase plate see **(h)**. *p* values are given. **l**, quantification (mean \pm s.d) of metaphase cells (%) in which BubR1 accumulated or persisted on centromeres non-uniformly in cells treated with siGCP6 and in which TUBGCP6 WT and TUBGCP6 mutants (ALL (R35D, K38D, K39E, Y42A, F46A); ΔN ($\Delta N56$ -GCP6)) were expressed. *p* values are given. **m**, quantification (mean \pm s.d) of metaphase cells (%) in which centrosomes detached from the spindle pole in cells treated with siGCP6 and in which TUBGCP6 WT and TUBGCP6 mutants (ALL (R35D, K38D, K39E, Y42A, F46A); ΔN ($\Delta N56$ -GCP6)) were expressed. *p* values are given. **n**, quantification (mean \pm s.d) of metaphase cells (%) in which chromosomes were aligned or close to alignment in the metaphase plate in cells treated with siGCP6 and in which TUBGCP6 WT and TUBGCP6 mutants (ALL (R35D, K38D, K39E, Y42A, F46A); ΔN ($\Delta N56$ -GCP6)) were expressed. *p* values are given. For all presented data with indicated *p* value, statistical analysis was derived from two-tail unpaired *t*-test analysis (3 replicates, 2 independent experiments). All experiments in cells were performed by Dr. Enrico Salvatore Atorino, and data visualization and evaluation of panels of this figure were done in collaboration with Dr. Enrico Salvatore Atorino. The figure was adapted from [372].

Importantly, Enrico confirmed GCP6 depletion and the subsequent GCP6 signal following FLAG construct overexpression through immunofluorescence microscopy and immunoblot analysis (Figure 22a,b). Due to the anomalies identified in both ΔN -GCP6 cells and siRNA experiments, an increase of about 10% in chromosome misalignment frequency was observed (Figure 21k,n). This misalignment might result in defective chromosomes segregation in emerging daughter cells.

To explore the impact of actin depletion on mitotic progression, Enrico created cell lines from both TUBGCP6 wild-type and ΔN -GCP6 variants that continuously express mNeonGreen-LMN1 and TUBG1-mRuby2. Using these markers, mitosis duration was measured via live cell imaging, revealing a 30-40 minute delay in ΔN -GCP6 clones compared to wild-type cells (Figure 22c,d). This delay suggests potential abnormalities in spindle formation and chromosome alignment in ΔN -GCP6 cells, hinting at a possible MT nucleation kinetic defect. To rule out the possibility that the γ -TuRC assembly is affected *in vivo* due to loss of actin integration (unlike observed

Results

in the insect cell expression system), Anna Böhler purified mutant γ -TuRC ^{Δ N56-GCP6} from HEK293T cells through a Δ N56-GCP6-FLAG pulldown. Using negative stain EM 2D class averaging, I confirmed that the γ -TuRC ^{Δ N56-GCP6} maintained structural integrity in the human cell model, closely resembling its counterpart from the insect cell expression system (Figure 22e).

Lastly, I delved into the aberrant MT nucleation kinetics hypothesis. Thus, for an *in vivo* examination of the MT nucleation activity of γ -TuRC with mutant GCP6 versions, Enrico performed a MT regrowth assay from the centrosome after cold-induced MT depolymerization [377]. Focusing on the centrosome, where the γ -TuRC is the primary MT nucleator, I jointly quantified the number and length of re-nucleated MTs. siRNA-mediated silencing of endogenous *TUBGCP6* markedly reduced MT regrowth. Still, transient expression of siRNA-resistant wild-type *TUBGCP6* restored MT regrowth to untreated or noncoding siControl-treated cell levels. However, MT re-nucleation was notably compromised by siRNA-resistant *TUBGCP6* mutants, especially those with all point mutations (ALL mut) or missing N-terminal helices (Δ N56-GCP6). These cells produced fewer and shorter MTs than the siControl or rescue groups (Figure 22f,g,h). Importantly, results from a repetition of the experiments in the Δ N-GCP6 cell line corroborated these findings (Figure 22i,j). These observations imply that actin binding-deficient γ -TuRC may have slower MT nucleation kinetics *in vivo*.

In essence, while actin is not crucial for γ -TuRCs assembly or structural integrity, its absence impairs MT re-nucleation *in vivo* and delays mitotic progression, slightly influencing spindle MT formation and chromosome segregation/positioning.

Results

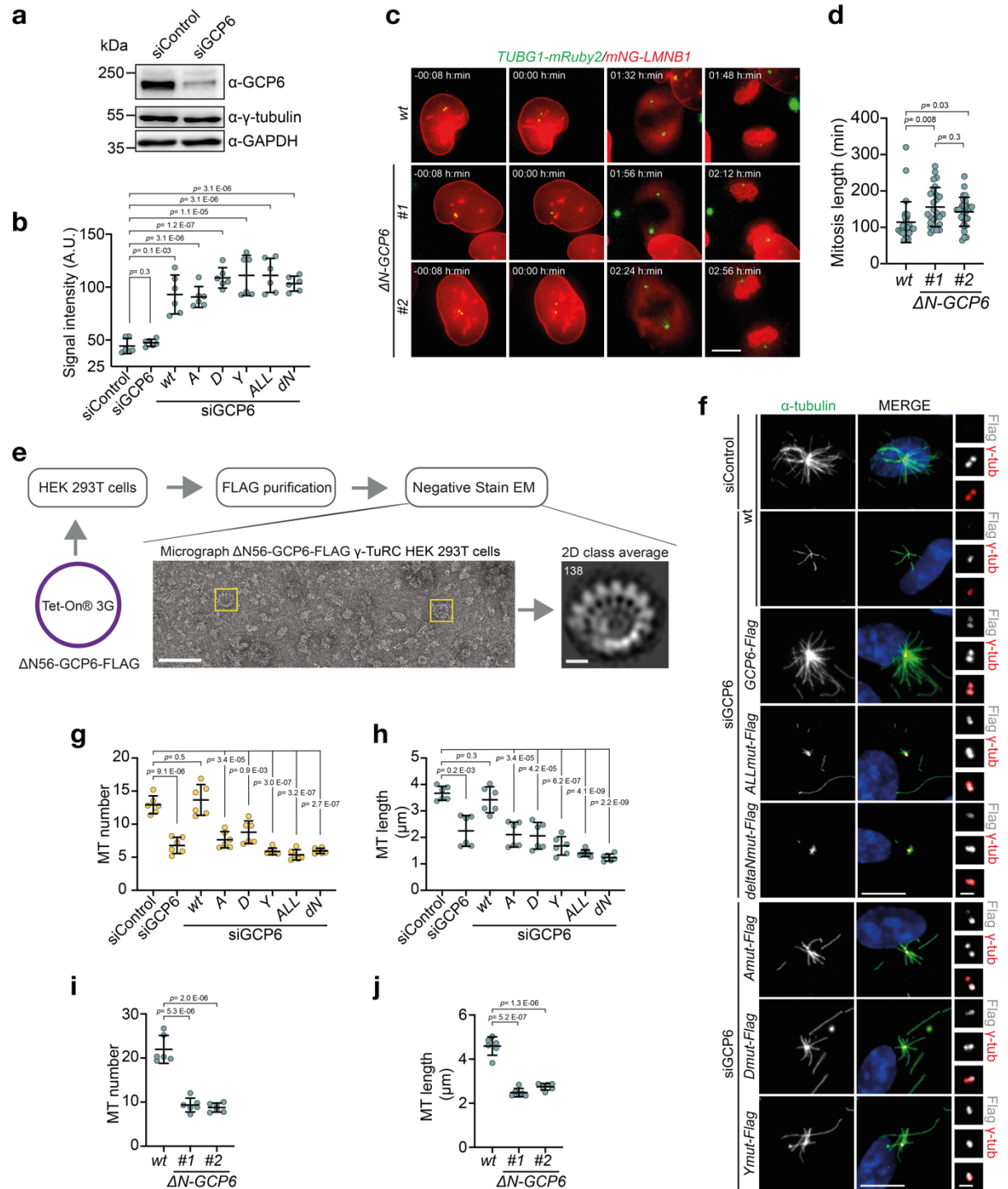


Figure 22 Mitotic delay and hampered MT re-nucleation by cells with actin-deficient γ -TuRC: **a**, immunoblot analysis of siGCP6 depletion efficiency. No effect on γ -tubulin levels in RPE1 cells after siGCP6 treatment could be observed. **b**, quantification (mean \pm s.d) of FLAG antibody intensity in immunofluorescence (IF) images (**f**) at the centrosome in the cells expressing TUBGCP6-C-terminal-FLAG constructs (wild-type (WT) and TUBGCP6-mutants: A (R35A, K38A, K39A); D (R35D, K38D, K39E); Y (Y42A, F46A); ALL (R35D, K38D, K39E, Y42A, F46A); Δ N (Δ N56-GCP6)). *p* values are given. **c**, representative images of live-cell imaging of RPE1 (mNeon-Green-LMNB1 and TUBG1-mRuby2) WT and Δ N-GCP6 mitotic cells at frames highlighting cohered centrosomes, centrosome separation, defined as time point 00:00 h:min, metaphase spindle and nuclear envelope reformation. Scale bar: 5 μ m. **d**, quantification (mean \pm s.d) of intervals from the stage of centrosome separation to nuclear envelope reformation (**c**). WT *n* = 27 cells, Δ N-GCP6 #1 *n* = 26 cells, and Δ N-GCP6 #2 *n* = 30 cells; from 4 independent data

Results

acquisitions, *p* values are given. **e**, negative stain EM analysis of $\Delta N56$ -GCP6-FLAG γ -TuRC purified from HEK293T cells. Individual particles (yellow boxes) on the micrograph and a 2D class are shown. Scale bar micrograph: 100 nm; and 2D class: 10 nm. Particle number is given. **f**, MT regrowth assay in RPE1 cells showing representative IF images of MT asters nucleated from the centrosome (γ -tubulin signal). Cells were treated with siRNA (siGCP6 or siControl) and TUBGCP6-C-terminal-FLAG (WT or TUBGCP6 mutants: A (R35A, K38A, K39A); D (R35D, K38D, K39E); Y (Y42A, F46A); ALL (R35D, K38D, K39E, Y42A, F46A); ΔN ($\Delta N56$ -GCP6)) were expressed (FLAG signal). Scale bar: 5 μ m; magnification 1 μ m. **g**, quantification (mean \pm s.d) of the average number of nucleated MTs in the MT regrowth assay (**f**). *p* values are given. **h**, quantification (mean \pm s.d) of the average length of nucleated MTs in the MT regrowth assay (**f**). *p* values are given. **i**, similar to (**f,g**), quantification (mean \pm s.d) of the average number of nucleated MTs in the MT regrowth assay in WT and ΔN -GCP6 (#1, #2) RPE1 cells. *p* values are given. **j**, similar to (**f,h**), quantification (mean \pm s.d) of the average length of nucleated MTs in the MT regrowth assay in WT and ΔN -GCP6 (#1, #2) RPE1 cells. *p* values are given. For all presented data with indicated *p* value, statistical analysis was derived from two-tail unpaired *t*-test analysis (3 replicates, 2 independent experiments). All experiments in cells were performed by Dr. Enrico Salvatore Atorino, and data visualization and evaluation of panels of this figure were done in collaboration with Dr. Enrico Salvatore Atorino. The figure was adapted from [372].

All in all, the findings emphasize the value of the recombinant γ -TuRC system in understanding γ -TuRC foundational function, enabling precise mutations to study the role of individual components, which can then be applied to other experimental methods to assess the impact of mutations within a cellular context. Consequently, this workflow emerges as a valuable blueprint to further investigate the functional sites of this MT nucleation machinery.

2.5 Unraveling the molecular architecture of the augmin complex by an integrative structural biology approach

Cryo-EM analysis of γ -tubulin complexes was a major step towards understanding the regulation of the MT nucleation process. This approach, in conjunction with a recombinant expression system, facilitates a targeted and systematic analysis of the involved components and their interactions. In this thesis, I have already demonstrated the establishment of a recombinant expression system pipeline that enables the cryo-EM analysis of wild-type and modified protein complexes. This was shown for the targeted investigation of actin integration into the lumen of the γ -TuRC, a phenomenon crucial to its function *in vivo*.

In addition to the core components of the γ -TuRC, the interaction with various related factors is essential for its *in vivo* function. Among these interaction partners, one major complex is augmin, an evolutionarily conserved hetero-octameric complex pivotal for MT branching [330]. Despite its identification across diverse organisms and a basic structural characterization portraying an elongated, flexible h-shaped rod [364,365], a comprehensive structural understanding remains elusive. Thus, I used the pipeline

Results

that I had established with the recombinant γ -TuRC to characterize the subcomplex architecture of augmin and extended it to an integrative structural biology approach. Experiments including cryo-EM, crosslinking MS analysis, AF-Multimer predictions and model building were performed in collaboration with Dr. Erik Zupa (RG Pfeffer), and the results presented herein have been published with me as co-first author [369].

2.5.1 Characterization of the augmin TIII tetramer

I chose to investigate the *X. laevis* complex because of its well-established status as a model organism for MT branching [324]. Notably, the structure of the *X. laevis* γ -TuRC has been elucidated [35], and prior published findings indicated that the *X. laevis* augmin complex could be subdivided into two tetramers [365]. The significance of this modular approach, the division into sub-complexes lies in its facilitation of a divide-and-conquer methodology, enabling the separate characterization of simpler tetrameric subunits.

First, I designed gene fragments corresponding to the *X. laevis* genes Table 24 (see Methods, Chapter 4.2) – namely HAUS1-7 – optimized for expression in insect cells and obtained the cDNA of the augmin MT-binding subunit, HAUS8. Subsequently, I integrated the genes of HAUS1 with an EGFP-His₆-TAG, 2xFLAG-HAUS3, HAUS4, and HAUS5 into the modular MultiBac system. This strategy paralleled the approach employed for human γ -TuRC (see Chapter 2.1). The outcome was the generation of a recombinant baculovirus for the augmin TIII tetramer (Figure 23a). Following expression and batch FLAG-based purification (Figure 23), I performed AEC to attain a higher level of purity for the TIII tetramer (Figure 23b). Subsequent SDS-PAGE analysis (Figure 23c) highlighted the successful purification of the recombinantly expressed proteins, as indicated by bands corresponding to the expected molecular weight. Furthermore, negative stain EM 2D and 3D class averaging (Figure 23d,e) confirmed the elongated overall shape, consistent with prior observations [365]. While the resolution was not sufficient to discern the relative arrangement of the individual components, the obtained class averages reveal a middle-region bulge and conformational flexibility along the two arms of the tetramer.

Next, I submitted the protein sequences of the expressed TIII tetramer to AF-Multimer [60] prediction, which was done by Erik Zupa in collaboration with EMBL Heidelberg (RG Eustermann).

Results

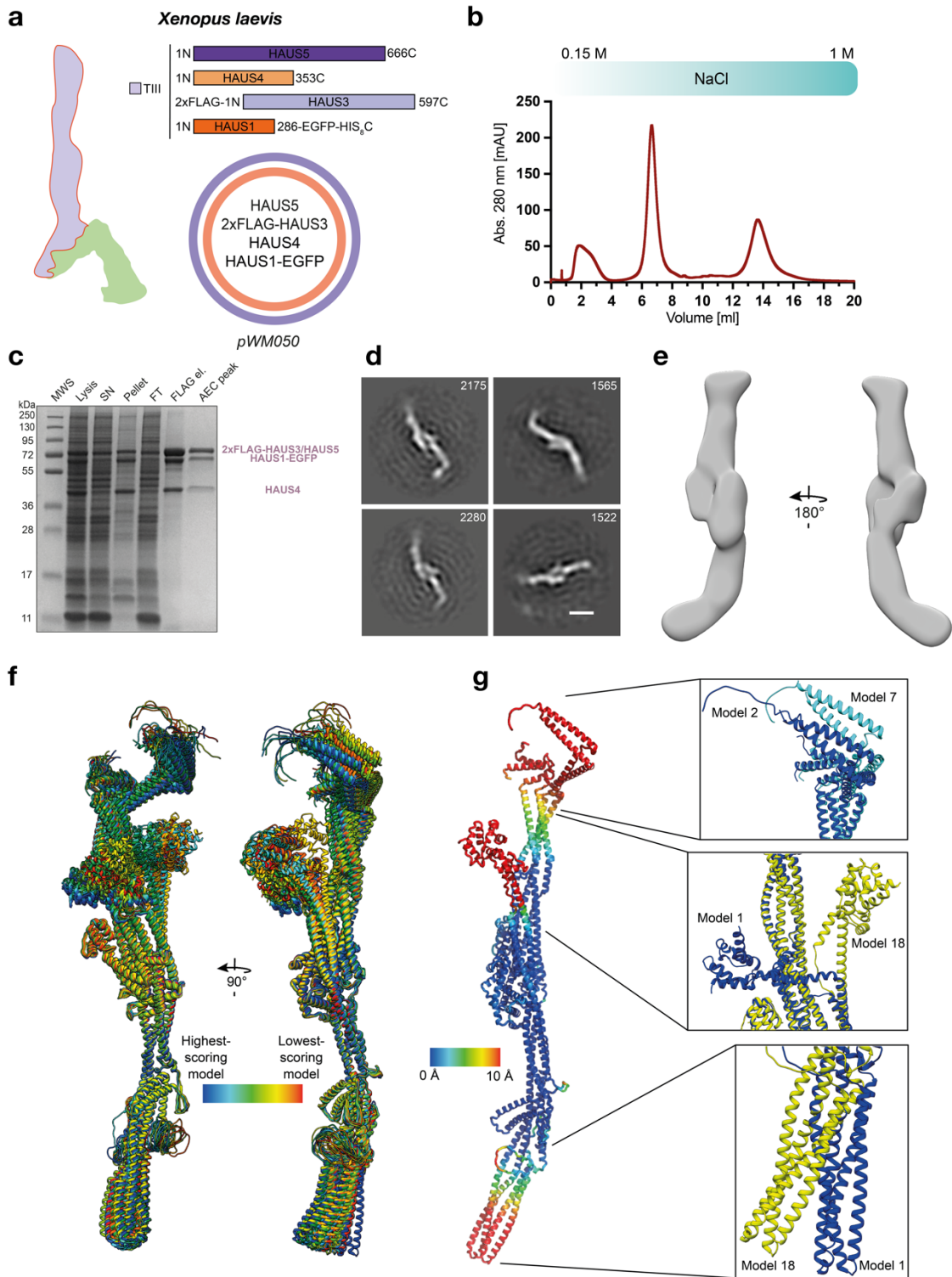


Figure 23 Characterization of the augmin TIII tetramer: **a**, left: schematic of the augmin octamer with tetramer TIII (purple, highlighted with red edges) and TII tetramer (green). Right: pWM050 construct of the genes encoding HAUS proteins of the *X. laevis* augmin TIII tetramer was used to produce baculoviruses for co-expression in insect cells, followed by single-step FLAG purification and subsequent AEC (**b**). Lengths of the genes and affinity TAGs are indicated. **b**, AEC chromatogram of CaptoHiRes Q 5/50 (Cytiva) run. Proteins were eluted via a gradient from 150 mM NaCl to 1 M NaCl (turquoise gradient). **c**, Coomassie blue-stained SDS-PAGE of the augmin TIII purification showing: Molecular weight standard (MWS); Lysis; Supernatant (SN); Pellet; Flow through (FT); FLAG elution (FLAG el.); Peak fraction from AEC (AEC peak). Expected protein sizes are indicated (purple). **d-e**, Negative stain EM 2D (**d**) and 3D (**e**) classes of augmin TIII after AEC purification. In **d**, particle numbers are given. Scale bar: 10 nm. **f**, AF-Multimer-predicted models of

Results

augmin TIII were superposed, forming an ensemble displayed in a rainbow scheme that transitions from high (blue) to low (red) prediction scores. **g**, left: the AF-Multimer model with the highest score was colored according to its root-mean-square deviation (RMSD) against the model with the maximum deviation, represented by colors ranging from blue (minimal deviation) to red (up to 10 Å of deviation). Right: close-up views of segments within the model that were predicted to exhibit flexibility. The two most extreme conformations of these segments are shown, illustrating the span of flexibility inherent in the structure as predicted by AF-Multimer. Negative stain EM data acquisition was done by Dr. Annett Neuner and AF-Multimer analysis and visualization were done by Dr. Erik Zupa. Data were jointly evaluated. The figure was adapted from [369].

All 25 predicted models for the TIII subcomplexes were characterized by similar scores in the predicted local distance difference test (pLDDT) (Table 3). These TIII models accurately replicated the overall fold and exhibited only minor variations in the global arrangement of the domains (Figure 23f,g). Strikingly, the predicted models of the TIII complex show an elongated structure that is remarkably similar to the negative stain EM 2D and 3D classes, featuring extended coiled-coil segments that span the entire length of the complex.

Table 3 AF-Multimer-predicted *X. laevis augmin TIII* models ordered according to pLDDT score. The table was created in collaboration with Dr. Erik Zupa.

Model	pLDDT
Augmin TIII tetramer 1	0.625
Augmin TIII tetramer 2	0.617
Augmin TIII tetramer 3	0.611
Augmin TIII tetramer 4	0.611
Augmin TIII tetramer 5	0.610
Augmin TIII tetramer 6	0.608
Augmin TIII tetramer 7	0.608
Augmin TIII tetramer 8	0.607
Augmin TIII tetramer 9	0.607
Augmin TIII tetramer 10	0.604
Augmin TIII tetramer 11	0.603
Augmin TIII tetramer 12	0.602
Augmin TIII tetramer 13	0.602
Augmin TIII tetramer 14	0.600
Augmin TIII tetramer 15	0.597
Augmin TIII tetramer 16	0.597
Augmin TIII tetramer 17	0.596
Augmin TIII tetramer 18	0.594
Augmin TIII tetramer 19	0.593
Augmin TIII tetramer 20	0.593
Augmin TIII tetramer 21	0.593
Augmin TIII tetramer 22	0.591
Augmin TIII tetramer 23	0.591
Augmin TIII tetramer 24	0.59
Augmin TIII tetramer 25	0.588

Next, in collaboration with Erik Zupa, I performed cryo-EM SPA on the purified *augmin TIII* tetramer. The analysis by Erik Zupa resulted in a cryo-EM reconstruction at a global resolution of 7.7 Å (Figure 24a-d). Notably, the predicted TIII models exhibited an excellent fit with the cryo-EM reconstruction, accurately recapitulating all resolved density segments at the secondary structure level (Figure 24d, Table 4).

Results

Table 4 Cross-correlation scores of AF-Multimer-predicted augmin TIII models fitted into the TIII cryo-EM density (see Figure 24). The table was created in collaboration with Dr. Erik Zupa.

Model	Correlation
Augmin TIII tetramer 1	0.7316
Augmin TIII tetramer 2	0.7334
Augmin TIII tetramer 3	0.7394
Augmin TIII tetramer 4	0.7235
Augmin TIII tetramer 5	0.7332
Augmin TIII tetramer 6	0.7389
Augmin TIII tetramer 7	0.7287
Augmin TIII tetramer 8	0.7397
Augmin TIII tetramer 9	0.7322
Augmin TIII tetramer 10	0.7503
Augmin TIII tetramer 11	0.7176
Augmin TIII tetramer 12	0.7454
Augmin TIII tetramer 13	0.7285
Augmin TIII tetramer 14	0.6482
Augmin TIII tetramer 15	0.7078
Augmin TIII tetramer 16	0.7084
Augmin TIII tetramer 17	0.7124
Augmin TIII tetramer 18	0.7453
Augmin TIII tetramer 19	0.7194
Augmin TIII tetramer 20	0.7220
Augmin TIII tetramer 21	0.7167
Augmin TIII tetramer 22	0.7303
Augmin TIII tetramer 23	0.7323
Augmin TIII tetramer 24	0.7187
Augmin TIII tetramer 25	0.7130

Dr. Erik Zupa further refined the fit of the highest-scoring AF-Multimer model into the cryo-EM density using molecular dynamics flexible fitting (MDFF), which required only minor adjustments (Figure 24e). It is worth mentioning that certain segments of the AF-Multimer model were not entirely encompassed by the cryo-EM density, indicating increased flexibility in those regions. Interestingly, these flexible regions coincided with the model segments that AF-Multimer predicted to have different conformations (Figure 23g, 24d), suggesting that AF-Multimer has the ability to identify regions characterized by enhanced conformational plasticity. This is further supported by the similar cross-correlation value of all predicted models fitted to the cryo-EM density (Table 4), in contrast to the marked differences in the root-mean-square deviation (RMSD) of all models towards the highest scoring model, resulting from the more flexible regions (Table 5).

Results

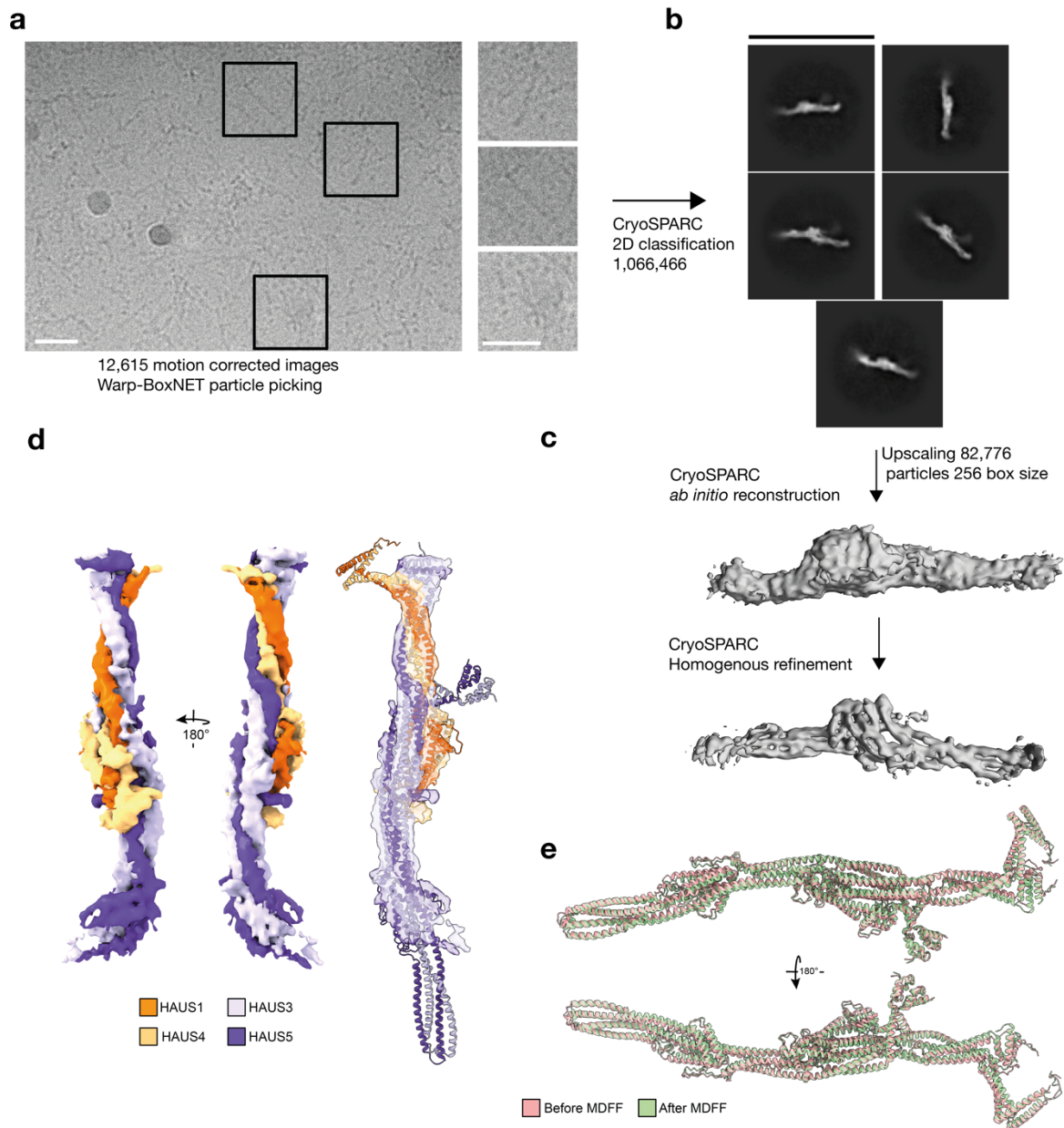


Figure 24 Cryo-EM analysis of the augmin TIII tetramer: **a**, representative micrograph highlighting TIII particles. Number of micrographs and picked particles for 2D classification are given. Scale bars: 30 nm. **b**, 2D class averages containing 82,776 particles used for final 3D reconstructions. Scale bar: 54.8 nm. **c**, upper panel: *ab-initio* reconstruction of the augmin TIII tetramer. Lower panel: reconstruction after homogeneous refinement of the augmin TIII tetramer. **d**, left: cryo-EM density (segmented and colored) of the augmin TIII tetramer. Right: fit of the predicted model after MDFF into the density. **e**, superposition of the highest-scoring predicted model before and after MDFF. All cryo-EM data shown in the figure were produced by Dr. Erik Zupa. Data were jointly evaluated. Figure was adapted from [369].

To further validate the TIII tetramer model, I conducted crosslinking MS experiments with the purified complex. Therefore, I optimized the crosslinking conditions using the crosslinking agent BS3, aiming at intermediate crosslinking efficiency (Figure 25a). After crosslinking and sample digestion, I submitted the sample to Dr. Mandy Rettel at EMBL-MS Core Facility for MS analysis.

Results

During evaluation of the results, Erik Zupa mapped the top 190 highest-scoring crosslinks (88 intramolecular and 102 intermolecular) back to the TIII model after MDFF for evaluation (Figure 25b). The results demonstrated that most of high-confidence crosslinks (91%) were consistent with the predictions from AF-Multimer and cryo-EM structural analysis, providing further validation for the model. Importantly, a clear pattern emerged: the majority of crosslinks that did not comply with the distance restraints in the predicted structures were located in the same segments that were identified and predicted to be the most flexible (see Figure 23g, 24d and 25b-d).

Table 5 RMSD of the AF-Multimer predicted *X. laevis* augmin TIII models towards the highest scoring model. The table was created in collaboration with Dr. Erik Zupa.

Model	RMSD
Augmin TIII tetramer 2	8.259
Augmin TIII tetramer 3	6.262
Augmin TIII tetramer 4	19.271
Augmin TIII tetramer 5	6.311
Augmin TIII tetramer 6	4.579
Augmin TIII tetramer 7	21.706
Augmin TIII tetramer 8	16.455
Augmin TIII tetramer 9	6.782
Augmin TIII tetramer 10	19.175
Augmin TIII tetramer 11	9.264
Augmin TIII tetramer 12	17.070
Augmin TIII tetramer 13	7.720
Augmin TIII tetramer 14	31.214
Augmin TIII tetramer 15	7.246
Augmin TIII tetramer 16	12.756
Augmin TIII tetramer 17	8.411
Augmin TIII tetramer 18	19.900
Augmin TIII tetramer 19	11.674
Augmin TIII tetramer 20	22.879
Augmin TIII tetramer 21	20.538
Augmin TIII tetramer 22	19.234
Augmin TIII tetramer 23	21.358
Augmin TIII tetramer 24	7.611
Augmin TIII tetramer 25	19.629

By integrating structural data from cryo-EM, crosslinking MS, and neural network-based structure prediction, I gained detailed insights into the architecture of the augmin TIII tetramer. The overall elongated structure of the TIII tetramer is predominantly characterized by extensive coiled-coil segments, which form pairs between HAUS3-HAUS5 and HAUS1-HAUS4. The coiled-coil segments are oriented in an overall N- to C-terminal direction (Figure 26). It is worth noting that HAUS3 and HAUS5 fold onto each other, in such a way that they are bringing segments located closer to their termini into spatial proximity. This spatial arrangement is supported by the crosslinks observed between the corresponding segments of these two subunits (Figure 25).

Results

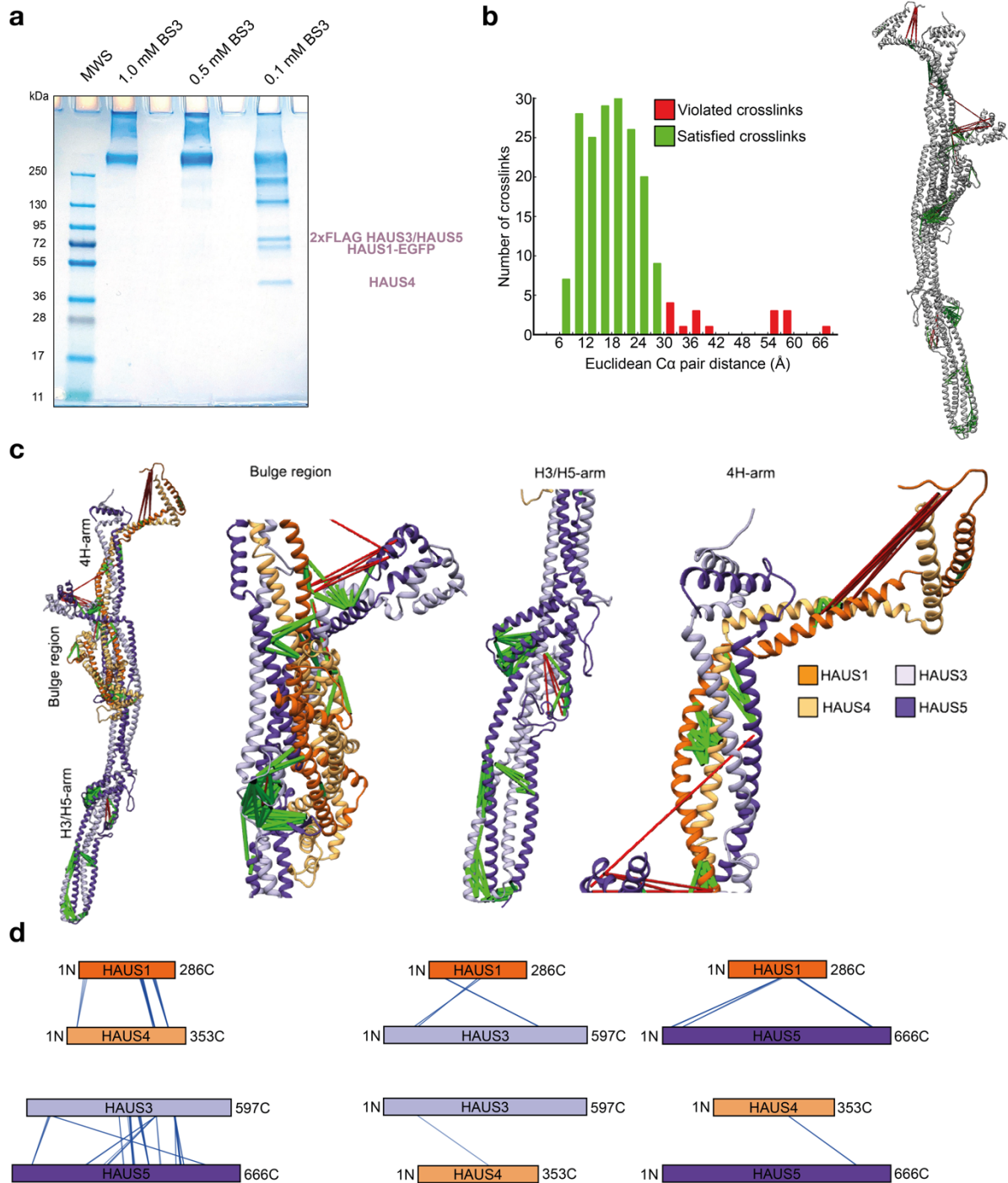


Figure 25 Crosslinking MS of the augmin TIII tetramer: **a**, Coomassie-blue stained SDS-PAGE of augmin TIII tetramer samples after crosslinking with varying BS3 concentrations. 0.1 mM BS3 was used for the final crosslinking experiment. **b**, quantification (left) and visualization (right) of crosslinks used for model validation mapped back to the TIII model. Satisfied (green) and violated (red) crosslinks according to a distance threshold (30 Å). **c**, left: augmin TIII model with indicated crosslinks. Right: zoomed views on different TIII regions. **d**, bar plot representation of crosslinks from individual pairs of HAUS proteins. All data shown in the figure were produced in collaboration with EMBL-MS Core Facility (EMBL Heidelberg) and analyzed and visualized in collaboration with Dr. Erik Zupa. The figure was adapted from [369].

Results

In the TIII structure, a distinctive "bulge" region emerges, which comprises all four HAUS proteins and demarcates the TIII tetramer into two distinct segments. One of these is represented by the central segment of HAUS3 and HAUS5 that folds into an antiparallel 4-helix coiled-coil bundle, forming the `H3/H5-arm`. The other segment, designated as the `4H-arm`, encompasses all four C-termini of the HAUS proteins of TIII. Noteworthy, the C-terminal segments of HAUS1 and HAUS4 reside at the tip of the 4H-arm, with predictions suggesting the formation of a flexible, kinked coiled-coil configuration (Figure 25c). Consistently, the segment is not visible in the cryo-EM reconstruction, and several high-confidence crosslinks violating the distance restraints are enriched in this region, indicating high degree of mobility (Figure 24d).

Docked on the surface of the bulge region in the highest-scoring model, the N-termini of HAUS3 and HAUS5 create a compact α -helical bundle, the "H3/H5 N-bundle". Nonetheless, the ensemble of predicted models presents various orientations for the H3/H5 N-bundle relative to the TIII tetramer's core fold (Figure 23f). Consistently, the cryo-EM reconstruction does not distinctly depict the H3/H5 N-bundle, however the presence of high-confidence crosslinks mapping to these segments and spanning an area with a radius of 11 nm is apparent (Figure 25c). Taken together, the data support the correctness of the prediction and the inherent flexibility of this region.

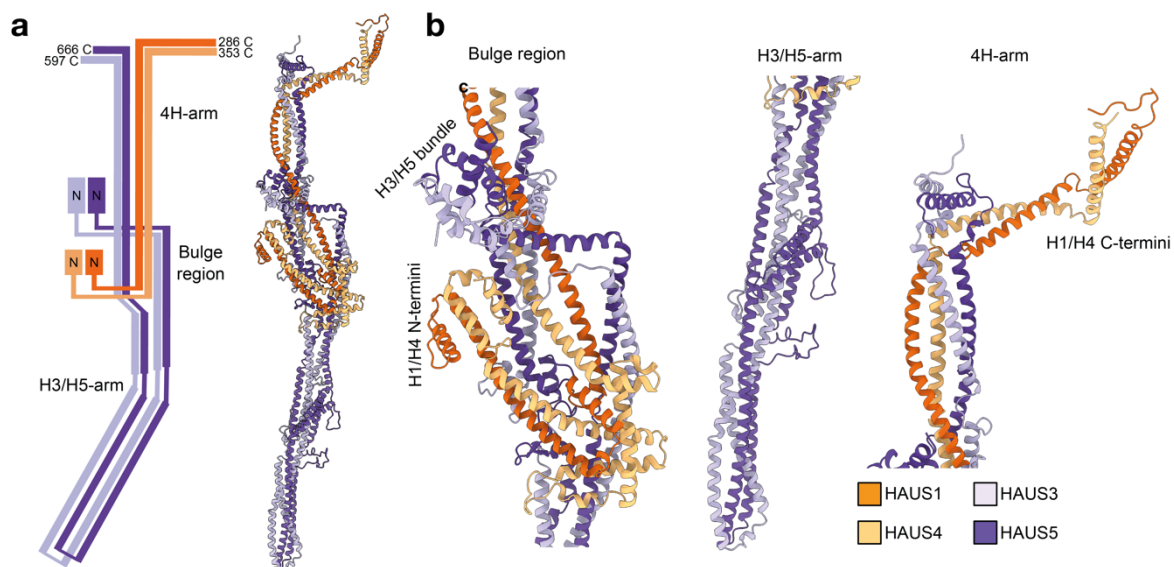


Figure 26 Molecular organization of the augmin TIII tetramer: a, schematic representation of the subunit organization of the augmin TIII tetramer with zooms on the three regions in b. All data visualized in the figure were produced in collaboration with Dr. Erik Zupa. Figure was adapted from [369].

2.5.2 Characterization of the augmin octamer architecture

Having delineated the molecular architecture of the isolated TIII tetramer, I conducted a thorough analysis of the TII tetramer structure, and its interface towards TIII (Figure 27). Predicted models from AF-Multimer depicted a tetrameric parallel N- to C-terminus organized overall clamp-like structure characterized by two halves separated by a hinge (Figure 27b). All predicted models showed an overall similar pLDDT score, as observed for the TIII tetramer (Table 6). The two halves of TII consist of coiled-coil helices of all HAUS proteins within the TII tetramer, which form the N-terminal (N-clamp) and C-terminal segments (C-clamp). Within the N-clamp, a hammerhead-like configuration, termed the "N-clamp HH", is built by two globular domains found in the N-termini of HAUS6 and HAUS7 (Figure 27b).

Table 6 AF-Multimer predicted *X. laevis* augmin TII models ordered according to pLDDT score. The table was created in collaboration with Dr. Erik Zupa.

Model	pLDDT
Augmin TII tetramer 1	0.569
Augmin TII tetramer 2	0.564
Augmin TII tetramer 3	0.561
Augmin TII tetramer 4	0.559
Augmin TII tetramer 5	0.559
Augmin TII tetramer 6	0.558
Augmin TII tetramer 7	0.556
Augmin TII tetramer 8	0.556
Augmin TII tetramer 9	0.555
Augmin TII tetramer 10	0.554
Augmin TII tetramer 11	0.550
Augmin TII tetramer 12	0.549
Augmin TII tetramer 13	0.548
Augmin TII tetramer 14	0.542
Augmin TII tetramer 15	0.541
Augmin TII tetramer 16	0.541
Augmin TII tetramer 17	0.540
Augmin TII tetramer 18	0.536
Augmin TII tetramer 19	0.535
Augmin TII tetramer 20	0.533
Augmin TII tetramer 21	0.533
Augmin TII tetramer 22	0.530
Augmin TII tetramer 23	0.530
Augmin TII tetramer 24	0.530
Augmin TII tetramer 25	0.528

Subsequently, I sought to validate the predicted models of the TII tetramer through orthogonal structural analysis via negative stain EM. Given reports of inefficient production and unsuccessful negative stain EM analysis of the isolated full length TII tetramer [365], I adopted an approach involving the co-expression of all eight augmin subunits to reconstruct the complete augmin holocomplex. This strategy not only aimed to address the challenge of TII tetramer expression and purification but was also selected for attempting to shed light on the interaction between the TII and TIII

Results

tetramers, thus uncovering the architecture of the full octameric augmin complex. Therefore, I designed a construct for augmin TII, incorporating a 2xFLAG TAG on HAUS6.

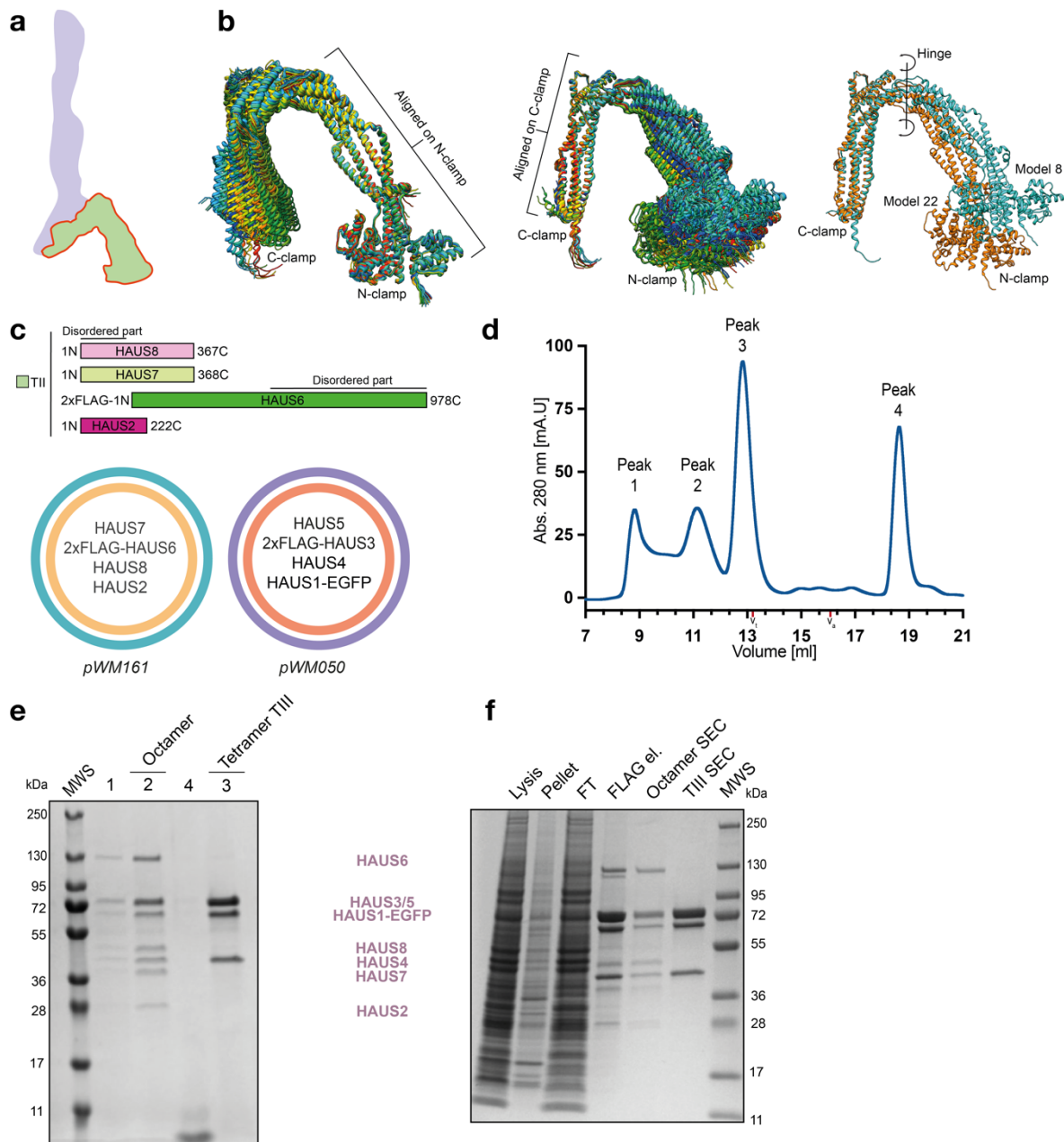


Figure 27 Characterization of augmin TII via the purification of the augmin holocomplex: a, schematic of the organization of the augmin octamer with tetramer TIII (purple) and highlighting the TII tetramer (green, red edges). **b**, predicted models for the TII tetramer were superposed either onto the N-clamp (left), or onto the C-clamp (middle). The ensemble of predicted models was colored in rainbow scheme from high (blue) to low (red) score. Right: the two predictions (model 8 and model 22) with the highest deviation in conformation were aligned on the C-clamp. The N- and C-clamp and the hinge region are indicated. **c**, pWMM050 and pWMM161 constructs of the genes encoding HAUS proteins of the *X. laevis* augmin TIII+TII tetramers were used to produce baculoviruses for co-expression in insect cells, followed by single-step FLAG purification and subsequent SEC (d). Lengths of the genes of TII and affinity TAGs are indicated. **d**, SEC chromatogram of Superose 6 increase (10/300, Cytiva) column run of augmin octamer FLAG elutions. Size markers Thyroglobulin 669 kDa (13.2 ml, v_i) and aldolase 158 kDa (16.3 ml, v_a) were

Results

used in independent runs. e, Coomassie blue-stained SDS-PAGE analysis of the four peak fractions from the SEC highlighting the octamer and tetramer fraction. f, Coomassie blue-stained SDS-PAGE analysis of the augmin octamer purification: Molecular weight standard (MWS); Lysis; Pellet; Flow through (FT); FLAG elution (FLAG el.); octamer peak after SEC (peak 2, Octamer SEC:); TIII peak after SEC (peak 3, TIII SEC). Expected protein size is indicated (purple). AF-Multimer prediction and data visualization were done in collaboration with Dr. Erik Zupa. The figure was adapted from [369].

This construct for TII and the previously produced TIII construct were co-expressed in insect cells (Figure 27c). Through SEC, I effectively separated the augmin octamer from the augmin TIII tetramer sub-complex (Figure 27d). SDS-PAGE analysis of the FLAG-elution samples revealed a prevalence of augmin TIII tetramer bands over those of TII tetramer proteins. The peak observed during the SEC run validated the stoichiometric purification of the octameric complex (Figure 27d-f). The sizes of the proteins matched the anticipated lengths taking into account the substantial unstructured regions inherent in TII, contributed by HAUS8 and HAUS6 (Figure 27c, 28a). Therefore, the complete augmin octamer comprising all eight subunits could be efficiently purified.

The AF-Multimer predictions of TII indicate that either the C-clamp or the N-clamp half of the tetrameric complex could potentially serve as the platform for the TII/TIII interface (Figure 28a). Therefore, I analyzed the purified augmin octamer through negative stain EM (Figure 28). The resulting 2D classes captured the elongated contour of the TIII tetramer, with additional density distinctly delineating the TII tetramer (Figure 28b,d). The appearance of these 2D classes aligns with the previously described h-like shape of the augmin octamer holocomplex [364,365], however more details are discernible (Figure 28b,d).

Moreover, I subjected the augmin particles on the negative stain micrographs to 3D classification, which resulted in a low-resolution, 3D reconstruction of the augmin holocomplex in two specific conformational states (Figure 28c,f). Within this reconstruction, the TIII tetramer was unequivocally identifiable (Figure 28c). Strikingly, the remaining density matched the anticipated clamp-like configuration of the predicted TII tetramer models. This 3D density enabled a confident determination of the orientation of TII and showed that the TII/TIII interface is formed between the H3/H5-arm and the TII C-clamp.

Leveraging the insights gained regarding the overall organization of the augmin holocomplex, Erik Zupa employed AF-Multimer to predict the structure of the TIII

Results

H3/H5-arm in complex with the TII tetramer (Figure 28e, Table 7). Across all predicted models, the TII C-clamp interacts with the TIII H3/H5-arm, harmoniously aligning with the 3D reconstruction from negative stain analysis of the augmin holocomplex. This alignment provides a model for the interface linking the TII and TIII tetramers.

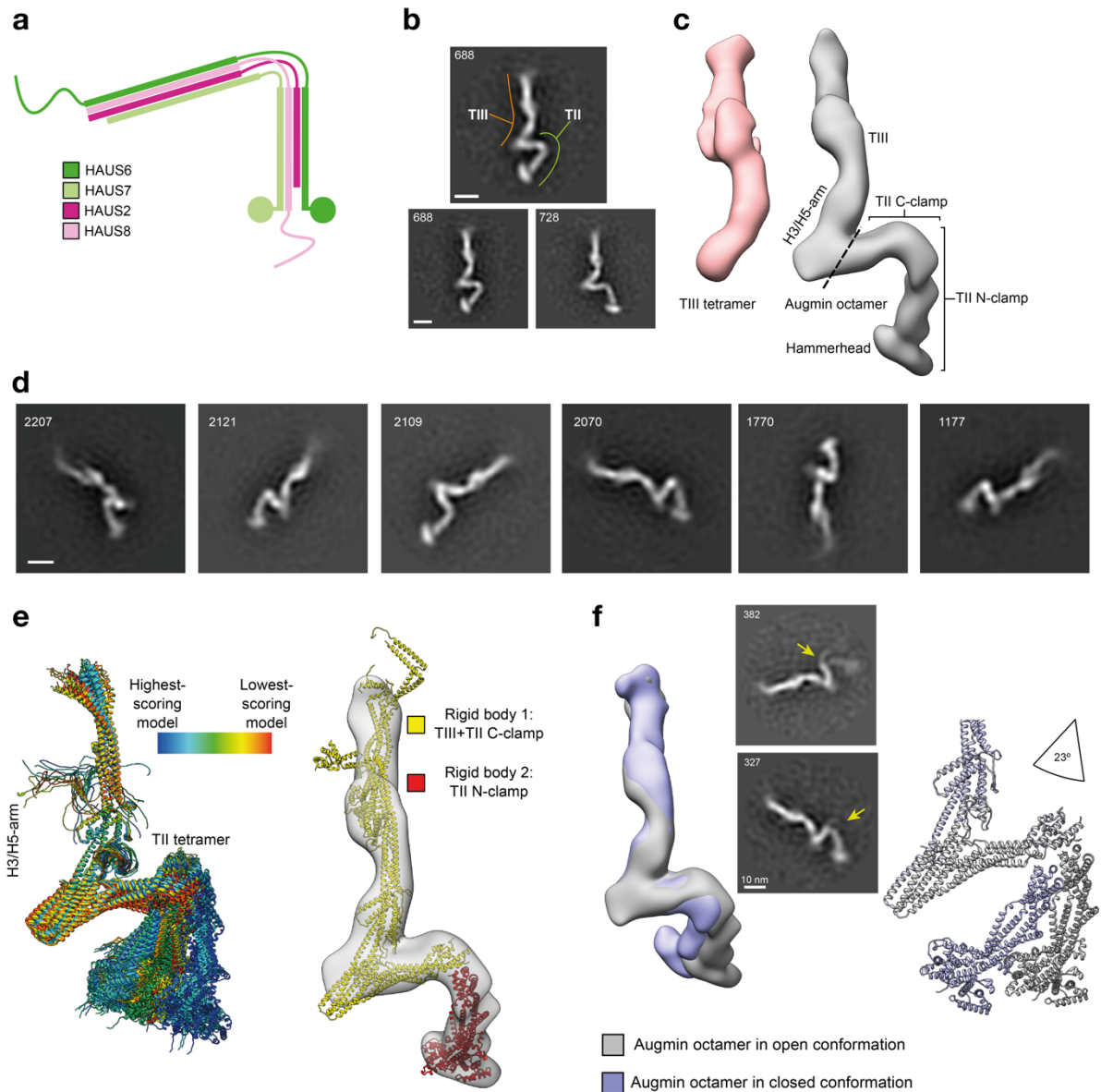


Figure 28 Architecture of the augmin holocomplex: **a**, schematic representation of the subunit organization of the augmin TII tetramer. **b**, two representative negative stain EM 2D classes of the augmin octamer after SEC show distinct conformations of the TII tetramer. Scale bar: 10 nm, particle numbers are given. The TIII tetramer (orange) and TII tetramer (green) are indicated in the enlarged class. **c**, negative stain EM 3D reconstructions of the isolated TIII tetramer (red) and the augmin holocomplex in the open conformation (grey). **d**, representative negative stain EM 2D classes of the augmin octamer after SEC, similar to (b). Scale bar: 10 nm; particle numbers are given. **e**, left: superposition of AF-Multimer predicted models for the augmin TII in complex with the TIII H3/H5 arm. The prediction ensemble was colored in rainbow scheme from high (blue) to low (red) score. Right: two model segments were docked into the negative stain EM 3D reconstruction (open conformation) of the augmin holocomplex as rigid bodies: TIII + TII C-clamp (yellow); TII N-clamp (red). **f**, left: negative stain EM 3D reconstructions of the augmin octamer resulted in two conformations. Open conformation (grey also shown in b and e) and closed (blue). Middle: two representative negative stain EM 2D classes of the augmin octamer after SEC highlighting flexibility

Results

provided by the hinge region, indicated with yellow arrowheads. Right: the two 3D reconstructions of the augmin octamer vary by an angle of 23° of the N-clamp. Negative stain EM data acquisition was done by Dr. Annett Neuner. AF-Multimer prediction, model building, and data representation were produced in collaboration with Dr. Erik Zupa. Figure was adapted from [369].

Table 7 AF-Multimer predicted *X. laevis* augmin TII + H3/H5-arm models ordered according to pLDDT score. The table was created in collaboration with Dr. Erik Zupa.

Model	pLDDT
Augmin TII +H3/H5 arm 1	0.512
Augmin TII +H3/H5 arm 2	0.511
Augmin TII +H3/H5 arm 3	0.509
Augmin TII +H3/H5 arm 4	0.507
Augmin TII +H3/H5 arm 5	0.506
Augmin TII +H3/H5 arm 6	0.506
Augmin TII +H3/H5 arm 7	0.506
Augmin TII +H3/H5 arm 8	0.503
Augmin TII +H3/H5 arm 9	0.503
Augmin TII +H3/H5 arm 10	0.496
Augmin TII +H3/H5 arm 11	0.477
Augmin TII +H3/H5 arm 12	0.477
Augmin TII +H3/H5 arm 13	0.474
Augmin TII +H3/H5 arm 14	0.473
Augmin TII +H3/H5 arm 15	0.469
Augmin TII +H3/H5 arm 16	0.469
Augmin TII +H3/H5 arm 17	0.468
Augmin TII +H3/H5 arm 18	0.467
Augmin TII +H3/H5 arm 19	0.467
Augmin TII +H3/H5 arm 20	0.465
Augmin TII +H3/H5 arm 21	0.464
Augmin TII +H3/H5 arm 22	0.463
Augmin TII +H3/H5 arm 23	0.462
Augmin TII +H3/H5 arm 24	0.46
Augmin TII +H3/H5 arm 25	0.458

It is important to note that none of the predicted models illustrated a compatible alignment between the orientation of the TII N-clamp and the EM data. This divergence could potentially be an artefact of negative stain EM or be partly attributed to the observed flexibility provided by the hinge region within TII, positioned between the N-clamp and C-clamp. Erik Zupa created two models of the different conformations obtained from my 3D reconstructions. This intrinsic flexibility was underscored by the representative 2D classes (Figure 28b,d,f), and the 3D reconstructions. The analysis showed that the two conformations differ by an angle of approximately 23° between the N-clamp and the C-clamp (Figure 28f).

2.5.3 The HAUS architecture reveals the N-clamp as composite MT binding unit

Employing this integrative structural biology approach, I achieved a comprehensive understanding of the augmin complex architecture. This complex comprises an octamer formed by TIII and TII tetramers, both organized in an N-to-C-terminal coiled-coil arrangement (Figure 29a). These tetramers interconnect through the C-terminal part of TII (the C-clamp) and the H3/H5-arm, revealing HAUS3 and HAUS5 as the

Results

central scaffold components within the octamer. Notably, TII encompasses a flexible hinge, as indicated by negative stain EM data, which suggests the potential for diverse orientations within the augmin structure, relevant for the angle of branched MTs.

Furthermore, the investigation aimed to illuminate how the architectural layout of augmin might contribute to the understanding of its interaction with pre-existing microtubules, facilitating γ -TuRC anchoring and subsequent branched MT nucleation. Prior studies have established the significance of the unstructured, positively charged N-terminus of HAUS8 (comprising in the human complex 141 residues) for the interaction between augmin and MTs [364,366]. The deletion of the unstructured HAUS8 N-terminus from recombinant augmin variants resulted in a complete failure to bind to MTs [364]. However, it was observed that the MT binding affinity of the HAUS8 N-terminus in isolation is approximately ten-fold weaker compared to the affinity exhibited by the HAUS6-HAUS8 dimer or the complete TII [364]. This discrepancy implies that additional contacts between TII and the MT lattice significantly contribute to strong augmin recruitment to MTs.

A more detailed inspection of the N-clamp HH structure, from which the disordered HAUS8 N-terminus extends, reveals the N-termini of HAUS6 and HAUS7 to adopt highly similar globular domains. These domains exhibit a structural resemblance to the CH domain present in the kinetochore MT-binding protein Ndc80 (Figure 29a,b). CH domains have been recognized as MT-binding domains in diverse MT-binding proteins such as EB1, EB3, Ndc80, and Nuf2 [298,299,378,379]. Importantly, the CH domains of these proteins share a sequence identity of 10-20% with each other and with the CH domains of HAUS6 and HAUS7 (Table 8).

Table 8 Sequence identity of HAUS6/7 CH domains and different structurally characterized MT-binding proteins. The table was created in collaboration with Dr. Erik Zupa.

Protein Name	Sequence identity (%)					
	HAUS7	HAUS6	Ndc80/Hec1	Nuf2	EB1	EB3
HAUS7	100	11.43	22.43	10.74	17.78	16.3
HAUS6	11.43	100	13.11	14.6	14.81	14.81
Ndc80/Hec1	22.43	13.11	100	15.65	13.39	12.28
Nuf2	10.74	14.6	15.65	100	15.00	13.33
EB1	17.78	14.81	13.39	15.00	100	80.41
EB3	16.3	14.81	12.28	13.33	80.41	100

The fold into CH domains underlines the probable contribution of HAUS6 and HAUS7 to the MT binding function of the augmin complex, which might rationalize the MT-binding synergy observed between the HAUS8 N-terminus and other TII proteins [364]

Results

from a structural standpoint. This indicates that augmin possibly shares similarities with the MT binding site of the Ndc80 complex, given the analogous composition of both complexes.

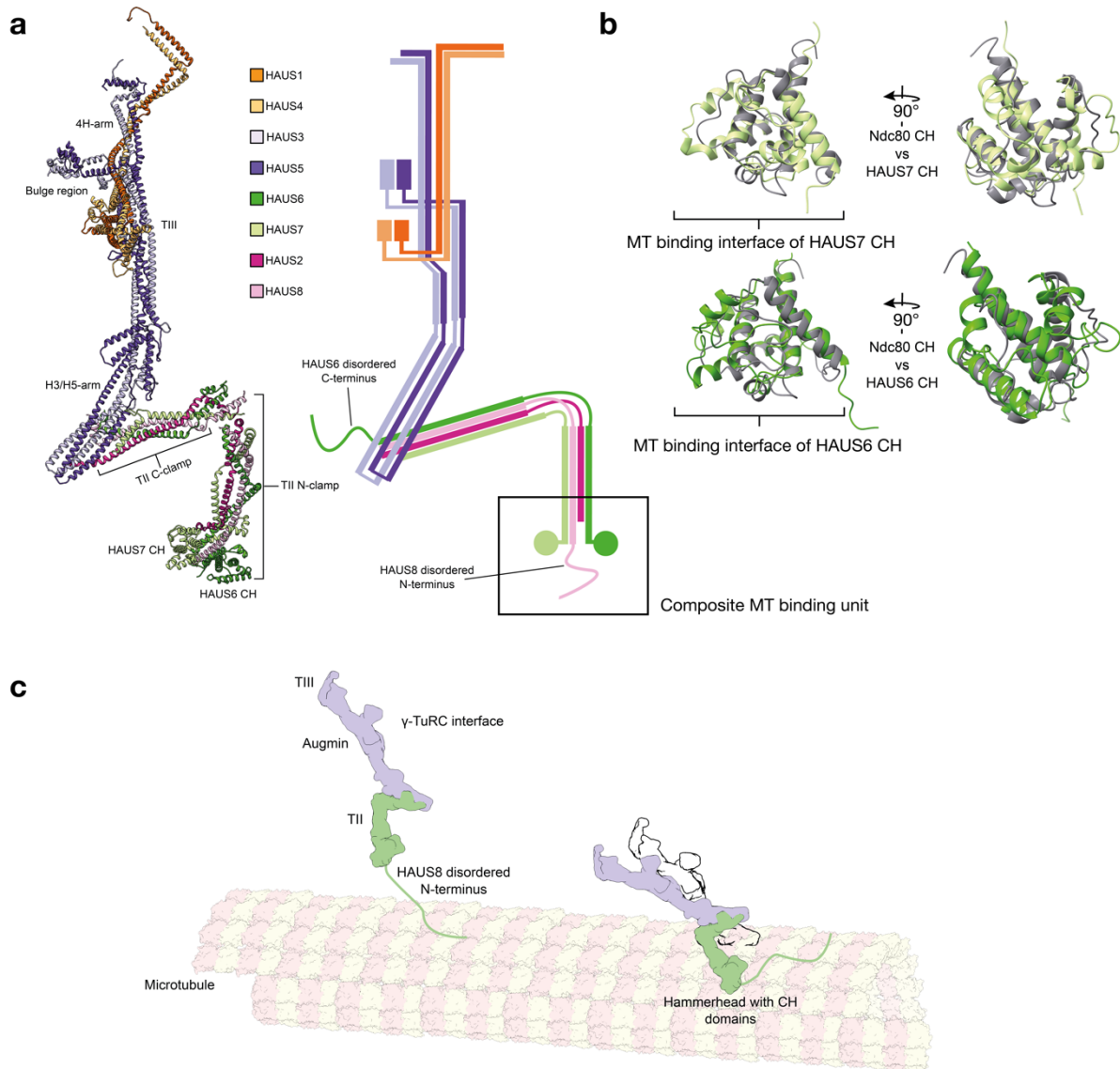


Figure 29 The augmin TII N-clamp is a composite MT binding unit: a, left: composite model, integrating different techniques, of the *X. laevis* augmin holocomplex in the open conformation (see Figure 28). Right: schematic representation of the subunit architecture of the augmin holocomplex. Flexible regions of HAUS6 and HAUS8 are indicated. **b**, superposition of the Ndc80-CH domain (grey; PDB-3IZ0) on the N-termini of HAUS6 (dark green; RMSD of 5.4 Å) and HAUS7 (bright green; RMSD of 4.6 Å). **c**, schematic representation of the potential augmin-MT association pathway. Left: augmin is recruited to the pre-existing MT via the HAUS8 N-terminus. Right: augmin is stabilized and oriented on the MT lattice via HAUS6 CH and/or HAUS7 CH domain binding. In addition, the conformational flexibility of TII may allow to adjust the configuration on the pre-existing MT (indicated by the black outline), and therefore the nucleation angle of the branched MT. All figure panels were generated in collaboration with Dr. Erik Zupa. Figure was adapted from [369].

Concerning augmin's potential MT binding pathway, the HAUS8 N-terminus engages with the MT through electrostatic interactions, cooperating with one or both CH domains to establish a specific orientation on the MT surface. This orientation may

Results

potentially adapt in response to modifications or interactions with various partners, leading to changes in configuration (Figure 29c). This hypothetical two-step binding mechanism, involving diffusion followed by stable binding and branching initiation, aligns with the dynamics recently observed via TIRF microscopy imaging [329].

In conclusion, the integrated structural biology approach I employed in this thesis has effectively elucidated the sub-complex architecture of the augmin complex. This accomplishment lays a cornerstone for comprehending the functional interfaces of augmin, offering a solid foundation upon which future endeavors can further dissect and explore these interfaces.

3 Discussion

In this thesis, I worked on the characterization of recombinant γ -tubulin-related protein complexes, which are fundamental for the MT nucleation process. My research was conducted in a rapidly evolving field, as demonstrated by the influx of several recent publications on this topic. My results, along with the work of others, have contributed to a deeper functional understanding of the key players in the MT nucleation process. In the following sections, I will discuss the findings of my thesis, placing them within the context of previous studies and recent publications. These have not only inspired, but also influenced the interpretation of my work, and vice versa.

3.1 The recombinant γ -TuRC expression system allows structural and functional analysis of γ -tubulin complexes

Earlier studies reported successful expression of yeast γ -TuSCs in insect cells, but the recombinant expression of human γ -TuRC components had been mainly restricted to GCP4 [137] and γ -tubulin [120]. Hence, reconstituting the full γ -TuRC represented a challenging goal for a long time. The cloning approach I employed involved integrating modules of the MultiBac system, limiting to two genes per plasmid, with subsequent Cre-recombination of the four possible backbones. This method proved crucial for flexibly adapting and creating multiple constructs for screening, despite requiring more time for initial construct generation and a more rigorous screening process compared to other methods like the biGBac system [30]. However, the approach that I have chosen facilitated module combination and construct adaptation. As summarized in Table 1 (see Results, Chapter 2.1), there were two additional independent attempts at reconstituting the recombinant γ -TuRC that nicely complemented the work presented here [373,374]. These studies, including the current one [371], demonstrated that the recombinantly expressed γ -TuRC mimics the asymmetric arrangement and GCP architecture of native purified complexes (Figure 10).

Interestingly, Table 1 illustrates the significant variations in purification strategies for both native and recombinant γ -TuRC. The method I employed here, involving a single-step batch FLAG purification focused on a single specific protein in the complex,

Discussion

facilitated rapid and comprehensive analysis of the structural and functional characteristics of modified γ -TuRC variants in subsequent experiments. This approach demonstrates that GCP5 N-terminus is accessible for the purification, while the diversity of strategies suggests that there are multiple accessible sites within this large complex for successful isolation and characterization of intact complexes.

With the established protocol I could purify γ -TuRC complexes in a fast and straightforward manner, whereby 100 ml insect cell culture was sufficient for subsequent experiments, for instance, structural characterization via cryo-EM. However, it is important to consider that in other instances, a second purification step might be required, and therefore the size of the insect cell culture has to be adapted. Importantly, the strategy established in my thesis, along with experiments conducted by other groups, lays the foundation for the targeted analysis of both the core structural components and the more flexible N- and C-terminal extensions of the complex.

Even though the co-expressed protein composition and purification schemes in the studies by Wieczorek *et al.*, Zimmerman *et al.* and this thesis differed, the results were comparable. I demonstrated that the γ -TuRC, with a minimal set of 8 co-expressed proteins, can be purified and resembles the overall architecture of native complexes, as shown via negative staining EM (Figure 10). These complexes enhanced MT nucleation and capped MT -ENDs. However, the relatively low amount of purified complex and the significant bands of GCP2/3 in the pellet fraction on SDS-PAGE gels after omitting MZT1 from the set of co-expressed components (Figure 11) suggest that MZT2 might also enhance the efficiency of ring reconstitution. This might be due to the insolubility of the GCP N-termini. Consistent with cryo-EM structures from native reconstructions, MZT1 is essential for stable ring formation, as expressions without MZT1 were unsuccessful (Figure 11f). Similarly, removing MZT1 together with actin from the expression system led to the purification of incomplete rings [374], which can be attributed to the lack of MZT1 since actin in the γ -TuRC lumen can be replaced by insect cell actin [373], as discussed in Chapter 3.3.

Zimmermann *et al.* highlighted the importance of the AAA+ ATPases RUVBL1/2 in the assembly of recombinant γ -TuRC, which are known for their various cellular roles, including chromatin remodeling [380]. Earlier γ -TuRC purifications from human cells had previously identified these ATPases via MS analysis [147]. Zimmermann *et al.*

Discussion

found that, in their expression system, RUVBL1/2 associated with γ -TuSC oligomers. Although not essential for γ -TuSC assembly, their presence enhanced the reconstitution of γ -TuSC oligomers [373]. In my experiments, I successfully reconstituted a minimal γ -TuRC without co-expressing RUVBL1/2. However, in subsequent constructs where RUVBL1/2 and MZT2 were included, I observed a marked increase in yield, suggesting the effect could be attributed to either or both components. Zimmermann *et al.* did not observe significant amounts of RUVBL1/2 associated with the assembled γ -TuRC, in line with my MS (Table 2, Results, Chapter 2.2) and subsequent cryo-EM analyses. Importantly, also assembly intermediates did not show a clear density that could be attributed to these ATPases in cryo-EM (Figure 12). Interestingly, γ -TuRC complexes containing MZT2-EGFP and NEDD1 were effectively reconstituted without co-expressing human RUVBL1/2 [374]. Comparing different systems remains challenging, but one possibility is that the role of RUVBL1/2 is replicated by their counterparts in insect cells. Therefore, although the work of Zimmermann *et al.* provides valuable insights, future studies should systematically explore this aspect using identical systems (effect of insect cell lines) and comparable constructs (removing the RUVBL1/2 module), including the knockdown or inhibition of the insect cell ATPases. Additionally, employing ATPase-deficient mutations, such as RUVBL1_{E303Q} and RUVBL2_{E00Q}, could further clarify the role of the ATPase activity of these complexes for the γ -TuRC assembly [380].

In addition to the effect observed for MZT proteins, I indirectly demonstrated that co-expression of γ -TuRC associated factors like NEDD1 or NME7 is not essential for the assembly of the complex, in agreement with the findings of [373], and earlier studies [177,381]. However, research by Wieczorek *et al.* indicated that although NEDD1 was integrated into the reconstituted complexes (verified by MS), they were not able to unambiguously detect it in negative stain EM data. This finding is in line with previous cryo-EM studies [35–37]. Determining the specific binding sites and functional roles of these two proteins within the γ -TuRC represents a crucial aspect for future studies. The recombinant expression system outlined in this thesis provides an ideal platform for such investigations, enabling targeted modifications to elucidate the functions of NEDD1 and NME7 for the γ -TuRC.

Discussion

In summary, the recombinant reconstitutions indicated that the ring architecture depends on specific protein interactions, suggesting a uniform organization of the vertebrate γ -TuRC into a 14-spoke left-handed spiral. Consistent with these results, all vertebrate γ -TuRCs studied so far exhibit a uniform GCP order of (GCP2-3)₄-GCP4-GCP5-GCP4-GCP6-(GCP2-3)₁ [154]. However, variations in vertebrate γ -TuRC composition may involve factors other than the GCP scaffold, like the aforementioned NME7 and NEDD1, but also the incorporation of isoforms like *TUBG2* [118]. In contrast to vertebrates, in species like *S. pombe* or *D. melanogaster*, evidence suggests that there exist differing ring complex compositions at the GCP level [129,168], as well as at the level of the interactions with centrosomal factors, as recently revealed by [382]. This study indicated that recruitment of GCP4/5/6-containing γ -tubulin complexes to centrosomes depends on the homolog of CEP192, while functional complexes consisting of exclusively of γ -TuSC depend on Cnn [382], similarly to the system found in *S. cerevisiae* [128]. In this context, the recombinant γ -TuRC system allows a stepwise reconstitution of the γ -TuRC in conjugation with its co-factors, like CEP192.

As for future studies using the here-established recombinant system, it is important to note that the γ -TuRC and its associated factors are regulated in the context of the cell cycle; thus, PTMs may be crucial for investigating their interactions and functions. In this regard, employing active cell cycle kinases like CDK1/CyclinB1 AURORA or PLK1, either by including them in the insect cell expression system or via an incubation step with the isolated complexes should be considered, akin to other approaches as for example kinetochore reconstitutions [383,384]. Moreover, an emerging alternative is represented by the expression of multi-gene constructs in mammalian cells, increasingly adopted in recent years [329,385,386]. This might become a viable complementary approach in future studies investigating the cell cycle-dependent regulation of the γ -TuRC and associated factors. Construct design for such studies can benefit from the methodologies outlined in this thesis.

3.2 Cryo-EM analysis of recombinant human γ -TuRC reveals a modular assembly mechanism

The cryo-EM analysis of the vertebrate γ -TuRC was pivotal for advancing our understanding of MT nucleation and enabling its functional dissection. In my thesis, I produced recombinant complexes for cryo-EM analysis. The utilized modular

Discussion

approach facilitated the reconstruction of both the full γ -TuRC and its sub-complexes. Using the expression construct pWM104, I successfully reconstructed the human γ -TuSC (Figure 15). Negative stain EM class averages highlighted a cherry-like structure arrangement for the GCP backbone and γ -tubulin, similar to results achieved on purified yeast complexes [131,135,152]. Negative stain EM showed various views of γ -TuSC, including a dominant one with a visible single GRIP domain and γ -tubulin, reminiscent of side views observed in yeast [152]. Following FLAG and AEC purification, the isolated γ -TuSC did not exhibit detectable signs of RUVBL1/2 in SDS-PAGE and negative stain EM. The successful reconstitution of γ -TuSC indicates the association of MZT1 and MZT2 with the complex. The SDS-PAGE results after AEC show slight bands for MZT2 and less distinct bands for the markedly smaller MZT1. Although unlikely, I cannot rule out the possibility that MZT proteins dissociated from the complex during AEC. However, in some 2D classes, unassigned globular densities might correspond to these modules (Figure 12d). This suggests they might still be associated with the complex, possibly via the flexible, unstructured regions in the N-termini of GCP2 and GCP3 which are not visible in most negative stain EM 2D classes. However, future crosslinking MS analysis might be performed to further elucidate the composition of the γ -TuSC after different purification methods and to delve deeper in the mobility of the MZT modules within this basic γ -TuRC subunit.

Interestingly, in negative stain analysis of γ -TuSC after AEC, I observed a small fraction of γ -TuSC dimers, indicating a tendency to oligomerization. This process appears to be concentration-dependent (Figure 16), with higher concentrations leading to more and larger oligomers. Although *in vitro* conditions may not fully replicate the cellular environment, these findings suggest that the γ -TuSC requires additional elements within the context of the γ -TuRC to ensure stability at lower concentrations. In my experiments, oligomerization of the γ -TuSC occurred independently of other factors. Zimmermann *et al.* have shown that adding RUVBL1/2 to purified γ -TuSC results in their association with the complex, which may facilitate the assembly of γ -TuSC oligomers [373]. Further research is needed to determine whether RUVBL1/2 influences the dynamics of this assembly process or if unique contacts compared to those seen in concentration-dependent oligomerization are formed. Moreover, performing cryo-EM studies on γ -TuSC oligomers could provide deeper insights into their overall geometry and how they compare with the

Discussion

architecture in the context of the fully assembled γ -TuRC, also with regard to the MZT modules within these oligomers.

In addition to γ -TuSC, GCP4, GCP5, and GCP6 are also integral components of the γ -TuRC complex. Previous biochemical studies, including salt fragmentation analysis of native γ -TuRC, have shown that these GCPs can form a stable complex [35,162]. However, their structural architecture and integrity have yet to be visually confirmed. Of these, only GCP4 has been reconstituted and characterized structurally using X-ray crystallography [137]. Interestingly, GCP4 forms a dimer when isolated from its ring interaction partners. This observation leads to questions about the potential of GCP4, GCP5, and GCP6 to either mimic γ -TuSC structures or form a distinct 4-spoke intermediate, and whether these potential associations are consistent or vary in inter-GCP-GCP contacts. In this thesis, using a recombinant system, I was able to reconstitute a minimal 4-spoke system, the GCP4-5-4-6 intermediate, by excluding GCP2/3 from the expression system. Negative stain EM and subsequent cryo-EM analyses confirmed that the GCP4-5-4-6 can assemble and be reconstituted in insect cells (Figure 17). Negative staining EM revealed classes of a single spoke, likely comprising 2xFLAG-GCP5 in complex with γ -tubulin, potentially as a result of the purification scheme. These bottom-up reconstitution experiments suggest that the expression of these three GCP proteins leads to the formation of a complex that might serve as the initial seed for γ -TuRC assembly, as previously hypothesized by top-down salt fragmentation experiments. Notably, the N-termini of GCP6, potentially bound with MZT1 and actin molecules, could not be resolved, suggesting flexibility at the 4-spoke stage. This, together with the analyses of the FLAG elution from the optimized γ -TuRC construct (pWM026+pWM086), as detailed in Figure 12 indicates that the 4-spoke intermediate acts as the foundational element in γ -TuRC assembly but is in presence of γ -TuSC rapidly expanded by one γ -TuSC unit to form the 6-spoke intermediate. Using negative stain EM and cryo-EM, assembly intermediates could be mapped and integrated into a modular assembly pathway (Figure 30a). The 6-spoke intermediate, which includes the 4-spoke core expanded by a γ -TuSC at positions 7/8, was the most prevalent γ -TuRC sub-complex. This intermediate is distinctively marked by the MZT1-GCP5 module on its exterior and the MZT1 module from GCP3 on the luminal side, initiating the formation of the luminal bridge. The prevalence of this intermediate assembly complex in the cryo-EM analysis and the

Discussion

additional contacts formed at the luminal bridge start indicates, that the 6-spoke is the most stable entity. This aligns with the independent approach taken by Haren and colleagues. Their salt fragmentation experiments identified the 4-spoke core (GCP4-5-4-6) as the most stable intermediate. However, their analysis revealed the presence of about one γ -TuSC unit remaining in their 4-spoke sample [162].

In this context, a future challenge will be the investigation of the regulation of γ -TuRC assembly within the cell. While factors involved in the turnover of γ -TuRC components have been identified [387], how the assembly of this multi-subunit complex is regulated on a transcriptional and translational level remains elusive. Biochemical data and the here-performed reconstitutions indicate that the assembly starts with the γ -TuRC specific GCP proteins (GCP4, GCP5, GCP6), and therefore it might represent part of a regulatory mechanism. Notably, *TUBGCP5* is a primary target of BANP (BTG3-associated nuclear protein), a recently identified transcription factor linked to CpG islands [388]. Further investigation into how BANP regulates *TUBGCP5*, especially in relation to other γ -TuRC components like the directly associated MZT1, GCP4, and γ -tubulin proteins, could provide insights into γ -TuRCs regulation at both the transcriptional and translational levels.

Based on the here-presented cryo-EM analysis, the assembly process of the γ -TuRC entails the sequential addition and conformational locking of γ -TuSC units. On the GCP4 side (position 9), γ -TuSC units are incrementally added, and they become “locked” upon binding of the subsequent γ -TuSC (Figure 30a). Conversely, on the GCP6 side (position 12), the presence or absence of one additional γ -TuSC in equal ratios (positions 13,14) indicates an equilibrium between γ -TuSC “on-off”. Notably, once the luminal bridge is stabilized (following the addition of γ -TuSC_(3,4)) and actin is docked, the position of the γ -TuSC_(13,14) shifts significantly downwards, aligning more closely with a configuration compatible with the one of the fully assembled γ -TuRC. This process concludes with the addition of spokes 1,2. In sum, these structures suggest a modular, interdependent assembly mechanism for the γ -TuRC components, which is reminiscent of the assembly processes observed for multi-protein complexes like eukaryotic chromatin remodelers [389]. In agreement, previous sucrose gradient experiments from cell extracts suggested that various γ -TuRC sub-complexes can exist in cells [136,148]. Therefore, the structural data gathered on the vertebrate γ -TuRC, along with the assembly mechanism described here, suggest that

Discussion

various assembly intermediates, such as the γ -TuSC and the 4-spoke/6-spoke intermediate, with an increasing number of associated γ -TuSCs can exist independently of the full γ -TuRC. Crucially, these γ -TuRC sub-complexes result from the assembly and potentially disassembly processes that are integral to the same 14-spoke GCP arrangement of the γ -TuRC.

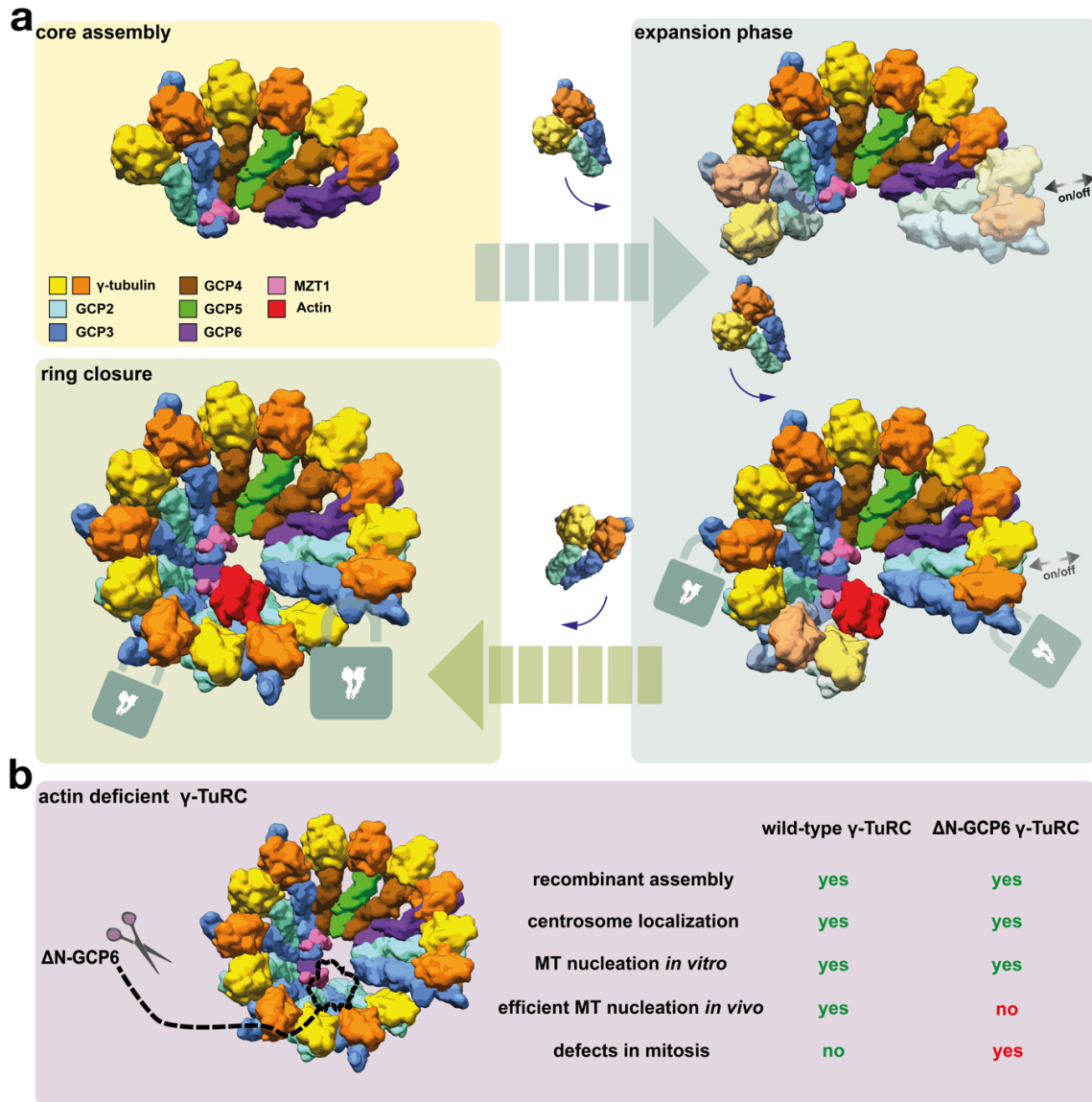


Figure 30 Modular assembly of γ -TuRC does not require actin integration: **a**, the first phase in the assembly of γ -TuRC involves the formation of the 6-spoke, stable core composed of GCP2-3-4-5-4-6. This structure is stabilized by the interaction between the MZT1-GCP3 module and the GCP6-N-terminal extension. The assembly process progresses (indicated by a yellow arrow) through the addition of γ -TuSC units. In this phase of expansion, each γ -TuSC unit becomes structurally locked (represented by a schematic lock icon) when it connects with a newly added adjacent γ -TuSC unit (indicated by lighter color). During this stage, the γ -TuSC_(13,14) unit can repeatedly attach and detach. This unit is repositioned following the formation of the luminal bridge. The expansion concludes (marked by a green arrow) with ring closure, whereby the integration of the γ -TuSC_(1,2) unit finalizes the stabilization of the γ -TuSC_(13,14) and secures the completely assembled 14-spoked complex. **b**, on the left, γ -TuRC ^{Δ N56-GCP6} is depicted, with a schematic scissor indicating the removal of actin via deletion of GCP6 N-terminus. Color scheme as in **a**. On the right, a comparison between wild-type γ -TuRC and the Δ N-GCP6 variant is shown. The figure was adapted from [372].

Discussion

The presence of MZT1 in the luminal bridge is crucial for γ -TuRCs structural stability. This is evidenced by multiple contacts identified in cryo-EM experiments [150], summarized in [154], and the formation of defective rings when MZT1 is excluded from the expression system [374]. Furthermore, the solubility of GCP proteins seems compromised without MZT proteins, as shown in Figure 11. Interestingly, the multifaceted function of MZT1 seems to play an essential role in the interaction with actin. The impaired assembly of ring complexes when MZT1 and actin are omitted from the expression system may be primarily due to the absence of MZT1 [374]. This is supported by the finding of Zimmermann *et al.* showing that ring complexes can form without co-expressing actin, suggesting that γ -TuRC is able to integrate insect cell actin [373]. My thesis highlights the integral aspect of actin incorporation into the γ -TuRC, primarily through its binding to the N-terminus of GCP6 that is associated with MZT1. This key mechanism is further discussed in the next chapter.

3.3 Actin is not required for γ -TuRC assembly and structural integrity but modulates its function *in vivo*

The role of actin within the γ -TuRC has been puzzling since its discovery. In previous work early on, actin was identified in γ -TuRC purifications [129,148], but whether this represented a specific interaction or just a co-purification artifact was uncertain. This question was clarified by recent cryo-EM structures [149]. Actin interacts within the γ -TuRC through its barbed end groove and D-loop [154], engaging with the N-terminus of GCP6 and γ -tubulin at spoke 2, respectively.

My research underscores the crucial role of GCP6 in the γ -TuRC, as indicated by actin-IP experiments where the GCP6-MZT1 module forms a stable actin binding motif (Figure 18). Expanding this research, the IP experiment, initially designed for human proteins, might be adapted to explore the evolution of the γ -TuRC. This would involve examining the consistency of actin integration within the γ -TuRC lumen across different species. Additionally, integrating AF-Multimer predictions into this expanded assay could provide an additional approach to structurally characterize the evolutionary development of the γ -TuRC. Overall, this method may offer insights into how actin became integrated into the “tubulin ring“, potentially linked to associated functional adaptations.

My findings suggest that while actin is not essential for the assembly or structural integrity, its absence impairs γ -TuRCs function (Figure 30b). Experiments involving

Discussion

the targeted deletion of actin from γ -TuRC in both recombinant reconstitution and *in vivo* contexts provided intriguing results. The purified reconstituted γ -TuRC ^{Δ N56-GCP6} surprisingly formed intact ring complexes, suggesting that actin is dispensable for the γ -TuRC assembly (Figure 20). Previous hypotheses, supported by IP experiments, suggested that the large insertion domain of GCP6 forms the luminal bridge, thereby facilitating its interaction with actin [35]. Interestingly, experiments using cells overexpressing various GCP6 variants indicated that a significant portion of the GCP6 insertion domain, which contains nine tandem repeats of 27 amino acids [390], is not required for the structural integrity of the γ -TuRC. Further investigation is required to shed light on the specific function of the GCP6 insertion domain. Potential approaches might entail an integrated functional and structural analysis using the recombinant γ -TuRC system with specific mutations. Additionally, incubation of the purified recombinant ring complex with kinases and subsequent MS analysis may allow for the precise mapping of PTMs. This approach would potentially verify the phosphorylation sites of GCP6 by PLK4 [390], and enable their functional dissection.

Despite the lack of structural data by Haren *et al.*, the findings from their study underline the results of my thesis through an independent biochemical approach. In contrast to the previously surmised insertion domain, Haren *et al.* demonstrated that the entire N-terminus of GCP6, extending up to the GRIP1 domain, is critical for the structural integrity of the γ -TuRC. This can be rationalized by the stabilizing function of the luminal bridge during the γ -TuRC assembly, as outlined in Chapter 2.2. Notably, the deletion of the very N-terminus (the first 72 amino acids) of GCP6, which is akin to the Δ 56/60 amino acid deletion made in this study, which should disrupt the integration of actin into the γ -TuRC, was shown to have a mild effect on γ -TuRC integrity [162]. Strikingly, the phenotypes observed in these experiments are comparable to those presented here, hence reinforcing the validity and significance of my data.

Importantly, the repositioning of spokes 1 and 2 may influence MT nucleation dynamics. *In vitro* batch MT nucleation assays did not show reduced activity, but this does not fully represent the mode of action of γ -TuRC *in vivo*. Δ N-GCP6 cells can nucleate MTs and survive, indicating a basic functional γ -TuRC. However, Δ N-GCP6 cells showed an altered MT nucleation dynamics, as denoted by slight defects during

Discussion

mitosis and reduced re-nucleation efficiency in MT regrowth assays (Figures 21, 22). To characterize the MT nucleation properties more thoroughly, additional functional assays such as single-molecule TIRF measurements could be employed [36,175]. However, these assays do not always accurately represent the real nucleation function of the γ -TuRC. This is underscored by the observation that even incomplete ring complexes, formed in the absence of MZT1 and actin during recombinant expression, exhibit MT nucleation activity that is comparable to 14-spoked entities [374]. Therefore, these assays need to be performed under strictly controlled conditions.

The intricate dynamics between actin and MT networks is crucial, especially during cell division events, and recently, the role of actin at the centrosomes has been more recognized [159,160,391,392]. The observed changes in MT nucleation and organization in ΔN -GCP6 cells emphasize the necessity for an in-depth characterization, which could be effectively achieved through cryo-ET. This structural approach would not only aid the identification of interaction partners, but also provide detailed insights into the composition and organization of MT nucleation complexes and the network of interactions between the different factors underpinning the formation of active MTOCs. Additionally, this method could also potentially demonstrate whether actin is absent from the γ -TuRC lumen in ΔN -GCP6 cells. In fact, although the primary interaction is disrupted, it is possible that, within cells, actin may still be loosely attached to the complex, for instance, via its D-loop, thus partially fulfilling its function. This aspect could not be ruled out by my work, as the *in vitro* characterization of γ -TuRC involved a purification step, and potentially weak interactions got lost.

Furthermore, the identification of which actin isoforms are incorporated into the γ -TuRC and its nucleotide state remains uncertain due to the limited resolution achieved so far on this complex. However, Zimmermann's *et al.* observation that insect cell actin correctly assembles into the human γ -TuRC suggests that various actin isoforms might be integrated [373]. Despite being firmly embedded in the γ -TuRC structure, the interfaces usually occupied in F-actin or recognized by actin binding proteins are accessible to those or to potential actin-GCP6-N-terminus binders in the native γ -TuRC state. Future research should aim at identifying the actin type incorporated in

the γ -TuRC. In this context, employing recombinant systems in which the N-terminus of GCP6 is fused to different actin isoforms might be insightful. This strategy could emphasize the extensive applicability and adaptability of tunable recombinant systems, as I initially demonstrated in this thesis.

3.4 Identification of all 7 MZT1 modules on γ -TuRC

The discovery of MZT1-GCP module binding sites on the outer surface of γ -TuRC (Figure 13,14), including GCP5-MZT1, was unexpected. These modules play a crucial role in γ -TuRC assembly, especially in the formation of the luminal bridge. The interaction between GCP3 and GCP4, where MZT1-GCP5 docks, could be key in determining the preferred binding site in the lumen for the MZT1-GCP3₍₈₎ (Figure14). Notably, these modules persist in the fully-formed rings of both wild-type γ -TuRC and γ -TuRC ^{Δ N56-GCP6}, suggesting a potential role independent of the assembly pathway or hinting at alternative PTM patterns affecting their binding stability on the γ -TuRC. The recombinant system used here is particularly relevant to address these aspects, as these MZT1 modules on the outer surface were not observed in other reconstructions [35,36,373,374], and it may allow to investigate the molecular basis of this recruitment.

While variation in expressed genes (human genes used in this thesis (see Methods Table 23, compared to the other studies) seems unlikely, modifications specific to the insect cells could be a factor. Indeed, I used Sf21 cells as expression system, as opposed to Sf9 in the other two studies [373,374]. An experiment involving the expression of the γ -TuRC in Sf9 cells followed by its purification and comparative MS analysis between ring complexes from Sf9 and Sf21 could be used to probe differences in MZT1 module binding stoichiometry between the two systems and reveal differences in modification patterns. Additionally, introducing mutations at the interface between the MZT1 modules and GCP outer surface (GRIP2 domain and C-terminal extensions) could provide further insights.

It is fascinating to observe that the MZT1 modules, involving three different GCP proteins, are positioned and recruited at three distinct locations: the luminal bridge, the interface between spokes 14 and 1, and the outer surface of γ -TuRC (Figure 13). The release of the MZT1 module from the outer surface of the γ -TuRC could serve as a regulatory mechanism during its attachment to the centrosome or other MTOCs. Hence, understanding the regulation of these modules might be crucial to elucidate

Discussion

the recruitment of γ -TuRC to MTOCs and its activation. Interestingly, the identification of one MZT2 module in complex with the CM1 motif in cryo-EM reconstructions [37] suggests that the MZT modules are regulated by additional interaction partners. In the case of MZT2, this involves CM1-containing proteins, as demonstrated by structural means in human cells [150] and through similar purification methods in *X. laevis* [393].

Previous data showed the importance of the MZT1-GCP3 module for interactions with NEDD1 [151,152], which might also mediate contacts with the augmin complex in the MT branching pathway [57,343,368], as recently evidenced in pull-down experiments [329]. It would be interesting to explore whether factors like NEDD1 might influence the release of MZT1 modules upon binding with augmin, thereby representing part of a broader regulatory mechanism of γ -TuRC activity, or whether these modules form an anchoring platform on the outer surface of the ring complex that may help orient the γ -TuRC (spoke 1-spoke 8).

3.5 The molecular architecture of the augmin complex reveals a composite MT binding unit

Finally, I examined the architecture of the vertebrate augmin complex, an essential γ -TuRC cofactor in the branching MT nucleation pathway. This incorporated several structural biology methods, including neural network-based structure prediction, negative stain and cryo-EM, and crosslinking MS. This integrative approach was essential for dissecting the elongated and flexible structure of the γ -TuRC recruiting factor. Cryo-EM was pivotal for elucidating the architecture of the TIII tetramer, especially its coiled-coil regions, as shown in Figure 24. Although the cryo-EM reconstruction of TIII offered significant insights, its resolution was insufficient for the unambiguous assignment of the individual HAUS proteins. Crosslinking MS provided deeper insights into the interactions between the different subunits of the TIII tetramer (Figure 25). Overall, the AF-Multimer predictions accurately represented the TII and TIII sub-complexes, however the predictions for the composite full octameric augmin complex required experimental validation (Figures 23, 27, and 28). My analysis verified that the augmin complex structure comprises two distinct structural elements, each serving complementary roles in MT branching (Figure 31).

The TIII tetramer and the TII C-clamp form a mostly rigid scaffold for the positioning of the γ -TuRC at a precise distance and orientation relative to the existing MT. IP

Discussion

experiments indicate that the N-termini of HAUS3 and HAUS5 are crucial for this interaction [57,365], indicating that the region from the H3/H5 bundle towards the H3/H5 arm may represent a docking site for γ -TuRC. Interestingly, the C-terminus of HAUS6, which was shown to interact with NEDD1 and protrudes from the H3/H5-arm, further supports the model of γ -TuRC docking on TIII [343,367,368]. Another aspect deserving future investigation is the yet unknown function of the 4H-arm, characterized by its notable kink in the H1/H4-C-termini. Interestingly, in that context is the work of Hsia *et al.*, who reconstituted a tetramer including HAUS6(Δ -C-terminus), HAUS8, HAUS1, and HAUS4 [364], which reveals a composition distinct from that observed in *X. laevis* [365] and differs from the augmin architecture that I determined in this thesis, as there is no interface between HAUS6/8 and HAUS1/4. The identification of different compositions of HAUS proteins in reconstitution studies could be an artifact of the method but might also potentially reflect the possibility of diverse augmin compositions. This notion might be especially relevant in plant biology, where research on *A. thaliana* revealed intriguing complexities. In this species, two distinct HAUS8 homologues are known to assemble into distinct augmin complexes [340], suggesting a sophisticated and dynamic regulation of MT in different cellular locations and during different phases of the cell cycle. Investigating these variants offers a valuable opportunity to advance our understanding about the augmin complex diversity and its functional implications.

The TII N-clamp serves as a bridge linking this γ -TuRC-binding scaffold with the existing MT. While our current understanding about the structural relationship between the augmin complex and the γ -TuRC remains limited, the research I presented in this thesis contributed to shed light on a critical aspect, namely the presence of two CH domains located at the N-termini of HAUS6 and HAUS7 proteins, which are likely involved in MT binding. Negative stain EM provided substantial support for the AF-Multimer predictions, particularly in visualizing the CH domain arrangement in the HH configuration (Figure 28). A comparison between the predicted structures of HAUS6 and HAUS7 CH domains and those known to bind MT, like CH domains from human Ndc80, EB1, and EB3, reveals a notable similarity to Ndc80 (Table 8, Figure 29). The CH domains may act in synergy with the HAUS8 N-terminus within the TII N-clamp, forming a composite unit for MT binding. The structural organization of this augmin MT-binding site bears a remarkable resemblance to that

Discussion

of the kinetochore-localized Ndc80 complex. As for the Ndc80 complex, Ndc80, together with Nuf2 (parallel to HAUS6 and HAUS7), and an additional unstructured and positively charged extension α of Ndc80 (similar to HAUS8 N-terminus), jointly constitute the MT-binding site at the kinetochore. Cryo-EM investigations of the minimal binding unit of Ndc80, termed the Ndc80 Bonsai construct [299], revealed that this minimal MT-interacting complex binds at the junctions between every α - and β -tubulin subunits [301,302]. It would be intriguing to explore whether a similar approach could be applied to the augmin complex by reconstructing a minimal MT binding unit. A promising strategy could involve co-expression of the segments of TII that comprise the TII-N-clamp. Interestingly, the MT-binding affinity of both the Ndc80 complex and augmin are modulated through the phosphorylation of their unstructured, positively charged tails [280,370,394,395]. Additionally, published data indicate interactions between components of augmin and the Ndc80 complex [367]. Given the crucial role of augmin in the formation and maintenance of kinetochore fibers [332,344,345], along with the observation that HAUS8 exhibits MT bundling activity [366] points to a possible functional convergence between these two MT-binding complexes, opening up an intriguing avenue for future research. For instance, based on the here-determined augmin architecture, specific mutations in the relevant parts of HAUS8, and HAUS6, or HAUS7 can be introduced and analyzed in cells via microinjection using fluorescently labelled augmin complexes as performed for the Ndc80 complex [299].

The research conducted by Hsia *et al.* reveals that the HAUS8 N-terminus is essential for MT binding, as augmin variants lacking this domain are unable to bind MTs [364]. However, the binding efficiency of the HAUS8 N-terminus on its own is substantially weaker compared to that of the HAUS6-HAUS8 dimer or the TII [364]. This suggests that additional interactions between TII and the MT lattice are crucial for the docking of augmin. With this thesis, I laid the groundwork for further investigation into augmin's MT binding mechanisms. Indeed, the structure enables the design of minimal MT binding versions of augmin and allows for the precise modification of these versions to regulate MT binding and dissect the functions of individual components as the CH domains of the HAUS6 and HAUS7 augmin subunits and their interaction with other factors.

Discussion

Notably, the findings of my thesis on the augmin complex, published in [369], were underscored by two independent studies focusing on human [396] and *X. laevis* [397] augmin complexes, published in the same journal and reviewed by the same reviewers. As highlighted by a comment from Szymon Manka [398], all three independent studies employed a similar set of methods to refine the understanding of the augmin complex architecture, which was found to be consistent from *X. laevis* to humans. Previously established for the γ -TuRC [35–37], the similarity in the overall fold and global arrangement of proteins is similarly conserved for the augmin complex, thus reinforcing the notion of a universal γ -TuRC-augmin tandem at the core of cell division. However, it is crucial to investigate the subtle differences that have evolved over time, which could illuminate their specific functions and phenomena, such as species-specific variations in MT branching angles [360]. In this context, I demonstrated that the TII hinge region, which separates two clamp-like elements (N- and C-clamp), may provide a controlled degree of flexibility in positioning the γ -TuRC relative to an existing MT (Figure 28). It is important to note that the angles observed in negative stain EM reconstructions might be influenced by the method. Nonetheless, the flexible hinge region appears to be a conserved feature from frogs to humans, potentially allowing to withstand and adapt to mechanical forces within the spindle, as suggested by Manka, S. [398].

Interestingly, AF-Multimer predictions have identified segments of greater conformational flexibility in the augmin complex (Figure 23), including the hinge region (Figure 28). While these predictions are accurate in pinpointing flexible regions, they do not fully align with the negative stain EM data regarding the conformations of the TII hinge. However, future improvements in protein structure prediction and associated tools could offer more comprehensive insights into the dynamics and flexible structural aspects of proteins. It is crucial to recognize the role of neural-network protein structure prediction in accelerating the analysis of augmin complexes, leading to precise models like those of the TIII complex presented in this thesis, showcasing augmin as a prime example of how neural network-based structure prediction is transformative for contemporary research. This aligns with similar advancements with other tools [59,399] and on other protein, and complex structures [61,62,64,400]. Of note, similarly to the augmin complex, AF predicts a CH domain for the Centrosomal Protein of 44 kDa (CEP44), a centrosomal factor located

Discussion

in the centriolar lumen, that possesses the ability to bind MTs [377] most likely via its CH domain [400]. The presence of both CEP44 and augmin [196] in the centriolar lumen raises interesting questions. Investigating if and how each protein interacts uniquely with MTs could shed light on their individual roles in the centriolar lumen and potentially reveal diverse functional mechanisms within this cellular structure.

In summary, in this chapter, I discussed how leveraging multiple techniques, anchored by an efficient recombinant expression system in insect cells, enabled the purification and characterization of recombinant augmin holo-octamers (Figure 27). This foundational work provides a platform for future research targeting specific functions of augmin. Such understanding is vital for elucidating the MT branching pathway in mitosis and exploring augmin's roles in interphase, for example in axons or within the centriolar lumen.

3.6 Conclusions and perspectives on the γ -TuRC-augmin axis

The recombinant system I established in this thesis has proven to be a valuable addition to the research toolbox. When combined with structural biology techniques, notably cryo-EM, and various biochemical and cell biology methods, it allows for systematic assessment of the functions of individual proteins. Looking ahead, this approach can be expanded beyond the identification and characterization of γ -TuRC components. It holds potential for investigating disease-related point mutations *in vitro* to understand their molecular basis. This includes, for example, mutations in proteins like GCP2 [245,401], microcephaly-related mutations in GCP4 [243], or components of the augmin complex, such as HAUS7 [402].

Furthermore, future research focusing on the functional sites of the augmin complex will be instrumental in enhancing our understanding of its roles in fundamental cellular processes such as mitosis. As summarized in Figure 31, this can be distilled into three main questions. Experimental structures of the augmin complexes in conjunction with MT will be crucial in understanding the arrangement and number of complexes at a branching site. Moreover, a thorough investigation that includes both *in vitro* studies and functional assays in cells is essential to uncover the full spectrum of the augmin- γ -TuRC interplay. To uncover the molecular basis of their synergistic action in branching MT nucleation, it is essential to study their interplay in a targeted fashion.

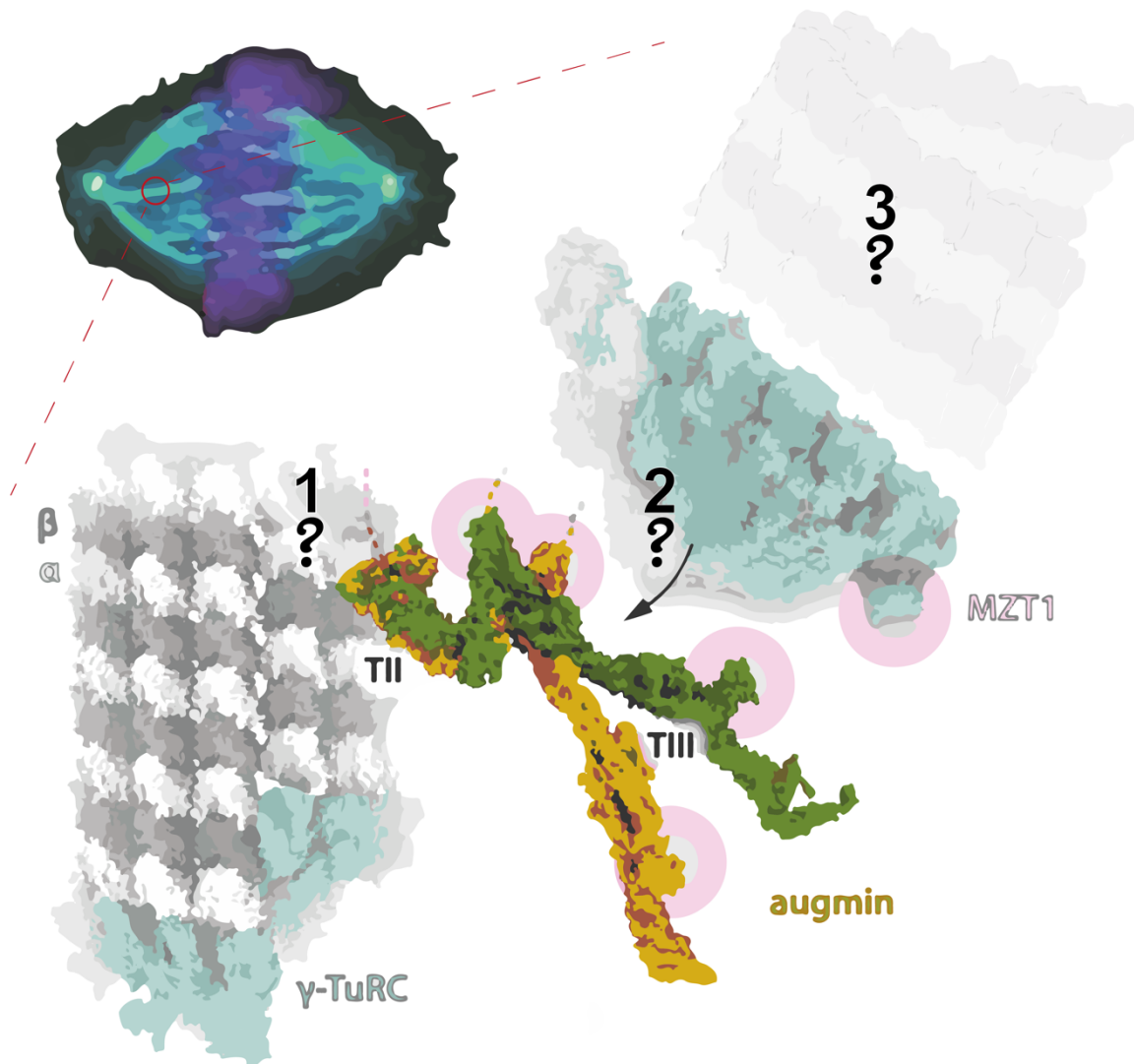


Figure 31 Building upon HAUS architecture: Schematic illustration of the mitotic spindle in the top left corner. The γ -TuRC (turquoise), acts as the primary MT nucleator and is recruited to pre-existing MTs (grey/white) via the augmin complex (green/yellow). The augmin complex is shown in two distinct conformations, reflecting variations in the hinge region of the TII tetramer. Pink circles indicate potential interaction sites between augmin and the γ -TuRC, focusing on the TIII tetramer of augmin and the MZT1 modules of γ -TuRC. The numbers and question mark highlight three critical future research areas: 1) The mechanism of MT binding by the augmin composite MT binding site. 2) The precise interface between augmin TIII and γ -TuRC, including PTMs and additional binding factors. 3) The process of branched MT nucleation following γ -TuRC recruitment by augmin. This figure was adapted from [398].

Although the direct interaction of γ -TuRC and augmin in solution is subject of current discussion [241], a stable γ -TuRC-augmin complex has not been convincingly demonstrated. However, their interaction on MTs is evident [355,359], suggesting that the interaction between augmin and γ -TuRC might be influenced by their association with MTs. Therefore, reconstitution studies should be performed in presence of tubulin complemented by advanced structural methods such as cryo-EM SPA and cryo-ET. These approaches will be valuable in exploring MT branching, both *in vitro*

Discussion

and in physiological contexts like cellular environments or *X. laevis* egg extracts. As discussed earlier, the γ -TuRC adapter unit NEDD1 forms the core of the interaction between γ -TuRC and augmin. Recent findings indicate that PTMs on both augmin and NEDD1 are crucial for facilitating their binding. Intriguingly, NEDD1 also exhibits MT binding activity to a certain extent [329], further underscoring the complexity of the γ -TuRC-augmin interaction with MTs. As the branching events might be difficult to assess experimentally, another promising way to gain more detailed structural insights into γ -TuRC-augmin interaction might be to study the proposed complex within centrioles via cryo-ET.

In conclusion, this thesis establishes a foundation for future research and markedly augments our understanding of fundamental cellular mechanisms naming MT nucleation. In this context, scientific progress reflects the search for "the one ring", which is central to unravelling the essential processes of cell structure and division.

4 Material and Methods

Methods described in this chapter were published, and methods performed mainly by the collaborators are described in [369], [371], and [372].

4.1 Materials

Table 9 Cell lines:

Cell line	Company/Details
<i>E.coli</i> DH10Multibac	Geneva-Biotech
<i>E.coli</i> DH10EmBacY	Geneva-Biotech
<i>E.coli</i> pirHC	Geneva-Biotech
<i>E.coli</i> DH5α	Sigma-Aldrich
<i>E. coli</i> BL21 CodonPlus-RIL	Stratagene
Sf9 insect cells (<i>Spodoptera frugiperda</i>)	Sigma-Aldrich
Sf21 insect cells (<i>Spodoptera frugiperda</i>)	EMBL protein expression facility
High Five inset cells (<i>Trichoplusia ni</i>)	Invitrogen (BTI-TN-5B1-4 cat no B855-02)

Table 10 Plasmids:

Plasmid	Source
pACEBac1	MultiBac system GENEVA Biotech
pIDC	MultiBac system GENEVA Biotech
pIDK	MultiBac system GENEVA Biotech
pIDS	MultiBac system GENEVA Biotech
pIDK ^{poolH}	(Eustermann et a. 2018)
pIDS ^{poolH}	(Eustermann et a. 2018)
pETDUET-1	Novagen
pet26b	Novagen

Table 11 Kits:

Kit	Company/Details
MultiBac™	Geneva-Biotech
Fluorescence-based Tubulin Polymerization assay kit	Cytoskeleton, Inc BK011
QIAquick® Gel extraction kit	Qiagen, 28704
InFusion HD cloning kit	Takara Bio
NEBuilder Hifi DNA Assembly	New England Biolabs (NEB)
Q5 High-Fidelity DNA Polymerase	New England Biolabs (NEB)
Trans-Blot Turbo Transfer kit	BIO-RAD Laboratories, Inc., (CAT No: 1704150)

Material and Methods

Table 12 Instruments:

Instrument	Company/Details
FastGene B/G LED Transilluminator	NIPPON Genetic EUROPE, GmbH
Gel-Doc XR Imaging System	Bio-Rad Laboratories, Inc.
LAS4000IR	FUJIFILM
Amersham Imager 600	GR Healthcare
Bio-Rad C1000 Touch® Thermal Cycler	Bio-Rad Laboratories, Inc.
Äkta go	Cytiva
Nanodrop® ND-1000	Thermo Fisher Scientific
Sonicator UP50H	Hielscher
RC 6 Plus centrifuge	Sorvall
Discovery 90 SE centrifuge	Sorvall
Discovery M120 SE centrifuge	Sorvall
Eppendorf Centrifuge 5810R, 5702R, 5424R, 5417R	Eppendorf AG
Bio-Rad Trans-Blot® Turbo Transfer System	Bio-Rad Laboratories Inc.
Neubauer improved cell counting	Paul Marienfeld GmbH & Co. KG.
Luna-II®Automated Cell Counter	Logos Biosystem
Bio-Rad Trans-Blot® Turbo Transfer System	Bio-Rad Laboratories Inc.
Bio-Rad PowerPac® HC	Bio-Rad Laboratories, Inc.
Bio-Rad DNA Sub Cell	Bio-Rad Laboratories, Inc.
Bio-Rad mini-PROTEAN® Tetra System	Bio-Rad Laboratories, Inc.
CLARIOstar	BMG Labtech
Deltavision RT microscope	Applied Precision, GE
Talos L120C	Thermo Fisher Scientific
4k × 4K Ceta CMOS camera	Thermo Fisher Scientific
JEOL JEM1400	Jeol
Titan Krios G1 (300 kV and Quanta GIF energy filter , 20 eV)	Thermo Fisher Scientific
K3 camera (at Krios)	Gatan, Inc.

Material and Methods

Table 13 Chemicals and equipment:

Item	Company/Details
400 mesh Cu/Pd hexagonal mesh	Plano
200 mesh R2/1 holey carbon copper	Quantifoil
Mono Q® 5/50 GL column	Cytiva
Capto HiRes™ Q 5/50 GL column	Cytiva
Superose 6 10/300 GL column	Cytiva
Superose 6 Increase 10/300 GL column	Cytiva
Rotor S100-AT3	Sorvall
Rotor S120-AT2	Sorvall
HB-6 Swinging-Bucket Rotor	Beckman
Type 45 Ti	Beckman
F9S 4x1000y	Thermo Fischer Scientific
SS-34	Thermo Fischer Scientific
Rotor SLC-4000	Sorvall
4-20% Mini-PROTEAN® TGX Stain-Free™ Protein Gels, 10/15 well	BIO-RAD, 4568093, 4568096
PVDF 0.45 µm	Millipore Merck
Coomassie Brilliant Blue G250	Sigma Aldrich
Ethidium bromide	Sigma Aldrich, E8751
DNA ladder, 1kb	New England Biolabs GmbH
PageRuler™ Plus	Thermo Fisher Scientific
Whatman 1 filter paper	GE Healthcare, CAT No:1001-055
Whatman 50 filter paper	GE Healthcare, CAT No:1450-070
Filter 0.2µm/0.4µm	Whatman GE Healthcare Life Science
Amicon Ultra-0,5 30 kDa MWCO	MERCK UFC5030
EDTA-free protease inhibitor tablets	Roche, 90087-000001
Ni-NTA Agarose	Qiagen, 163023770
Profinity™ IMAC Ni-Charged Resin	Bio-Rad
Anti-FLAG M2 Affinity Magnetic Beads	Sigma-Aldrich
Anti-FLAG M2 Affinity Resin	Sigma-Aldrich
3x FLAG peptide	Gentaur Molecular Products BVBA
Cellfectin® II	Thermo Fisher Scientific
FBS	Gibco by Life Technologies Ltd
Sf-900® III medium	Thermo Fisher Scientific
Trypan blue solution	Sigma-Aldrich, Lot # RNBj7454
Luna® Cell Counting Slide	Logos Biosystem
Actin, rabbit skeletal muscle	Cytoskeleton Inc., SKU: AKL99 (>99% Pure)
IPTG (Isopropyl-β-D- thiogalactopyranoside)	Apollo Scientific
ATP (Adenosine triphosphate)	AppliChem GmbH
GTP (Guanidine Triphosphate)	AppliChem GmbH
BamHI	New England Biolabs (NEB)
EcoRI	New England Biolabs (NEB)
NdeI	New England Biolabs (NEB)
Cre recombinase	New England Biolabs (NEB)
XhoI	New England Biolabs (NEB)
DpnI	New England Biolabs (NEB)
Benzonase®	Sigma-Aldrich
Trans-Blot Turbo RTA Mini 0.2 µm PVDF Transfer Kit	BIO-RAD Laboratories, Inc., 1704272
Trans-Blot Turbo Transfer Pack Mini format 0.2 µm PVDF	BIO-RAD Laboratories, Inc.
Clarity™ Western ECL Substrate Luminol/Enhancer solution	BIO-RAD Laboratories, Inc.
Clarity™ Western ECL Substrate Peroxide solution	BIO-RAD Laboratories, Inc.

Material and Methods

Table 14 Software:

Software	Company/Details
Fiji	Schindelin et al, 2012
PRISM	Graphpad (version 9.1/9.2)
Unicorn	Cytiva (Version 7.5)
EPU	Thermo Fischer Scientific (version 2.6, 2.9)
Gctf	Zhang et al., 2016 (version 1.06)
UCSF-Chimera	Pettersen et al., 2004 version 1.13.1)
Relion	Zivanov et al., 2018 version 3.1
LAS4000IR	FUJIFILM, v2.1
SnapGene	GSL Biotech LLC
Nanodrop 2000/2000c	Thermo Fisher Scientific
AlphaFold	v2.2.0
PyMOL	(PyMOL v2.1, Schrödinger)
Namdinator	(Kidmose et al., 2019)
Microsoft Excel	Microsoft (v16.46.21021202)
Adobe Illustrator	Adobe

Table 15 General buffers:

Buffer Name	Compositon
1x TBS	10 mM TRIS pH 8, 150 mM NaCl
1x TBS-T	10 mM TRIS pH 8, 150 mM NaCl, 0.05% v/v Tween20
1x TAE	20 mM TRIS, 1 mM EDTA, pH 7.5 adjusted with acetic acid
6x DNA loading buffer	0.25% w/v Bromophenol blue, 0.25% w/v Xylene cyanol, 30%, v/v Glycerol
1x SDS running buffer	25 mM TRIS, 192 mM Glycine, 0.1% w/v SDS
4x Lämmli buffer	200 mM TRIS, 40% v/v glycerol, 8% w/v SDS, 100 mM DTT, 0.08% w/v Bromphenol blue
Coomassie staining solution	90 mg Coomassie Brilliant Blue G250, 3 ml HCl (37%) in 1 l H ₂ O
Blotting buffer	25 mM TRIS, 192 mM Glycine, 0.25% w/v SDS, 20% v/v Methanol
Immunoblot blocking buffer	3% w/v nonfat dry milk in TBS-T
BRB80	80 mM K-PIPES pH 6.8, 1 mM MgCl ₂ , 1 mM EGTA
Minipreparation resuspension (S1)	50 mM TRIS pH 8.0, 10 mM EDTA, 100 µg/ml RNase A (DNase free)
Minipreparation lysis buffer(S2)	200 mM NaOH, 1% SDS
Minipreparation neutralization buffer (S3)	2.8 M K-Acetate, pH 5.1
LB-Medium (Luria/Miller) (C.Roth X968)	Trypton 10 g/l Yeast extract 5 g/l NaCl 10 g/l pH 7,0 ±0,2
LB-Agar (Luria/Miller) (C.Roth X969)	Trypton 10 g/l Yeast extract 5 g/l NaCl 10 g/l Agar-Agar 15 g/l pH 7,0 ±0,2
2xYT-Medium (C.Roth)	Trypton 16 g/l Yeast extract 10 g/l NaCl 5 g/l pH 7,0 ±0,2

4.2 Molecular cloning methods

4.2.1 PCR

As reported in the results section, cloning was executed using the InFusion/NEBuilder Hifi assembly method. Plasmids and inserts were amplified via PCR following the standard procedure, utilizing the Q5 High-Fidelity DNA Polymerase Kit (NEB) in 50 μ l or 100 μ l volumes, detailed in Table 16. The PCR thermocycler settings are listed in Table 17. For cases where the standard protocol failed, the reaction was supplemented with either the Q5 High GC Enhancer or 2% dimethyl sulfoxid (DMSO). The NEBuilder Assembly Tool (<https://nebuilder.neb.com/#/>) was used to design primers.

Table 16 Composition of the PCR Master Mix:

Component	Composition	50 μ l Reaction	100 μ l Reaction
5X Q5 Reaction Buffer	1X	10 μ l	20 μ l
2 mM dNTPs	200 μ M	5 μ l	10 μ l
10 μ M Forward Primer	0.5 μ M	2.5 μ l	5 μ l
10 μ M Reverse Primer	0.5 μ M	2.5 μ l	5 μ l
Template DNA	< 10 ng	0.5 μ l	0.5 μ l
Q5 High-Fidelity DNA Polymerase	0.02 U/ μ l	0.5 μ l	1 μ l
Nuclease-Free Water	1X	29.0 μ l	58.5 μ l

Table 17 Program of the PCR reaction: The * indicates that the annealing temperature is dependent on the used primers.

Step	Temperature	Time
Initial Denaturation	98°C	60 sec
25-35 Cycles	98°C	8 sec
	56-72°C*	30 sec
	72°C	35 sec per 1000 bp
Final Extension	72°C	120 sec
Hold	4°C	

4.2.2 Gel electrophoresis

PCR products of cloning intermediates were run on an agarose gel with subsequent DNA extraction. Control PCR reactions run only for visualization purposes. Gel electrophoresis was performed with 1% agarose (Biozym) dissolved in 1xTAE buffer. The samples run at constant 140 V, with 1 kb GeneRuler (Thermo Scientific) as size marker. The gel was then incubated in an ethidium bromide solution for 10 min.

Material and Methods

Afterwards, DNA fragments were cut using a scalpel upon visualization with a LED Transilluminator. For visualization purposes, a Bio-Rad machine (Gel Doc XR) was used, and visualization of stained DNA fragments was done via ultraviolet (UV) light. Importantly, DNA fragments for further cloning purposes were never exposed to UV light. DNA fragments excised from the gel were extracted using a Qiagen gel extraction kit following manufacturer instructions.

4.2.3 InFusion/NEBuilder Hifi assembly, mutagenesis, and Cre-recombination

For the molecular cloning, DNA fragments extracted from the gel were combined using InFusion/NEBuilder Hifi assembly kits following manufacturer's instructions, with the only exception that all given volumes were divided by two. If gene fragments were ordered (IDT USA), the required DNA overhangs were already attached to the ordered sequences, and the purchased DNA fragments were used for the InFusion/NEBuilder assembly reactions without prior PCR amplification. For point mutations of plasmids, specific mutation primers were designed (Table 20, 21), and the corresponding plasmids were amplified in a standard 50 μ l PCR reactions with 25 cycles. After the PCR, 1 μ l of the restriction enzyme *Dpn1* (NEB) was added (1 μ l in 50 μ l PCR reaction) and the mix was incubated for 1 h at 37°C. Afterwards, 1 μ l was used for a standard *E. coli* transformation, described in the following chapter. For the Cre-recombination of MultiBac plasmids, the protocol provided by the company was used (Geneva Biotech, MultiBac Manual version 5.1). Briefly, 1-3 μ g of each plasmid were mixed in a 1:1 ratio in a 20 μ l reaction volume with 1.5 μ l of Cre-recombinase (NEB) and incubated at 37°C for 1 h. Afterwards, 10 μ l were used for transformation.

4.2.4 Transformation into *E. coli*

In general, cloning was done in *DH5alpha cells*. Cloning steps of the MultiBac protocol for pIDC, pIDK, and pIDS were done into pirHC cells or for bacmid production into DH10MultiBacTM/DH10EmBacY cells (Geneva Biotech, MultiBac manual version 5.1). Chemically competent bacterial cultures (100 μ l) stored at -80°C were incubated for 20 min on ice. Afterwards, the following DNA amount was applied to the culture: 2 μ l (DNA inserts < 3000 bp) - 10 μ l (DNA inserts > 3000 bp) for InFusion/NEBuilder reactions; 10 μ l for Cre-recombination reactions; 50 ng - 500 ng for transformation into DH10Mbac/DH10MbacY. After 20 min of incubation on ice, cells were heat-shocked at 42°C for 42 seconds and subsequently incubated for 2 min on ice. Then,

Material and Methods

600 μ l of LB medium was added to the transformed cells, and they were incubated for 20-60 min shaking at 37°C. For Cre-recombination reactions and transformation into DH10MultiBac/DH10EmBacY, recovery was performed overnight. Afterwards, bacteria were plated on LB plates supplemented with the corresponding antibiotics. *E. coli* used in this thesis were grown either in LB or 2xYT medium with the corresponding antibiotics. Constructs of the MultiBac system after Cre-recombination were always grown and plated with all the required antibiotics for each of the combined plasmid backbones (Gentamycin, Kanamycin, Chloramphenicol and Spectinomycin) in concentrations provided by the company (Geneva Biotech, MultiBac Manual version 5.1). All chemically competent cells were provided by Ursula Jäkle. Briefly, *E. coli* colonies grown on an agar plate were transferred to a liquid culture (LB medium) and grown until an optical density (OD) at 600 nm of 0.6. Afterwards, cells were centrifuged at 4,000 x g for 10 min at 4°C. All subsequent steps were performed in the cold room with precooled equipment. The supernatant was discarded, and cells were resuspended in ice-cold TB buffer (50 ml for 200 ml *E. coli* pre-culture). Cells were centrifuged again at 4,000 x g for 10 min at 4°C. The supernatant was discarded, and cells were resuspended in TB buffer (16 ml for 200 ml *E. coli* pre-culture). Then DMSO was added (1.2 ml for 16 ml TB buffer suspension) and cells were aliquoted and flash frozen using liquid N₂ and stored at -80°C until further usage.

Table 18 Buffer for competent cells:

TB buffer composition (400 ml) pH 6.7
--

1.2 g PIPES
0.86 g CaCl ₂
7.44 mg KCl
4.36 g MnCl ₂ · 4 H ₂ O

4.2.5 Mini DNA preparation

For the Mini DNA preparation, 300 μ l S1 buffer (see general buffer list Table 15) was added to pellets from 2 ml cell culture (2 ml Eppendorf tube) and thoroughly mixed. Afterwards, 300 μ l of S2 buffer was added, and the Eppendorf tube was turned 6-8 times. Next, 350 μ l S3 buffer was added, and the Eppendorf tube was rotated again 6-8 times. The sample was then centrifuged 20,000 x g at 4°C for 10 min. 900 μ l of supernatant was transferred to a new 1.5 ml Eppendorf tube and 80% of the volume

Material and Methods

was added in isopropanol (720 µl) and centrifuged 20,000 x g at 4°C for 20 min. Following the centrifugation, the DNA pellet was washed with 200 µl 70% ethanol for 2 min and spun again for 2 min at 20,000 x g. The pellet was air-dried and dissolved in 35 µl of ultrapure water. The DNA concentration was measured using the NanoDrop® spectrophotometer.

4.2.6 DNA construct verification and Sequencing

To confirm the integrity of DNA constructs, PCR amplifications were conducted using general primers in conjunction with gene-specific primers (Tables 19-22). For both the MultiBac system cloning and bacterial expression constructs, complete inserts were sequenced ensuring correctness of the entire sequence including the region around start and stop codons. For constructs containing multiple genes, each gene inclusion was verified at every cloning stage via PCR and/or Sanger sequencing. Additionally, bacmids for baculovirus production were checked for proper gene integration through PCR. Sanger sequencing was performed by Microsynth Seqlab GmbH, and sequence alignment was performed using SnapGene software.

Table 19 General primers: Primer sequences were published [371,372].

Primer name	Sequence (5' - 3')	Description
MultiBac_vector_fwd	TCTAGAGCCTGCAGTCTCG	General primer to amplify and open MultiBac ^{polH} vectors
MultiBac_vector_rev	CAGTTTTGTAATAAAAAACCTATAAATAT	General primer to amplify and open MultiBac ^{polH} vectors
Combination_vector_fwd	TTCGCGACCTACTCCGGA	General primer to amplify and open MultiBac ^{polH} vectors for the combination of two expression cassettes
Combination_vector_rev	CAGATAACTTCGTATAATGTATGCT	General primer to amplify and open MultiBac ^{polH} vectors for the combination of two expression cassettes
Combination_insert_fwd	ATACGAAGTTATCTGTTCGCGACCTACTCCGGA	General primer to amplify a polH expression cassette from MultiBac ^{polH} vectors for the combination of two expression cassettes
Combination_insert_rev	GGAGTAGGTCGCGAAGATCCAGACATGATAAGATAATTG	General primer to amplify a polH expression cassette from MultiBac ^{polH} vectors for the combination of two expression cassettes
FastBac_fwd	TACTGTTTTTCGTAACAGTTTTG	Sequencing and control PCR
FastBac_rev	CATTTTATGTTTCAGGTTTCAGG	Sequencing and control PCR
inbetween_insertsF	ATGTCTGGATCTTCGCGA	Sequencing and control PCR
inbetween_insertsR	GAGTAGGTCGCGAAGATC	Sequencing and control PCR
pACEBac1_speziF	TTACGAACCGAACAGGC	Sequencing and control PCR
pACEBac1_speziR	GGTTCCAATTAGATGGG	Sequencing and control PCR
pID_speziF	GAGAGCTTAGTACGTAC	Sequencing and control PCR
pID_speziR	TGCGGAGAAAGAGGTAA	Sequencing and control PCR

4.2.7 Molecular cloning of the recombinant human γ -TuRC

Methods, as well as the used primers were published along with a detailed description of the cloning procedure [371,372]. Briefly, the constructs were adapted from the MultiBac system (Geneva Biotech, MultiBac Manual version 5.1) as described in Chapter 2.1.1 and Figure 8. For the MultiBac constructs, only modified versions of pIDK and pIDS with polH expression cassette, were used (Figure 8) [34]. The used cDNAs for the cloning of the human γ -TuRC are listed in Table 23. Gene fragments of *RUVBL1* and *RUVBL2* were purchased (IDT, USA) with InFusion/NEBuilder 5'- and 3'-overhangs (5'-AAAACCTATAAATATG, 3'-TCTAGAGCCTGCAG) and optimized for expression in insect cells. Primers used for the cloning of the human genes of the γ -TuRC are listed in Table 20 and the relevant intermediates and final constructs used for baculovirus production are listed in Table 25.

Table 23 Gene variants of the human γ -TuRC used for MultiBac constructs:

Protein	Gene and identifier	Natural variant
γ -tubulin	TUBG1, P23258	-
GCP2	TUBGCP2, Q9BSJ2	-
GCP3	TUBGCP3, Q96CW5	-
GCP4	TUBGCP4 Q9UGJ1-2	427
GCP5	TUBGCP5, Q96RT8	AAH71560, R198G
GCP6	TUBGCP6, Q96RT7	-
MZT1	MZT1, Q08AG7	VAR_043562 S5G
MZT2B	MZT2B, Q6NZ67	-
Actin beta	ACTB, P60709	-
RuvB-like 1	RUVBL1, Q9Y265	-
RuvB-like 2	RUVBL2, Q9Y230	-

4.2.8 Molecular cloning of the recombinant *X. laevis* augmin complex

Methods, as well as the used primers were published along with a detailed description of the cloning procedure [369]. The used genes, ordered as fragments, are listed in Table 24 using primers described in Tables 19 and 22. The purchased gene fragments were ordered with the following overhangs: 5'-AAAACCTATAAAT and 3'-TCTAGAGCCTGCAGT (HAUS4, HAUS5); 5'-AAAACCTATAAATATGGACTACAAGGACGATGACGACAAGGATTACAAGGATGACGACGATAAGATCCCAACGACCGAAAACCTGTATTTTCAGGGCGCCATG and 3'-TCTAGAGCCTGCAGT (HAUS3 and HAUS6, additional N-terminal 2xFLAG-TEV tag); 5'-ATTCCCCTCTAGAAATA and 3'-GAAAACCTGTATTTTCAGGGCGGATCCGCTGGCTCCGCT (HAUS1, for cloning into pET26b-EGFP vector [369]). To insert the C-terminal TEV-EGFP-3C-8xHis TAG following HAUS1, the ordered gene fragment was cloned into pET26b-EGFP using

Material and Methods

primers listed in Table 22. For the cloning of HAUS8, a cDNA template was used for PCR amplification and subsequent cloning into the MultiBac vectors. Intermediate constructs and final constructs used for baculovirus production are listed in Table 25.

Table 24 Gene variants of the *X. laevis* augmin complex used for MultiBac constructs:

Protein	Identifier	Source
HAUS1	XM_018267162.1	IDT codon optimized for <i>Spodoptera frugiperda</i>
HAUS2	NP_001085195.1	IDT codon optimized for <i>Spodoptera frugiperda</i>
HAUS3	XM_018226568.1	IDT codon optimized for <i>Spodoptera frugiperda</i>
HAUS4	NM_001096090.1	IDT codon optimized for <i>Spodoptera frugiperda</i>
HAUS5	XM_018226568.1	IDT codon optimized for <i>Spodoptera frugiperda</i>
HAUS6	NM_001097095.1	IDT codon optimized for <i>Spodoptera frugiperda</i>
HAUS7	NP_001121229.1	IDT codon optimized for <i>Spodoptera frugiperda</i>
HAUS8	XB-GENEPAGE-579	Prof. Dr. Simone Reber, cDNA

4.2.9 Molecular cloning of *E. coli* expression constructs

Methods described as well as the used primers were published, along with a detailed description of the cloning procedure [372]. *FLAG-MZT1* was inserted into the *NcoI* and *EcoRI* cleavage site of pETDuet-1 vector, while *TUBGCP6*_{N126} with a C-terminal 8xHis tag was cloned into *NdeI* and *XhoI* cleavage site of pETDuet-1. For the vector containing only GCP6_{N126}-8xHis TAG, the amplified DNA was inserted into the *NdeI* and *BamHI* cleavage site of the pET26b expression vector. The primers used to generate the *GCP6*-N-terminus and *MZT1* constructs as well as point mutations are listed in Table 21, and the final constructs used for *E. coli* expression are listed in Table 25.

Material and Methods

Table 25 Plasmids generated in this thesis:

Name	Identifier	Vector backbone	Resitency
pIDC-Actin-Beta	pWM001	pIDC	Chloramphenicol
pACEBac1-2xFLAG-TEV-GCP5	pWM002	pACEBac1	Gentamicin
pIDC-GCP2	pWM003	pIDC	Chloramphenicol
pIDC-GCP3	pWM004	pIDC	Chloramphenicol
pIDK-TUBG1	pWM006	pIDK ^{poolH}	Kanamycin
pIDK-GCP4	pWM007	pIDK ^{poolH}	Kanamycin
pIDC-Actin-Beta+GCP3	pWM008	pIDC	Chloramphenicol
pACEBac1-MZT1	pWM012	pACEBac1	Gentamicin
pIDC-GCP2_GCP3	pWM013	pIDC	Chloramphenicol
pIDK-TUBG1_GCP6	pWM014	pIDK ^{poolH}	Kanamycin
pIDK-TUBG1_GCP4	pWM015	pIDK ^{poolH}	Kanamycin
pIDS-GCP4	pWM016	pIDS ^{poolH}	Spectinomycin
pIDS-Actin-Beta	pWM017	pIDS ^{poolH}	Spectinomycin
pIDC-GCP6	pWM018	pIDC	Chloramphenicol
Cre-2xFLAG-TEV-GCP5+GCP6	pWM019	pACEBac1, pIDC	Gentamicin, Chloramphenicol
Cre-2xFLAG-TEV-GCP5+GCP6	pWM020	pACEBac1, pIDC	Gentamicin, Chloramphenicol
pIDS-Actin-Beta_GCP4	pWM021	pIDS ^{poolH}	Spectinomycin
pACEBac1-2xFLAG-TEV-GCP5_MZT1	pWM022	pACEBac1	Gentamicin
Cre-GCP6_TUBG1+MZT1	pWM023	pACEBac1, pIDK ^{poolH}	Gentamicin, Kanamycin
Cre-2xFLAG-TEV-GCP5+GCP2_GCP3	pWM024	pACEBac1, pIDC	Gentamicin, Chloramphenicol
Cre-2xFLAG-TEV-GCP5+GCP6+GCP4_TUBG1	pWM025	pACEBac1, pIDC, pIDK ^{poolH}	Gentamicin, Chloramphenicol, Kanamycin
Cre-2xFLAG-TEV-GCP5+GCP6+GCP4_TUBG1_Actin-Beta	pWM026	pACEBac1, pIDC, pIDK ^{poolH} , pIDS ^{poolH}	Gentamicin, Chloramphenicol, Kanamycin, Spectinomycin
Cre-2xFLAG-TEV-GCP5+GCP2_GCP3+GCP4_TUBG1	pWM027	pACEBac1, pIDC, pIDK ^{poolH}	Gentamicin, Chloramphenicol, Kanamycin
Cre-GCP6_TUBG1+MZT1+Actin-Beta	pWM028	pACEBac1, pIDK ^{poolH} , pIDS ^{poolH}	Gentamicin, Kanamycin, Spectinomycin
Cre-Mzt1+GCP2_GCP3	pWM030	pACEBac1, pIDC	Gentamicin, Chloramphenicol

Material and Methods

Name	Identifier	Vector backbone	Resitency
pIDC-2xFLAG-TEV-xHAUS3	pWM031	pIDC	Chloramphenicol
pIDC-2xFLAG-TEV-xHAUS3	pWM032	pIDC	Chloramphenicol
pACEBac1-xHAUS4	pWM033	pACEBac1	Gentamicin
pIDK-xHAUS4	pWM034	pIDK ^{poolH}	Kanamycin
pIDC-2xFLAG-TEV-xHAUS3	pWM035	pIDC	Chloramphenicol
pIDK-xHAUS2	pWM037	pIDK ^{poolH}	Kanamycin
pACEBac1-xHAUS5	pWM039	pACEBac1	Gentamicin
pACEBac1-xHAUS7	pWM040	pACEBac1	Gentamicin
pIDS-xHAUS1-EGFP-8xHIS	pWM041	pIDS ^{poolH}	Spectinomycin
pIDS-xHAUS8	pWM042	pIDS ^{poolH}	Spectinomycin
pIDS-NEDD1	pWM043	pIDS ^{poolH}	Spectinomycin
pACEBac1-NME7	pWM044	pACEBac1	Gentamicin
pACEBac1-GCP2-FLAG	pWM045	pACEBac1	Gentamicin
pIDC-2xFLAG-TEV-xHAUS3_xHAUS4	pWM046	pIDK ^{poolH}	Kanamycin
Cre-xHAUS5+xHAUS1-EGFP-8xHIS	pWM047	pACEBac1, pIDS ^{poolH}	Gentamicin, Spectinomycin
pIDK-GCP5	pWM048	pIDK ^{poolH}	Kanamycin
pACEBac1-MZT1_GCP2	pWM049	pACEBac1	Gentamicin
Cre-TIIl-xHAUS5+xHAUS1-EGFP-8xHIS+2xFLAG-TEV-xHAUS3_xHAUS4	pWM050	pACEBac1, pIDK ^{poolH} , pIDS ^{poolH}	Gentamicin, Kanamycin, Spectinomycin
pACEBac1-MZT1_NME7	pWM051	pACEBac1	Gentamicin
Cre-GCP2-FLAG+GCP3_Actin-Beta	pWM052	pACEBac1, pIDC	Gentamicin, Chloramphenicol
Cre-MZT1_NME7+NEDD1	pWM053	pACEBac1, pIDS ^{poolH}	Gentamicin, Spectinomycin
Cre-MZT1_NME7+NEDD1	pWM054	pACEBac1, pIDS ^{poolH}	Gentamicin, Spectinomycin
pIDK-MZT2B	pWM055	pIDK ^{poolH}	Kanamycin
Cre-GCP2-FLAG+GCP3_Actin-Beta+TUBG1	pWM056	pACEBac1, pIDC, pIDK ^{poolH}	Gentamicin, Chloramphenicol, Kanamycin
Cre-GCP2-FLAG+GCP3_Actin-Beta+TUBG1_GCP6	pWM057	pACEBac1, pIDC, pIDK ^{poolH}	Gentamicin, Chloramphenicol, Kanamycin
pIDK-GCP4_GCP5	pWM058	pIDK ^{poolH}	Kanamycin
Cre-MZT1_NME7+NEDD1_MZT2B	pWM059	pACEBac1, pIDS ^{poolH} , pIDK ^{poolH}	Gentamicin, Spectinomycin, Kanamycin
Cre-GCP2-FLAG+GCP3_Actin-Beta+TUBG1_GCP6+GCP4_GCP5	pWM060	pACEBac1, pIDC, pIDK ^{poolH} , pIDS ^{poolH}	Gentamicin, Chloramphenicol, Kanamycin, Spectinomycin
pACEBac1-Actin-Beta	pWM061	pACEBac1	Gentamicin
pIDK-2xFLAG-TEV-xHAUS6	pWM062	pIDK ^{poolH}	Kanamycin
pIDS-xHAUS2_xHAUS8	pWM063	pIDS ^{poolH}	Spectinomycin
Cre-xHAUS7+2xFLAG-xHAUS6	pWM064	pACEBac1, pIDK ^{poolH}	Gentamicin, Kanamycin
Cre-xHAUS7+xHAUS2_xHAUS8	pWM065	pACEBac1, pIDS ^{poolH}	Gentamicin, Spectinomycin
Cre-TIIl-xHAUS7+2xFLAG-xHAUS6-xHAUS2_xHAUS8	pWM066	pACEBac1, pIDK ^{poolH} , pIDS ^{poolH}	Gentamicin, Kanamycin, Spectinomycin
Cre-MZT1+GCP2_GCP3+MZT2B	pWM067	pACEBac1, pIDC, pIDK ^{poolH}	Gentamicin, Chloramphenicol, Kanamycin
pIDC-ΔN56-GCP6	pWM069	pIDC	Chloramphenicol
pIDK-TUBG1_MZT2B	pWM070	pIDK ^{poolH}	Kanamycin
Cre-2xFLAG-TEV-GCP5+GCP4_TUBG1	pWM071	pACEBac1, pIDK ^{poolH}	Gentamicin, Kanamycin
Cre-GCP4_TUBG1+GCP3_Actin-Beta	pWM072	pIDC, pIDK ^{poolH}	Chloramphenicol, Kanamycin
pIDS-MZT1	pWM073	pIDS ^{poolH}	Spectinomycin
Cre-GCP2-8xHIS+GCP3_Actin-Beta+TUBG1_MZT2B	pWM074	pACEBac1, pIDC, pIDK ^{poolH}	Gentamicin, Chloramphenicol, Kanamycin
Cre-GCP2-8xHIS+GCP3_Actin-Beta+TUBG1_MZT2B+MZT1	pWM075	pACEBac1, pIDC, pIDK ^{poolH} , pIDS ^{poolH}	Gentamicin, Chloramphenicol, Kanamycin, Spectinomycin
Cre-2xFLAG-TEV-GCP5+ΔN56-GCP6	pWM076	pACEBac1, pIDC	Gentamicin, Chloramphenicol
Cre-2xFLAG-TEV-GCP5+ΔN56-GCP6+GCP4_TUBG1	pWM077	pACEBac1, pIDC, pIDK ^{poolH}	Gentamicin, Chloramphenicol, Kanamycin
Cre-2xFLAG-TEV-GCP5+ΔN56-GCP6+GCP4_TUBG1+Actin-Beta	pWM079	pACEBac1, pIDC, pIDK ^{poolH} , pIDS ^{poolH}	Gentamicin, Chloramphenicol, Kanamycin, Spectinomycin

Material and Methods

Name	Identifier	Vector backbone	Resitency
pIDS-RuvBL1	pWM080	pIDS ^{polH}	Spectinomycin
pIDS-RuvBL2	pWM081	pIDS ^{polH}	Spectinomycin
Cre-MZT1+GCP2_GCP3+MZT2B_TUBG1	pWM082	pACEBac1, pIDC, pIDK ^{polH}	Gentamicin, Chloramphenicol, Kanamycin
pIDS-RuvBL1_RuvBL2	pWM083	pIDS ^{polH}	Spectinomycin
pIDS-RuvBL1_RuvBL2	pWM084	pIDS ^{polH}	Spectinomycin
pACEBac1-MZT1_MZT2B	pWM085	pACEBac1	Gentamicin
Cre-MZT1+GCP2_GCP3+MZT2B_TUBG1+ RuvBL1_RuvBL2	pWM086	pACEBac1, pIDC, pIDK ^{polH} , pIDS ^{polH}	Gentamicin, Chloramphenicol, Kanamycin, Spectinomycin
pACEBac1-GCP6-2xFLAG	pWM087	pACEBac1	Gentamicin
pACEBac1-GCP3-2xFLAG	pWM088	pACEBac1	Gentamicin
Cre-MZT1_MZT2B + RuvBL1_RuvBL2	pWM089	pACEBac1, pIDS ^{polH}	Gentamicin, Spectinomycin
pIDC-GCP2_GCP3-2xFLAG	pWM090	pIDC	Chloramphenicol
Cre-MZT1_MZT2B + RuvBL1_RuvBL2+ GCP2_GCP3	pWM091	pACEBac1, pIDC, pIDS ^{polH}	Gentamicin, Chloramphenicol, Spectinomycin
pACEBac1-2xFLAG-xNEDD1	pWM100	pACEBac1	Gentamicin
Cre-MZT1_MZT2B + RuvBL1_RuvBL2+ GCP6	pWM101	pACEBac1, pIDC, pIDS ^{polH}	Gentamicin, Chloramphenicol, Spectinomycin
Cre-2xFLAG-TEV-GCP5+GCP6+GCP4_Actin-Beta	pWM102	pACEBac1, pIDC, pIDS ^{polH}	Gentamicin, Chloramphenicol, Spectinomycin
Cre-MZT1_MZT2B + RuvBL1_RuvBL2+ GCP2_GCP3-2xFLAG	pWM103	pACEBac1, pIDC, pIDS ^{polH}	Gentamicin, Chloramphenicol, Spectinomycin
Cre-MZT1_MZT2B + RuvBL1_RuvBL2+ GCP2_GCP3-2xFLAG + TUBG1	pWM104	pACEBac1, pIDC, pIDK ^{polH} , pIDS ^{polH}	Gentamicin, Chloramphenicol, Kanamycin, Spectinomycin
pIDK-TUBG1(R295D R296D R301A)	pWM105	pIDK ^{polH}	Kanamycin
petDuet-FLAG-MZT1_GCP6 _{231-8xHis}	pWM107	petDuet	Ampicillin
petDuet-FLAG-MZT1_GCP6 _{280-8xHis}	pWM108	petDuet	Ampicillin
petDuet-FLAG-MZT1_GCP6 _{126-8xHis(35D,38D,39D,46A)}	pWM109	petDuet	Ampicillin
petDuet-FLAG-MZT1_GCP6 _{126-8xHis(35A,42A,46A)}	pWM110	petDuet	Ampicillin
petDuet-FLAG-MZT1_GCP6 _{126-8xHis(35A,38A,39A)}	pWM113	petDuet	Ampicillin
petDuet-FLAG-MZT1_GCP6 _{126-8xHis(35D,38D,39D)}	pWM114	petDuet	Ampicillin
petDuet-FLAG-MZT1_GCP6 _{57-126-8xHis}	pWM115	petDuet	Ampicillin
petDuet-FLAG-MZT1_GCP6 _{126-8xHis(35D,38D,39D,42A,46A)}	pWM116	petDuet	Ampicillin
pIDK-TUBG1_ΔN126-GCP6	pWM122	pIDK ^{polH}	Kanamycin
pIDK-TUBG1_ΔN280-GCP6	pWM123	pIDK ^{polH}	Kanamycin
Cre-MZT1_MZT2B + RuvBL1_RuvBL2 + TUBG1	pWM127	pACEBac1, pIDK ^{polH} , pIDS ^{polH}	Gentamicin, Kanamycin, Spectinomycin
Cre-2xFLAG-TEV-GCP5 + GCP2_GCP3 + GCP4_Actin-Beta	pWM129	pACEBac1, pIDC, pIDS ^{polH}	Gentamicin, Chloramphenicol, Spectinomycin
Cre-2xFLAG-TEV-GCP5 + GCP2_GCP3 + GCP4_Actin-Beta+TUBG1	pWM139	pACEBac1, pIDC, pIDK ^{polH} , pIDS ^{polH}	Gentamicin, Chloramphenicol, Kanamycin, Spectinomycin
Cre-GCP6-2xFLAG + GCP4_TUBG1	pWM140	pACEBac1, pIDK ^{polH}	Gentamicin, Kanamycin
pIDC-Actin-Beta_NEDD1	pWM145	pIDC	Chloramphenicol
Cre-GCP6-2xFLAG + GCP4_TUBG1_Actin-Beta_NEDD1	pWM146	pACEBac1, pIDC, pIDK ^{polH}	Gentamicin, Chloramphenicol, Kanamycin
Cre-8xHIS-TEV-RuvBL1 + RuvBL2	pWM147	pACEBac1, pIDS ^{polH}	Gentamicin, Spectinomycin
pACEBac1-MZT1_Spot-MZT2B-EGFP-Strep	pWM151	pACEBac1	Gentamicin
pIDK-TUBG1_NEDD1	pWM152	pIDK ^{polH}	Kanamycin
Cre-MZT1_Spot-MZT2B-EGFP-Strep + TUBG1_NEDD1	pWM153	pACEBac1, pIDK ^{polH}	Gentamicin, Kanamycin
Cre-MZT1_Spot-MZT2B-EGFP-Strep + GCP2_GCP3	pWM154	pACEBac1, pIDC	Gentamicin, Chloramphenicol
Cre-MZT1_Spot-MZT2B-EGFP-Strep + GCP2_GCP3 + TUBG1_NEDD1	pWM155	pACEBac1, pIDC, pIDK ^{polH}	Gentamicin, Chloramphenicol, Kanamycin
Cre-MZT1_Spot-MZT2B-EGFP-Strep + GCP2_GCP3 + TUBG1_NEDD1 + RuvBL1_RuvBL2	pWM156	pACEBac1, pIDC, pIDK ^{polH} , pIDS ^{polH}	Gentamicin, Chloramphenicol, Kanamycin, Spectinomycin
pACEBac1-xHAUS7_2xFLAG-xHAUS6	pWM160	pACEBac1	Gentamicin
Cre-TII-xHAUS7_2xFLAG-xHAUS6+xHAUS2_xHAUS8	pWM161	pACEBac1, pIDS ^{polH}	Gentamicin, Spectinomycin

4.2.10 Molecular cloning of GCP6 constructs for experiments in human cell culture system

Methods described as well as the used primers were published, along with a detailed description of the cloning procedure [372].

4.3 Protein expression

4.3.1 General handling of *E. coli* strains for baculovirus production and protein expression

Liquid cultures and antibiotic selection plates for the MultiBac constructs were performed as described in the manufacturer's instructions (Geneva Biotech, MultiBac Manual version 5.1). For long-term storage, *E. coli* cells were kept in a 15% glycerol stock at -80°C. To take the *E. coli* cells in culture, they were plated under sterile conditions on a selective plate and incubated at 37°C overnight. For baculovirus production, on the day before virus production, single colonies were inoculated in 2xYT medium supplemented with antibiotics (Kanamycin, Gentamycin and Tetracycline) for overnight incubation. For protein expression in *E. coli*, multiple colonies were used to start a liquid culture in LB or 2xYT medium with the corresponding antibiotics. For protein expression in *E. coli*, 25 µg/ml chloramphenicol and 100 µg/ml ampicillin (pETDuet-1) or 50 µg/ml Kanamycin (pET26b) were used.

4.3.2 Protein expression in *E. coli* for actin IP experiments

The detailed protocol was published [372] and performed by Ariani S. Rahadian. Briefly, proteins were expressed in *E. coli* BL21 CodonPlus-RIL (Stratagene) and expression was induced with 0.2 mM isopropyl-β-D-thiogalactopyranoside (IPTG) at an OD at 600 nm of 0.6 - 0.8. Expression was done at 18°C overnight. Bacterial cultures were harvested, aliquoted, and flash frozen using liquid N₂ and stored at -80°C until further usage.

4.3.3 Insect cell culture

Insect cells, Sf21, Sf9 or High5 were kept at a density of 0.8-1 x 10⁶/ml in Sf-900 III medium (Thermo Fisher Scientific) supplemented with 100 units/ml penicillin 100 µg/ml (Thermo Fisher Scientific) and were split every second or third day. Cells were counted using a Neubauer counting chamber (0.1 mm, Profondeur) or Luna II (Logos Biosystems) automated cell counter using Trypan blue (Sigma-Aldrich). The general culturing of insect cells was done by Ursula Jäkle.

4.3.4 Recombinant baculovirus production

The baculovirus production follows established protocols, and the used protocols were published [369,371,372]. v0 baculovirus production begins with a transfection process (as illustrated in Figure 1a). To purify the DNA (always freshly prepared), the

Material and Methods

Mini preparation protocol was followed until reaching the isopropanol centrifugation stage. After this, the isopropanol was discarded, and the Eppendorf tube was completely filled with 70% ethanol. The sample was then centrifuged at 20,000 x g for 3 min. Post-centrifugation, the Eppendorf tube was transferred to a sterile hood where all the supernatant was carefully removed, and the tube was left open to incubate for drying the pellet for around 15 min. The following protocol mainly recapitulates Cellfectin® II manufactures instructions (Invitrogen, Thermo Fisher Scientific, Bac-to-Bac TOPO expression system Version A10606). Briefly, 20 ml of plating medium was prepared by combining SF900 (Thermo Fisher Scientific) with 1.5% fetal bovine serum (FBS, Gibco). Afterwards, 0.8×10^5 Sf21 or Sf9 cells were plated per well of a 6-well plate. Importantly, the cells were spitted the day before to ensure that these cells were in the logarithmic growth phase. The cells were allowed to attach for about 15 min at room temperature (RT) within the hood. It is important to note that for each construct, two wells were prepared. The medium was then removed, and 2 ml of the freshly prepared plating medium was added to each well. To prepare for transfection, Cellfectin® II (Invitrogen, Thermo Fisher Scientific) was mixed diluted at a ratio of 8 μ l into 100 μ l SF900 III (Thermo Fisher Scientific) for each well, ensuring this mixture was left at RT no longer than 30 min. In the meantime, the bacmid pellet was resuspended in 30 μ l of sterile H₂O. A 5 μ l sample from this resuspension was then taken to another Eppendorf tube to measure DNA concentration. 1-3 μ g of bacmid DNA was diluted in 100 μ l SF900 III (Thermo Fisher Scientific). This diluted DNA was then combined with the Cellfectin® II mix. After gentle mixing, the solution was left to incubate at RT for 15-30 min. This DNA-transfection mixture was then added dropwise onto the cells. The cells were then incubated at 27°C for a duration of 3-5 h. Subsequent to this incubation, the plating medium was replaced in one of the two replicates with fresh SF900 III medium that contained antibiotics (100 units/ml penicillin 100 μ g/ml (Thermo Fisher Scientific)). The second replicate remained unchanged. The cells were further incubated at 27°C and for 72 h protected from light until there were visible signs of viral infection. Afterwards, the supernatant was harvested by centrifugation (800 x g for 5 min) and stored protected from light at 4°C until further usage.

For the v1 generation, a volume of 30 ml of Sf21/Sf9 cells (at a density of 1×10^6 /ml, which were in the logarithmic phase as the cells were split the day before) was

Material and Methods

inoculated with 2-3 ml of the v0 baculovirus. A negative control was set up simultaneously, consisting of non-infected cells. Daily cell counts were performed, and the cells were diluted if required to maintain the volume at 30 ml and the density at 1×10^6 /ml. Once cell division stopped, an additional 48 h incubation period, followed and baculoviruses were harvested (Figure 1). Prior to the harvesting, a final cell count was carried out and the average cell diameter was measured (as sign for the infection). For harvesting, the cell suspension was transferred into a 50 ml falcon tube and centrifuged at 800 x g for 5 min. The resultant supernatant, which contained the virus, was transferred to a fresh 50 ml falcon tube, to which 5-10% FBS was added.

4.3.5 Recombinant protein expression in insect cells

For protein expression in insect cells, exclusively the v1 generation of recombinant baculoviruses were used. Individual constructs that were used for baculovirus production are listed in Table 25 and highlighted in the individual figures in the results section. For each expression, up to three independently produced baculoviruses were diluted 1:100 in Sf21 or High5 cells ($1-1.5 \times 10^6$ cells/ml) expression cultures. Infected cells were kept shaking at 27°C for 60 h, harvested via centrifugation (800 x g for 5 min), flash frozen in liquid N₂ and stored at -80°C until further usage. Expression volumes ranged from 50 – 400 ml. For recombinant human γ -TuRC 100 ml culture volume was used.

4.4 Protein purification

4.4.1 Protein purification of constructs expressed in insect cells

Detailed protocols of the protein purification workflow established and used in this thesis were published for the minimal γ -TuRC construct [371], the optimized γ -TuRC, γ -TuRC mutants, and γ -TuRC sub-complexes [372]. The protocol for the purification of augmin complexes is published [369]. The following general protocol, which relies on purification via FLAG affinity beads using a single-step batch protocol (Figure 9), was applied for γ -TuRC and augmin complexes. In general, cell pellets from storage at -80°C were thawed and lysed in cold lysis buffer. Resuspended cells were sonicated (3 x 1 min with 0.6 amplitude, Hielscher UP50H) and centrifuged at 20,000 x g for 30 min at 4°C. Anti-FLAG M2 affinity resin (Sigma-Aldrich), equilibrated in lysis buffer was incubated with the cleared lysate for 90 min with rotation at 4°C. FLAG resin (beads) was separated by centrifugation (800 x g, 3 min). Afterwards, beads were

Material and Methods

washed in lysis and basic buffer. After each washing step, beads were sedimented via centrifugation (800 x g, 3 min). Elution was done with one bead volume of elution buffer (basic buffer supplemented with 0.2 - 0.5 mg/ml 3xFLAG peptide (Gentaur)) and 20-30 min incubation rotating at 4°C in an Eppendorf tube. Afterwards, the eluate was separated from the beads by centrifugation (800 x g, 3 min). Elution was repeated one to two times, and samples were used for subsequent purification steps and experiments after concentration using an Amicon 30 kDa MWCO concentrator (Merck), or flash frozen in liquid N₂ and stored at -80°C.

4.4.2 Purification of minimal recombinant γ -TuRC

The protocol was published [371] and followed the general batch FLAG purification protocol. The basic buffer for purification is listed in Table 26.

Table 26 Buffer for the minimal recombinant γ -TuRC purification:

Composition
50 mM HEPES pH 7.4
150 mM KCl
5 mM MgCl ₂
1 mM EGTA
0.5 mM DTT
0.1 mM GTP

For lysis, 0.5 mM DTT, 0.02% (v/v) Brij-35, 250 units Benzonase (Sigma Aldrich), and one complete EDTA-free protease inhibitor tablet (Roche) per 15 ml lysis buffer was added. After centrifugation, the supernatant was filtered (Whatman sterile filters 0.45 μ m pore size) and incubated with anti-FLAG M2 affinity resin (Sigma-Aldrich). Samples were washed once with lysis and twice with basic buffer (Table 26) and eluted with basic buffer supplemented with 0.2 mg/ml 3xFLAG peptide (Gentaur).

4.4.3 Purification of optimized γ -TuRC, γ -TuRC ^{Δ N56-GCP6}, γ -TuSC and γ -TuRC ^{Δ GCP2/3}

The protocol was published [372] and followed the general batch FLAG purification protocol. The basic buffer for purification is listed in Table 27. For the lysis buffer, 0.1% (v/v) Tween-20, 250 units Benzonase (Sigma Aldrich), and one complete EDTA-free protease inhibitor tablet (Roche) per 15 ml lysis buffer was added.

Table 27 Buffer for the optimized recombinant γ -TuRC purification:

Composition
50 mM TRIS pH 7.5
150 mM NaCl
1 mM MgCl ₂
1 mM EGTA
0.5 mM DTT

After centrifugation, the supernatant was incubated with anti-FLAG M2 affinity resin (Sigma-Aldrich). Samples were washed once with lysis and twice with basic buffer (Table 27) and eluted (2x 100 μ l) with basic buffer supplemented with 0.5 mg/ml 3xFLAG peptide (Gentaur). Purification of γ -TuRC ^{Δ N56-GCP6} from HEK cells was done by Anna Böhler following a similar protocol published in [372].

4.4.4 Purification of augmin complexes

The protocol was published [372] and followed the general batch FLAG purification protocol. The basic buffer for purification is listed in Table 28. For lysis buffer, 0.05% (v/v) Tween-20, 250 units Benzonase (Sigma Aldrich), and one complete EDTA-free protease inhibitor tablet (Roche) per 30 ml lysis buffer) were added.

Table 28 Buffers for the recombinant augmin complex purification:

Composition EM	Composition MS
20 mM TRIS pH 7.5	20 mM HEPES pH 7.4
150 mM NaCl	150 mM NaCl
1 mM MgCl ₂	4 mM MgCl ₂
1 mM EGTA	1 mM EGTA
1 mM DTT	0.5 mM DTT

Cleared supernatant was filtered (Whatman sterile filters 0.45 μ m pore size) and incubated with anti-FLAG M2 affinity resin (Sigma-Aldrich). Samples were washed once with lysis and twice with basic buffer (Table 28) and eluted with basic buffer supplemented with 0.5 mg/ml 3xFLAG peptide (Gentaur).

4.4.5 Size exclusion chromatography and anion exchange chromatography

Following initial FLAG tag-based purification, γ -TuSC and the augmin complexes were further purified using an ÄktaGo instrument (Cytiva) controlled by Unicorn software (version 7.6) and the descriptions of the methods were published [369,372].

Material and Methods

SEC was conducted on a Superose 6 Increase 10/300 GL column (Cytiva), which had been equilibrated in SEC buffer (Table 29). The chromatography elution process was done at a steady flow rate of 0.25 ml/min. To run size markers on the column, blue dextran 2000 (Cytiva) was applied to determine the void volume (measured at 8.8 ml), and protein standards including thyroglobulin (669 kDa, eluting at 13.2 ml) and aldolase (158 kDa, at 16.3 ml) were used.

AEC was performed using either a Mono Q® 5/50 GL or a Capto™ HiRes Q 5/50 column (Cytiva), both equilibrated with a low-salt buffer (Buffer A, Table 29). It is important to note that the buffers for augmin TIII varied based on the experimental requirements, such as EM or crosslinking MS analyses (Table 29). The elution of complexes was executed at a flow rate of 0.5 ml/min, employing a salt gradient that ranged from 150 mM NaCl (Buffer A) to 1 M NaCl (Buffer B) over 20 column volumes.

Table 29 Buffers of the chromatography runs using the ÄktaGo system: Purifications for augmin TIII were performed in TRIS (for EM experiments) and HEPES buffer (for crosslinking MS experiments).

SEC	AEC TIII (EM)	AEC TIII (MS)	AEC γ -TuSC
20 mM TRIS pH 7.5	20 mM TRIS pH 7.5	20 mM HEPES pH 7.4	50 mM TRIS pH 7.5
150 mM NaCl	150 mM NaCl (Buffer A); 1M NaCl (Buffer B)	150 mM NaCl (Buffer A); 1M NaCl (Buffer B)	150 mM NaCl (Buffer A); 1M NaCl (Buffer B)
1 mM MgCl ₂	1 mM MgCl ₂	4 mM MgCl ₂	1 mM MgCl ₂
1 mM EGTA	1 mM EGTA	1 mM EGTA	1 mM EGTA
0.5 mM DTT	0.5 mM DTT	0.5 mM DTT	0.5 mM DTT

4.5 Biochemistry methods

4.5.1 SDS-polyacrylamide gel electrophoresis (SDS-PAGE)

To separate proteins according to their size, SDS-PAGE was applied (Mini-PROTEAN® Tetra system, Bio-Rad) using 4-20% gradient gels (PROTEAN® TGX Stain-Free™ Bio-Rad). Protein samples in 1x Lämmli buffer were run together with Page Ruler Plus (Thermo Fisher Scientific) at constant 30 mA. After the run, the gels were either used for immunoblot analysis or stained with Coomassie Brilliant Blue G250 buffer (Sigma Aldrich) and visualized.

4.5.2 Immunoblot analysis

To analyze protein samples via antibodies, the SDS-PAGE-separated proteins were transferred using the Trans-Blot Turbo Transfer kit (Bio-Rad) following manufacturer instructions. The settings were 1xGel-Turbo setup. After transfer, the membrane was blocked in 3% w/v milk powder in 1x TBS-T buffer for 30 min. In the next step, the

Material and Methods

membrane was incubated overnight in the primary antibody solution diluted in blocking buffer at 4°C. The next day, the membrane was washed three times in TBS-T and subsequently incubated with the secondary antibody diluted in blocking buffer for 1 h at RT. Afterwards, the membrane was washed three times with TBS, and the membrane was shortly incubated with enhanced chemiluminescence (ECL) solutions and documented at the LAS/Amersham imaging system. Antibodies used are listed in Table 30, and data were processed using Fiji [403].

Table 30 Antibodies:

Target	Species	Purchaser and Identification
β-Actin	mouse	Sigma-Aldrich (PN: A5316)
β-Actin	mouse	Proteintech 66009-1-Ig monoclonal
γ-tubulin	rabbit	Polyclonal against c-terminal peptide (Liu et al.)
γ-tubulin	mouse	Monoclonal Abcam (TU-30) (ab27074)
γ-tubulin	Guinea pig	Atorino et al. 2020
GCP2	rabbit	Thermo Fisher Scientific (PA5-21433)
GCP3	rabbit	Proteintech 15719-1-AP
GCP4	rabbit	Polyclonal against full length human GCP4 (Liu et al.2020)
GCP6	rabbit	Polyclonal Thermo Fisher Scientific (A302-662A)
GCP6	rabbit	Bethyl A302-662A polyclonal
GAPDH	rabbit	CellSignalling 14C10
Vinculin	mouse	Proteintech 66305-1-Ig
His	mouse	Proteintech HRP-66005 monoclonal HRP conjugated
Penta-His	mouse	QIAGEN 34660
DDDDK tag (FLAG)	rabbit	Proteintech 20543-1-AP Polyclonal
FLAG	mouse	Cell signaling 9A3
α-tubulin	rabbit	MBL PM054
α-tubulin	mouse	SigmaAldrich DM1A
BubR1	mouse	Abcam Ab4637
Pericentrin	rabbit	Abcam Ab4448
Anti rabbit	donkey	Jackson 711-035.0152 Secondary-HRP
Anti mouse	donkey	Jackson 711-035.0155 Secondary-HRP

4.5.3 Actin IP experiment

The procedure of actin IP experiments was published [372] and performed in collaboration with Ariani S. Rahadian using buffers listed in Table 31. For actin IP experiments, bacterial cell pellets from the expressed GCP6-MZT1 constructs (4 ml expression culture) were lysed in 300 µl of IP-lysis buffer supplemented with a complete EDTA-free protease inhibitor tablet (Roche) (1:100 dilution). The mixture was sonicated (5 x 30 sec, Bioruptor) and afterwards centrifuged for 10 min, 20,000 x g at 4°C. The supernatant was mixed with 20 µl of His Beads (Bio-Rad) and incubated for 1 h at 4°C. Beads were washed 3x with IP-wash buffer and equilibrated with 400 µl G-buffer. Afterwards, the G-buffer was removed, 100 µl of actin solution (0.1 mg/ml

Material and Methods

actin, Cytoskeleton, Inc. SKU: AKL99, dissolved in G-buffer) was added and samples were incubated for 30 min at 4°C. The samples were then washed with 400 µl ice-cold G-buffer and eluted with 60 µl IP-elution buffer.

Table 31 Buffers for actin IP experiment:

IP-Lysis	IP-Wash	G-Buffer	IP-Elution
20 mM TRIS pH 8	50 mM TRIS pH 8	5 mM TRIS pH 8	50 mM TRIS pH 8
150 mM NaCl	150 mM NaCl	0.2 mM CaCl ₂	150 mM NaCl
5 mM MgCl ₂	10 mM Imidazole	0.2 mM ATP	500 mM Imidazole
1% v/v Triton-X		0.5 mM DTT	
5 mM ATP			
1 mM DTT			
1 mM PMSF			

4.5.4 *In vitro* MT nucleation assay for negative stain EM

Methods for the MT nucleation of recombinant γ -TuRC are published [371] and were performed in collaboration with Anna Böhler. 30 µM porcine brain tubulin containing 4% Cy3-labelled tubulin [35] in 1x BRB80 buffer supplemented with 12.5% (w/v) glycerol was centrifuged for 5 min at 352,860 x g, 4°C with a S100-AT3 rotor (Thermo Fisher Scientific). The supernatant was mixed in a 1:1 ratio with γ -TuRC premix (1:20 dilution of γ -TuRC elution sample (construct pWM026/pWM030), in 1x BRB80 supplemented with 12.5% (w/v) glycerol and 1 mM GTP). Samples were incubated for 15-30 min on ice and transferred to 37°C for 3 min for MT polymerization. After MT nucleation, samples were crosslinked with 1% glutaraldehyde and used for negative stain EM.

4.5.5 *In vitro* MT nucleation assay for comparing recombinant γ -TuRC constructs

The procedure of actin IP experiments is published [372] and performed in collaboration with Anna Böhler and Dr. Lukas Rohland. To analyze MT nucleation of recombinant γ -TuRC *in vitro*, a fluorescence-based tubulin polymerization assay kit (Cytoskeleton, Denver Com cat. no. BK011P) was used following manufactures instructions. Concentration of two biological replicas of wild-type γ -TuRC (construct pWM026/pWM086) and γ -TuRC^{ΔN56-GCP6} (construct pWM076/pWM086) was normalized to γ -tubulin signal via immunoblot analysis and diluted in elution buffer (Chapter 4.4.3) accordingly. The γ -tubulin reference for comparative immunoblot analysis was recombinant γ -tubulin with c-terminal Myc-His₆ TAG purified according

Material and Methods

to published protocols [120,121] and provided by Ursula Jäkle. Intensities of protein bands were determined using Fiji software [403]. 2 μ l of elution buffer, wild-type γ -TuRC and γ -TuRC ^{Δ N56-GCP6} samples, or 3 μ M paclitaxel were pipetted into a 384-well microtiter plate and mixed with 30 μ l of $\alpha\beta$ -tubulin premix (2 mg/ml porcine tubulin in 80 mM PIPES pH 6.9, 2 mM MgCl₂, 0.5 mM EGTA, 1 mM GTP, 15% (w/v) glycerol), (provided with the kit) at 4°C. The plate was transferred to a prewarmed (37°C) plate reader chamber, starting the reaction. Fluorescence signal was measured at constant temperature (37°C) for 60 min in 1 min intervals (CLARIOstar, BMG Labtech, excitation, F: 360-10, emission, F: 450-10). Data were processed using PRISM software (GraphPad version 9.1).

4.6 Electron microscopy methods

EM experiments were conducted using instruments and equipment provided by the Cryo-Electron Microscopy Network of Heidelberg University (HDcryoNet). The SDS@hd and bwHPC services were used for data storage and processing.

4.6.1 Negative staining and general EM data processing

Methods of negative staining EM experiments were published in [371], [372], and [369] and negative staining procedure and image acquisition were performed by Dr. Annett Neuner. Briefly, for negative staining, 5 μ l of sample was applied on glow-discharged copper-palladium 400-mesh EM grids (Plano) covered with an approximately 10 nm-thick continuous carbon layer. After 30 sec of incubation at RT, grids were blotted with a Whatman filter paper 50 (CAT N.1450-070) and washed with 3 drops of water. Sample on grids was stained with 3% uranyl acetate in water. Negative stain EM data for 2D classification were acquired on a Talos L120C TEM equipped with 4k \times 4K Ceta CMOS camera (Thermo Fisher Scientific). Data were acquired using EPU (Thermo Fischer Scientific) at a nominal defocus of approximately -2 μ m and an object pixel size of either: 0.2552 nm; 0.328 nm; 0.4125 nm. Image processing for all datasets for 2D and 3D class averaging was performed in Relion 3.1 [404]. The contrast transfer function (CTF) of micrographs was estimated using Gctf [405]. For all datasets, approximately 500 particles were selected manually. Afterwards an initial 2D classification run was performed for automated particle picking (Relion 3.1). Alternatively, an already generated 2D class of the same data type was used. The

particles were extracted, either scaled or at full spatial resolution, and the number of classes for each subsequent 2D classification round varied between 50 and 200.

4.6.2 Negative stain EM of minimal γ -TuRC

The method details were published [371] and negative staining was performed as described in section 4.6.1. Micrographs shown in Figure 10 were acquired on Jeol JE-1400 (Jeol Ltd., Tokyo, Japan) operating at 80 kV equipped with a 4 k × 4 k digital camera (F416, TVIPS, Gauting, Germany). Micrographs were processed using Fiji software [403]. However, for class averaging of native *X. laevis* γ -TuRC and recombinant human γ -TuRC (construct pWM026/ pWM030) images were acquired on a Talos L120C TEM equipped with 4 k × 4 K Ceta CMOS camera (Thermo Fisher Scientific). Data were partially acquired at a stage tilting angle of 20 degrees at an object pixel size of 0.4125 nm. 2D classifications were performed at a translational search range of 20 pixels at 2 pixels increment, using a T-factor of 2 and a mask diameter of 450 Å and are summarized in Table 32.

Table 32 Negative stain EM comparison of recombinant human and native *X. laevis* γ -TuRC:

Parameter	Recombinant γ -TuRC	<i>X. laevis</i> γ -TuRC
Micrographs	957 untilted; 640 at 20° stage tilt	500 untilted, 600 at 20° stage tilt
Autopicked particles	374,389	192,845
Particles used for initial 3D classification	12,402	12,271

For 3D classification, a translation search range of 20 pixels with 2 pixel increment was used. Particles were aligned using a γ -TuRC cryo-EM density (PDB-6TF9 [35]) as reference, after low-pass filtering and omitting the GRIP2 domains and γ -tubulins from spokes 5 and 6. These aligned particles underwent another round of 3D classification into 6 groups, without image alignment and focusing on the deleted spokes. This differentiated true positive particles (with density in spokes 5 and 6) from those without. Subsequently, the selected particles (6,253 for human γ -TuRC and 6,827 for *X. laevis* γ -TuRC) were classified again in 3D into three classes with image alignment. The best classes were then chosen, resulting in 2,064 particles for the human recombinant γ -TuRC and 2,490 for the *X. laevis* γ -TuRC for further analysis and representation in the figure with docked model of PDB-6V6S [37].

4.6.3 Negative stain EM of γ -TuRC, γ -TuRC ^{Δ N56-GCP6}, γ -TuSC and γ -TuRC ^{Δ GCP2/3}

The method details were published [372] and negative staining was performed as described in section 4.6.1. 2D classifications were performed at a translational search range of 20 pixels at 2 pixels increment using a T-factor of 2, and a mask with 400 Å diameter. 2D classification steps are summarized in Table 33 Representative 2D class averages with the corresponding particle numbers are shown in the corresponding figures. For the recombinant γ -TuSC dilution series, number of particles in single γ -TuSC or γ -TuSC oligomer classes were counted and compared (Figure 16c).

Table 33 Negative stain EM analysis of recombinant γ -tubulin complexes:

Sample	Micrographs	Pixel size of micrographs	Autopicked particles
Recombinant wild-type γ -TuRC	876	4.125 Å	1,197,806
Recombinant γ -TuRC ^{ΔN56-GCP6}	267	3.28 Å	194,874
Recombinant γ -TuSC	530	2.552 Å	268,126
Recombinant γ -TuRC ^{ΔGCP2/3} (4-spoke)	329	3.28 Å	183,636
γ -TuRC ^{ΔN56-GCP6} HEK293T	319	3.28 Å	110,331
Recombinant γ -TuSC 1:2 dilution	100	3.28 Å	134,246
Recombinant γ -TuSC 1:5 dilution	100	3.28 Å	122,712
Recombinant γ -TuSC 1:10 dilution	100	3.28 Å	110,642
Recombinant γ -TuSC 1:20 dilution	100	3.28 Å	76,325
Recombinant γ -TuSC 1:50 dilution	100	3.28 Å	65,732
Recombinant γ -TuSC 1:100 dilution	100	3.28 Å	51,950

4.6.4 Negative stain EM of augmin complexes

The method details were published [369] and negative staining was performed as described in section 4.6.1. 2D classifications were performed at a translational search range of 20 pixels at 2 pixels increment using a T-factor of 2 and mask diameters of 400–650Å. 2D classification steps are summarized in Table 34.

Table 34 Negative stain EM analysis of recombinant augmin complexes:

Parameter	TIII	TII+TIII
Micrographs	504	583
Pixel size of micrographs	3.28 Å	2.552 Å
Autopicked particles	412,188	80,837
Particles used for initial 3D classification	13,594	56,021

The 3D classification runs were initiated using the cryo-EM density of the augmin TIII tetramer, which was low-pass filtered to a resolution of 60Å, serving as the initial

Material and Methods

reference. A mask diameter of 450 Å (for TIII) or 600 Å (for the octamer), a T-factor of 4, 6 classes, and an offset search range of 20 pixels with a step of 2 pixels were employed. For the TIII dataset, 11,897 particles were selected after the initial 3D classification. For the octamer dataset (TII+TIII), two separate classes were identified, containing 21% (11,969 particles) and 19% (10,658 particles) of the total particles, respectively. The final sets of particles were subjected to individual 3D refinement runs, post-processing, and an additional round of 2D classification without image alignment to characterize the conformational plasticity of the augmin octamer in 2D. Before docking the atomic models, the pixel size of the negative stain EM 3D reconstructions was adjusted from the nominal 2.552 Å to a calibrated 2.35 Å. Representative 2D class averages with the corresponding particle numbers are shown in the corresponding figures.

4.6.5 Cryo-EM experiments

Cryo-EM experiments as well as model building based on cryo-EM densities were performed by Dr. Erik Zupa and are described in detail for recombinant γ -tubulin complexes in [372] and for recombinant augmin complexes in [369], respectively. All relevant information about processing are published open access and the generated models and densities are deposited in the corresponding databases.

4.7 Integrative structural biology methods

4.7.1 Liquid chromatography tandem-MS of recombinant γ -TuRC

For LC-MS/MS analysis of the recombinant γ -TuRC, three independent expressions were purified separately and for each of the $n=3$ purifications, 5 μ l of the FLAG elutions (combined elution 1 and 2) were run on a precast 10% SDS-PAGE (Bio-Rad) over a distance of 1.5 cm. SDS-PAGE was stained with Coomassie Brilliant Blue G250 and processed by the Core Facility for Mass Spectrometry & Proteomics at the ZMBH as described before [35]. Briefly, samples were reduced, alkylated, and digested with trypsin. Peptides were extracted from the gel, concentrated using a vacuum centrifuge, and dissolved in 15 μ l 0.1% trifluoroacetic acid (TFA). Samples were run on Ultimate 3000 liquid chromatography system coupled to an Orbitrap Elite mass spectrometer (Thermo-Fisher) and analyzed using the MaxQuant software (1.6.2.6a).

4.7.2 Crosslinking MS

To perform crosslinking experiments of the augmin TIII sub-complex, 50 µg of AEC-purified TIII tetramer in HEPES buffer was digested with 0.1 mM BS3 (Thermo Fisher) for 15 min at room temperature with gentle shaking at 600 rpm. The reaction was halted by adding Tris-HCl to achieve a final concentration of 100 mM. Subsequently, the sample was incubated for 30 min at 50°C with a dithiothreitol (DTT) concentration adjusted to 10 mM. Following this, 2-chloroacetamide (CAA) was added to reach a final concentration of 50 mM, and the reaction was incubated for 30 min at room temperature while protected from light. Next, trypsin (Promega, V511A) was added at a ratio of 1:50 (trypsin to augmin protein concentration), and the mixture was incubated for 4 h at 37°C. The reaction was terminated by adding TFA to a final concentration of 1% (v/v). Subsequently, the sample was submitted to EMBL Proteomics Core Facility and processed following the published protocol [369], alongside the deposited raw crosslinking MS data. Briefly, the digested peptides were concentrated and desalted using an OASIS® HLB µElution Plate (Waters) following the manufacturer's instructions. To enrich crosslinked peptides, a SEC approach was employed using a Superdex Peptide PC 3.2/30 column (Cytiva) on a 1200 Infinity HPLC system (Agilent) at a flow rate of 50 ml/min. The collected fractions were subjected to analysis via liquid chromatography (LC)-coupled tandem mass spectrometry (MS/MS) utilizing an UltiMate 3000 RSLC nano LC system (Dionex). The setup included a trapping cartridge (µ-Pre-column C18 PepMap 100, 5 µm, 300 µm i.d. x 5mm, 100 Å) and an analytical column (nanoEase™ M/Z HSS T3 column 75 µm x 250 mm C18, 1.8 µm, 100 Å, Waters). The outlet of the analytical column was connected to an Orbitrap Fusion Lumos mass spectrometer (Thermo Scientific) through a Pico-Tip Emitter (360 µm OD x 20 µm ID; 10 µm tip, CoAnn Technologies) using an applied spray voltage of 2.1 kV in positive mode.

4.7.3 Crosslinking MS data analysis

Data analysis and visualization were performed by Dr. Erik Zupa and are described in detail in [369].

4.7.4 AF-Multimer predictions

AF-Multimer predictions using AlphaFold v2.2.0 were performed and evaluated in collaboration with Dr. Erik Zupa using input and resources from EMBL Heidelberg and

Material and Methods

are published [369], alongside the deposited models. The settings were: Multimer present, utilization of full databases, omission of the relaxation step, and maximum template date to 2050/01/01. The various predictions of augmin complexes were generated by inputting FASTA files containing the sequences of the constituent proteins in each complex. Specifically, the augmin holocomplex (comprising HAUS1-8), the augmin TIII tetramer (containing HAUS1, HAUS3, HAUS4, and HAUS5), the augmin TII tetramer (composed of HAUS2, HAUS6, HAUS7, and HAUS8), and the TIII H3/H5-arm in complex with TII (consisting of HAUS3 residues 96-434, HAUS5 residues 80-489, HAUS2 residues 1-222, HAUS6 residues 1-478, HAUS7 residues 1-348, and HAUS8 residues 155-367) were predicted.

To assess differences among the predictions, models were aligned using the "matchmake" command in UCSF Chimera [406]. For the TIII models, the full-length models were superposed. The TII models were superposed based on either the N-clamp (HAUS2 residues 1-117, HAUS6 residues 1-267, HAUS7 residues 1-270, HAUS8 residues 155-260) or the C-clamp (HAUS2 residues 118-222, HAUS6 residues 268-398, HAUS7 residues 271-348, HAUS8 residues 261-367). When examining the TIII H3/H5-arm in complex with TII, all the predicted models were superposed to the H3/H5-arm of the highest-scoring TIII model (HAUS3 residues 198-242, 364-392, and HAUS5 residues 172-275, 419-446).

To visualize the structural differences, the predicted models were coloured according to the RMSD in PyMOL (PyMOL v2.1, Schrödinger). The two most distinct conformations from each ensemble were used, and a coloring scale ranging from 0 Å to 10 Å was applied. Additionally, rigid-body docking of the predicted TIII tetramer models into the cryo-EM density of the TIII tetramer was conducted in UCSF Chimera. This involved simulating densities at an 8 Å resolution and measuring the cross-correlation coefficient for each model. The model with the highest prediction score was refined by performing MDFF in Namdinator [407] with 2000 minimization steps and 20,000 simulation steps with 0 phenix real space refinement cycles. Model building of composite augmin structural models was done by Dr. Erik Zupa as described [369].

4.8 Cell biology methods

The experiments in the human cell culture system were performed by Dr. Enrico Salvatore Atorino and, the method details can be found in [372].

4.9 Image processing and statistical analysis

4.9.1 Image processing

For representation, images and figure panels were assembled in Adobe Illustrator (Adobe). EM images were processed using Relion 3.1 [404] as described in Chapter 4.6 and prepared for representation in Figures using Fiji [403]. Images of Coomassie-stained SDS-PAGES were acquired on LAS4000IR instrument in DIA mode and prepared for representation using Fiji. Immunoblot data were processed using Fiji for preparation of figure panels as well as for the quantification of band intensities using the standard intensity blot function of Fiji.

Plots of chromatography runs were generated using PRISM software (version 9.1). Microscopy data from the MT regrowth assay were analyzed using Fiji. The number of MT per centrosome and the MT size (length) were quantified using the segmented line tool. The lines were drawn from the center of the centrosome (γ -tubulin signal) to the end of the individual MTs [372].

4.9.2 Statistical analysis

Detailed statistical methodologies were outlined in the legends accompanying each figure. Data within the graphs represent the mean \pm standard deviation (SD), with each blot representing the average of at least three experimental replicates. Statistical significance was assessed using two-tailed unpaired t-tests, with a predefined significance level set at $p \leq 0.05$. For the statistical computations, GraphPad Prism (version 9.1 or 9.2) and Microsoft Excel (version 16.46.21021202) were employed.

5 Publications

List of publications to which I contributed during my PhD.

* Equal contribution

Research articles:

- [369] Zupa E*, **Würtz M***, Neuner A, Hoffmann T, Rettel M, Böhler A, Vermeulen BJA, Eustermann S, Schiebel E, Pfeffer S: The augmin complex architecture reveals structural insights into microtubule branching. *Nature Communications* 2022 13:5635
- [372] **Würtz M***, Zupa E*, Atorino ES*, Neuner A, Böhler A, Rahadian AS, Vermeulen BJA, Tonon G, Eustermann S, Schiebel E, Pfeffer S: Modular assembly of the principal microtubule nucleator γ -TuRC. *Nature Communications* **2022**, **13**:473.
- [371] **Würtz M***, Böhler A*, Neuner A, Zupa E, Rohland L, Liu P, Vermeulen BJA, Pfeffer S, Eustermann S, Schiebel E: Reconstitution of the recombinant human γ -tubulin ring complex. *Open Biol* **2021**, 11:200325.
- [135] Zupa E, Zheng A, Neuner A, **Würtz M**, Liu P, Böhler A, Schiebel E, Pfeffer S: The cryo-EM structure of a γ -TuSC elucidates architecture and regulation of minimal microtubule nucleation systems. *Nature Communications* **2020**, 11:5705.

Review articles:

- [111] Böhler A*, Vermeulen BJA*, **Würtz M***, Zupa E*, Pfeffer S*, Schiebel E*: The gamma-tubulin ring complex: Deciphering the molecular organization and assembly mechanism of a major vertebrate microtubule nucleator. *BioEssays* 2021, 2100114.
- [149] Liu P*, **Würtz M***, Zupa E, Pfeffer S, Schiebel E: Microtubule nucleation: The waltz between γ -tubulin ring complex and associated proteins. *Curr Opin Cell Biol* **2021**, 68:124–131.
- [154] Zupa E, Liu P, **Würtz M**, Schiebel E, Pfeffer S: The structure of the γ -TuRC: a 25-years-old molecular puzzle. *Curr Opin Struct Biol* **2021**, 66:15–21.

6 References

1. Watson JD, Crick FHC: **Molecular Structure of Nucleic Acids: A Structure for Deoxyribose Nucleic Acid.** *Nature* 1953, **171**:737–738.
2. Crick F: **Central Dogma of Molecular Biology.** *Nature* 1970, **227**:561.
3. Xu Y, Zhu TF: **Mirror-image T7 transcription of chirally inverted ribosomal and functional RNAs.** *Science (80-)* 2022, **378**:405–412.
4. Wang M, Jiang W, Liu X, Wang J, Zhang B, Fan C, Liu L, Pena-Alcantara G, Ling J-J, Chen J, et al.: **Mirror-Image Gene Transcription and Reverse Transcription.** *Chem* 2019, **5**:848–857.
5. Wang Z, Xu W, Liu L, Zhu TF: **A synthetic molecular system capable of mirror-image genetic replication and transcription.** *Nat Chem* 2016, **8**:698–704.
6. Pasteur 1822-1895 L: *Researches on the molecular asymmetry of natural organic products [microform] / by Louis Pasteur.* The Alembic Club; 1905.
7. Vantomme G, Crassous J: **Pasteur and chirality: A story of how serendipity favors the prepared minds.** *Chirality* 2021, **33**:597–601.
8. Bastings JAJ, van Eijk HM, Olde Damink SW, Rensen SS: **d-amino Acids in Health and Disease: A Focus on Cancer.** *Nutrients* 2019, **11**.
9. Alberts B, Johnson A, Wilson J, Lewis J, Hunt T, Roberts K, Raff M, Walter P: *Molecular Biology of the Cell.* Garland Science; 2008.
10. Jackson DA, Symons RH, Berg P: **Biochemical method for inserting new genetic information into DNA of Simian Virus 40: circular SV40 DNA molecules containing lambda phage genes and the galactose operon of Escherichia coli.** *Proc Natl Acad Sci U S A* 1972, **69**:2904–2909.
11. Cohen SN, Chang AC, Boyer HW, Helling RB: **Construction of biologically functional bacterial plasmids in vitro.** *Proc Natl Acad Sci U S A* 1973, **70**:3240–3244.
12. Cohen SN: **DNA cloning: A personal view after 40 years.** *Proc Natl Acad Sci* 2013, **110**:15521–15529.
13. Hamilton DL, Abremski K: **Site-specific recombination by the bacteriophage P1 lox-Cre system: Cre-mediated synapsis of two lox sites.** *J Mol Biol* 1984, **178**:481–486.
14. Abremski K, Hoess R: **Bacteriophage P1 site-specific recombination. Purification and properties of the Cre recombinase protein.** *J Biol Chem* 1984, **259**:1509–1514.
15. Nagy A: **Cre recombinase: the universal reagent for genome tailoring.** *genesis* 2000, **26**:99–109.
16. Kleppe K, Ohtsuka E, Kleppe R, Molineux I, Khorana HG: **Studies on polynucleotides. XCVI. Repair replications of short synthetic DNA's as catalyzed by DNA polymerases.** *J Mol Biol* 1971, **56**:341–361.
17. Templeton NS: **The polymerase chain reaction. History, methods, and applications.** *Diagnostic Mol Pathol Am J Surg Pathol part B* 1992, **1**:58–72.
18. Gibson DG, Young L, Chuang R-Y, Venter JC, Hutchison CA, Smith HO: **Enzymatic assembly of DNA molecules up to several hundred kilobases.** *Nat Methods* 2009, **6**:343–345.
19. Rosano GL, Ceccarelli EA: **Recombinant protein expression in Escherichia coli: advances and challenges.** *Front Microbiol* 2014, **5**:172.
20. Possee RD: **Baculoviruses as expression vectors.** *Curr Opin Biotechnol* 1997, **8**:569–572.

References

21. Kost TA, Condreay JP, Jarvis DL: **Baculovirus as versatile vectors for protein expression in insect and mammalian cells.** *Nat Biotechnol* 2005, **23**:567–575.
22. Luckow VA, Lee SC, Barry GF, Olins PO: **Efficient generation of infectious recombinant baculoviruses by site-specific transposon-mediated insertion of foreign genes into a baculovirus genome propagated in Escherichia coli.** *J Virol* 1993, **67**:4566–4579.
23. Airene KJ, Peltomaa E, Hytönen VP, Laitinen OH, Ylä-Herttuala S: **Improved generation of recombinant baculovirus genomes in Escherichia coli.** *Nucleic Acids Res* 2003, **31**:e101–e101.
24. Laitinen OH, Airene KJ, Hytönen VP, Peltomaa E, Mähönen AJ, Wirth T, Lind MM, Mäkelä KA, Toivanen PI, Schenkwein D, et al.: **A multipurpose vector system for the screening of libraries in bacteria, insect and mammalian cells and expression in vivo.** *Nucleic Acids Res* 2005, **33**:e42.
25. Pijlman GP, van den Born E, Martens DE, Vlak JM: **Autographa californica Baculoviruses with Large Genomic Deletions Are Rapidly Generated in Infected Insect Cells.** *Virology* 2001, **283**:132–138.
26. Pijlman GP, van Schijndel JE, Vlak JM: **Spontaneous excision of BAC vector sequences from bacmid-derived baculovirus expression vectors upon passage in insect cells.** *J Gen Virol* 2003, **84**:2669–2678.
27. Berger I, Fitzgerald DJ, Richmond TJ: **Baculovirus expression system for heterologous multiprotein complexes.** *Nat Biotechnol* 2004, **22**:1583–1587.
28. Fitzgerald DJ, Berger P, Schaffitzel C, Yamada K, Richmond TJ, Berger I: **Protein complex expression by using multigene baculoviral vectors.** *Nat Methods* 2006, **3**:1021–1032.
29. Trowitzsch S, Bieniossek C, Nie Y, Garzoni F, Berger I: **New baculovirus expression tools for recombinant protein complex production.** *J Struct Biol* 2010, **172**:45–54.
30. Weissmann F, Petzold G, VanderLinden R, Huis in 't Veld PJ, Brown NG, Lampert F, Westermann S, Stark H, Schulman BA, Peters J-M: **biGBac enables rapid gene assembly for the expression of large multisubunit protein complexes.** *Proc Natl Acad Sci* 2016, **113**:E2564–E2569.
31. Bieniossek C, Imasaki T, Takagi Y, Berger I: **MultiBac: expanding the research toolbox for multiprotein complexes.** *Trends Biochem Sci* 2012, **37**:49–57.
32. Young CL, Britton ZT, Robinson AS: **Recombinant protein expression and purification: A comprehensive review of affinity tags and microbial applications.** *Biotechnol J* 2012, **7**:620–634.
33. Willhoft O, Bythell-Douglas R, McCormack EA, Wigley DB: **Synergy and antagonism in regulation of recombinant human INO80 chromatin remodeling complex.** *Nucleic Acids Res* 2016, **44**:8179–8188.
34. Eustermann S, Schall K, Kostrewa D, Lakomek K, Strauss M, Moldt M, Hopfner K-P: **Structural basis for ATP-dependent chromatin remodelling by the INO80 complex.** *Nature* 2018, **556**:386–390.
35. Liu P, Zupa E, Neuner A, Böhlér A, Loerke J, Flemming D, Ruppert T, Rudack T, Peter C, Spahn C, et al.: **Insights into the assembly and activation of the microtubule nucleator γ -TuRC.** *Nature* 2019, doi:10.1038/s41586-019-1896-6.
36. Consolati T, Locke J, Roostalu J, Chen ZA, Gannon J, Asthana J, Lim WM, Martino F, Cvetkovic MA, Rappsilber J, et al.: **Microtubule Nucleation Properties of Single Human γ -TuRCs Explained by Their Cryo-EM Structure.** *Dev Cell* 2020, doi:10.1016/j.devcel.2020.04.019.

References

37. Wieczorek M, Urnavicius L, Ti S-C, Molloy KR, Chait BT, Kapoor TM: **Asymmetric Molecular Architecture of the Human γ -Tubulin Ring Complex**. *Cell* 2020, **180**:165-175.e16.
38. Olins AL, Olins DE: **Spheroid chromatin units (ν bodies)**. *Science* 1974, **183**:330-332.
39. Kornberg RD: **Chromatin structure: a repeating unit of histones and DNA**. *Science* 1974, **184**:868-871.
40. Barreto-Vieira DF, Barth OM: **Negative and Positive Staining in Transmission Electron Microscopy for Virus Diagnosis**. In Edited by Shah MM. IntechOpen; 2015:Ch. 3.
41. Adrian M, Dubochet J, Lepault J, McDowell AW: **Cryo-electron microscopy of viruses**. *Nature* 1984, **308**:32-36.
42. Dubochet J, McDowell AW: **VITRIFICATION OF PURE WATER FOR ELECTRON MICROSCOPY**. *J Microsc* 1981, **124**:3-4.
43. Kühlbrandt W: **Biochemistry. The resolution revolution**. *Science* 2014, **343**:1443-1444.
44. Amunts A, Brown A, Bai X-C, Llácer JL, Hussain T, Emsley P, Long F, Murshudov G, Scheres SHW, Ramakrishnan V: **Structure of the yeast mitochondrial large ribosomal subunit**. *Science* 2014, **343**:1485-1489.
45. Faruqi AR, Henderson R: **Electronic detectors for electron microscopy**. *Curr Opin Struct Biol* 2007, **17**:549-555.
46. Scheres SHW: **RELION: implementation of a Bayesian approach to cryo-EM structure determination**. *J Struct Biol* 2012, **180**:519-530.
47. Wagner T, Merino F, Stabrin M, Moriya T, Antoni C, Apelbaum A, Hagel P, Sitsel O, Raisch T, Prumbaum D, et al.: **SPHIRE-crYOLO is a fast and accurate fully automated particle picker for cryo-EM**. *Commun Biol* 2019, **2**:218.
48. Punjani A, Rubinstein JL, Fleet DJ, Brubaker MA: **cryoSPARC: algorithms for rapid unsupervised cryo-EM structure determination**. *Nat Methods* 2017, **14**:290-296.
49. Bepler T, Morin A, Rapp M, Brasch J, Shapiro L, Noble AJ, Berger B: **Positive-unlabeled convolutional neural networks for particle picking in cryo-electron micrographs**. *Nat Methods* 2019, **16**:1153-1160.
50. Yip KM, Fischer N, Paknia E, Chari A, Stark H: **Atomic-resolution protein structure determination by cryo-EM**. *Nature* 2020, **587**:157-161.
51. Nakane T, Kotecha A, Sente A, McMullan G, Masiulis S, Brown PMGE, Grigoras IT, Malinauskaitė L, Malinauskas T, Miehl J, et al.: **Single-particle cryo-EM at atomic resolution**. *Nature* 2020, **587**:152-156.
52. Graziadei A, Rappsilber J: **Leveraging crosslinking mass spectrometry in structural and cell biology**. *Structure* 2022, **30**:37-54.
53. O'Reilly FJ, Rappsilber J: **Cross-linking mass spectrometry: methods and applications in structural, molecular and systems biology**. *Nat Struct Mol Biol* 2018, **25**:1000-1008.
54. Fischer L, Rappsilber J: **Quirks of Error Estimation in Cross-Linking/Mass Spectrometry**. *Anal Chem* 2017, **89**:3829-3833.
55. Kim SJ, Fernandez-Martinez J, Nudelman I, Shi Y, Zhang W, Raveh B, Herricks T, Slaughter BD, Hogan JA, Upla P, et al.: **Integrative structure and functional anatomy of a nuclear pore complex**. *Nature* 2018, **555**:475-482.

References

56. Yan K, Yang J, Zhang Z, McLaughlin SH, Chang L, Fasci D, Ehrenhofer-Murray AE, Heck AJR, Barford D: **Structure of the inner kinetochore CCAN complex assembled onto a centromeric nucleosome.** *Nature* 2019, **574**:278–282.
57. Chen JWC, Chen ZA, Rogala KB, Metz J, Deane CM, Rappsilber J, Wakefield JG: **Cross-linking mass spectrometry identifies new interfaces of Augmin required to localise the gamma-tubulin ring complex to the mitotic spindle.** *Biol Open* 2017, **6**:654–663.
58. Jumper J, Evans R, Pritzel A, Green T, Figurnov M, Ronneberger O, Tunyasuvunakool K, Bates R, Žídek A, Potapenko A, et al.: **Highly accurate protein structure prediction with AlphaFold.** *Nature* 2021, doi:10.1038/s41586-021-03819-2.
59. Baek M, DiMaio F, Anishchenko I, Dauparas J, Ovchinnikov S, Lee GR, Wang J, Cong Q, Kinch LN, Schaeffer RD, et al.: **Accurate prediction of protein structures and interactions using a three-track neural network.** *Science (80-)* 2021, doi:10.1126/science.abj8754.
60. Evans R, O'Neill M, Pritzel A, Antropova N, Senior A, Green T, Žídek A, Bates R, Blackwell S, Yim J, et al.: **Protein complex prediction with AlphaFold-Multimer.** *bioRxiv* 2022, doi:10.1101/2021.10.04.463034.
61. Pietro F, Ying D, Xiong P, B. TA, W. HC, Longfei W, Tian-Min F, Carlos B, Hao W: **Structure of cytoplasmic ring of nuclear pore complex by integrative cryo-EM and AlphaFold.** *Science (80-)* 2022, **376**:eabm9326.
62. Shyamal M, Agnieszka O-K, Marc S, Reiya T, Beata T, E. ZC, Katarzyna B, H. SF, Erica M, Marie-Therese M, et al.: **AI-based structure prediction empowers integrative structural analysis of human nuclear pores.** *Science (80-)* 2022, **376**:eabm9506.
63. Akdel M, Pires DE V, Pardo EP, Jänes J, Zalevsky AO, Mészáros B, Bryant P, Good LL, Laskowski RA, Pozzati G, et al.: **A structural biology community assessment of AlphaFold2 applications.** *Nat Struct Mol Biol* 2022, **29**:1056–1067.
64. Ziemianowicz DS, Kosinski J: **New opportunities in integrative structural modeling.** *Curr Opin Struct Biol* 2022, **77**:102488.
65. Schrödinger E: *What is Life? The Physical Aspect of the Living Cell.* Cambridge University Press; 1944.
66. Schrödinger E: *What is Life?: With Mind and Matter and Autobiographical Sketches.* Cambridge University Press; 1992.
67. Mojzsis SJ, Arrhenius G, McKeegan KD, Harrison TM, Nutman AP, Friend CRL: **Evidence for life on Earth before 3,800 million years ago.** *Nature* 1996, **384**:55–59.
68. Pross A, Pascal R: **The origin of life: what we know, what we can know and what we will never know.** *Open Biol* 2022, **3**:120190.
69. Kitadai N, Maruyama S: **Origins of building blocks of life: A review.** *Geosci Front* 2018, **9**:1117–1153.
70. Woese CR, Kandler O, Wheelis ML: **Towards a natural system of organisms: proposal for the domains Archaea, Bacteria, and Eucarya.** *Proc Natl Acad Sci U S A* 1990, **87**:4576–4579.
71. Eme L, Spang A, Lombard J, Stairs CW, Ettema TJG: **Archaea and the origin of eukaryotes.** *Nat Rev Microbiol* 2017, **15**:711–723.
72. Dominguez R, Holmes KC: **Actin structure and function.** *Annu Rev Biophys* 2011, **40**:169–186.

References

73. Pollard TD, Cooper JA: **Actin, a central player in cell shape and movement.** *Science* 2009, **326**:1208–1212.
74. Pollard TD, Borisy GG: **Cellular motility driven by assembly and disassembly of actin filaments.** *Cell* 2003, **112**:453–465.
75. Goley ED, Welch MD: **The ARP2/3 complex: an actin nucleator comes of age.** *Nat Rev Mol Cell Biol* 2006, **7**:713–726.
76. Steinert PM, Roop DR: **Molecular and cellular biology of intermediate filaments.** *Annu Rev Biochem* 1988, **57**:593–625.
77. Fuchs E, Weber K: **Intermediate filaments: structure, dynamics, function, and disease.** *Annu Rev Biochem* 1994, **63**:345–382.
78. Aebi U, Cohn J, Buhle L, Gerace L: **The nuclear lamina is a meshwork of intermediate-type filaments.** *Nature* 1986, **323**:560–564.
79. Taheri F, Isbilir B, Müller G, Krieger JW, Chirico G, Langowski J, Tóth K: **Random Motion of Chromatin Is Influenced by Lamin A Interconnections.** *Biophys J* 2018, **114**:2465–2472.
80. Borisy GG, Taylor EW: **The mechanism of action of colchicine. Colchicine binding to sea urchin eggs and the mitotic apparatus.** *J Cell Biol* 1967, **34**:535–548.
81. Weisenberg RC, Borisy GG, Taylor EW: **The colchicine-binding protein of mammalian brain and its relation to microtubules.** *Biochemistry* 1968, **7**:4466–4479.
82. Ledbetter MC, Porter KR: **A “MICROTUBULE” IN PLANT CELL FINE STRUCTURE.** *J Cell Biol* 1963, **19**:239–250.
83. Desai A, Mitchison TJ: **Microtubule polymerization dynamics.** *Annu Rev Cell Dev Biol* 1997, **13**:83–117.
84. Downing KH, Nogales E: **Tubulin and microtubule structure.** *Curr Opin Cell Biol* 1998, **10**:16–22.
85. Gestaut D, Zhao Y, Park J, Ma B, Leitner A, Collier M, Pintilie G, Roh S-H, Chiu W, Frydman J: **Structural visualization of the tubulin folding pathway directed by human chaperonin TRiC/CCT.** *Cell* 2022, **185**:4770–4787.e20.
86. Kelly JJ, Tranter D, Pardon E, Chi G, Kramer H, Happonen L, Knee KM, Janz JM, Steyaert J, Bulawa C, et al.: **Snapshots of actin and tubulin folding inside the TRiC chaperonin.** *Nat Struct Mol Biol* 2022, **29**:420–429.
87. Tian G, Cowan NJ: **Chapter 11 - Tubulin-Specific Chaperones: Components of a Molecular Machine That Assembles the α/β Heterodimer.** In *Microtubules*, . Edited by Correia JJ, Wilson LBT-M in CB. Academic Press; 2013:155–171.
88. Cowan NJ, Lewis S: **Type II chaperonins, prefoldin, and the tubulin-specific chaperones.** In *Protein Folding in the Cell*. . Academic Press; 2001:73–104.
89. Pierson GB, Burton PR, Himes RH: **Alterations in number of protofilaments in microtubules assembled in vitro.** *J Cell Biol* 1978, **76**:223–228.
90. Tilney LG, Bryan J, Bush DJ, Fujiwara K, Mooseker MS, Murphy DB, Snyder DH: **Microtubules: evidence for 13 protofilaments.** *J Cell Biol* 1973, **59**:267–275.
91. Guyomar C, Bousquet C, Ku S, Heumann JM, Guilloux G, Gaillard N, Heichette C, Duchesne L, Steinmetz MO, Gibeaux R, et al.: **Changes in seam number and location induce holes within microtubules assembled from porcine brain tubulin and in *Xenopus* egg cytoplasmic extracts.**

References

- Elife* 2022, **11**:e83021.
92. Manka SW, Moores CA: **The role of tubulin-tubulin lattice contacts in the mechanism of microtubule dynamic instability.** *Nat Struct Mol Biol* 2018, **25**:607–615.
 93. Mitchison TJ: **Localization of an exchangeable GTP binding site at the plus end of microtubules.** *Science* 1993, **261**:1044–1047.
 94. Nogales E, Wolf SG, Downing KH: **Structure of the $\alpha\beta$ tubulin dimer by electron crystallography.** *Nature* 1998, **391**:199–203.
 95. Nogales E, Whittaker M, Milligan RA, Downing KH: **High-Resolution Model of the Microtubule.** *Cell* 1999, **96**:79–88.
 96. Carlier MF, Pantaloni D: **Kinetic analysis of guanosine 5'-triphosphate hydrolysis associated with tubulin polymerization.** *Biochemistry* 1981, **20**:1918–1924.
 97. Alushin GM, Lander GC, Kellogg EH, Zhang R, Baker D, Nogales E: **High-Resolution Microtubule Structures Reveal the Structural Transitions in $\alpha\beta$ -Tubulin upon GTP Hydrolysis.** *Cell* 2014, **157**:1117–1129.
 98. Mitchison T, Kirschner M: **Dynamic instability of microtubule growth.** *Nature* 1984, **312**:237–242.
 99. Ludueña RF: **Chapter Two - A Hypothesis on the Origin and Evolution of Tubulin.** In Edited by Jeon KWBT-IR of C and MB. Academic Press; 2013:41–185.
 100. Snustad DP, Haas NA, Kopczak SD, Silflow CD: **The small genome of Arabidopsis contains at least nine expressed beta-tubulin genes.** *Plant Cell* 1992, **4**:549–556.
 101. Kopczak SD, Haas NA, Hussey PJ, Silflow CD, Snustad DP: **The small genome of Arabidopsis contains at least six expressed alpha-tubulin genes.** *Plant Cell* 1992, **4**:539–547.
 102. Hashimoto T: **Microtubules in plants.** *Arab B* 2015, **13**:e0179.
 103. Roll-Mecak A: **The Tubulin Code in Microtubule Dynamics and Information Encoding.** *Dev Cell* 2020, **54**:7–20.
 104. Jonasson EM, Mauro AJ, Li C, Labuz EC, Mahserejian SM, Scripture JP, Gregoretti I V, Alber M, Goodson H V: **Behaviors of individual microtubules and microtubule populations relative to critical concentrations: dynamic instability occurs when critical concentrations are driven apart by nucleotide hydrolysis.** *Mol Biol Cell* 2020, **31**:589–618.
 105. Kapitein LC, Hoogenraad CC: **Building the Neuronal Microtubule Cytoskeleton.** *Neuron* 2015, **87**:492–506.
 106. Kiewisz R, Fabig G, Conway W, Baum D, Needleman D, Müller-Reichert T: **Three-dimensional structure of kinetochore-fibers in human mitotic spindles.** *Elife* 2022, **11**:e75459.
 107. Brouhard GJ, Rice LM: **Microtubule dynamics: an interplay of biochemistry and mechanics.** *Nat Rev Mol Cell Biol* 2018, **19**:451–463.
 108. Bodakuntla S, Jijumon AS, Villablanca C, Gonzalez-Billault C, Janke C: **Microtubule-Associated Proteins: Structuring the Cytoskeleton.** *Trends Cell Biol* 2019, **29**:804–819.
 109. Vitre B, Coquelle FM, Heichette C, Garnier C, Chrétien D, Arnal I: **EB1 regulates microtubule dynamics and tubulin sheet closure in vitro.** *Nat Cell Biol* 2008, **10**:415–421.
 110. Oakley CE, Oakley BR: **Identification of gamma-tubulin, a new member of the tubulin superfamily encoded by mipA gene of Aspergillus nidulans.** *Nature* 1989, **338**:662–664.
 111. Böhler A, Vermeulen BJA, Würtz M, Zupa E, Pfeffer S, Schiebel E: **The gamma-tubulin ring**

References

- complex: Deciphering the molecular organization and assembly mechanism of a major vertebrate microtubule nucleator.** *BioEssays* 2021, n/a:2100114.
112. Wise DO, Krahe R, Oakley BR: **The γ -Tubulin Gene Family in Humans.** *Genomics* 2000, **67**:164–170.
113. Sulimenko V, Dráberová E, Dráber P: **γ -Tubulin in microtubule nucleation and beyond.** *Front cell Dev Biol* 2022, **10**:880761.
114. Findeisen P, Mühlhausen S, Dempewolf S, Hertzog J, Zietlow A, Carlomagno T, Kollmar M: **Six subgroups and extensive recent duplications characterize the evolution of the eukaryotic tubulin protein family.** *Genome Biol Evol* 2014, **6**:2274–2288.
115. Spang A, Geissler S, Grein K, Schiebel E: **gamma-Tubulin-like Tub4p of *Saccharomyces cerevisiae* is associated with the spindle pole body substructures that organize microtubules and is required for mitotic spindle formation.** *J Cell Biol* 1996, **134**:429–441.
116. Horio T, Oakley BR: **Human gamma-tubulin functions in fission yeast.** *J Cell Biol* 1994, **126**:1465–1473.
117. Horio T, Oakley BR: **Expression of Arabidopsis gamma-tubulin in fission yeast reveals conserved and novel functions of gamma-tubulin.** *Plant Physiol* 2003, **133**:1926–1934.
118. Yuba-Kubo A, Kubo A, Hata M, Tsukita S: **Gene knockout analysis of two γ -tubulin isoforms in mice.** *Dev Biol* 2005, **282**:361–373.
119. Dráberová E, Sulimenko V, Vinopal S, Sulimenko T, Sládková V, D'Agostino L, Sobol M, Hozák P, Křen L, Katsetos CD, et al.: **Differential expression of human γ -tubulin isotypes during neuronal development and oxidative stress points to a γ -tubulin-2 prosurvival function.** *FASEB J Off Publ Fed Am Soc Exp Biol* 2017, **31**:1828–1846.
120. Murphy SM, Urbani L, Stearns T: **The mammalian gamma-tubulin complex contains homologues of the yeast spindle pole body components spc97p and spc98p.** *J Cell Biol* 1998, **141**:663–674.
121. Aldaz H, Rice LM, Stearns T, Agard DA: **Insights into microtubule nucleation from the crystal structure of human γ -tubulin.** *Nature* 2005, **435**:523–527.
122. Rice LM, Montabana EA, Agard DA: **The lattice as allosteric effector: structural studies of alphabeta- and gamma-tubulin clarify the role of GTP in microtubule assembly.** *Proc Natl Acad Sci U S A* 2008, **105**:5378–5383.
123. Gombos L, Neuner A, Berynskyy M, Fava LL, Wade RC, Sachse C, Schiebel E: **GTP regulates the microtubule nucleation activity of γ -tubulin.** *Nat Cell Biol* 2013, **15**:1317–1327.
124. Lindström L, Li T, Malycheva D, Kancharla A, Nilsson H, Vishnu N, Mulder H, Johansson M, Rosselló CA, Alvarado-Kristensson M: **The GTPase domain of gamma-tubulin is required for normal mitochondrial function and spatial organization.** *Commun Biol* 2018, **1**:37.
125. Stearns T, Evans L, Kirschner M: **Gamma-tubulin is a highly conserved component of the centrosome.** *Cell* 1991, **65**:825–836.
126. Zheng Y, Wong ML, Alberts B, Mitchison T: **Nucleation of microtubule assembly by a γ -tubulin-containing ring complex.** *Nature* 1995, **378**:578–583.
127. Knop M, Schiebel E: **Spc98p and Spc97p of the yeast gamma-tubulin complex mediate binding to the spindle pole body via their interaction with Spc110p.** *EMBO J* 1997, **16**:6985–6995.
128. Knop M, Pereira G, Geissler S, Grein K, Schiebel E: **The spindle pole body component Spc97p**

References

- interacts with the gamma-tubulin of *Saccharomyces cerevisiae* and functions in microtubule organization and spindle pole body duplication. *EMBO J* 1997, **16**:1550–1564.
129. Oegema K, Wiese C, Martin OC, Milligan RA, Iwamatsu A, Mitchison TJ, Zheng Y: **Characterization of two related *Drosophila* gamma-tubulin complexes that differ in their ability to nucleate microtubules.** *J Cell Biol* 1999, **144**:721–733.
130. Moritz M, Braunfeld MB, Guénebaut V, Heuser J, Agard DA: **Structure of the γ -tubulin ring complex: a template for microtubule nucleation.** *Nat Cell Biol* 2000, **2**:365–370.
131. Kollman JM, Zelter A, Muller EGD, Fox B, Rice LM, Davis TN, Agard DA: **The structure of the gamma-tubulin small complex: implications of its architecture and flexibility for microtubule nucleation.** *Mol Biol Cell* 2008, **19**:207–215.
132. Kollman JM, Polka JK, Zelter A, Davis TN, Agard DA: **Microtubule nucleating γ -TuSC assembles structures with 13-fold microtubule-like symmetry.** *Nature* 2010, **466**:879–882.
133. Wiese C, Zheng Y: **A new function for the γ -tubulin ring complex as a microtubule minus-end cap.** *Nat Cell Biol* 2000, **2**:358–364.
134. Brilot AF, Lyon AS, Zelter A, Viswanath S, Maxwell A, MacCoss MJ, Muller EG, Sali A, Davis TN, Agard DA: **CM1-driven assembly and activation of yeast γ -tubulin small complex underlies microtubule nucleation.** *Elife* 2021, **10**:e65168.
135. Zupa E, Zheng A, Neuner A, Würtz M, Liu P, Böhler A, Schiebel E, Pfeffer S: **The cryo-EM structure of a γ -TuSC elucidates architecture and regulation of minimal microtubule nucleation systems.** *Nat Commun* 2020, **11**:5705.
136. Murphy SM, Preble AM, Patel UK, O'Connell KL, Dias DP, Moritz M, Agard D, Stults JT, Stearns T: **GCP5 and GCP6: two new members of the human gamma-tubulin complex.** *Mol Biol Cell* 2001, **12**:3340–3352.
137. Guillet V, Knibiehler M, Gregory-Pauron L, Remy M-H, Chemin C, Raynaud-Messina B, Bon C, Kollman JM, Agard DA, Merdes A, et al.: **Crystal structure of γ -tubulin complex protein GCP4 provides insight into microtubule nucleation.** *Nat Struct Mol Biol* 2011, **18**:915–919.
138. Gunawardane RN, Martin OC, Cao K, Zhang L, Dej K, Iwamatsu A, Zheng Y: **Characterization and reconstitution of *Drosophila* gamma-tubulin ring complex subunits.** *J Cell Biol* 2000, **151**:1513–1524.
139. Gunawardane RN, Martin OC, Zheng Y: **Characterization of a new gammaTuRC subunit with WD repeats.** *Mol Biol Cell* 2003, **14**:1017–1026.
140. Haren L, Remy M-H, Bazin I, Callebaut I, Wright M, Merdes A: **NEDD1-dependent recruitment of the γ -tubulin ring complex to the centrosome is necessary for centriole duplication and spindle assembly.** *J Cell Biol* 2006, **172**:505–515.
141. Luders J, Patel UK, Stearns T: **GCP-WD is a gamma-tubulin targeting factor required for centrosomal and chromatin-mediated microtubule nucleation.** *Nat Cell Biol* 2006, **8**:137–147.
142. Kumar S, Tomooka Y, Noda M: **Identification of a set of genes with developmentally down-regulated expression in the mouse brain.** *Biochem Biophys Res Commun* 1992, **185**:1155–1161.
143. Kumar S, Matsuzaki T, Yoshida Y, Noda M: **Molecular cloning and biological activity of a novel developmentally regulated gene encoding a protein with beta-transducin-like structure.** *J Biol Chem* 1994, **269**:11318–11326.

References

144. Zeng CJT, Lee Y-RJ, Liu B: **The WD40 repeat protein NEDD1 functions in microtubule organization during cell division in Arabidopsis thaliana.** *Plant Cell* 2009, **21**:1129–1140.
145. Hutchins JRA, Toyoda Y, Hegemann B, Poser I, Heriche J-K, Sykora MM, Augsburg M, Hudecz O, Buschhorn BA, Bulkescher J, et al.: **Systematic analysis of human protein complexes identifies chromosome segregation proteins.** *Science* 2010, **328**:593–599.
146. Lin T, Neuner A, Schiebel E: **Targeting of gamma-tubulin complexes to microtubule organizing centers: conservation and divergence.** *Trends Cell Biol* 2015, **25**:296–307.
147. Teixidó-Travesa N, Villén J, Lacasa C, Bertran MT, Archinti M, Gygi SP, Caelles C, Roig J, Lüders J: **The gammaTuRC revisited: a comparative analysis of interphase and mitotic human gammaTuRC redefines the set of core components and identifies the novel subunit GCP8.** *Mol Biol Cell* 2010, **21**:3963–3972.
148. Choi Y-K, Liu P, Sze SK, Dai C, Qi RZ: **CDK5RAP2 stimulates microtubule nucleation by the gamma-tubulin ring complex.** *J Cell Biol* 2010, **191**:1089–1095.
149. Liu P, Würtz M, Zupa E, Pfeffer S, Schiebel E: **Microtubule nucleation: The waltz between γ -tubulin ring complex and associated proteins.** *Curr Opin Cell Biol* 2020, **68**:124–131.
150. Wieczorek M, Huang T-L, Urnavicius L, Hsia K-C, Kapoor TM: **MZT Proteins Form Multi-Faceted Structural Modules in the γ -Tubulin Ring Complex.** *Cell Rep* 2020, **31**:107791.
151. Cota RR, Teixidó-Travesa N, Ezquerro A, Eibes S, Lacasa C, Roig J, Lüders J: **MZT1 regulates microtubule nucleation by linking γ TuRC assembly to adapter-mediated targeting and activation.** *J Cell Sci* 2017, **130**:406–419.
152. Lin T, Neuner A, Flemming D, Liu P, Chinen T, Jäkle U, Arkowitz R, Schiebel E: **MOZART1 and γ -tubulin complex receptors are both required to turn γ -TuSC into an active microtubule nucleation template.** *J Cell Biol* 2016, **215**:823–840.
153. Huang T-L, Wang H-J, Chang Y-C, Wang S-W, Hsia K-C: **Promiscuous Binding of Microprotein Mozart1 to γ -Tubulin Complex Mediates Specific Subcellular Targeting to Control Microtubule Array Formation.** *Cell Rep* 2020, **31**:107836.
154. Zupa E, Liu P, Würtz M, Schiebel E, Pfeffer S: **The structure of the γ -TuRC: a 25-years-old molecular puzzle.** *Curr Opin Struct Biol* 2020, **66**:15–21.
155. Urnavicius L, Zhang K, Diamant AG, Motz C, Schlager MA, Yu M, Patel NA, Robinson C V, Carter AP: **The structure of the dynactin complex and its interaction with dynein.** *Science* 2015, **347**:1441–1446.
156. Qu K, Chen K, Wang H, Li X, Chen Z: **Structure of the NuA4 acetyltransferase complex bound to the nucleosome.** *Nature* 2022, doi:10.1038/s41586-022-05303-x.
157. Nguyen VQ, Ranjan A, Stengel F, Wei D, Aebersold R, Wu C, Leschziner AE: **Molecular Architecture of the ATP-Dependent Chromatin-Remodeling Complex SWR1.** *Cell* 2013, **154**:1220–1231.
158. Nejedlá M, Klebanovych A, Sulimenko V, Sulimenko T, Dráberová E, Dráber P, Karlsson R: **The actin regulator profilin 1 is functionally associated with the mammalian centrosome.** *Life Sci Alliance* 2021, **4**:e202000655.
159. Farina F, Ramkumar N, Brown L, Samandar Eweis D, Anstatt J, Waring T, Bithell J, Scita G, They M, Blanchoin L, et al.: **Local actin nucleation tunes centrosomal microtubule nucleation during passage through mitosis.** *EMBO J* 2019, **38**:e99843.

References

160. Farina F, Gaillard J, Guérin C, Couté Y, Sillibourne J, Blanchoin L, Théry M: **The centrosome is an actin-organizing centre.** *Nat Cell Biol* 2016, **18**:65–75.
161. Paul DM, Mantell J, Borucu U, Coombs J, SurrIDGE KJ, Squire JM, Verkade P, Dodding MP: **In situ cryo-electron tomography reveals filamentous actin within the microtubule lumen.** *J Cell Biol* 2020, **219**.
162. Haren L, Farache D, Emorine L, Merdes A: **A stable core of GCPs 4, 5 and 6 promotes the assembly of γ -tubulin ring complexes.** *J Cell Sci* 2020, doi:10.1242/jcs.244368.
163. Tsuchiya K, Goshima G: **Microtubule-associated proteins promote microtubule generation in the absence of γ -tubulin in human colon cancer cells.** *J Cell Biol* 2021, **220**:e202104114.
164. Zhang J, Megraw TL: **Proper recruitment of gamma-tubulin and D-TACC/Msps to embryonic Drosophila centrosomes requires Centrosomin Motif 1.** *Mol Biol Cell* 2007, **18**:4037–4049.
165. Sawin KE, Lourenco PCC, Snaith HA: **Microtubule Nucleation at Non-Spindle Pole Body Microtubule-Organizing Centers Requires Fission Yeast Centrosomin-Related Protein mod20p.** *Curr Biol* 2004, **14**:763–775.
166. Lin T, Neuner A, Schlosser YT, Scharf AND, Weber L, Schiebel E: **Cell-cycle dependent phosphorylation of yeast pericentrin regulates γ -TuSC-mediated microtubule nucleation.** *Elife* 2014, **3**:e02208.
167. Fong K-W, Choi Y-K, Rattner JB, Qi RZ: **CDK5RAP2 is a pericentriolar protein that functions in centrosomal attachment of the gamma-tubulin ring complex.** *Mol Biol Cell* 2008, **19**:115–125.
168. Tovey CA, Conduit PT: **Microtubule nucleation by γ -tubulin complexes and beyond.** *Essays Biochem* 2018, **62**:765–780.
169. Alfaro-Aco R, Thawani A, Petry S: **Structural analysis of the role of TPX2 in branching microtubule nucleation.** *J Cell Biol* 2017, **216**:983–997.
170. Tovey CA, Tsuji C, Egerton A, Bernard F, Guichet A, de la Roche M, Conduit PT: **Autoinhibition of Cnn binding to γ -TuRCs prevents ectopic microtubule nucleation and cell division defects.** *J Cell Biol* 2021, **220**.
171. Gard DL, Kirschner MW: **A microtubule-associated protein from Xenopus eggs that specifically promotes assembly at the plus-end.** *J Cell Biol* 1987, **105**:2203–2215.
172. Gunzelmann J, Rütznick D, Lin T, Zhang W, Neuner A, Jäkle U, Schiebel E: **The microtubule polymerase Stu2 promotes oligomerization of the γ -TuSC for cytoplasmic microtubule nucleation.** *Elife* 2018, **7**:e39932.
173. Flor-Parra I, Iglesias-Romero AB, Chang F: **The XMAP215 Ortholog Alp14 Promotes Microtubule Nucleation in Fission Yeast.** *Curr Biol* 2018, **28**:1681-1691.e4.
174. Thawani A, Kadzik RS, Petry S: **XMAP215 is a microtubule nucleation factor that functions synergistically with the gamma-tubulin ring complex.** *Nat Cell Biol* 2018, **20**:575–585.
175. Thawani A, Rale MJ, Coudray N, Bhabha G, Stone HA, Shaevitz JW, Petry S: **The transition state and regulation of γ -TuRC-mediated microtubule nucleation revealed by single molecule microscopy.** *Elife* 2020, **9**:e54253.
176. Gard DL, Becker BE, Josh Romney S: **MAPping the eukaryotic tree of life: structure, function, and evolution of the MAP215/Dis1 family of microtubule-associated proteins.** *Int Rev Cytol* 2004, **239**:179–272.

References

177. Liu P, Choi Y-K, Qi RZ: **NME7 is a functional component of the γ -tubulin ring complex.** *Mol Biol Cell* 2014, **25**:2017–2025.
178. Bornens M: **The centrosome in cells and organisms.** *Science* 2012, **335**:422–426.
179. Boveri T: *Ueber den Antheil des Spermatozoon an der Theilung des Eies.* Gesellschaft für Morphologie und Physiologie zu München; 1887.
180. Gall JG: **Early Studies on Centrioles and Centrosomes.** In *Centrosomes in Development and Disease.* . 2004:1–15.
181. Scheer U: **Historical roots of centrosome research: discovery of Boveri's microscope slides in Würzburg.** *Philos Trans R Soc London Ser B, Biol Sci* 2014, **369**.
182. Azimzadeh J, Marshall WF: **Building the centriole.** *Curr Biol* 2010, **20**:R816–25.
183. Gönczy P: **Towards a molecular architecture of centriole assembly.** *Nat Rev Mol Cell Biol* 2012, **13**:425–435.
184. Seeley ES, Nachury M V: **The perennial organelle: assembly and disassembly of the primary cilium.** *J Cell Sci* 2010, **123**:511–518.
185. Kurtulmus B, Yuan C, Schuy J, Neuner A, Hata S, Kalamakis G, Martin-Villalba A, Pereira G: **LRRC45 contributes to early steps of axoneme extension.** *J Cell Sci* 2018, **131**:jcs223594.
186. Bahe S, Stierhof Y-D, Wilkinson CJ, Leiss F, Nigg EA: **Rootletin forms centriole-associated filaments and functions in centrosome cohesion.** *J Cell Biol* 2005, **171**:27–33.
187. Vlijm R, Li X, Panic M, Rütznick D, Hata S, Herrmannsdörfer F, Kuner T, Heilemann M, Engelhardt J, Hell SW, et al.: **STED nanoscopy of the centrosome linker reveals a CEP68-organized, periodic rootletin network anchored to a C-Nap1 ring at centrioles.** *Proc Natl Acad Sci* 2018, **115**:E2246–E2253.
188. van Breugel M, Hirono M, Andreeva A, Yanagisawa H, Yamaguchi S, Nakazawa Y, Morgner N, Petrovich M, Ebong I-O, Robinson C V, et al.: **Structures of SAS-6 suggest its organization in centrioles.** *Science* 2011, **331**:1196–1199.
189. Banterle N, Nievergelt AP, de Buhr S, Hatzopoulos GN, Brillard C, Andany S, Hübscher T, Sorgenfrei FA, Schwarz US, Gräter F, et al.: **Kinetic and structural roles for the surface in guiding SAS-6 self-assembly to direct centriole architecture.** *Nat Commun* 2021, **12**:6180.
190. Habedanck R, Stierhof Y-D, Wilkinson CJ, Nigg EA: **The Polo kinase Plk4 functions in centriole duplication.** *Nat Cell Biol* 2005, **7**:1140–1146.
191. Gupta H, Rajeev R, Sasmal R, Radhakrishnan RM, Anand U, Chandran H, Aparna NR, Agasti S, Manna TK: **SAS-6 Association with γ -Tubulin Ring Complex Is Required for Centriole Duplication in Human Cells.** *Curr Biol* 2020, doi:10.1016/j.cub.2020.04.036.
192. Guichard P, Chrétien D, Marco S, Tassin A-M: **Procentriole assembly revealed by cryo-electron tomography.** *EMBO J* 2010, **29**:1565–1572.
193. Klena N, Le Guennec M, Tassin A-M, van den Hoek H, Erdmann PS, Schaffer M, Geimer S, Aeschlimann G, Kovacic L, Sadian Y, et al.: **Architecture of the centriole cartwheel-containing region revealed by cryo-electron tomography.** *EMBO J* 2020, **39**:e106246.
194. Chen F, Tillberg PW, Boyden ES: **Expansion microscopy.** *Science (80-)* 2015, **347**:543–548.
195. Wassie AT, Zhao Y, Boyden ES: **Expansion microscopy: principles and uses in biological research.** *Nat Methods* 2019, **16**:33–41.

References

196. Schweizer N, Haren L, Dutto I, Viais R, Lacasa C, Merdes A, Lüders J: **Sub-centrosomal mapping identifies augmin- γ TuRC as part of a centriole-stabilizing scaffold.** *Nat Commun* 2021, **12**:6042.
197. Azimzadeh J, Hergert P, Delouée A, Euteneuer U, Formstecher E, Khodjakov A, Bornens M: **hPOC5 is a centrin-binding protein required for assembly of full-length centrioles.** *J Cell Biol* 2009, **185**:101–114.
198. Lawo S, Hasegan M, Gupta GD, Pelletier L: **Subdiffraction imaging of centrosomes reveals higher-order organizational features of pericentriolar material.** *Nat Cell Biol* 2012, **14**:1148–1158.
199. Woodruff JB, Wueseke O, Hyman AA: **Pericentriolar material structure and dynamics.** *Philos Trans R Soc London Ser B, Biol Sci* 2014, **369**.
200. Moritz M, Braunfeld MB, Sedat JW, Alberts B, Agard DA: **Microtubule nucleation by γ -tubulin-containing rings in the centrosome.** *Nature* 1995, **378**:638–640.
201. Khodjakov A, Rieder CL: **The Sudden Recruitment of γ -Tubulin to the Centrosome at the Onset of Mitosis and Its Dynamic Exchange Throughout the Cell Cycle, Do Not Require Microtubules.** *J Cell Biol* 1999, **146**:585–596.
202. Zhu F, Lawo S, Bird A, Pinchev D, Ralph A, Richter C, Müller-Reichert T, Kittler R, Hyman AA, Pelletier L: **The mammalian SPD-2 ortholog Cep192 regulates centrosome biogenesis.** *Curr Biol* 2008, **18**:136–141.
203. Dichtenberg JB, Zimmerman W, Sparks CA, Young A, Vidair C, Zheng Y, Carrington W, Fay FS, Doxsey SJ: **Pericentrin and gamma-tubulin form a protein complex and are organized into a novel lattice at the centrosome.** *J Cell Biol* 1998, **141**:163–174.
204. Doxsey SJ, Stein P, Evans L, Calarco PD, Kirschner M: **Pericentrin, a highly conserved centrosome protein involved in microtubule organization.** *Cell* 1994, **76**:639–650.
205. Megraw TL, Li K, Kao LR, Kaufman TC: **The centrosomin protein is required for centrosome assembly and function during cleavage in *Drosophila*.** *Development* 1999, **126**:2829–2839.
206. Schweizer N, Lüders J: **From tip to toe – dressing centrioles in γ TuRC.** *J Cell Sci* 2021, **134**.
207. Gomez-Ferreria MA, Rath U, Buster DW, Chanda SK, Caldwell JS, Rines DR, Sharp DJ: **Human Cep192 is required for mitotic centrosome and spindle assembly.** *Curr Biol* 2007, **17**:1960–1966.
208. Joukov V, Walter JC, De Nicolo A: **The Cep192-Organized Aurora A-Plk1 Cascade Is Essential for Centrosome Cycle and Bipolar Spindle Assembly.** *Mol Cell* 2014, **55**:578–591.
209. Conduit PT, Brunk K, Dobbelaere J, Dix CI, Lucas EP, Raff JW: **Centrioles regulate centrosome size by controlling the rate of Cnn incorporation into the PCM.** *Curr Biol* 2010, **20**:2178–2186.
210. Chinen T, Yamazaki K, Hashimoto K, Fujii K, Watanabe K, Takeda Y, Yamamoto S, Nozaki Y, Tsuchiya Y, Takao D, et al.: **Centriole and PCM cooperatively recruit CEP192 to spindle poles to promote bipolar spindle assembly.** *J Cell Biol* 2021, **220**:e202006085.
211. O'Rourke BP, Gomez-Ferreria MA, Berk RH, Hackl AMU, Nicholas MP, O'Rourke SC, Pelletier L, Sharp DJ: **Cep192 Controls the Balance of Centrosome and Non-Centrosomal Microtubules during Interphase.** *PLoS One* 2014, **9**:e101001.
212. Muroyama A, Seldin L, Lechler T: **Divergent regulation of functionally distinct γ -tubulin complexes during differentiation.** *J Cell Biol* 2016, **213**:679–692.
213. Moudjou M, Bordes N, Paintrand M, Bornens M: **gamma-Tubulin in mammalian cells: the**

References

- centrosomal and the cytosolic forms. *J Cell Sci* 1996, **109** (Pt 4:875–887.**
214. Janson ME, Setty TG, Paoletti A, Tran PT: **Efficient formation of bipolar microtubule bundles requires microtubule-bound gamma-tubulin complexes. *J Cell Biol* 2005, **169**:297–308.**
215. Murata T, Sonobe S, Baskin TI, Hyodo S, Hasezawa S, Nagata T, Horio T, Hasebe M: **Microtubule-dependent microtubule nucleation based on recruitment of gamma-tubulin in higher plants. *Nat Cell Biol* 2005, **7**:961–968.**
216. O. WASTENEYS G, E. WILLIAMSON R: **Reassembly of microtubules in *Nitella tasmanica*: assembly of cortical microtubules in branching clusters and its relevance to steady-state microtubule assembly. *J Cell Sci* 1989, **93**:705–714.**
217. Goshima G, Wollman R, Goodwin SS, Zhang N, Scholey JM, Vale RD, Stuurman N: **Genes required for mitotic spindle assembly in *Drosophila* S2 cells. *Science* 2007, **316**:417–421.**
218. Kreis TE: **Role of microtubules in the organisation of the Golgi apparatus. *Cell Motil Cytoskeleton* 1990, **15**:67–70.**
219. Rivero S, Cardenas J, Bornens M, Rios RM: **Microtubule nucleation at the cis-side of the Golgi apparatus requires AKAP450 and GM130. *EMBO J* 2009, **28**:1016–1028.**
220. Sanders AAWM, Kaverina I: **Nucleation and Dynamics of Golgi-derived Microtubules. *Front Neurosci* 2015, **9**:431.**
221. Wang Z, Wu T, Shi L, Zhang L, Zheng W, Qu JY, Niu R, Qi RZ: **Conserved motif of CDK5RAP2 mediates its localization to centrosomes and the Golgi complex. *J Biol Chem* 2010, **285**:22658–22665.**
222. Miller PM, Folkmann AW, Maia ARR, Efimova N, Efimov A, Kaverina I: **Golgi-derived CLASP-dependent microtubules control Golgi organization and polarized trafficking in motile cells. *Nat Cell Biol* 2009, **11**:1069–1080.**
223. Batzenschlager M, Masoud K, Janski N, Houlné G, Herzog E, Evrard J-L, Baumberger N, Ehrardt M, Nominé Y, Kieffer B, et al.: **The GIP gamma-tubulin complex-associated proteins are involved in nuclear architecture in *Arabidopsis thaliana*.** *Front Plant Sci* 2013, **4**.
224. Stoppin V, Vantard M, Schmit AC, Lambert AM: **Isolated Plant Nuclei Nucleate Microtubule Assembly: The Nuclear Surface in Higher Plants Has Centrosome-like Activity. *Plant Cell* 1994, **6**:1099–1106.**
225. Tassin AM, Maro B, Bornens M: **Fate of microtubule-organizing centers during myogenesis in vitro. *J Cell Biol* 1985, **100**:35–46.**
226. Sanchez AD, Feldman JL: **Microtubule-organizing centers: from the centrosome to non-centrosomal sites. *Curr Opin Cell Biol* 2017, **44**:93–101.**
227. Byers B, Goetsch L: **Duplication of spindle plaques and integration of the yeast cell cycle. *Cold Spring Harb Symp Quant Biol* 1974, **38**:123–131.**
228. Rüttnick D, Schiebel E: **Duplication and Nuclear Envelope Insertion of the Yeast Microtubule Organizing Centre, the Spindle Pole Body. *Cells* 2018, **7**.**
229. Jaspersen SL, Winey M: **The budding yeast spindle pole body: structure, duplication, and function. *Annu Rev Cell Dev Biol* 2004, **20**:1–28.**
230. Cavanaugh AM, Jaspersen SL: **Big Lessons from Little Yeast: Budding and Fission Yeast Centrosome Structure, Duplication, and Function. *Annu Rev Genet* 2017, **51**:361–383.**

References

231. Knop M, Schiebel E: **Receptors determine the cellular localization of a γ -tubulin complex and thereby the site of microtubule formation.** *EMBO J* 1998, **17**:3952–3967.
232. Oakley BR, Oakley CE, Yoon Y, Jung MK: **Gamma-tubulin is a component of the spindle pole body that is essential for microtubule function in *Aspergillus nidulans*.** *Cell* 1990, **61**:1289–1301.
233. Wang T, Birsoy K, Hughes NW, Krupczak KM, Post Y, Wei JJ, Lander ES, Sabatini DM: **Identification and characterization of essential genes in the human genome.** *Science* 2015, **350**:1096–1101.
234. Funk L, Su K-C, Ly J, Feldman D, Singh A, Moodie B, Blainey PC, Cheeseman IM: **The phenotypic landscape of essential human genes.** *Cell* 2022, doi:10.1016/j.cell.2022.10.017.
235. Nigg EA: **Centrosome aberrations: cause or consequence of cancer progression?** *Nat Rev Cancer* 2002, **2**:815–825.
236. Dráberová E, D'Agostino L, Caracciolo V, Sládková V, Sulimenko T, Sulimenko V, Sobol M, Maounis NF, Tzelepis E, Mahera E, et al.: **Overexpression and Nucleolar Localization of γ -Tubulin Small Complex Proteins GCP2 and GCP3 in Glioblastoma.** *J Neuropathol Exp Neurol* 2015, **74**:723–742.
237. Godinho SA, Kwon M, Pellman D: **Centrosomes and cancer: how cancer cells divide with too many centrosomes.** *Cancer Metastasis Rev* 2009, **28**:85–98.
238. Gordon DJ, Resio B, Pellman D: **Causes and consequences of aneuploidy in cancer.** *Nat Rev Genet* 2012, **13**:189–203.
239. Bettencourt-Dias M, Hildebrandt F, Pellman D, Woods G, Godinho SA: **Centrosomes and cilia in human disease.** *Trends Genet* 2011, **27**:307–315.
240. Badano JL, Teslovich TM, Katsanis N: **The centrosome in human genetic disease.** *Nat Rev Genet* 2005, **6**:194–205.
241. Travis SM, Mahon BP, Petry S: **How Microtubules Build the Spindle Branch by Branch.** *Annu Rev Cell Dev Biol* 2022, doi:10.1146/annurev-cellbio-120420-114559.
242. Barbelanne M, Tsang WY: **Molecular and cellular basis of autosomal recessive primary microcephaly.** *Biomed Res Int* 2014, **2014**:547986.
243. Scheidecker S, Etard C, Haren L, Stoetzel C, Hull S, Arno G, Plagnol V, Drunat S, Passemard S, Toutain A, et al.: **Mutations in TUBGCP4 alter microtubule organization via the γ -tubulin ring complex in autosomal-recessive microcephaly with chorioretinopathy.** *Am J Hum Genet* 2015, **96**:666–674.
244. Maver A, Čuturilo G, Kovanda A, Miletić A, Peterlin B: **Rare missense TUBGCP5 gene variant in a patient with primary microcephaly.** *Eur J Med Genet* 2019, **62**:103598.
245. Gungor S, Oktay Y, Hiz S, Aranguren-Ibáñez Á, Kalafatcilar I, Yaramis A, Karaca E, Yis U, Sonmezler E, Ekinci B, et al.: **Autosomal recessive variants in TUBGCP2 alter the γ -tubulin ring complex leading to neurodevelopmental disease.** *iScience* 2021, **24**:101948.
246. Foster DA, Yellen P, Xu L, Saqcena M: **Regulation of G1 Cell Cycle Progression: Distinguishing the Restriction Point from a Nutrient-Sensing Cell Growth Checkpoint(s).** *Genes Cancer* 2010, **1**:1124–1131.
247. Hartwell LH, Mortimer RK, Culotti J, Culotti M: **Genetic Control of the Cell Division Cycle in Yeast: V. Genetic Analysis of cdc Mutants.** *Genetics* 1973, **74**:267–286.
248. Olsen J V, Vermeulen M, Santamaria A, Kumar C, Miller ML, Jensen LJ, Gnäd F, Cox J, Jensen TS,

References

- Nigg EA, et al.: **Quantitative Phosphoproteomics Reveals Widespread Full Phosphorylation Site Occupancy During Mitosis.** *Sci Signal* 2010, **3**:ra3–ra3.
249. Malumbres M: **Cyclin-dependent kinases.** *Genome Biol* 2014, **15**:122.
250. Glotzer M, Murray AW, Kirschner MW: **Cyclin is degraded by the ubiquitin pathway.** *Nature* 1991, **349**:132–138.
251. Kaldis P: **The cdk-activating kinase (CAK): from yeast to mammals.** *Cell Mol Life Sci* 1999, **55**:284–296.
252. Lim S, Kaldis P: **Cdks, cyclins and CKIs: roles beyond cell cycle regulation.** *Development* 2013, **140**:3079–3093.
253. Skowyra D, Craig KL, Tyers M, Elledge SJ, Harper JW: **F-box proteins are receptors that recruit phosphorylated substrates to the SCF ubiquitin-ligase complex.** *Cell* 1997, **91**:209–219.
254. Feldman RM, Correll CC, Kaplan KB, Deshaies RJ: **A complex of Cdc4p, Skp1p, and Cdc53p/cullin catalyzes ubiquitination of the phosphorylated CDK inhibitor Sic1p.** *Cell* 1997, **91**:221–230.
255. Patton EE, Willems AR, Tyers M: **Combinatorial control in ubiquitin-dependent proteolysis: don't Skp the F-box hypothesis.** *Trends Genet* 1998, **14**:236–243.
256. Peters J-M: **The anaphase promoting complex/cyclosome: a machine designed to destroy.** *Nat Rev Mol Cell Biol* 2006, **7**:644–656.
257. Chang L, Zhang Z, Yang J, McLaughlin SH, Barford D: **Molecular architecture and mechanism of the anaphase-promoting complex.** *Nature* 2014, **513**:388–393.
258. Nigg EA, Holland AJ: **Once and only once: mechanisms of centriole duplication and their deregulation in disease.** *Nat Rev Mol Cell Biol* 2018, **19**:297–312.
259. Fu J, Lipinszki Z, Rangone H, Min M, Mykura C, Chao-Chu J, Schneider S, Dzhindzhev NS, Gottardo M, Riparbelli MG, et al.: **Conserved molecular interactions in centriole-to-centrosome conversion.** *Nat Cell Biol* 2016, **18**:87–99.
260. Ohta M, Ashikawa T, Nozaki Y, Kozuka-Hata H, Goto H, Inagaki M, Oyama M, Kitagawa D: **Direct interaction of Plk4 with STIL ensures formation of a single procentriole per parental centriole.** *Nat Commun* 2014, **5**:5267.
261. Arquint C, Sonnen KF, Stierhof Y-D, Nigg EA: **Cell-cycle-regulated expression of STIL controls centriole number in human cells.** *J Cell Sci* 2012, **125**:1342–1352.
262. Agircan FG, Schiebel E, Mardin BR: **Separate to operate: control of centrosome positioning and separation.** *Philos Trans R Soc London Ser B, Biol Sci* 2014, **369**.
263. Levine AJ: **p53: 800 million years of evolution and 40 years of discovery.** *Nat Rev Cancer* 2020, **20**:471–480.
264. Baker SJ, Markowitz S, Fearon ER, Willson JK V, Vogelstein B: **Suppression of Human Colorectal Carcinoma Cell Growth by Wild-Type p53.** *Science (80-)* 1990, **249**:912–915.
265. Olivier M, Eeles R, Hollstein M, Khan MA, Harris CC, Hainaut P: **The IARC TP53 database: new online mutation analysis and recommendations to users.** *Hum Mutat* 2002, **19**:607–614.
266. Fischer M, Quaas M, Steiner L, Engeland K: **The p53-p21-DREAM-CDE/CHR pathway regulates G2/M cell cycle genes.** *Nucleic Acids Res* 2016, **44**:164–174.
267. El-Deiry WS, Tokino T, Velculescu VE, Levy DB, Parsons R, Trent JM, Lin D, Mercer WE, Kinzler KW, Vogelstein B: **WAF1, a potential mediator of p53 tumor suppression.** *Cell* 1993, **75**:817–825.

References

268. Xiong Y, Hannon GJ, Zhang H, Casso D, Kobayashi R, Beach D: **p21 is a universal inhibitor of cyclin kinases.** *Nature* 1993, **366**:701–704.
269. Engeland K: **Cell cycle regulation: p53-p21-RB signaling.** *Cell Death Differ* 2022, **29**:946–960.
270. Lohka MJ, Hayes MK, Maller JL: **Purification of maturation-promoting factor, an intracellular regulator of early mitotic events.** *Proc Natl Acad Sci U S A* 1988, **85**:3009–3013.
271. Nurse P, Thuriaux P: **Regulatory genes controlling mitosis in the fission yeast *Schizosaccharomyces pombe*.** *Genetics* 1980, **96**:627–637.
272. Gavet O, Pines J: **Progressive activation of CyclinB1-Cdk1 coordinates entry to mitosis.** *Dev Cell* 2010, **18**:533–543.
273. Gautier J, Minshull J, Lohka M, Glotzer M, Hunt T, Maller JL: **Cyclin is a component of maturation-promoting factor from *Xenopus*.** *Cell* 1990, **60**:487–494.
274. Gomez-Ferreria MA, Bashkurov M, Helbig AO, Larsen B, Pawson T, Gingras A-C, Pelletier L: **Novel NEDD1 phosphorylation sites regulate γ -tubulin binding and mitotic spindle assembly.** *J Cell Sci* 2012, **125**:3745–3751.
275. Haren L, Stearns T, Lüders J: **Plk1-dependent recruitment of gamma-tubulin complexes to mitotic centrosomes involves multiple PCM components.** *PLoS One* 2009, **4**:e5976.
276. Sdelci S, Schütz M, Pinyol R, Bertran MT, Regué L, Caelles C, Vernos I, Roig J: **Nek9 Phosphorylation of NEDD1/GCP-WD Contributes to Plk1 Control of γ -Tubulin Recruitment to the Mitotic Centrosome.** *Curr Biol* 2012, **22**:1516–1523.
277. Zhang X, Chen Q, Feng J, Hou J, Yang F, Liu J, Jiang Q, Zhang C: **Sequential phosphorylation of Nedd1 by Cdk1 and Plk1 is required for targeting of the gammaTuRC to the centrosome.** *J Cell Sci* 2009, **122**:2240–2251.
278. Joukov V, De Nicolo A: **Aurora-PLK1 cascades as key signaling modules in the regulation of mitosis.** *Sci Signal* 2018, **11**:1–26.
279. Park J-G, Jeon H, Shin S, Song C, Lee H, Kim N-K, Kim EE, Hwang KY, Lee B-J, Lee I-G: **Structural basis for CEP192-mediated regulation of centrosomal AURKA.** *Sci Adv* 2023, **9**:eadf8582.
280. Johmura Y, Soung N-K, Park J-E, Yu L-R, Zhou M, Bang JK, Kim B-Y, Veenstra TD, Erikson RL, Lee KS: **Regulation of microtubule-based microtubule nucleation by mammalian polo-like kinase 1.** *Proc Natl Acad Sci* 2011, **108**:11446 LP – 11451.
281. Beaudouin J, Gerlich D, Daigle N, Eils R, Ellenberg J: **Nuclear envelope breakdown proceeds by microtubule-induced tearing of the lamina.** *Cell* 2002, **108**:83–96.
282. Vale RD, Reese TS, Sheetz MP: **Identification of a novel force-generating protein, kinesin, involved in microtubule-based motility.** *Cell* 1985, **42**:39–50.
283. Hirokawa N, Noda Y, Tanaka Y, Niwa S: **Kinesin superfamily motor proteins and intracellular transport.** *Nat Rev Mol Cell Biol* 2009, **10**:682–696.
284. Roberts AJ, Kon T, Knight PJ, Sutoh K, Burgess SA: **Functions and mechanics of dynein motor proteins.** *Nat Rev Mol Cell Biol* 2013, **14**:713–726.
285. Gibbons IR, Rowe AJ: **Dynein: A Protein with Adenosine Triphosphatase Activity from Cilia.** *Science (80-)* 1965, **149**:424–426.
286. Goshima G, Vale RD: **The roles of microtubule-based motor proteins in mitosis: comprehensive RNAi analysis in the *Drosophila* S2 cell line.** *J Cell Biol* 2003, **162**:1003–1016.

References

287. Blangy A, Lane HA, d'Hérin P, Harper M, Kress M, Nigg EA: **Phosphorylation by p34cdc2 regulates spindle association of human Eg5, a kinesin-related motor essential for bipolar spindle formation in vivo.** *Cell* 1995, **83**:1159–1169.
288. Musacchio A, Desai A: **A Molecular View of Kinetochores Assembly and Function.** *Biology (Basel)* 2017, **6**.
289. Van Holde KE: *Chromatin*. Springer-Verlag; 1989.
290. Luger K, Mader AW, Richmond RK, Sargent DF, Richmond TJ: **Crystal structure of the nucleosome core particle at 2.8 Å resolution.** *Nature* 1997, **389**:251–260.
291. Jenuwein T, Allis CD: **Translating the Histone Code.** *Science (80-)* 2001, **293**:1074–1080.
292. Martire S, Banaszynski LA: **The roles of histone variants in fine-tuning chromatin organization and function.** *Nat Rev Mol Cell Biol* 2020, **21**:522–541.
293. Kinkade J, Cole R: **The resolution of four lysine-rich histones derived from calf thymus.** *J Biol Chem* 1966, **241**:
294. Bednar J, Garcia-Saez I, Boopathi R, Cutter AR, Papai G, Reymer A, Syed SH, Lone IN, Tonchev O, Crucifix C, et al.: **Structure and dynamics of a 197 base-pair nucleosome in complex with linker histone H1.** *Mol Cell* 2017, **66**:384–397.e8.
295. Carroll CW, Straight AF: **Centromere formation: from epigenetics to self-assembly.** *Trends Cell Biol* 2006, **16**:70–78.
296. Earnshaw WC, Rothfield N: **Identification of a family of human centromere proteins using autoimmune sera from patients with scleroderma.** *Chromosoma* 1985, **91**:313–321.
297. Stumme-Diers MP, Banerjee S, Hashemi M, Sun Z, Lyubchenko YL: **Nanoscale dynamics of centromere nucleosomes and the critical roles of CENP-A.** *Nucleic Acids Res* 2018, **46**:94–103.
298. Wei RR, Al-Bassam J, Harrison SC: **The Ndc80/HEC1 complex is a contact point for kinetochore-microtubule attachment.** *Nat Struct Mol Biol* 2007, **14**:54–59.
299. Ciferri C, Pasqualato S, Screpanti E, Varetti G, Santaguida S, Dos Reis G, Maiolica A, Polka J, De Luca JG, De Wulf P, et al.: **Implications for Kinetochore-Microtubule Attachment from the Structure of an Engineered Ndc80 Complex.** *Cell* 2008, **133**:427–439.
300. Wilson-Kubalek EM, Cheeseman IM, Yoshioka C, Desai A, Milligan RA: **Orientation and structure of the Ndc80 complex on the microtubule lattice.** *J Cell Biol* 2008, **182**:1055–1061.
301. Alushin GM, Ramey VH, Pasqualato S, Ball DA, Grigorieff N, Musacchio A, Nogales E: **The Ndc80 kinetochore complex forms oligomeric arrays along microtubules.** *Nature* 2010, **467**:805–810.
302. Alushin GM, Musinipally V, Matson D, Tooley J, Stukenberg PT, Nogales E: **Multimodal microtubule binding by the Ndc80 kinetochore complex.** *Nat Struct Mol Biol* 2012, **19**:1161–1167.
303. Magescas J, Zonka JC, Feldman JL: **A two-step mechanism for the inactivation of microtubule organizing center function at the centrosome.** *Elife* 2019, **8**.
304. Inoue D, Wittbrodt J, Gruss OJ: **Loss and Rebirth of the Animal Microtubule Organizing Center: How Maternal Expression of Centrosomal Proteins Cooperates with the Sperm Centriole in Zygotic Centrosome Reformation.** *Bioessays* 2018, **40**:e1700135.
305. Rosenblatt J: **Spindle assembly: asters part their separate ways.** *Nat Cell Biol* 2005, **7**:219–222.
306. Brinkley BR, Cartwright JJ: **Cold-labile and cold-stable microtubules in the mitotic spindle of mammalian cells.** *Ann N Y Acad Sci* 1975, **253**:428–439.

References

307. Zhai Y, Kronebusch PJ, Borisy GG: **Kinetochore microtubule dynamics and the metaphase-anaphase transition.** *J Cell Biol* 1995, **131**:721–734.
308. Kirschner M, Mitchison T: **Beyond self-assembly: from microtubules to morphogenesis.** *Cell* 1986, **45**:329–342.
309. Wollman R, Cytrynbaum EN, Jones JT, Meyer T, Scholey JM, Mogilner A: **Efficient chromosome capture requires a bias in the “search-and-capture” process during mitotic-spindle assembly.** *Curr Biol* 2005, **15**:828–832.
310. Heald R, Khodjakov A: **Thirty years of search and capture: The complex simplicity of mitotic spindle assembly.** *J Cell Biol* 2015, **211**:1103–1111.
311. Heald R, Tournebize R, Blank T, Sandaltzopoulos R, Becker P, Hyman A, Karsenti E: **Self-organization of microtubules into bipolar spindles around artificial chromosomes in *Xenopus* egg extracts.** *Nature* 1996, **382**:420–425.
312. Moore JD: **The Ran-GTPase and cell-cycle control.** *Bioessays* 2001, **23**:77–85.
313. Carazo-Salas RE, Guarguaglini G, Gruss OJ, Segref A, Karsenti E, Mattaj IW: **Generation of GTP-bound Ran by RCC1 is required for chromatin-induced mitotic spindle formation.** *Nature* 1999, **400**:178–181.
314. Ohtsubo M, Okazaki H, Nishimoto T: **The RCC1 protein, a regulator for the onset of chromosome condensation locates in the nucleus and binds to DNA.** *J Cell Biol* 1989, **109**:1389–1397.
315. Cingolani G, Petosa C, Weis K, Müller CW: **Structure of importin- β bound to the IBB domain of importin- α .** *Nature* 1999, **399**:221–229.
316. Ohba T, Nakamura M, Nishitani H, Nishimoto T: **Self-organization of microtubule asters induced in *Xenopus* egg extracts by GTP-bound Ran.** *Science* 1999, **284**:1356–1358.
317. Kalab P, Weis K, Heald R: **Visualization of a Ran-GTP gradient in interphase and mitotic *Xenopus* egg extracts.** *Science* 2002, **295**:2452–2456.
318. Wittmann T, Boleti H, Antony C, Karsenti E, Vernos I: **Localization of the kinesin-like protein Xklp2 to spindle poles requires a leucine zipper, a microtubule-associated protein, and dynein.** *J Cell Biol* 1998, **143**:673–685.
319. Wittmann T, Wilm M, Karsenti E, Vernos I: **TPX2, A novel *xenopus* MAP involved in spindle pole organization.** *J Cell Biol* 2000, **149**:1405–1418.
320. Caudron M, Bunt G, Bastiaens P, Karsenti E: **Spatial coordination of spindle assembly by chromosome-mediated signaling gradients.** *Science* 2005, **309**:1373–1376.
321. Gruss OJ, Carazo-Salas RE, Schatz CA, Guarguaglini G, Kast J, Wilm M, Le Bot N, Vernos I, Karsenti E, Mattaj IW: **Ran Induces Spindle Assembly by Reversing the Inhibitory Effect of Importin α on TPX2 Activity.** *Cell* 2001, **104**:83–93.
322. Safari MS, King MR, Brangwynne CP, Petry S: **Interaction of spindle assembly factor TPX2 with importins- α / β inhibits protein phase separation.** *J Biol Chem* 2021, **297**.
323. King MR, Petry S: **Phase separation of TPX2 enhances and spatially coordinates microtubule nucleation.** *Nat Commun* 2020, **11**:270.
324. Petry S, Groen AC, Ishihara K, Mitchison TJ, Vale RD: **Branching Microtubule Nucleation in *Xenopus* Egg Extracts Mediated by Augmin and TPX2.** *Cell* 2013, **152**:768–777.
325. Zhang R, Roostalu J, Surrey T, Nogales E: **Structural insight into TPX2-stimulated microtubule**

References

- assembly.** *Elife* 2017, **6**:e30959.
326. Setru SU, Gouveia B, Alfaro-Aco R, Shaevitz JW, Stone HA, Petry S: **A hydrodynamic instability drives protein droplet formation on microtubules to nucleate branches.** *Nat Phys* 2021, **17**:493–498.
327. Scrofani J, Sardon T, Meunier S, Vernos I: **Microtubule nucleation in mitosis by a RanGTP-dependent protein complex.** *Curr Biol* 2015, **25**:131–140.
328. Pinyol R, Scrofani J, Vernos I: **The role of NEDD1 phosphorylation by Aurora A in chromosomal microtubule nucleation and spindle function.** *Curr Biol* 2013, **23**:143–149.
329. Zhang Y, Hong X, Hua S, Jiang K: **Reconstitution and mechanistic dissection of the human microtubule branching machinery.** *J Cell Biol* 2022, **221**:e202109053.
330. Goshima G, Mayer M, Zhang N, Stuurman N, Vale RD: **Augmin: a protein complex required for centrosome-independent microtubule generation within the spindle .** *J Cell Biol* 2008, **181**:421–429.
331. Mahoney NM, Goshima G, Douglass AD, Vale RD: **Making microtubules and mitotic spindles in cells without functional centrosomes.** *Curr Biol* 2006, **16**:564–569.
332. Lawo S, Bashkurov M, Mullin M, Ferreria MG, Kittler R, Habermann B, Tagliaferro A, Poser I, Hutchins JRA, Hegemann B, et al.: **HAUS, the 8-Subunit Human Augmin Complex, Regulates Centrosome and Spindle Integrity.** *Curr Biol* 2009, **19**:816–826.
333. Edzuka T, Yamada L, Kanamaru K, Sawada H, Goshima G: **Identification of the Augmin Complex in the Filamentous Fungus *Aspergillus nidulans*.** *PLoS One* 2014, **9**:e101471.
334. Hotta T, Kong Z, Ho C-MK, Zeng CJT, Horio T, Fong S, Vuong T, Lee Y-RJ, Liu B: **Characterization of the Arabidopsis Augmin Complex Uncovers Its Critical Function in the Assembly of the Acentrosomal Spindle and Phragmoplast Microtubule Arrays.** *Plant Cell* 2012, **24**:1494–1509.
335. Nakaoka Y, Miki T, Fujioka R, Uehara R, Tomioka A, Obuse C, Kubo M, Hiwatashi Y, Goshima G: **An Inducible RNA Interference System in *Physcomitrella patens* Reveals a Dominant Role of Augmin in Phragmoplast Microtubule Generation .** *Plant Cell* 2012, **24**:1478–1493.
336. Kimmy Ho C-M, Hotta T, Kong Z, Tracy Zeng CJ, Sun J, Julie Lee Y-R, Liu B: **Augmin Plays a Critical Role in Organizing the Spindle and Phragmoplast Microtubule Arrays in Arabidopsis.** *Plant Cell* 2011, **23**:2606–2618.
337. Liu T, Tian J, Wang G, Yu Y, Wang C, Ma Y, Zhang X, Xia G, Liu B, Kong Z: **Augmin Triggers Microtubule-Dependent Microtubule Nucleation in Interphase Plant Cells.** *Curr Biol* 2014, **24**:2708–2713.
338. Tian J, Kong Z: **The role of the augmin complex in establishing microtubule arrays.** *J Exp Bot* 2019, **70**:3035–3041.
339. Yi P, Goshima G: **Microtubule nucleation and organization without centrosomes.** *Curr Opin Plant Biol* 2018, **46**:1–7.
340. Lee Y-RJ, Hiwatashi Y, Hotta T, Xie T, Doonan JH, Liu B: **The Mitotic Function of Augmin Is Dependent on Its Microtubule-Associated Protein Subunit EDE1 in Arabidopsis thaliana.** *Curr Biol* 2017, **27**:3891–3897.e4.
341. Meireles AM, Fisher KH, Colombié N, Wakefield JG, Ohkura H: **Wac: a new Augmin subunit required for chromosome alignment but not for acentrosomal microtubule assembly in female**

References

- meiosis. *J Cell Biol* 2009, **184**:777–784.
342. Petry S, Pugieux C, Nédélec FJ, Vale RD: **Augmin promotes meiotic spindle formation and bipolarity in *Xenopus* egg extracts.** *Proc Natl Acad Sci U S A* 2011, **108**:14473–14478.
343. Uehara R, Nozawa R, Tomioka A, Petry S, Vale RD, Obuse C, Goshima G: **The augmin complex plays a critical role in spindle microtubule generation for mitotic progression and cytokinesis in human cells.** *Proc Natl Acad Sci U S A* 2009, **106**:6998–7003.
344. David AF, Roudot P, Legant WR, Betzig E, Danuser G, Gerlich DW: **Augmin accumulation on long-lived microtubules drives amplification and kinetochore-directed growth.** *J Cell Biol* 2019, **218**:2150–2168.
345. Almeida AC, Soares-de-Oliveira J, Drpic D, Cheeseman LP, Damas J, Lewin HA, Larkin DM, Aguiar P, Pereira AJ, Maiato H: **Augmin-dependent microtubule self-organization drives kinetochore fiber maturation in mammals.** *Cell Rep* 2022, **39**:110610.
346. Štimac V, Koprivec I, Manenica M, Simunić J, Tolić IM: **Augmin prevents merotelic attachments by promoting proper arrangement of bridging and kinetochore fibers.** *Elife* 2022, **11**:e83287.
347. Trupinić M, Kokanović B, Ponjavić I, Barišić I, Šegvić S, Iveć A, Tolić IM: **The chirality of the mitotic spindle provides a mechanical response to forces and depends on microtubule motors and augmin.** *Curr Biol* 2022, **32**:2480–2493.e6.
348. Kamasaki T, O'Toole E, Kita S, Osumi M, Usukura J, McIntosh JR, Goshima G: **Augmin-dependent microtubule nucleation at microtubule walls in the spindle.** *J Cell Biol* 2013, **202**:25–33.
349. Weiner AT, Thyagarajan P, Shen Y, Rolls MM: **To nucleate or not, that is the question in neurons.** *Neurosci Lett* 2021, **751**:135806.
350. Sanchez-Huertas C, Freixo F, Viais R, Lacasa C, Soriano E, Luders J: **Non-centrosomal nucleation mediated by augmin organizes microtubules in post-mitotic neurons and controls axonal microtubule polarity.** *Nat Commun* 2016, **7**:12187.
351. Viais R, Fariña-Mosquera M, Villamor-Payà M, Watanabe S, Palenzuela L, Lacasa C, Lüders J: **Augmin deficiency in neural stem cells causes p53-dependent apoptosis and aborts brain development.** *Elife* 2021, **10**:e67989.
352. Cunha-Ferreira I, Chazeau A, Buijs RR, Stucchi R, Will L, Pan X, Adolfs Y, van der Meer C, Wolthuis JC, Kahn OI, et al.: **The HAUS Complex Is a Key Regulator of Non-centrosomal Microtubule Organization during Neuronal Development.** *Cell Rep* 2018, **24**:791–800.
353. So C, Seres KB, Steyer AM, Mönnich E, Clift D, Pejkovska A, Möbius W, Schuh M: **A liquid-like spindle domain promotes acentrosomal spindle assembly in mammalian oocytes.** *Science* 2019, **364**.
354. Watanabe S, Shioi G, Furuta Y, Goshima G: **Intra-spindle Microtubule Assembly Regulates Clustering of Microtubule-Organizing Centers during Early Mouse Development.** *Cell Rep* 2016, **15**:54–60.
355. Alfaro-Aco R, Thawani A, Petry S: **Biochemical reconstitution of branching microtubule nucleation.** *Elife* 2020, **9**.
356. Thawani A, Stone HA, Shaevitz JW, Petry S: **Spatiotemporal organization of branched microtubule networks.** *Elife* 2019, **8**.
357. Goshima G: **Identification of a TPX2-Like Microtubule-Associated Protein in *Drosophila*.** *PLoS*

References

- One* 2011, **6**:e28120.
358. Verma V, Maresca TJ: **Direct observation of branching MT nucleation in living animal cells.** *J Cell Biol* 2019, **218**:2829–2840.
359. Tariq A, Green L, Jeynes JCG, Soeller C, Wakefield JG: **In vitro reconstitution of branching microtubule nucleation.** *Elife* 2020, **9**.
360. Sánchez-Huertas C, Lüders J: **The Augmin Connection in the Geometry of Microtubule Networks.** *Curr Biol* 2015, **25**:R294–R299.
361. Luo J, Yang B, Xin G, Sun M, Zhang B, Guo X, Jiang Q, Zhang C: **The microtubule-associated protein EML3 regulates mitotic spindle assembly by recruiting the Augmin complex to spindle microtubules.** *J Biol Chem* 2019, **294**:5643–5656.
362. Wu G, Wei R, Cheng E, Ngo B, Lee W-H: **Hec1 Contributes to Mitotic Centrosomal Microtubule Growth for Proper Spindle Assembly through Interaction with Hice1.** *Biol Cell* 2009, **20**:4686–4695.
363. Bucciarelli E, Pellacani C, Naim V, Palena A, Gatti M, Somma MP: **Drosophila Dgt6 Interacts with Ndc80, Msps/XMAP215, and γ -Tubulin to Promote Kinetochores-Driven MT Formation.** *Curr Biol* 2009, **19**:1839–1845.
364. Hsia K-C, Wilson-Kubalek EM, Dottore A, Hao Q, Tsai K-L, Forth S, Shimamoto Y, Milligan RA, Kapoor TM: **Reconstitution of the augmin complex provides insights into its architecture and function.** *Nat Cell Biol* 2014, **16**:852–863.
365. Song J-G, King MR, Zhang R, Kadzik RS, Thawani A, Petry S: **Mechanism of how augmin directly targets the gamma-tubulin ring complex to microtubules.** *J Cell Biol* 2018, **217**:2417–2428.
366. Wu G, Lin Y-T, Wei R, Chen Y, Shan Z, Lee W-H: **Hice1, a novel microtubule-associated protein required for maintenance of spindle integrity and chromosomal stability in human cells.** *Mol Cell Biol* 2008, **28**:3652–3662.
367. Bucciarelli E, Pellacani C, Naim V, Palena A, Gatti M, Somma MP: **Drosophila Dgt6 interacts with Ndc80, Msps/XMAP215, and gamma-tubulin to promote kinetochores-driven MT formation.** *Curr Biol* 2009, **19**:1839–1845.
368. Zhu H, Coppinger JA, Jang C-Y, Yates III JR, Fang G: **FAM29A promotes microtubule amplification via recruitment of the NEDD1- γ -tubulin complex to the mitotic spindle.** *J Cell Biol* 2008, **183**:835–848.
369. Zupa E, Würtz M, Neuner A, Hoffmann T, Rettel M, Böhler A, Vermeulen BJA, Eustermann S, Schiebel E, Pfeffer S: **The augmin complex architecture reveals structural insights into microtubule branching.** *Nat Commun* 2022, **13**.
370. Tsai CY, Ngo B, Tapadia A, Hsu P-H, Wu G, Lee W-H: **Aurora-A Phosphorylates Augmin Complex Component Hice1 Protein at an N-terminal Serine/Threonine Cluster to Modulate Its Microtubule Binding Activity during Spindle Assembly*.** *J Biol Chem* 2011, **286**:30097–30106.
371. Würtz M, Böhler A, Neuner A, Zupa E, Rohland L, Liu P, Vermeulen BJA, Pfeffer S, Eustermann S, Schiebel E: **Reconstitution of the recombinant human γ -tubulin ring complex.** *Open Biol* 2021, **11**:200325.
372. Würtz M, Zupa E, Atorino ES, Neuner A, Böhler A, Rahadian AS, Vermeulen BJA, Tonon G, Eustermann S, Schiebel E, et al.: **Modular assembly of the principal microtubule nucleator γ -**

References

- TuRC**. *Nat Commun* 2022, **13**:473.
373. Zimmermann F, Serna M, Ezquerro A, Fernandez-Leiro R, Llorca O, Luders J: **Assembly of the asymmetric human γ -tubulin ring complex by RUVBL1-RUVBL2 AAA ATPase**. *Sci Adv* 2020, **6**:eabe0894.
374. Wieczorek M, Ti S-C, Urnavicius L, Molloy KR, Aher A, Chait BT, Kapoor TM: **Biochemical reconstitutions reveal principles of human γ -TuRC assembly and function**. *J Cell Biol* 2021, **220**.
375. Jinek M, Chylinski K, Fonfara I, Hauer M, Doudna JA, Charpentier E: **A programmable dual-RNA-guided DNA endonuclease in adaptive bacterial immunity**. *Science* 2012, **337**:816–821.
376. Taylor SS, Hussein D, Wang Y, Elderkin S, Morrow CJ: **Kinetochores localisation and phosphorylation of the mitotic checkpoint components Bub1 and BubR1 are differentially regulated by spindle events in human cells**. *J Cell Sci* 2001, **114**:4385–4395.
377. Atorino ES, Hata S, Funaya C, Neuner A, Schiebel E: **CEP44 ensures the formation of bona fide centriole wall, a requirement for the centriole-to-centrosome conversion**. *Nat Commun* 2020, **11**:903.
378. Komarova Y, De Groot CO, Grigoriev I, Gouveia SM, Munteanu EL, Schober JM, Honnappa S, Buey RM, Hoogenraad CC, Dogterom M, et al.: **Mammalian end binding proteins control persistent microtubule growth**. *J Cell Biol* 2009, **184**:691–706.
379. Hayashi I, Ikura M: **Crystal structure of the amino-terminal microtubule-binding domain of end-binding protein 1 (EB1)**. *J Biol Chem* 2003, **278**:36430–36434.
380. Dauden MI, López-Perrote A, Llorca O: **RUVBL1-RUVBL2 AAA-ATPase: a versatile scaffold for multiple complexes and functions**. *Curr Opin Struct Biol* 2021, **67**:78–85.
381. Lüders J, Patel UK, Stearns T: **GCP-WD is a γ -tubulin targeting factor required for centrosomal and chromatin-mediated microtubule nucleation**. *Nat Cell Biol* 2006, **8**:137–147.
382. Zhu Z, Becam I, Tovey CA, Elfarkouchi A, Yen EC, Bernard F, Guichet A, Conduit PT: **Multifaceted modes of γ -tubulin complex recruitment and microtubule nucleation at mitotic centrosomes**. *J Cell Biol* 2023, **222**:e202212043.
383. Pesenti ME, Prumbaum D, Auckland P, Smith CM, Faesen AC, Petrovic A, Erent M, Maffini S, Pentakota S, Weir JR, et al.: **Reconstitution of a 26-Subunit Human Kinetochores Reveals Cooperative Microtubule Binding by CENP-OPQUR and NDC80**. *Mol Cell* 2018, **71**:923–939.e10.
384. Walstein K, Petrovic A, Pan D, Hagemeyer B, Vogt D, Vetter IR, Musacchio A: **Assembly principles and stoichiometry of a complete human kinetochores module**. *Sci Adv* 2021, **7**:eabg1037.
385. Kriz A, Schmid K, Baumgartner N, Ziegler U, Berger I, Ballmer-Hofer K, Berger P: **A plasmid-based multigene expression system for mammalian cells**. *Nat Commun* 2010, **1**:120.
386. Mansouri M, Bellon-Echeverria I, Rizk A, Ehsaei Z, Cianciolo Cosentino C, Silva CS, Xie Y, Boyce FM, Davis MW, Neuhauss SCF, et al.: **Highly efficient baculovirus-mediated multigene delivery in primary cells**. *Nat Commun* 2016, **7**:11529.
387. Yin C, Lui ESW, Jiang T, Qi RZ: **Proteolysis of γ -tubulin small complex proteins is mediated by the ubiquitin-proteasome system**. *FEBS Lett* 2021, **595**:1987–1996.
388. Grand RS, Burger L, Gräwe C, Michael AK, Isbel L, Hess D, Hoerner L, Iesmantavicius V, Durdu S, Pregnotato M, et al.: **BANP opens chromatin and activates CpG-island-regulated genes**. *Nature* 2021, **596**:133–137.

References

389. Jungblut A, Hopfner K-P, Eustermann S: **Megadalton chromatin remodelers: common principles for versatile functions.** *Curr Opin Struct Biol* 2020, **64**:134–144.
390. Bahtz R, Seidler J, Arnold M, Haselmann-Weiss U, Antony C, Lehmann WD, Hoffmann I: **GCP6 is a substrate of Plk4 and required for centriole duplication.** *J Cell Sci* 2012, **125**:486–496.
391. Plessner M, Knerr J, Grosse R: **Centrosomal Actin Assembly Is Required for Proper Mitotic Spindle Formation and Chromosome Congression.** *iScience* 2019, **15**:274–281.
392. Nejedlá M, Klebanovych A, Sulimenko V, Sulimenko T, Dráberová E, Dráber P, Karlsson R: **The actin regulator profilin 1 is functionally associated with the mammalian centrosome.** *Life Sci Alliance* 2021, **4**:e202000655.
393. Rale MJ, Romer B, Mahon BP, Travis SM, Petry S: **The conserved centrosomin motif, γ TuNA, forms a dimer that directly activates microtubule nucleation by the γ -tubulin ring complex (γ TuRC).** *Elife* 2022, **11**:e80053.
394. Wimbish RT, DeLuca JG: **Hec1/Ndc80 Tail Domain Function at the Kinetochores-Microtubule Interface** . *Front Cell Dev Biol* 2020, **8**.
395. Zaytsev A V, Mick JE, Maslennikov E, Nikashin B, DeLuca JG, Grishchuk EL: **Multisite phosphorylation of the NDC80 complex gradually tunes its microtubule-binding affinity.** *Mol Biol Cell* 2015, **26**:1829–1844.
396. Gabel CA, Li Z, DeMarco AG, Zhang Z, Yang J, Hall MC, Barford D, Chang L: **Molecular architecture of the augmin complex.** *Nat Commun* 2022, **13**:5449.
397. Travis SM, Mahon BP, Huang W, Ma M, Rale MJ, Kraus J, Taylor DJ, Zhang R, Petry S: **Integrated model of the vertebrate augmin complex.** *Nat Commun* 2023, **14**:2072.
398. Manka SW: **Structural insights into how augmin augments the mitotic spindle.** *Nat Commun* 2023, **14**:2073.
399. Watson JL, Juergens D, Bennett NR, Trippe BL, Yim J, Eisenach HE, Ahern W, Borst AJ, Ragotte RJ, Milles LF, et al.: **De novo design of protein structure and function with RFdiffusion.** *Nature* 2023, **620**:1089–1100.
400. van Breugel M, Rosa e Silva I, Andreeva A: **Structural validation and assessment of AlphaFold2 predictions for centrosomal and centriolar proteins and their complexes.** *Commun Biol* 2022, **5**:312.
401. Mitani T, Punetha J, Akalin I, Pehlivan D, Dawidziuk M, Coban Akdemir Z, Yilmaz S, Aslan E, Hunter J V, Hijazi H, et al.: **Bi-allelic Pathogenic Variants in TUBGCP2 Cause Microcephaly and Lissencephaly Spectrum Disorders.** *Am J Hum Genet* 2019, **105**:1005–1015.
402. Li L, Sha Y-W, Su Z-Y, Mei L-B, Ji Z-Y, Zhang Q, Lin S-B, Wang X, Qiu P-P, Li P, et al.: **A novel mutation in HAUS7 results in severe oligozoospermia in two brothers.** *Gene* 2018, **639**:106–110.
403. Schindelin J, Arganda-Carreras I, Frise E, Kaynig V, Longair M, Pietzsch T, Preibisch S, Rueden C, Saalfeld S, Schmid B, et al.: **Fiji: an open-source platform for biological-image analysis.** *Nat Methods* 2012, **9**:676.
404. Zivanov J, Nakane T, Forsberg BO, Kimanius D, Hagen WJH, Lindahl E, Scheres SHW: **New tools for automated high-resolution cryo-EM structure determination in RELION-3.** *Elife* 2018, **7**:e42166.
405. Zhang K: **Gctf: Real-time CTF determination and correction.** *J Struct Biol* 2016, **193**:1–12.

References

406. Pettersen EF, Goddard TD, Huang CC, Couch GS, Greenblatt DM, Meng EC, Ferrin TE: **UCSF Chimera—A visualization system for exploratory research and analysis.** *J Comput Chem* 2004, **25**:1605–1612.
407. Kidmose RT, Juhl J, Nissen P, Boesen T, Karlsen JL, Pedersen BP: **Namdinator - automatic molecular dynamics flexible fitting of structural models into cryo-EM and crystallography experimental maps.** *IUCrJ* 2019, **6**:526–531.